Dissertation zur Erlangung des Doktorgrades

der Fakultät für Chemie und Pharmazie

der Ludwig-Maximilians-Universität München

Synthesis route for ultra-small nanoparticles for energy applications

Johann Martin Feckl

aus

Landshut, Deutschland

2013

Erklärung

Diese Dissertation wurde im Sinne von § 7 der Promotionsordnung vom 28. November 2011 von Herrn Prof. Dr. Thomas Bein betreut.

Eidesstattliche Versicherung

Diese Dissertation wurde eigenständig und ohne unerlaubte Hilfe bearbeitet.

München,

Johann Feckl

Dissertation eingereicht am 10.05.2013

1. Gutachter: Prof. Dr. Thomas Bein
2. Gutachter: Prof. Dr. Dina Fattakhova-Rohlfing

Mündliche Prüfung am 11.06.2013

Danksagung

Zuallererst möchte ich mich bei meinem Doktorvater Prof. Thomas Bein herzlich für die freundliche Aufnahme in seine Gruppe und das entgegengebrachte Vertrauen bedanken. Er gab mir die Möglichkeit eigenständig an einem sehr spannenden und zukunftsorientierten Projekt zu arbeiten. Dank seiner Unterstützung konnte ich meine Ergebnisse vielfach in Vorträgen und Postern auf nationalen und internationalen Konferenzen präsentieren und mich aufgrund seiner bereitgestellten Empfehlungsschreiben für den Römer-Preis (Masterarbeit) sowie für den E-MRS Graduate Student Award 2013 bewerben.

Prof. Dina Fattakhova-Rohlfing möchte ich ebenfalls sehr herzlich danken für die freundschaftliche Zusammenarbeit mit sehr erfolgreichem Ausgang über meine gesamte Doktorarbeit hinweg. Dies liegt unter anderem an den vielen kreativen Diskussionen und daraus entstandenen Ideen, sowie ihrer elektrochemischen Expertise. Zusätzlich bedanke ich mich für ihre großartige Hilfe beim Schreiben und Korrigieren der Veröffentlichungen und für die Erstellung des Zweitgutachtens zu dieser Arbeit.

Halina Dunn möchte ich für die sehr gut laufende Zusammenarbeit auf dem Gebiet der photokatalytischen Wasserspaltung danken. Bei meinen Kooperationspartnern aus Stanford, USA, George Margulis und Prof. Michael McGehee möchte ich mich für die fruchtbare Zusammenarbeit auf dem Gebiet der Energy Relay Dyes für Farbstoffsolarzellen bedanken. Des Weiteren möchte ich mich für die Krypton Sorptions-Messungen sowie die exzellente Zusammenarbeit beim Schreiben der gemeinsamen Veröffentlichungen bei meinen Kooperationspartnern Dr. Jiri Rathousky und Vit Kalousek vom J. Heyrovsky Institut in Prag bedanken. Florian Hinterholzinger, Bastian Rühle und Annekathrin Ranft (AK Lotsch) möchte ich für die Kooperation im Bereich der Bragg stacks danken. Yujing Liu danke ich für die Zusammenarbeit im Bereich der (Nb-)Titandioxid-Synthesen. Ksenia Fominykh danke ich für die tolle Zusammenarbeit beginnend mit ihrem F-Praktikum über die HIWI-Zeit und Masterarbeit hinweg bis zu ihrer Doktorarbeit. Markus Döblinger und Alexander Müller danke ich für die exzellenten TEM Bilder ohne die unsere Veröffentlichungen nicht möglich gewesen wären. Bei Johann Szeifert möchte ich mich ganz besonders für die sehr gute Betreuung während meiner Masterarbeit im Arbeitskreis Bein und dafür, dass er ein super Schreibtischnachbar war, bedanken.

Natürlich möchte ich mich auch bei meinen ganzen F-Praktikanten, NIM und RISE Studenten für die gute Arbeit im Labor bedanken: Masa, Ksenia, Kathleen, Felix, Peter, Jane, Simon, Laura, Julian, Matt, Petra, David. Alyssa und Sam möchte ich vor allem auch für die neu gewonnen Freundschaften danken, die sogar über den Atlantik hinweg aktiv gepflegt werden.

Die ausgezeichnete Zeit während der Doktorarbeit ist vor allem einem zu verdanken: Meinen wunderbaren Kollegen im Arbeitskreis Bein, die ich über die Jahre hinweg kennenlernen durfte. Die exzellenten Partys, Grillfeste, Weihnachtsfeiern, Wiesnbesuche und Stammtische sind und bleiben unvergessen und ergeben ein unerschöpfliches Sammelsurium an Anekdoten. Vielen Dank auch dafür, dass ihr immer bei allem, was ich (nicht nur) in meinem Gutscheinwahn organisiert habe, dabei wart (ich denke, es hat sich nicht nur finanziell gelohnt ;-)!

Das man es hier so lange aushalten kann, liegt auch daran, dass ich immer äußerst nette Bürokollegen hatte, die einem auch immer hilfreich zur Seite standen: Johann, Benni, Flo Aurator, Norma, Stefan, Fabi, Ilina und Mona, vielen Dank!

Wie Hiho schon sagte, war Sorrent ein Top-Einstieg in die große weite Welt der Konferenzen, die natürlich ohne gute Kollegen nur halb so spannend gewesen wären! Highlights waren dabei San Francisco mit Hiho, Mirjam und Benni; Valencia mit Benni und Flo; Hannover mit Stefan; 2xVenedig mit der CeNS Truppe und auch die Sol-tech meetings mit den ganzen „Solar“-Kollegen. Unser Workshop auf der Tutzinger Hütte war auch der Hammer, neben den ganzen super Vorträgen vor allem auch wegen des tollen Wetters und der atemberaubenden Aussicht.

Norma, Basti, Mona und Flo möchte ich für die vielen tollen Spieleabende danken und für eure Bereitschaft, immer wieder neue, „hochkomplexe“ Regeln von neuen Spielen mit mir zu enträtseln. Flo Hiho möchte ich nochmal für seine „weibliche“ Seite und sein Auftreten als Mediator und guter Zuhörer in allen Lagen danken; Benni dafür, dass er uns immer wieder darauf hingewiesen hat, wie das denn jetzt in einer Firma geregelt werden würde (kurzer Dienstweg und privater Druckjob!). Stefan danke ich für die gute „Nachbarschaft“ und die gemeinsame Ahnungslosigkeit beim Aktienhandel. Jörg, Christian, Alex, Fabi, Halina, Dana, Maria, Alesja, Enrico, Erika, Cindy, Ksenia, Noggi, Andi, Martina, Stefan D., Adrien, Lissi, Karin, Sonni, Anderl, Camilla, Valentina, Ralf, Doro, Keili, Axel, Johann, Yan und Yujing sind oder waren ebenfalls sehr gute Kollegen im AK Bein, vielen Dank euch allen für die gute Zeit!

Besonderer Dank geht an Tina für zahllose Messungen und Hilfe bei allen möglichen Dingen, an Steffen, Flo, Benni und Basti für unzählige SEM-Sessions und an Basti nochmal für die tollen POV-ray Bilder. Markus, danke nochmal für die TEM Untersuchungen und für die Überraschtheit, dass so jemand wie ich so kleine Dinger herstellen kann und die Proben selten „Schlonze“ waren. Regina möchte ich für ihr offenes Ohr in allen Belangen und die großartige Hilfe bei allem Organisatorischen danken, ohne dich wären wir schon längst alle von den Mühlen der Bürokratie unerbittlich zermahlen worden.

Ganz besonders möchte ich Norma dafür danken, dass wir gemeinsam eine so schöne Zeit verbringen konnten und dass sie die stressige Endphase der Promotion mit mir gemeinsam überstanden hat.

Der größte Dank gilt meinen Eltern, meiner Schwester und meiner ganzen Familie für ihre großartige Unterstützung während meines gesamten Studiums und der Doktorarbeit. Ohne Euch wäre all dies niemals möglich gewesen!

Abstract

One of the most demanding fields of research in this century is the development of sustainable and high performance energy conversion and storage technologies. This goal is closely connected to the development of suitable materials. In addition to the design of completely new materials, the properties of already existing materials can be improved and modified by nanostructuring. Nanostructuring has the potential for greatly enhancing the performance of materials in many applications, for example due to an increased surface area and short diffusion pathways in porous systems. For example, a new generation of non-silicon solar cells or water splitting devices for a hydrogen economy can benefit significantly from nanostructuring of the utilized materials. Additionally, high energy density battery systems for mobile devices or electro-mobility with short charging times can be realized in this way. Hence, green, non-toxic and low-temperature bottom-up syntheses of nanomaterials and their building blocks with defined properties are of great interest.

This thesis is focused on the synthesis of nanomaterials for energy storage and conversion applications, such as lithium ion batteries, dye-sensitized solar cells and photoelectrochemical water splitting. In order to achieve this, we have developed a novel synthesis approach based on solvothermal reactions in *tert*-butanol to obtain ultra-small, crystalline metal-oxide nanoparticles. In these reactions *tert*-butanol acts both as solvent and as reactant. The nanoparticles obtained in this way exhibit a very good dispersibility and extremely small sizes down to about 3 nm. These features make them promising building blocks for low-temperature bottom-up syntheses of porous nanomaterials via surfactant templated evaporation-induced self-assembly. Additionally, due to the small size and the good dispersibility, the nanoparticles can be homogeneously distributed on the surface of pre-formed porous nanostructures for catalytic applications. The absence of aromatic ligands on

the nanoparticle surface enables a very good electrical accessibility in the above-mentioned electronic applications.

The first successful nanoparticle synthesis in *tert*-butanol was accomplished for ultrasmall crystalline titania in a non-aqueous, fast and low-temperature microwave heating procedure. The titania nanoparticles have an extremely small size down to 3 nm and are highly dispersible without any additional stabilizing agents. Based on these features, the nanoparticles can be assembled to form crystalline mesoporous titania films using commercial Pluronic surfactants. The films possess a high surface area up to 300 $m^2 g^{-1}$ after template removal. Additionally, the films exhibit a high crystallinity due to a seeding effect of the nanoparticles. The advantages of the extremely thin nanocrystalline walls were shown in electrochemical lithium insertion experiments. The mesoporous films exhibited 10-fold increased insertion kinetics due to shortened ion diffusion pathways compared to a reference sample prepared from 20 nm anatase particles (Chapter 3).

The very high surface area of these mesoporous titania films can also be very advantageous for the application as photoanodes in thin dye-sensitized solar cells (DSCs), as the dye adsorption and thus the produced photocurrent are related to the surface area. The optimized standard procedure based on the self-assembly of nanoparticles with surfactants leads to films consisting of individual layers with a thickness below 700 nm, which are still too thin to be used in DSCs. We have developed a protocol to make thicker films by adding ethyl cellulose to the coating solutions. In this way, films of up to 2 µm per layer can be produced. Multiple coatings of these layers enabled the preparation of films of up to 10 µm thickness, which showed high efficiencies of 7.7 % in dye-sensitized solar cells (Chapter 4). Another application of thin titania layers is shown in Chapter 5 where their integration as high refractive-index porous layers in Bragg stacks for chemical vapor sorption is demonstrated.

The electrical properties of the titania nanoparticles and the resulting films can also be modified by doping the nanoparticles with niobium in an adapted *tert*-butanol nanoparticle synthesis yielding particles with sizes of about 4 – 5 nm. Nb-doped titania is a transparent conducting oxide that is highly interesting for optoelectronic devices. Mesoporous films with an increased conductivity compared to pure titania were prepared with Pluronic F127 as a structure-directing agent in a self-assembly procedure (Chapter 6).

The concept of decreasing the ion diffusion pathways in lithium ion batteries shown for titania films was extended to lithium titanate (LTO). LTO is a zero strain anode material for lithium ion batteries that is also used in commercially available devices (Chapter 7). This material was prepared in a non-aqueous solvothermal synthesis in *tert*-butanol. The fully crystalline interconnected mesoporous frameworks assembled by surfactant templating led to the fastest insertion of lithium ever reported. It features a gravimetric capacity of about 175 mA h g^{-1} and delivers up to 73 % of the maximum capacity at up to 800 C (4.5 s) without deterioration over 1000 cycles. The key to this performance are ultrasmall spinel nanocrystals of only a few nanometers in size that are used to construct the pore walls.

The final parts of this thesis mainly focus on the development of active materials and catalysts for (photo-) electrochemical water splitting. Ultra-small and dispersible nickel oxide nanoparticles were synthesized in *tert*-butanol with tunable sizes from 2.5 – 6 nm and assembled into thin film electrodes for electrochemical water splitting (Chapter 8). The onset potential for the oxygen evolution reaction was reduced by 180 mV, demonstrating the highly efficient catalytic properties of the material. The very small size of the nanoparticles and hence the resulting high surface to volume ratio leads to exceptionally high turn-over frequencies even outperforming expensive rare earth iridium oxide catalysts.

Another active material that is applied in photoelectrochemical water splitting is iron oxide in the form of hematite. However, the performance of hematite is strongly limited due to small electron and hole diffusion coefficients. These issues can be addressed by hematite nanostructuring, which was achieved in a sol-gel surfactant directed synthesis in *tert*-butanol. Furthermore, the addition of a Sn-precursor to the synthesis led to an enhanced performance of the mesoporous electrodes in photoelectrochemical water splitting by reducing recombination processes at the surface (Chapter 9). For a further reduction of recombination, a synthesis of ultra-small and highly dispersible cobalt oxide nanoparticles in *tert*-butanol was developed and the particles were homogeneously distributed on the surface and in the pores of the Sn-containing hematite host (Chapter 10). This surface treatment leads to a further increase in photocurrent by about 340 % attributed to substantially reduced recombination.

In conclusion, a general synthesis approach for ultra-small, crystalline and dispersible nanoparticles of various metal oxides in *tert*-butanol was successfully developed. The unique properties of the nanoparticles and the resulting porous nanostructures built thereof enabled high performance applications in various energy conversion and storage systems, such as dye-sensitized solar cells, photoelectrochemical water splitting and lithium ion batteries.

Table of contents

1 Introduction

1.1 Introduction to Nanotechnology

„A biological system can be exceedingly small. Many of the cells are very tiny, but they are very active; they manufacture various substances; they walk around; they wiggle; and they do all kinds of marvelous things – all on a very small scale. Also, they store information. Consider the possibility that we too can make a thing very small, which does what we want – that we can manufacture an object that maneuvers at that level!"[1]

This lecture given by Richard Feynman is often considered to be the founder's charta of nanotechnology. A common definition of nanomaterials is that at least one dimension of an object is on the length scale of less than about 100 nanometers (1 nm is a billionth of a meter or 10^{-9} m). This extremely small size compared to bulk materials often leads to drastically changed properties of materials, such as their color, melting point, electronic, catalytic or magnetic properties.[2] The changed or completely new properties often result from the increased fraction of surface atoms compared to the total number of atoms in a nanomaterial, which is called a size effect.[3] Nanotechnology in the media is often considered to be an advanced research field of the 21st century with exciting new improvements for everyday life such as the lotus effect or nano-carpolish for example, but it also dates back to previous centuries. One of the most prominent examples is the application of metal colloids, already in ancient times, for the coloration of glassware.[4] However, the techniques for the characterization of nanomaterials were developed much later, exemplified by the first scanning tunneling microscope in 1981 by Binnig and Rohrer.[5] The development of additional techniques such as atomic force microscopy combined with the well-established transmission electron microscopy allowed for the characterization and manipulation of materials down to

the atomic level.[6] This toolbox of techniques made it possible to develop and characterize a manifold of nanomaterials and made nanotechnology one of the most dynamic growing fields of research. This interdisciplinary field of research involves solid-state physicists, organic and inorganic chemists, physical chemists, colloid chemists, materials scientists, and more recently, biological scientists, medical scientists, and engineers. This non-exhaustive list shows the broad basis of nanotechnology, which has brought about applications in numerous fields such as materials and manufacturing, nanoelectronics, medicine and healthcare, biotechnology, catalysis and information and energy technologies.

The preparation techniques of nanomaterials can basically be divided into two categories, namely top-down and bottom-up approaches. A typical example for the top-down method is attrition or ball milling in which matter is ground until it is in the dimension of the nanoscale. This process inevitably leads to surface imperfections and broad size distributions of the resulting nanoobjects. Contrary to that, the bottom-up approach enables the production and build-up of materials from the bottom by assembling atoms, molecules or clusters, so that the resulting materials exhibit less defects, a more homogeneous chemical composition and a better short and long range ordering compared to materials prepared by top-down approaches such as milling.[6] The chemical synthesis of nanomaterials or the self-assembly of DNA origami can be named as examples.[7]

One of the most demanding fields of research in this century will be the development of sustainable and high performance energy technologies. Examples for it are low-cost solar cells or water splitting devices for a hydrogen economy and high energy density battery systems for mobile devices or electro-mobility, which can benefit drastically from nanostructuring of the utilized materials. Therefore, green, non-toxic and low-temperature bottom-up syntheses of nanomaterials and their building blocks with defined properties would

be desirable, this was also the focus of this work. In the following, a chemical bottom-up synthesis method for ultra-small metal-oxide nanoparticles in *tert*-butanol is described. These were applied as building blocks for porous materials or as homogeneously distributed catalytic particles on porous hosts and showed excellent properties in applications such as energy conversion and storage. The following introduction guides the reader through the different methods for nanoparticle syntheses and mesoporous materials and then describes the application fields of dye-sensitized solar cells, battery materials and photo-electrochemical water splitting devices.

1.2 Introduction to metal oxide nanoparticle synthesis methods

Nanoparticle research is an important field in nanotechnology not only because of the interesting intrinsic properties of nanoparticles but also because of the possibility of using them as building blocks for the assembly of more sophisticated nanostructures. The structural, morphological, compositional and surface characteristics of the nanoparticles have to be precisely defined and uniform to be suitable for the preparation of such complex superstructures. Nanoparticles with a defined size and a narrow size distribution, high crystallinity, and good dispersibility can be obtained by bottom-up synthetic approaches. Physical bottom-up methods of nanoparticle synthesis, such as the pyrolysis of liquid and gaseous metal precursors or physical vapor deposition techniques either lead to large aggregates or agglomerates or are slow and expensive, respectively.[8] Wet chemical synthesis pathways on the other hand can be versatile routes for the synthesis of metal oxide nanoparticles with desired properties.[9] The main techniques include the co-precipitation of salts in solution, the sol-gel processes and hydrothermal and solvothermal routes.[9-11]

Sol-gel reactions

Sol-gel processing dates back to 1846 and refers to the hydrolysis and condensation of metal halide or alkoxide-based precursors such as titanium tetrachloride ($TiCl_4$) or tetraethyl orthosilicate ($Si(OEt)_4$).[12,13] This method allows the formation of molecular nanoclusters, nanoparticles, or polymer-like metal oxide networks depending on the processing and the degree of condensation of the metal-organic precursors (Figure 1-1).[14,15] The reaction stages of the sol-gel process can be generally described by several distinct steps disregarding the nature of the precursors:

Step 1: Formation of stable solutions of the molecular metal precursor (the sol).

Step 2: Condensation reactions leading to the formation of an oxide- or alcohol-bridged network with increasing viscosity (the gel).

Step 3: Ageing of the gel (syneresis) by polycondensation mechanisms and formation of a solid mass upon contraction of the gel network and expulsion of solvent from the gel pores.

Step 4: Drying of the gel upon removal of water and solvents by either thermal treatment (xerogel) or by extraction at super-critical conditions (aerogel).

Step 5: Removal of surface-bound M-OH groups and stabilizing the gel against rehydration at high temperatures up to 800 °C and optional densification and decomposition of the gels at temperatures above 800 °C for the preparation of dense ceramics or glasses, for example.

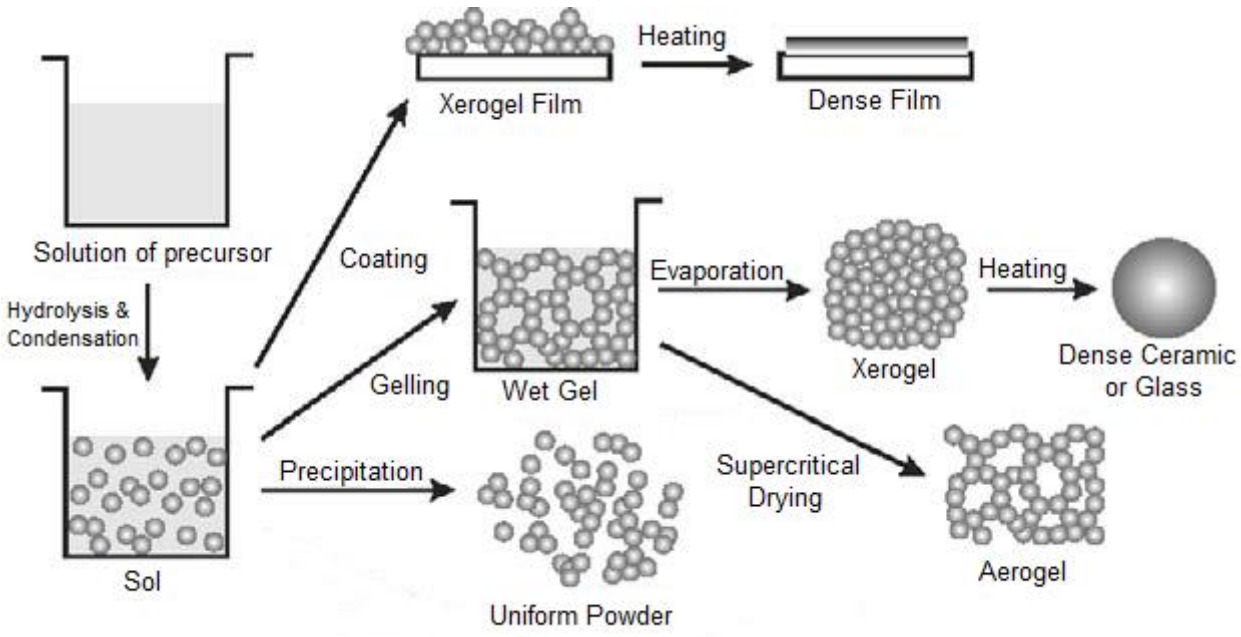

Figure 1-1: Various steps and resulting products in the sol-gel process. Figure adapted from Ref 16.

Sol-gel processes are conducted either in aqueous (hydrolytic) or non-aqueous (non-hydrolytic) solvents. The aqueous sol-gel chemistry is quite complex due to the double role of water as ligand and solvent and the high reactivity of the metal oxide precursors towards water. Additionally, the high number of reaction parameters, such as temperature, pH value, the hydrolysis and condensation rate of the metal oxide precursors and the method of mixing thereof have to be strictly controlled to allow reproducible syntheses.[17] The resulting precipitates of the aqueous sol-gel reactions are generally amorphous and therefore require additional post-synthetic annealing steps to induce the crystallization of the materials (if crystalline materials are desired). Hence, the control over crystal size and shape is very limited and therefore the aqueous synthesis pathways are more suitable for the synthesis of bulk metal oxides rather than nanoparticles.[16] In contrast, non-aqueous (or non-hydrolytic) sol-gel processes are conducted under the exclusion of water in organic solvents.[18,19] This difference leads to several advantages over the aqueous methods, resulting in the possibility to produce crystalline metal oxide nanoparticles with uniform crystallite sizes in the range of a few nanometers that exhibit good dispersibility in organic solvents. The advantages result

from the multiple roles of the organic solvents (ethers, alcohols, ketones or aldehydes) in the reaction. The solvent can also act as oxygen-supplier for the oxide formation and as organic ligand of the metal precursor molecule, as surfactant, or as a source of in situ formed organic condensation products. This, together with slower reaction rates due to the moderate reactivity of the oxygen carbon bond - compared to aqueous systems - enables the preparation of nanoparticles with defined particle sizes and shapes, being well dispersible in organic solvents.[20-22]

The main condensation steps in non-aqueous systems for the formation of the metal-oxygen-metal bond can be described in five distinct pathways depending on the utilized solvents (Scheme 1):[16,19,23]

Alkyl halide elimination

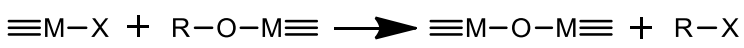

Ether elimination

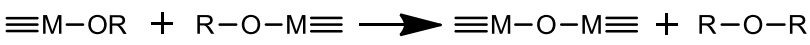

Condensation of carboxylate groups (ester and amide eliminations)

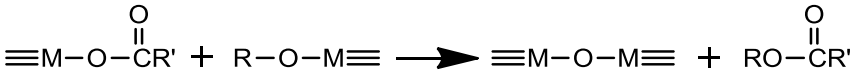

C-C coupling of benzylic alcohols and alkoxide molecules

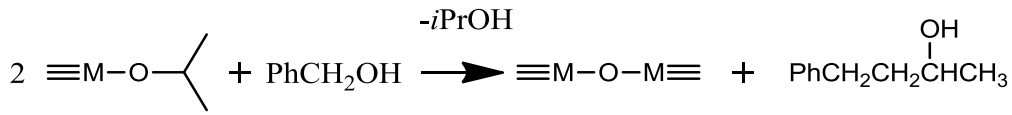

Aldol condensation

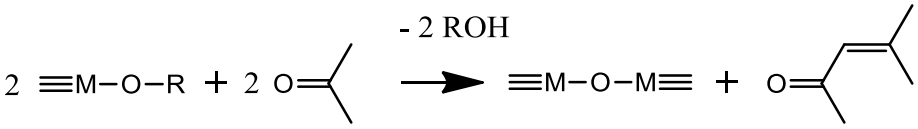

Scheme 1: Overview on the different condensation steps in non-aqueous sol-gel processes.

Surfactant-directed vs. solvent-controlled processes

Nanoparticle formation with control over the particle size and morphology in non-aqueous processes can either be surfactant-directed or solvent-controlled.[19] One example for surfactant-directed nanoparticle preparation is the so-called hot-injection technique. Metal precursor solutions are injected into a hot solvent containing surfactants which can coordinate to the precursors and prevent agglomeration of the formed nanoparticles.[19] The temperature is typically in the range of 250 to 350 °C and this technique is mainly used for the synthesis of semiconductor nanocrystals. Surfactant-controlled routes allow an exceptional control over the growth of metal oxide nanoparticles, yielding almost monodisperse samples with a low agglomeration tendency and excellent dispersibility.[22] However, the use of surfactants in the synthesis of nanoparticles leads to a large amount of organic impurities and therefore a restricted accessibility of the nanoparticle surface which can be detrimental for applications in gas sensing or catalysis.[16] Additionally, the toxicity of the surfactants and the non-predictable properties of the resulting materials can pose a problem.[24]

In contrast, solvent-controlled nanoparticle synthesis routes allow less control over crystallite size and shape, often show broader size distributions, the particles exhibit a limited redispersibility and tend to form agglomerates. Nevertheless, the advantages of solvent-controlled syntheses make them an elegant alternative to surfactant-controlled systems. The advantages include low synthesis temperatures typically in the range of 50 to 200 °C, and a low amount of organic impurities on the surface of the nanoparticles and therefore good accessibility of the nanoparticle surface. An additional attractive feature of these so-called soft-chemistry (or chimie douce)[25] reactions is that they are mainly carried out in non-toxic solvents.[26] The simple composition of the reaction solution of metal oxide precursor(s) and a

common organic solvent often enables a straight-forward characterization of the involved chemical reaction mechanisms.[16]

The polyol-mediated synthesis is an example of solvent-controlled methods to prepare many types of nanoparticles, such as elemental metal nanoparticles, phosphates, sulfides, halogenides and metal oxides.[27] The precursors are heated in high boiling alcohols such as glycol, glycerin or diethylene glycol and due to the possible high processing temperatures (150 – 300 °C) the syntheses often lead to highly crystalline material. Due to the stabilizing chelating effect of the polyols the growth of nanoparticles is limited and the particles are kept from agglomeration. Additionally, this type of synthesis is easy to perform and the nanoparticles can be obtained in high quantities. The size of the produced particles usually is in the range of 30 – 100 nm. Although such a relatively big particle size is desirable for several applications, it is not feasible for using the nanoparticles as building blocks for surfactant templated porous systems or for the incorporation and homogeneous distribution of nanoparticles in such mesoporous structures.

Another example for a solvent-controlled metal-oxide nanoparticle synthesis is the well-established benzyl alcohol route developed by Niederberger and his co-workers. In this reaction, dry benzyl alcohol is used as solvent, and at the same time as a capping agent and oxygen supply to react with metal halides, metal acetylacetonates and metal alkoxides.[18] This soft-chemistry route can be used to synthesize small nanoparticles (2 – 80 nm) in gram quantities with narrow size distributions, uniform particle shapes and high crystallinity without the use of surfactants. Mechanistic studies have been carried out to shed light on the role of the benzyl alcohol in the synthesis and on the various reaction steps.[28] Also a broad variety of binary, ternary and multi-metal oxides are accessible via the benzyl alcohol route.[29-31] Particularly, the reaction of $TiCl_4$ with benzyl alcohol is described extensively in the literature, yielding phase-pure anatase TiO_2 particles with a size of 4 – 8 nm at mild

temperatures as low as 40 °C.[32-35] The $TiCl_4$-to-solvent ratio and the reaction temperature can be used to influence and tune the crystallite size. Nanoparticles synthesized in this way have been successfully employed as building blocks for the preparation of mesoporous films due to their high crystallinity and redispersibility.[36] However, stabilizers have to be added to the solvent to redisperse the nanoparticles. This together with the highly stable benzyl alcohol ligands on the surface of the particles makes them less accessible for applications in electronic devices or in catalysis. Recently, the benzyl alcohol route has also been extended to the synthesis of metal sulfide nanoparticles.[37]

Some of the described processes are solvothermal reactions that are taking place at high pressures and temperatures above the boiling point of the solvent in sealed vessels. The reactions can also be conducted above the critical point of a solvent to exploit the lack of surface tension and the low viscosity of the supercritical solvents. Special names for several frequently used solvents in solvothermal processing were assigned, such as hydrothermal or ammonothermal for reactions in water and ammonia, respectively. In total, the solvothermal method provides an improved solubility and reactivity of reactants at elevated temperatures.

1.3 Mesoporous materials

According to IUPAC, porous solids can be classified and grouped into three categories depending on the pore diameter: microporous ($d < 2$ nm) and macroporous materials ($d > 50$ nm) with mesoporous materials lying in between with pore diameters in the range of 2 – 50 nm.[38] The latter have attracted a lot of interest since the discovery of MCM-41 and SBA-15 in 1990 and shortly thereafter.[39,40] This is mainly due to their wide range of possible applications, such as catalysis, adsorption, microelectronics, optics, medical diagnosis, energy conversion and storage.[41-46] These applications are based on the unique properties of

mesoporous materials, including the high surface area and good accessibility of the pore system.[47] Especially in energy conversion or storage devices, which involve charge transfer reactions and accompanying mass transport processes, large interfaces and free accessibility for diffusion are essential for the usability and efficiency of active materials.[47]

Basically two approaches are known for the preparation of mesoporous metal oxides, namely the assembly of nanoparticles and templating methods. The first method is based on the deposition of preformed nanocrystalline metal oxide particles. This is usually made from a paste or solution in screen-printing or doctor-blading experiments. The deposited particles are usually sintered by calcination. The resulting layers are highly crystalline, the film thickness can be easily tuned and they exhibit surface areas of about 80 – 90 m^2g^{-1} for titanium dioxide, for example.[48,49] Although the resulting films feature a high textural porosity, they do not feature periodically ordered porous structures.

Templating methods are employed for the synthesis of mesostructured and mesoporous materials. Depending on the nature of the template, soft- and hard-templating approaches are distinguished. The hard-templating method uses solid objects, such as silica or latex spheres that can arrange in a cubic close packing and the resulting voids can be filled by the metal oxide precursors. After crystallization of the metal oxide the template can be removed by dissolution or combustion to produce a mesoporous structure.[47] In contrast, the soft templating method utilizes the self-assembly properties of ionic surfactant or amphiphilic block-copolymer surfactant molecules as structure directing agents (SDA) together with molecular sol-gel precursors (Figure 1-2).[50]

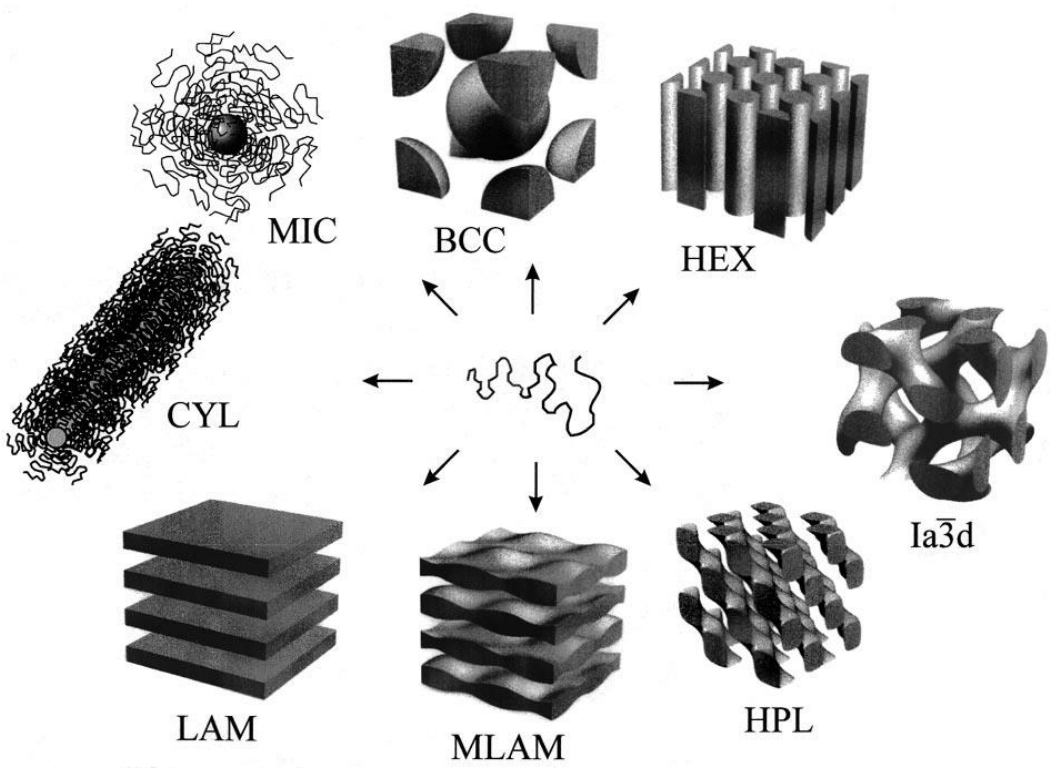

Figure 1-2: Common morphologies of microphase-separated block copolymers: body centered cubic (bcc) packed spheres (BCC), hexagonally ordered cylinders (HEX), gyroid (Ia3d), hexagonally perforated layers (HPL), modulated lamellae (MLAM), lamellae (LAM), cylindrical micelles (CYL), and spherical micelles (MIC).[50]

The periodic mesostructure in thin films can be formed in an evaporation-induced self-assembly (EISA) process. In the EISA process, the dissolved surfactants spontaneously organize into micellar aggregates as soon as they reach a critical micellar concentration (CMC) by evaporation of the solvent.[51] Depending on various factors, such as surfactant concentration, surfactant to metal oxide precursor ratio, temperature or relative ambient humidity, the resulting mesophase can be lamellar, cubic or hexagonal, among others.

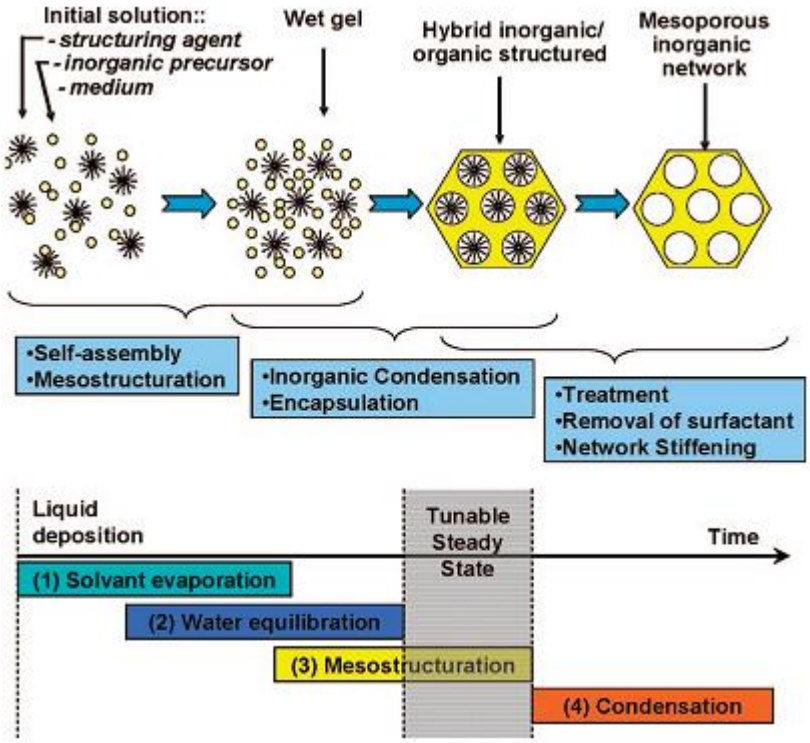

Figure 1-3: Mesostructured film formation employing an evaporation-induced self-assembly process by liquid deposition techniques.[52]

The EISA approach can be applied in spin- or dip-coating experiments and the steps of mesostructure formation in a thin film are: deposition of the surfactant and precursor-containing solution on a substrate, hydrolysis of the sol-gel precursors, micelle formation due to evaporation of the solvent, drying and further condensation of the network and template removal to form the mesoporous material.[53] Upon calcination the metal oxide precursor crystallizes and the surfactant is combusted, resulting in the transformation of the mesostructure to a mesoporous material (Figure 1-3). This soft-templating method allows the preparation of films with very high specific surface area.[54] However, this technique is limited to very thin film thicknesses and a lower crystallinity compared to the sintering of already crystalline nanoparticles.[55] Additionally, the strong contraction upon condensation and crystallization of the network can lead to crack formation and even delamination of the films.[56]

1.4 Semiconductor metal oxides

Inorganic metal oxide semiconductor materials are interesting due to numerous possible applications in sensing or energy storage and conversion, for example.[47] By combining their special intrinsic materials properties with the advantages and characteristics of nanostructures, materials with special shapes, compositions and chemical and physical properties can be obtained. In the following part of this thesis, the semiconductor metal oxides employed in our studies are briefly introduced.

Titanium dioxide (TiO_2)

Titanium dioxide is a transparent high refractive index material (2.5 – 2.9), which mainly occurs in three well-known phases: rutile, anatase and brookite. The metastable anatase and brookite phases convert to rutile upon heating to high temperatures.[57] Nanocrystalline titania however, with a size below around 14 nm is most stable in the anatase phase.[58] Titanium dioxide can be sourced from natural ores (ilmenite) or synthesized in various processes, such as the industrial preparation of Aeroxide P25 in a flame hydrolysis process by Degussa.[59] The P25 nanoparticles exhibit an average particle diameter of approximately 21 nm and consist of a mixture of anatase (~ 80 %) and rutile (~ 20 %). Other processes for the preparation of titania nanoparticles include flame hydrolysis,[60] and the wet chemistry approaches employing sol-gel, hydrothermal, or solvothermal processes such as the already described non-hydrolytic synthesis of nanoparticulate titania in benzyl alcohol.[9,32]

Titanium dioxide and its doped modifications are interesting for a broad field of applications, including its use as a pigment for wall paint, food coloring due to its low toxicity or as UV absorber in sunscreen due to its high band-gap of about 3 eV. Emerging important

applications of titania nanomaterials include the photocatalytic decomposition of organic residues, photo-catalytic water splitting, self-cleaning and antibacterial surfaces, or as photo-anodes in dye-sensitized solar cells.[36,61,62] The most interesting phase of titanium dioxide for such applications is anatase (Figure 1-4).

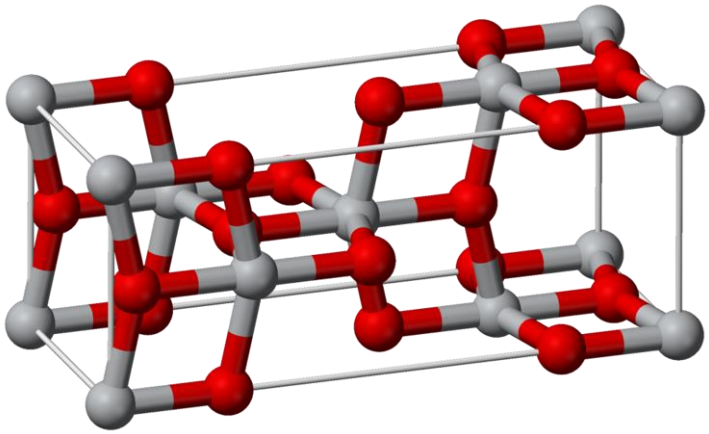

Figure 1-4: Crystal structure of TiO_2 in its anatase modification.[63]

Lithium titanate ($Li_4Ti_5O_{12}$)

Lithium titanium oxide (LTO) is a colorless material, which crystallizes in a spinel structure with the cubic space group Fd3m. Oxygen forms a cubic close packing (ccp) (32e sites) and lithium and titanium occupy the tetrahedral (8a) and octahedral sites (16d), respectively. However, LTO has a defect spinel structure type, because in 1/6 of the octahedral sites titanium is replaced by lithium. This can be expressed in the Wyckoff notation as $[Li_3]^{8a}[LiTi_5]^{16d}[O_{12}]^{32e}$. LTO is an interesting material as electrode in high rate rechargeable lithium ion batteries and asymmetric hybrid supercapacitors.[64,65] LTO is particularly interesting for its properties in lithium insertion with its high rate capability, cycling stability, low irreversibility, low cost and environmental friendliness. Additionally, the lower potential at which the lithium insertion reaction takes place compared to carbon anodes prevents the formation of lithium dendrites and therefore short circuiting of the batteries, making LTO a

safer electrode material. However, this also limits the overall power of the battery. The charging reaction of LTO involves the reduction of three titanium atoms and the subsequent incorporation of three lithium ions to retain the charge balance (Figure 1-5).

$$Li_3(LiTi_5)O_{12} + 3e^- + 3Li^+ \rightarrow Li_6(LiTi_3^{(III)}Ti_2^{(IV)})O_{12} \quad (1\text{-}1)$$

During the charging reaction $Li_4Ti_5O_{12}$ is topotactically transformed to $Li_7Ti_5O_{12}$, which in contrast has a rock-salt type structure, where the lithium ions either occupy the tetrahedral (8a) Li or octahedral (16c) sites in domains with sizes less than 9 nm. Due to the resulting random occupation of tetrahedral and octahedral vacancies, LTO exhibits a very high lithium ion mobility.[66]

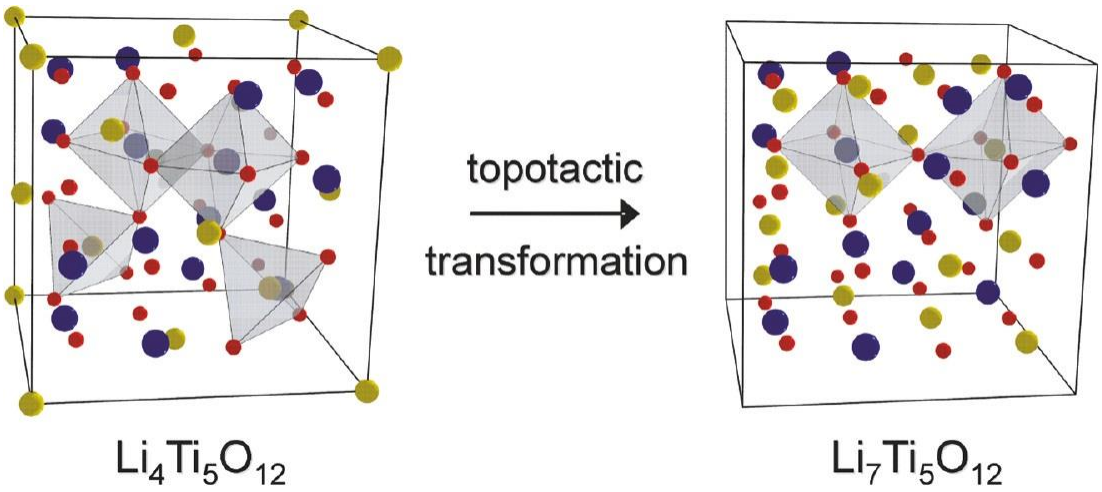

Figure 1-5: Structural changes of LTO during charging.[67]

Another beneficial property of LTO is the very small change in lattice parameters during phase transformation leading to a variance of the unit cell volume of only 0.2 %.[68] This "zero-strain" process leads to the exceptionally high cycling stability of the material in batteries.[69]

However, the drawbacks of LTO are the already mentioned high potential against lithium with the resulting limited power of the battery, its low gravimetric capacity and the rather low electrical conductivity.[67,70]

Various methods for the preparation of nanosized LTO are reported, such as flash annealing[71] or solid-state reactions of nanosized titania.[72] However, these lead to relatively large crystals of over 30 nm. Smaller crystals of lithium titanate can be obtained by solvothermal[73] and sol-gel reactions.[74]

Nickel oxide (NiO)

Nickel(II)oxide is a stable antiferromagnetic 3d transition metal oxide with the chemical composition NiO and is found in nature as the rare mineral bunsenite. Nickel oxide crystallizes in the cubic rock-salt type structure (Figure 1-6) and appears green in its stoichiometric form. Non-stoichiometry leads to a color change, with the non-stoichiometric NiO being black.[57] Nano-sized NiO with very small particle sizes is reported to be brown-yellow.[75] Stoichiometric pure nickel oxide is an insulator at room temperature with a wide bandgap of 3.6 – 4.0 eV. However, it becomes a p-type transparent semiconductor due to holes generated by Ni vacancies or by the presence of interstitial oxygen atoms.[76] Furthermore, NiO shows electrochromic properties, i.e. the ability to reversibly and persistently change its optical properties in an applied electric field.[76] Due to the mentioned unique magnetic and electrochemical properties, particularly nano-sized nickel oxide is of great interest for many applications. These involve the utilization of NiO as high capacity anode material in lithium ion batteries,[77] as high specific capacitance electrochemical capacitor or pseudocapacitor,[78] as photocathode in p-type dye-sensitized solar cells,[79] in chemical gas sensing[80] and catalysis.[81]

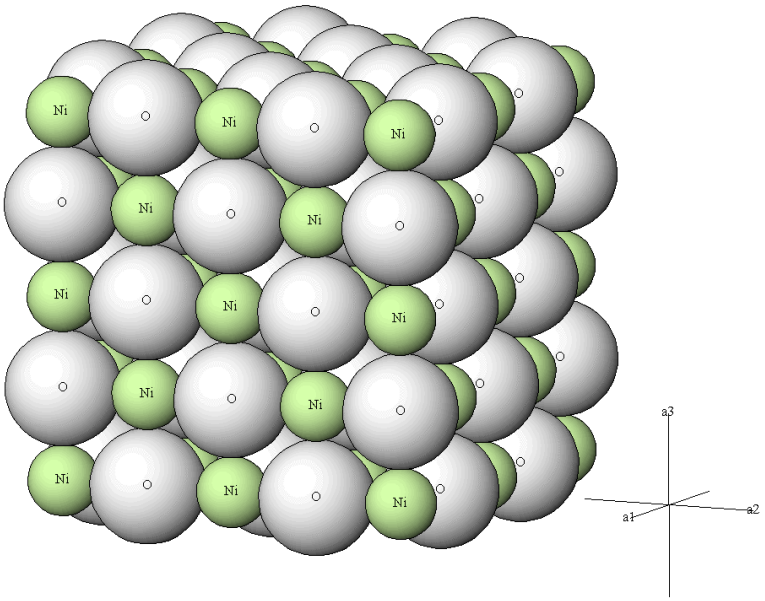

Figure 1-6: Crystal structure of NiO, rock-salt type.[82]

Nano-sized nickel oxide can be synthesized in many ways, such as thermal decomposition of nickel salts,[83] low pressure spray pyrolysis[84] or in an anodic arc plasma.[85] Chemical synthesis pathways involve sol-gel processing with subsequent calcination,[86] the hydrothermal synthesis of NiO nanoparticles[87] and solvothermal processes, which lead to smaller nanoparticles at lower processing temperatures.[88] However, very small non-agglomerating dispersible nanoparticles with a narrow size distribution are still difficult to obtain.

Iron oxide (Fe_2O_3)

Iron oxides are widespread in nature, non-toxic and appear in various oxidation states and phases: wüstite (FeO), magnetite (Fe_3O_4) and Fe_2O_3 in its alpha phase (α-Fe_2O_3, hematite), beta phase (β-Fe_2O_3), gamma phase (γ-Fe_2O_3 maghemite) and epsilon phase (ε-Fe_2O_3). Hematite is the most abundant iron oxide modification and also the major iron source for the steel industry. It crystallizes in a rhombohedral, corundum (α-Al_2O_3) structure (Figure 1-7) and shows weak ferromagnetism at room temperature.[89]

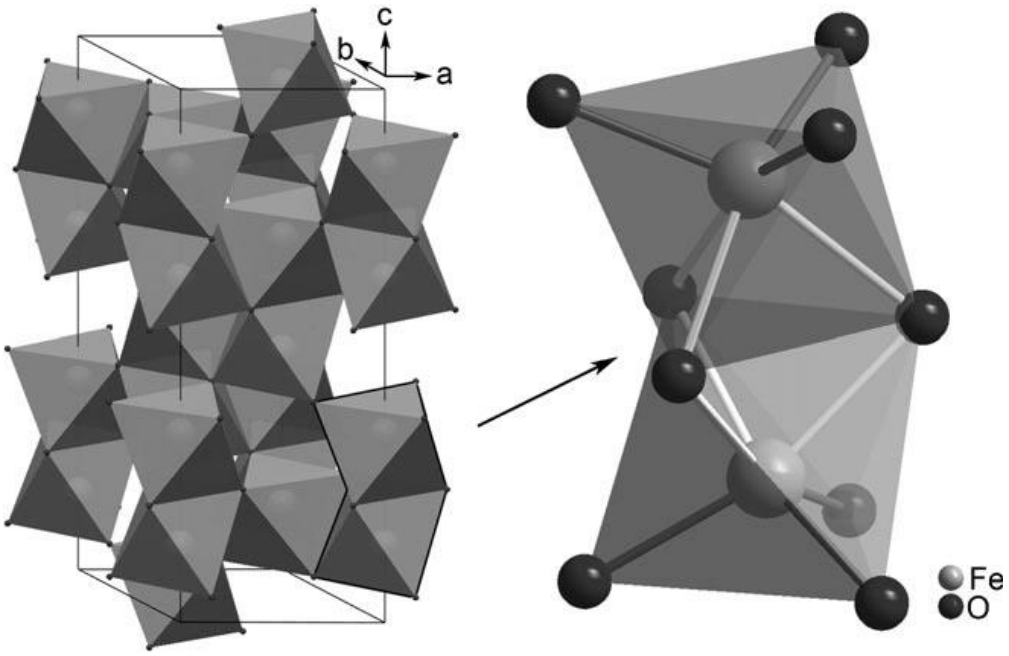

Figure 1-7: The unit cell (left) of hematite with octahedral face-sharing Fe_2O_9 dimers (right).[90]

The color of hematite is dark red, which enables its application as inexpensive, durable pigments in paints, coatings and colored concretes. The light absorption in the visible region is due to the small bandgap of about 2 eV.[91] Oxygen vacancies in the lattice of hematite that are compensated by Fe^{2+} ions to ensure electroneutrality make hematite an n-type semiconductor.[92] Additionally, hematite is stable in aqueous environments and its band alignment together with the aforementioned properties makes it a suitable candidate for photo-electrochemical water splitting.[91]

Various methods have been reported for the preparation of hematite dense or porous thin films for solar water splitting applications. These include: solution based colloidal methods for porous films in which pre-formed nanoparticles are sintered; a controlled precipitation of iron precursors in aqueous solutions; thermal oxidation of iron foils to form nanorods and wires; potentiostatic anodization of iron foils for ordered nanoporous materials. Thermal decomposition and oxidation of an iron precursor in an Atmospheric Pressure Chemical Vapor Deposition process (APCVD) leads to fractal-like cauliflower structures.[93] Non-porous

thin films can be obtained from spray pyrolysis of iron precursors from aqueous or ethanolic solutions.[89]

Cobalt oxide (Co_3O_4)

Cobalt oxides can comprise different oxidation states of the cobalt ion, namely CoO, Co_2O_3 and Co_3O_4. The latter is a black antiferromagnetic solid and since it is a mixed valence compound, its formula can also be written as $Co(II)Co(III)_2O_4$. The crystal structure of Co_3O_4 is a normal spinel structure with a cubic close-packed lattice of oxide anions with Co^{2+} ions in the tetrahedral interstices and Co^{3+} ions in the octahedral interstices (Figure 1-8).[94] Co_3O_4 is applied in many fields, such as heterogeneous catalysis,[95,96] in lithium ion batteries,[97,98] electrochromic devices,[99] as quantum dots,[100] magnetic materials,[101] and ceramic pigments.[102] Cobalt compounds are also reported to catalyze the oxygen evolution reaction in photo-electrochemical water splitting devices.[103,104]

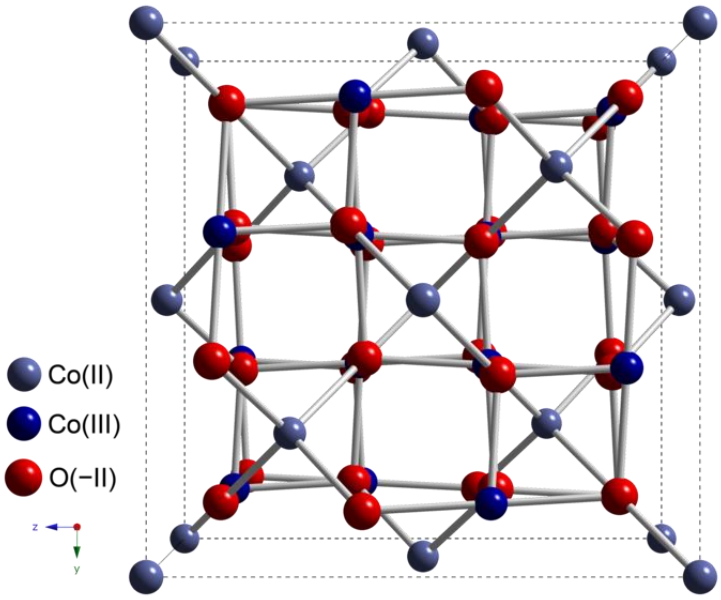

Figure 1-8: Spinel type crystal structure of Co_3O_4.[105]

Co_3O_4 can be synthesized in various ways, such as in chemical spray pyrolysis,[106] chemical vapor deposition,[99] pulsed laser deposition,[107] in a hydrothermal synthesis[98,108] or via a sol-gel method.[109] However, the syntheses either require relatively high temperatures, which makes it difficult to obtain nanocrystalline Co_3O_4, or the resulting material is agglomerated and not dispersible. Nevertheless, for the deposition of Co_3O_4 as a catalyst on porous supports a very small size of the nanoparticles and a good dispersibility would be highly desirable.

1.5 Dye-sensitized solar cells

The foreseeable depletion of fossil energy sources and the worldwide insatiable demand for cheap energy motivates the development of renewable energy sources like wind, biogas or solar power. Considering the huge available amount of free solar energy which is about 10000 times the current global energy consumption,[110] solar technologies could be a versatile alternative to fossil fuels. However, most photovoltaic devices are based on expensive silicon semiconductor p-n-junction cells, which also need a lot of energy for their fabrication. Photo-electrochemical cells should rather be considered as a complementary solution than an alternative to the typical silicon devices since their properties and composition differ significantly. As early as 1991 Grätzel et al. reported a low-cost, rather efficient solar cell based on dye-sensitized TiO_2 films which now show a light-to-electric energy conversion efficiency of more than 11 %.[61] DSCs are comprised of a mesoporous metal oxide electrode that is covered by a monolayer of absorber dye on top of a transparent conducting oxide glass substrate. The counter electrode is usually platinum-coated and the electrodes are connected through an external circuit and inside the cell through a redox electrolyte.[111] The operational principle of these dye-sensitized solar cells (DSC) is based on the absorption of a photon by the dye, subsequent injection of electrons into the conduction band of the semiconductor, the transport of electrons through an external circuit to a counter electrode and the reduction of

the redox electrolyte for the regeneration of the dye molecules (Figure 1-9).[110] Compared to silicon PV devices, DSCs feature several advantages such as utilization of cheap materials, simple and fast assembly that may enable roll-to-roll printing techniques and better conversion of stray light. However, there is still room to tune and improve these cells, e.g. the light-conversion efficiency and long-term stability by modification of its individual components.[111]

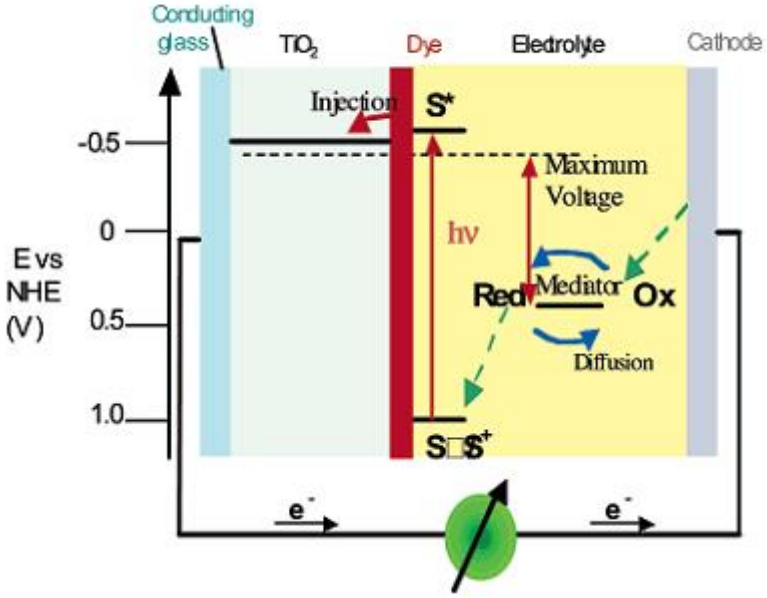

Figure 1-9: Scheme of the operational principle of a dye-sensitized solar cell.[111]

The following part gives a brief overview on the materials utilized in DSCs.

Electrodes in DSCs

The electrodes of DSCs are usually prepared on transparent conducting oxide (TCO) glass substrates, such as fluorine doped tin oxide (FTO) or tin-doped indium oxide (ITO). These substrates have a high transmittance in the range of the sunlight spectrum to allow the incident light to excite the dye. FTO is more commonly used due to its higher conductivity after

heating to high temperatures, which is necessary for the preparation of the counter electrodes and also the porous metal oxide layers.[112] The catalytic counter electrodes are usually prepared by the deposition of a solution of a platinum precursor (H_2PtCl_6) on the TCO substrate with a subsequent heat treatment to 400 °C. In this step, the platinum is reduced and forms finely distributed nanoparticles of elemental platinum on the surface of the TCO.[49]

A dense so-called blocking layer is usually employed as an underlayer to the porous layer to prevent recombination at the TCO electrode surface. Titania is the most typical material for the blocking layers. The porous n-type semiconductor morphologies are usually prepared from wide bandgap metal oxides such as ZnO, SnO_2[113] or Nb_2O_5.[114] TiO_2 in its anatase modification however is the most efficient and therefore most commonly used material. Recent developments in DSCs also showed the applicability of NiO as a p-type semiconductor electrode material which could be combined with n-type electrodes in tandem devices.[79] The porosity of the films is extremely important to provide a high surface area for the adsorption of dye-molecules and therefore to guarantee a high light absorption of the thin films. Additionally, the mesoporous metal oxides should exhibit a high crystallinity to ensure good electrical conductivity. Screen-printing or doctor-blading nanoparticle pastes are the standard procedures to prepare the working electrodes of DSCs. The deposition is followed by a high temperature treatment to remove the organic binders of the paste and to sinter the nanoparticles. Alternatively, surfactant templated sol-gel EISA procedures are used for the preparation of periodically ordered highly porous films which can offer a much better energy conversion to thickness ratio.[115] However, the resulting films can only be prepared with a very limited thickness and exhibit low crystallinity or the mesostructure collapses at least partially at the high calcination temperatures necessary for the crystallization of the films. One approach for the improvement of this method is the so-called brick and mortar approach developed in our group by Szeifert et al.[36] This technique involves pre-formed titania

nanoparticles (bricks) which are incorporated into the walls of the mesostructured material to act as crystallization seeds for the sol-gel (mortar) and therefore lowering the required calcination temperature. A more detailed overview on titania nanostructures for DSCs is given in Chapter 4.

Sensitizers

Sensitizers have to meet certain requirements to be suitable for application in DSCs. First of all, they have to show a high absorbance of solar light in the visible and near infrared range. An efficient injection of the electron from the excited state of the sensitizer into the conduction band of the semiconductor electrode with a quantum yield close to unity should be provided. This requires the energy level of the excited state of the sensitizer to be slightly above the conduction band of the semiconductor. Additionally, the redox potential of the dye has to be higher than that of the oxidized electrolyte to enable the reduction and therefore the regeneration of the dye. It should also exhibit adequate attachment groups for grafting the dye to the oxide surface of the porous framework and to allow an intimate contact with it, which is necessary for a highly efficient charge transfer. Finally, the dye needs to be stable at elevated temperatures under illumination and has to exhibit a high turnover stability in order to approach the desired lifetime of 20 years. Ruthenium-centered polypyridyl complexes can meet those requirements and therefore are widely applied in research studies as standard dyes. Examples include N719,[116] the black dye[117] or K19, which show an improved light absorption behavior in the near-infrared region.[118] Alternative sensitizing dyes are the porphyrin-based dyes, with a high absorption across the visible solar spectrum.[119] Other possible alternative sensitizers include extremely thin absorber layers (such as Sb_2S_3)[120] and quantum dots; semiconductor nanoparticles which exhibit size confinement effects and therefore a tunable

absorption spectrum and high extinction coefficients.[121] Recently, high-performance organometal halide perovskite-based solar cells have been reported, although in this case the role of the perovskite is not yet entirely clear.[122]

Electrolyte

The liquid electrolytes in DSCs consist of dissolved redox-active molecules in organic solvents. The requirements for the electrolyte for a good performance of photovoltaic cells involve a high thermal stability and reversibility of the redox process, and control of undesired recombination.[123] Contrary to the dye, the electrolyte should absorb a low amount of light and exhibit high diffusion coefficients. The maximum obtainable open circuit voltage is defined by the offset between the quasi-Fermi level of the semiconductor electrode and the Nernst potential of the redox system. Typically, the electrolyte consists of the iodide/triiodide redox couple in solvent mixtures of acetonitrile, valeronitrile and *tert*-butanol.[49] Various additives such as alkylimidazolium iodides, guadinium thiocyanate and *tert*-butyl pyridine are reported to advantageously align the band positions of the electrolyte redox couple with the semiconductor or to reduce recombination processes.[111] Recently, a new concept was introduced to enhance the performance of DSCs by adding highly photoluminescent chromophores to the electrolyte which can absorb high-energy photons and transfer the energy to the sensitizing dye by a Förster resonant energy transfer.[124] This allows for a broader spectral absorption and an increased dye loading in DSCs.

DSC assembly

The assembly of a DSC is schematically depicted in Figure 1-10.[49] The working electrode and the counter electrode are put together with a thermoplastic spacer (e.g. a Surlyn polymer foil) in a sandwich-type cell by melting them together on a hot plate. The spacer defines the

volume of the cell in which the electrolyte is enclosed later and the electrolyte is filled in through a hole in the counter electrode by vacuum-backfilling. In this technique the electrolyte is dropped onto the hole of the counter electrode and then vacuum is applied. Exposing the cell to normal pressure again, the electrolyte is sucked into the hole and fills the compartment. Finally, this hole is sealed with another thermoplastic polymer and a thin cover glass sheet. To improve contacting of the cell, silver lacquer is applied on the overhanging parts of the FTO electrodes.

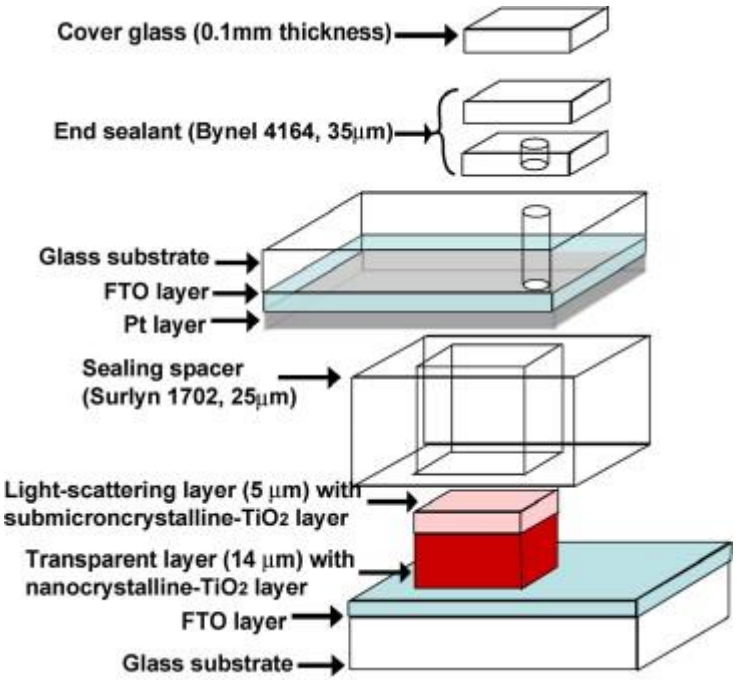

Figure 1-10: Configuration of a dye sensitized solar cell.[49]

Characteristics of DSCs

Solar cells in general are mainly specified by the following characteristics: The current that flows under short circuit conditions (short-circuit current, I_{SC}), which is closely related to the number of electrons generated in the dyes and injected into the conduction band of the semiconductor. The voltage at open circuit conditions (open circuit voltage, V_{OC}) corresponds

to the energetic difference between the (quasi-)Fermi level of the TiO_2 and the redox potential of the electrolyte.[125] The obtainable power of a solar cell can be calculated by multiplying the current times the corresponding voltage on the I-V-curve. Therefore, P_{max}, the maximum obtainable power point, is located on the curve where the product – and therefore the area of the rectangle under the curve – reaches a maximum (Figure 1-11). The electrical fill factor (*FF*) is a solar cell characteristic providing information on the quality of the photovoltaic device and is given by the ratio of maximum power P_{max} to the product of maximum current I_{SC} and maximum voltage V_{OC}:

$$\mathrm{ff} = \frac{P_{max}}{V_{OC} I_{SC}} \tag{1-2}$$

Finally, the overall solar conversion efficiency is a key factor to compare the effectiveness of converting sunlight to electrical energy. The ratio of the maximum obtainable power to the power of the incoming light gives the efficiency η:

$$\eta = \frac{P_{max}}{P_{inc}} = \frac{V_{OC} I_{SC} FF}{P_{inc}} \tag{1-3}$$

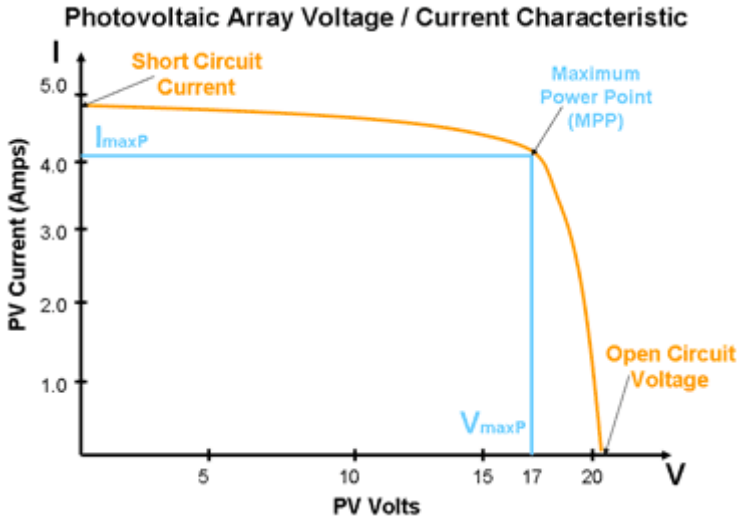

Figure 1-11: Idealized I-V-curve of a solar cell and corresponding maximum power generation.[126]

1.6 Battery materials

Energy storage in high performance rechargeable batteries has become a very attractive research field over the last years, especially with the growing markets of portable electronic devices and electric vehicles. The development and implementation of renewable energy sources into the energy grids require on the one hand an excellent infrastructure and management of the grid and on the other hand energy storage capabilities to compensate peak loads in sunny or windy phases or cloudy and windless phases, respectively. Besides mechanical energy storage, such as flywheel energy storage, pumped hydropower storage, and compressed-air energy storage, electrochemical energy storage can also be an attractive alternative, especially for short-time grid leveling.[127] Depending on the market penetration of electric vehicles in the next decade, in a smart grid the excess energy could be used to charge the batteries in electric vehicles and a reverse vehicle-to-grid energy transfer is also conceivable.

Electrochemical energy storage devices include supercapacitor and battery systems. The latter are divided in primary and secondary batteries for one-time or rechargeable use, respectively. Supercapacitors can provide a very high power, however their energy density cannot compete with battery systems (Figure 1-12). The typical functional elements of a battery include an anode, a cathode, an electrolyte, and a separator. The anode is defined as the negative electrode during discharge, it transfers electrons to the external circuit and is therefore oxidized during the discharge process. The antagonist, the positive cathode, accepts electrons from the external circuit and thus is reduced during the discharge reaction. The electrodes of a battery are spatially separated from each other by a separator, preventing electrical shorting of the devices. However, the separator must be permeable for the ions of the electrolyte which provides the ionic conductivity between the two electrodes of a battery.[128]

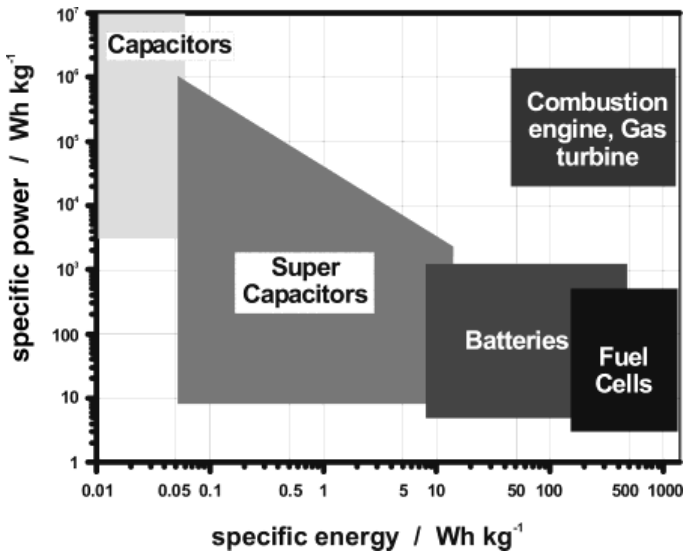

Figure 1-12: Ragone plot of the energy storage domains for super capacitors, batteries and fuel cells compared to an internal combustion engine or conventional capacitors.[128]

Batteries are characterized by several key figures: The nominal voltage (V) and the variation of it during operation of the battery (sloping) are set by the thermodynamic properties of the active electrode materials, the so-called cell chemistry. These factors determine the voltage a battery can supply for certain applications. Accordingly, the cut-off voltage (V) is the value to which a battery can be discharged without destroying it by irreversible processes. The capacity (Ah) or weight rated specific capacity (Ah g^{-1}) of a battery also depends on the utilized active electrode materials and is defined as product of the available charge (C, Coulomb) and the operating voltage (V) a battery can deliver over a certain time when discharging it from a completely charged state to the cut-off potential. The charge and discharge rate of a battery is usually given as the C-rate, with 1 C being the full charging or discharging of a battery within an hour, 2 C meaning full charging or discharging of a battery within a half hour and so on. The C-rate also determines the current with which a battery can be charged and therefore is a measure of the kinetics in a battery. For example a battery which is discharged at 25 C and has a nominal capacity of 1000 mAh can deliver a current of 25 A.

$$1000\ \text{mAh} \times 25\ \text{C} = 1000\ \text{mAh} \times 25\ \text{h}^{-1} = 25000\ \text{mA} = 25\ \text{A} \qquad (1\text{-}4)$$

The power (W) or specific power (W g^{-1}) is the product of voltage and current a battery can deliver and would correlate to how fast one can accelerate a car, for example. The energy (Wh) or specific energy (Wh g^{-1}) of a battery accordingly gives the time how long a battery can maintain a certain power and therefore would correlate to how far one can drive the car. These values are also often given in relation to the volume of a battery system, namely the power density (W L^{-1}) and energy density (Wh L^{-1}).

The durability of a rechargeable battery is described by its cycle life, i.e. the number of charge/recharge cycles it can perform before its capacity falls to 80 % of its original value. The application in commercial products typically requires a cycle life of batteries between 500 and 1200 cycles. Additionally, the shelf life is a measure how long a battery can be stored before it loses 20 % of its initial capacity due to self-discharging reactions.

With this requisite know-how the properties of and requirements for batteries can be discussed. In general, the applied electrode materials should exhibit suitable electrochemical potentials and high capacities to provide enough power and energy for applications. The materials should be stable in the respective electrolytes and show a high reversibility of the processes to be suitable for rechargeable batteries. The charging time, which is currently an extremely important issue for applications in battery electric vehicles and mobile devices, is governed by the kinetics in batteries. Furthermore, providing a high power requires large currents, large fluxes and a high mobility of charge carriers. One method to improve this characteristic is the nanostructuring of materials, which decreases diffusion pathways in the bulk and with its extremely high surface areas allows a good contact of the electrolyte with the active materials. In turn, the nanostructuring of materials would allow discharging a

battery quickly and therefore providing high power. Additionally, higher energy densities are highly desirable, since the lower attainable weight would allow one to operate mobile devices for a longer time or to propel a car more efficiently.[129]

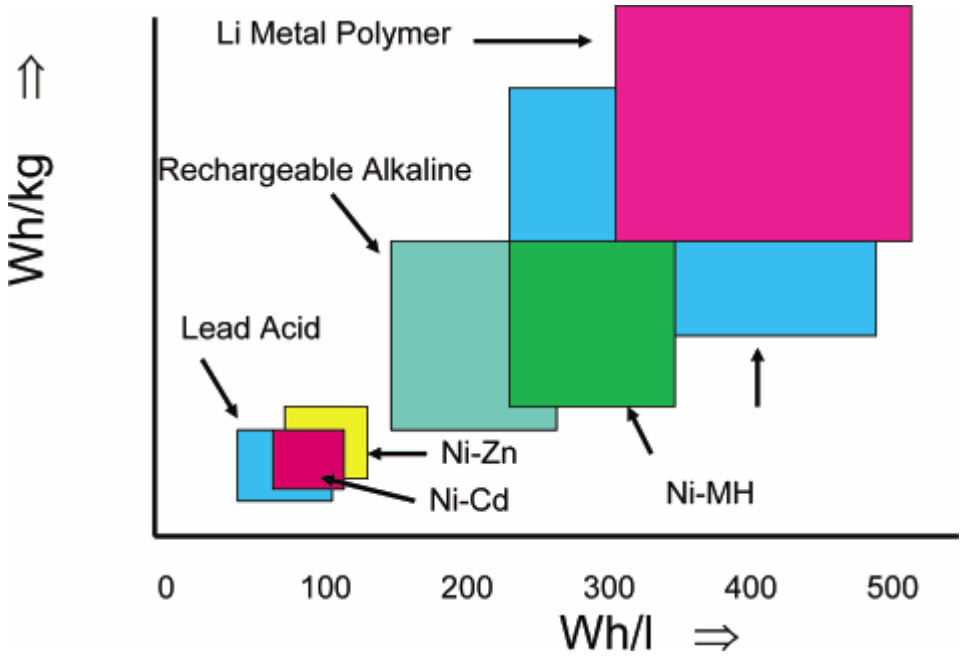

Figure 1-13: Energy storage capability of common rechargeable battery systems.[128]

Lithium ion batteries are the energy storage system that made the vast distribution of mobile devices possible in the first place and they are expected to be an important bridging technology until even higher capacity systems such as lithium air batteries are commercially available.[130] In contrast to the nickel metalhydride and nickel-cadmium batteries, lithium ion batteries do not show a memory-effect and exhibit a higher energy density, which makes them attractive for powering mobile devices or electric vehicles (Figure 1-13). The basic working principle of lithium ion batteries was discovered in the 1970s and it took about 20 years to reach commercialization.[131] The utilized materials are briefly introduced in the following chapter.

Cathode materials

Positive electrode materials include the spinel type oxides $LiCoO_2$, $LiNiO_2$, $LiMn_2O_4$ and the doped mixed oxides $LiNi_{1-x}Co_xO_2$, $LiNi_{0,85}Co_{0,1}Al_{0,05}O_2$ und $LiNi_{0,33}Co_{0,33}Mn_{0,33}O_2$.[132] The capacities of these materials are all around 150 mAh g^{-1}. Due to the expensive element cobalt for example, olivine type materials are applied as low-cost alternatives, mainly $LiFePO_4$ with iron being a highly abundant element.[133] Additionally, the latter shows a flatter charge and discharge curve with more stable potential over a broader region since the lithium deintercalation occurs as a two-phase process.

Anode materials

The material with the lowest standard potential is metallic lithium and therefore lithium would be the most suitable material to manufacture batteries with a high nominal voltage. Additionally, the very high theoretical capacity of 3860 mAh g^{-1} would allow building light-weight and high capacity battery systems. However, the high reactivity of metallic lithium in water and the dendritic growth of lithium upon charging and discharging, which can lead to short-circuiting of the cell, pose a severe safety issue. Therefore layered structures are utilized in lithium ion batteries in which the lithium ions can intercalate during charging. The most common material is graphite due its low potential, cheap manufacturing, high cyclability, acceptable capacity (372 mAh g^{-1}) and better safety compared to metallic lithium due to reduced dendrite formation.[134] Alternatives are the spinel structured metal oxides such as $Li_4Mn_5O_{12}$, $Li_4Ti_5O_{12}$ and $Li_2Mn_4O_9$, which show even better cyclability and a better thermal stability.[135] The improved cyclability can be attributed to the very low volume expansion upon charging and discharging of these materials. However, the capacity of these compounds is even lower than that for graphite, being around 150 mAh g^{-1}. Metal alloys or metals such as

silicon could be alternative high capacity energy storage materials but still suffer from their low cyclability due to the vast increase in volume upon charging.[136,137] Nanostructuring could be a suitable approach to accommodate the stress in the materials and to avoid the destruction of them upon cycling.

Electrolyte and separator

The liquid electrolyte in a lithium ion battery is usually composed of a lithium salt dissolved in an organic solvent. A key factor is the thermal and electrochemical stability of the electrolyte in the potential range at which a battery is operated. The solvent should be non-toxic and the electrolyte should show a high ion-mobility to enable fast charge transfer. Common applied lithium salts include $LiClO_4$, $LiBF_4$, $LiN(SO_2CF_3)_2$ and $LiPF_6$ in solvent mixtures of ethylenecarbonate and 1,2-dimethoxyethane, for example.[138] The requirements for separators are on the one hand a high ionic conductivity to efficiently close the circuit and on the other hand a low electrical conductivity to prevent short-circuiting.[139] Typical separators are porous membranes made from polyolefins (PP, PE, or laminates of PP and PE) or inorganic ceramics.[140]

The main techniques to characterize battery materials in laboratories are cyclovoltammetry and the galvanostatic technique, both described in detail in Chapter 2, Characterization.

1.7 Photo-electrochemical water splitting

Another possible approach to successfully integrate renewable energies into our energy mix is the direct conversion of sunlight to chemically stored energy or put simply, fuels. This would allow for storing excess solar energy during daytime and providing a constant energy supply during the night. Additionally, chemical fuels can be easily stored, can be transported efficiently due to their much higher energy density compared to battery systems and can be consumed according to demand.[141]

The easiest and probably least technologically demanding way of harnessing solar energy might be the use of bio-mass or bio-fuels produced in the photosynthesis of natural plants. However, this approach suffers from the rather low efficiency of photosynthesis which is typically less than 1 % and it often has to compete with food production for areas under cultivation.[142] Additionally, the conversion of bio-mass into fuels requires subsequent processing or distillation which decreases the efficiency further. Another indirect process of generating fuels is the electrolysis of water into hydrogen and oxygen with electricity from photovoltaic cells in separate electrolysers. The drawbacks of this multi-step process are the conversion efficiencies of the single steps, being 0.6 for the electrolysers and 0.4 for very high-performance solar cells, and therefore the loss of already converted and obtained energy.[143]

Direct methods, also called artificial photosynthesis, use the photons to directly produce a chemical fuel in a single process. When photogeneration electrodes are illuminated, water is oxidized at the surface without intermediate electricity generation. The produced electrons can be reacted, for example, with CO_2 to photo-reduce it to carbon-based fuels, however this process requires expensive and scarce catalysts. The alternative, to react the electrons simply

with protons, leads to the generation of hydrogen gas, which can be a promising future high energy density carrier in a so-called hydrogen economy. Furthermore, hydrogen could be easily stored in the already existing pipeline systems or gasometers for natural gas.[127]

The two separate water splitting reactions are shown in equation (1-5) and (1-6), with the oxygen evolution reaction (OER) occurring at the anode and hydrogen evolution occurring at the cathode (HER):

$$\text{OER: } 4\ OH^- + 4\ h^+ \rightarrow 2\ H_2O + O_2 \qquad (1\text{-}5)$$

$$\text{HER: } 4\ H_2O + 4\ e^- \rightarrow 2\ H_2 + 2\ OH^- \qquad (1\text{-}6)$$

Another possibility is to have the photoactive material in dispersion and both the HER and OER taking place at the particle surface. An extensive review on the so-called heterogeneous photocatalysis is given by Kudo and Miseki and is not discussed in detail here.[144] Alternatively, the light absorption properties of photosystem II proteins coupled to semiconductor electrodes and hydrogen evolution by hydrogenase are interesting alternative biomimetic approaches.[145]

The necessary free energy for splitting a water molecule under standard conditions is $\Delta G = 237.2\ kJ\ mol^{-1}$, which corresponds to $\Delta E° = 1.23\ V$ according to the Nernst equation.[141] In order to photo-chemically drive this reaction with a semiconductor, the absorbed photons require a minimum energy of 1.23 eV or a wavelength below 1000 nm. The generated charge carriers, electrons and holes have to travel to the respective electrode surfaces to react with water species. Additionally, the losses due to necessary concentration and kinetic overpotentials in electron-transfer processes at the semiconductor/liquid junction for the HER and the OER have to be taken into account. This leads to an overall necessary potential of around 1.6 – 2.4 eV per generated electron hole-pair.[146] The energy can be provided by either

one high energy photon absorbed by a semiconductor whose band positions straddle the electrochemical potentials E° (H^+/H_2) and E° (O_2/H_2O) (Figure 1-14, left), or two different semiconductors which ideally absorb photons with different wavelengths (tandem system).

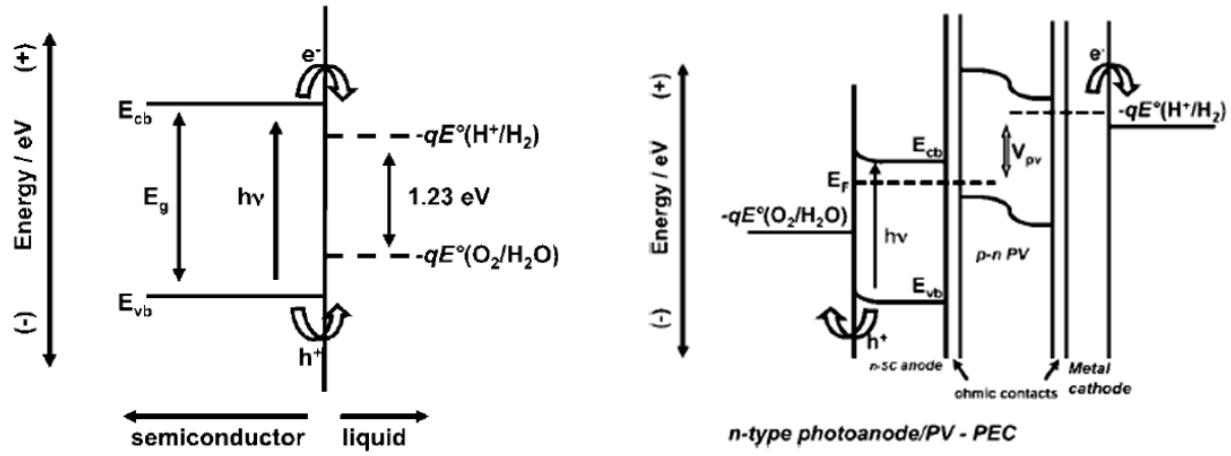

Figure 1-14: Left: Oxygen evolution reaction (OER) and hydrogen evolution reaction (HER) at a single semiconductor surface. The conduction band has to be above the hydrogen evolution and the valence band has to be below the redox potential for electrochemical oxygen evolution. Right: Series connection of a PV cell providing the necessary additional bias to drive the hydrogen evolution reaction at a metal cathode with a n-type photoelectrode at which the oxygen is evolved.[141]

In addition to the suitable energy levels and low overpotentials for the reduction/oxidation reactions, there are several other requirements an optimal semiconductor for water splitting should fulfill.[93] It should show a strong (visible) light absorption and a high chemical stability in aqueous solutions under harsh pH conditions in the dark and under illumination. Furthermore, it should be low cost and allow for an efficient internal charge transport, both for holes and electrons.

The first ever reported water splitting photocatalyst, TiO_2, delivers enough energy to split water and to produce both hydrogen and oxygen, however due to its high bandgap of 3.2 eV it only absorbs in the UV region, harnessing only a small part of the solar spectrum.[147] In order to shift the bandgap to lower values and therefore allow to absorb a greater part of the solar spectrum, experiments with doping the titania with metal ions such as Fe, Sb and Cr[129,130] or

anions such as nitrogen were conducted.[148] However, the still very low absorption coefficients and small absorption cross-sections led to limited performance of these systems. One means to overcome this issue is the nanostructuring of the electrodes to increase the optical thickness of the absorber layer while decreasing the hole diffusion pathways in n-type systems.[149] Another material capable of providing both electrons and holes for water splitting is $SrTiO_3$.[150] However the efficiency is again limited by its high bandgap and therefore small absorption of the solar spectrum.

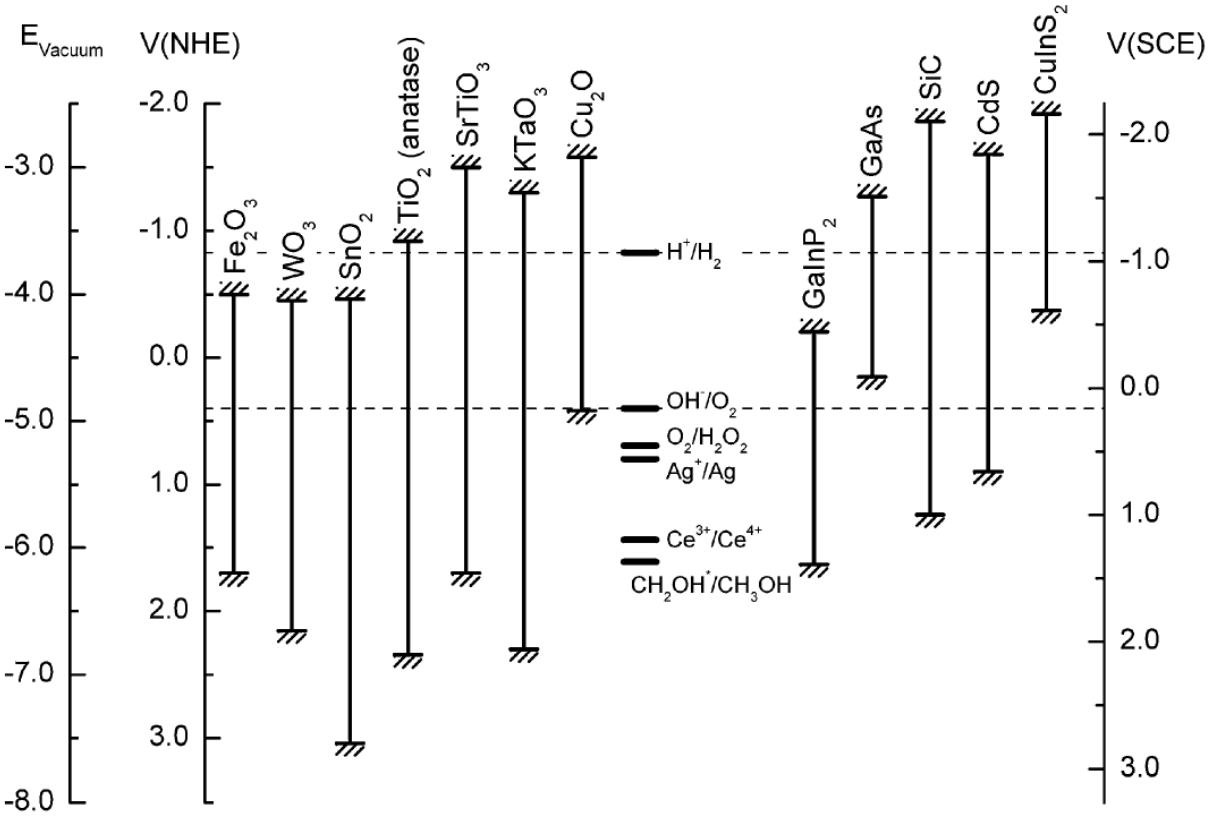

Figure 1-15: Energy band positions for various semiconductors at pH 14.[93]

Several of the materials depicted in Figure 1-15 are feasible candidates to drive at least one of the two necessary reactions for water splitting. Fe_2O_3, WO_3 and SnO_2 for example do not provide enough energy to drive both half-reactions in water splitting, thus an external bias voltage is necessary for the hydrogen evolution. One of the possibilities to provide this energy

would be to couple an external photovoltaic device to the system (Figure 1-14, right) or to combine photoanodes with photocathodes. Possible photocathode materials include several metal sulfides and selenides or copper(I)oxide. These materials are not described in detail here since they are beyond the scope of our studies.[141] Depending on the method, the hydrogen can be harvested from separate compartments or it has to be separated from the gas mixture. Furthermore, the smaller bandgap of the materials mentioned above allows absorption of visible light, thus increasing the overall photo-conversion efficiency.

Soon after the photocatalytic water splitting properties of TiO_2 were discovered, hematite or α-Fe_2O_3 was found to be a suitable material in 1976 by Bard and Hardee.[151] It meets several of the above-mentioned requirements: First of all, iron is one of the most abundant elements on earth and environmentally benign, therefore making it a cheap and safe alternative to other rare earth or noble metal containing electrodes or catalysts.[152] It shows a light absorption in the visible region resulting from its band gap of around 2 eV, which allows for absorbing a much higher fraction of the solar spectrum than wide bandgap semiconductors, resulting in a theoretical possible photocurrent density of 12 mA cm^{-2}.[152] The valence band position of hematite is below the potential for water oxidation making it an interesting photo-catalysis electrode for the OER.[153] Although the conduction band edge is not suitable for water reduction or hydrogen evolution, the necessary energy could be provided by the already described combination with a photocathode or coupling to an external PV cell.[154,155] Iron oxide exhibits a high chemical stability in basic aqueous solutions often employed for the OER in water splitting. The last requirement, the efficient internal charge transport is a major drawback of hematite leading to a strongly limited performance. As calculated by Hamman from the absorption coefficient according to Beers law, a film thickness of around 400 nm thick hematite would be necessary to absorb 95 % of the light with energy above its

bandgap.[152] This stands in drastic contrast to the very short hole diffusion length in hematite of only $2 - 4$ nm.[156] Additionally, the electron conductivity is limited due to low carrier concentrations and mobilities which results - inter alia - in high electron-hole recombination rates.[157] These issues are mainly addressed by two different approaches, nanostructuring the morphologies or doping the iron oxide with metal ions or a combination of both.

Significant improvements of the photo-conversion efficiency of hematite in water splitting experiments have been achieved by doping with Ti, Zr, Si, or Ge.[153,158-161] The effect of doping is usually ascribed to the change in carrier concentrations and/or increased carrier mobility therefore increasing the conductivity of the material.

Nanostructuring provides a higher surface area and therefore a larger amount of reaction sites on the active material and additionally decreases the diffusion pathways for holes to the surface. For hematite this concept was first reported for an approach similar to the fabrication of DSC electrodes by sintering nanoparticles of hematite.[162] Recent studies report a manifold of different iron oxide nanostructures such as nanowires, nanotubes, nanonets or nanocauliflowers that are summarized in excellent reviews.[91,93] In some cases, doping leads to an additional change in morphology, which is especially the case for Si doping and which results in the formation of dendritic nanostructures with drastically improved performance.[153] However, an increased surface area is not only advantageous as it provides more surface recombination sites.

To further increase the performance of nanostructured systems and to reduce surface recombination, surface treatments and catalysts are applied. The deposition of IrO_2 nanoparticles as a surface catalyst led to photocurrents in excess of $3\ mA\ cm^{-2}$.[163] Less expensive alternatives are usually based on cobalt compounds such as the deposition of Co^{2+} ions in the form of cobalt(II)-nitrate,[164] the electrodeposition of a cobalt-phosphate catalyst

("Co-Pi")[165-168] or the in-situ growth or ex-situ deposition of Co_3O_4 nanoparticles.[103] The role of these surface treatments is described in detail in Chapter 10.

1.8 References

(1) Feynman, R. P. *Engineering and Science* **1960**, *23*, 22.

(2) Eychmüller, A. *The Journal of Physical Chemistry B* **2000**, *104*, 6514.

(3) Rao, C. N. R.; Müller, A.; Cheetham, A. K. *The Chemistry of Nanomaterials: Synthesis, Properties and Applications*; John Wiley & Sons, 2006.

(4) Bradley, J. S. *Clusters and Colloids*; VCH (Hrsg.: G. Schmid),: Weinheim, 1994.

(5) Binnig, G.; Rohrer, H. *IBM J. Res. Dev.* **1986**, *30*, 355.

(6) Cao, G. Z.; Wang, Y. *Nanostructures and Nanomaterials: Synthesis, Properties, and Applications (2nd Edition)*; World Scientific, **2011**.

(7) Sobczak, J.-P. J.; Martin, T. G.; Gerling, T.; Dietz, H. *Science* **2012**, *338*, 1458.

(8) Kriechbaum, G. W.; Kleinschmit, P. *Angewandte Chemie* **1989**, *101*, 1446.

(9) Cushing, B. L.; Kolesnichenko, V. L.; O'Connor, C. J. *Chem. Rev.* **2004**, *104*, 3893.

(10) Caruntu, G.; Caruntu, D.; O'Connor, C. J. In *Encyclopedia of InorganicChemistry*; John Wiley & Sons, Ltd: **2006**.

(11) Ahn, T.; Kim, J. H.; Yang, H.-M.; Lee, J. W.; Kim, J.-D. *The Journal of Physical Chemistry C* **2012**, *116*, 6069.

(12) Rochow, E. G.; Gingold, K. *Journal of the American Chemical Society* **1954**, *76*, 4852.

(13) Ebelmen, M. *Ann. Chim. Phys.* **1846**, *16*, 129.

(14) Hench, L. L.; West, J. K. *Chemical Reviews* **1990**, *90*, 33.

(15) Boettcher, S. W.; Fan, J.; Tsung, C.-K.; Shi, Q.; Stucky, G. D. *Accounts of Chemical Research* **2007**, *40*, 784.

(16) Niederberger, M.; Pinna, N. *Metal Oxide Nanoparticles in Organic Solvents: Synthesis, Formation, Assembly and Application*; Springer London, **2009**.

(17) Livage, J. *Sol--Gel Science and Technology* **1989**, 103.

(18) Debecker, D.; Mutin, H. *Chem. Soc. Rev.* **2012**, *41*, 3624.

(19) Niederberger, M. *Accounts of Chemical Research* **2007**, *40*, 793.

(20) Niederberger, M.; Antonietti, M. In *Nanomaterials chemistry: Recent developments and new directions: Nonaqueous sol-gel routes to nanocrystalline metal oxides*; Wiley-VCH: **2007**, p 119.

(21) Jun, Y.-w.; Choi, J.-s.; Cheon, J. *Angewandte Chemie International Edition* **2006**, *45*, 3414.

(22) Park, J.; Joo, J.; Kwon, S. G.; Jang, Y.; Hyeon, T. *Angewandte Chemie International Edition* **2007**, *46*, 4630.

(23) Niederberger, M.; Garnweitner, G. *Chemistry – A European Journal* **2006**, *12*, 7282.

(24) Nel, A.; Xia, T.; Mädler, L.; Li, N. *Science* **2006**, *311*, 622.

(25) Sanchez, C.; Rozes, L.; Ribot, F.; Laberty-Robert, C.; Grosso, D.; Sassoye, C.; Boissiere, C.; Nicole, L. *Comptes Rendus Chimie* **2010**, *13*, 3.

(26) Pinna, N.; Niederberger, M. *Angewandte Chemie International Edition* **2008**, *47*, 5292.

(27) Feldmann, C. *Solid State Sciences* **2005**, *7*, 868.

(28) Ludi, B.; Suess, M. J.; Werner, I. A.; Niederberger, M. *Nanoscale* **2012**, *4*, 1982.

(29) Pinna, N.; Antonietti, M.; Niederberger, M. *Colloids and Surfaces A: Physicochemical and Engineering Aspects* **2004**, *250*, 211.

(30) Niederberger, M.; Garnweitner, G.; Buha, J.; Polleux, J.; Ba, J.; Pinna, N. *Journal of Sol-Gel Science and Technology* **2006**, *40*, 259.

(31) Pinna, N.; Karmaoui, M.; Willinger, M.-G. *Journal of Sol-Gel Science and Technology* **2011**, *57*, 323.

(32) Niederberger, M.; Bartl, M. H.; Stucky, G. D. *Chemistry of Materials* **2002**, *14*, 4364.

(33) Niederberger, M.; Bartl, M. H.; Stucky, G. D. *Journal of the American Chemical Society* **2002**, *124*, 13642.

(34) Wang, J.; Polleux, J.; Lim, J.; Dunn, B. *The Journal of Physical Chemistry C* **2007**, *111*, 14925.

(35) Zhu, J.; Yang, J.; Bian, Z.-F.; Ren, J.; Liu, Y.-M.; Cao, Y.; Li, H.-X.; He, H.-Y.; Fan, K.-N. *Applied Catalysis B: Environmental* **2007**, *76*, 82.

(36) Szeifert, J. M.; Fattakhova-Rohlfing, D.; Georgiadou, D.; Kalousek, V.; Rathouský, J.; Kuang, D.; Wenger, S.; Zakeeruddin, S. M.; Grätzel, M.; Bein, T. *Chemistry of Materials* **2009**, *21*, 1260.

(37) Ludi, B.; Olliges-Stadler, I.; Rossell, M. D.; Niederberger, M. *Chemical Communications* **2011**, *47*, 5280.

(38) McCusker, L. B.; Liebau, F.; Engelhardt, G. *Pure Appl. Chem.* **2001**, *73*, 381.

(39) Kresge, C. T.; Leonowicz, M. E.; Roth, W. J.; Vartuli, J. C.; Beck, J. S. *Nature* **1992**, *359*, 710.

(40) Zhao, D.; Feng, J.; Huo, Q.; Melosh, N.; Fredrickson, G. H.; Chmelka, B. F.; Stucky, G. D. *Science* **1998**, *279*, 548.

(41) Corma, A. *Chemical reviews* **1997**, *97*, 2373.

(42) Ying, J. Y.; Mehnert, C. P.; Wong, M. S. *Angewandte Chemie International Edition* **1999**, *38*, 56.

(43) Schüth, F. *Chemistry of Materials* **2001**, *13*, 3184.

(44) Davis, M. E. *Nature* **2002**, *417*, 813.

(45) Bruce, P. G.; Scrosati, B.; Tarascon, J.-M. *Angewandte Chemie International Edition* **2008**, *47*, 2930.

(46) Innocenzi, P.; Malfatti, L. *Chemical Society Reviews* **2013**.

(47) Ren, Y.; Ma, Z.; Bruce, P. G. *Chemical Society Reviews* **2012**, *41*, 4909.

(48) Barbé, C. J.; Arendse, F.; Comte, P.; Jirousek, M.; Lenzmann, F.; Shklover, V.; Grätzel, M. *Journal of the American Ceramic Society* **1997**, *80*, 3157.

(49) Ito, S.; Murakami, T. N.; Comte, P.; Liska, P.; Grätzel, C.; Nazeeruddin, M. K.; Grätzel, M. *Thin Solid Films* **2008**, *516*, 4613.

(50) Förster, S.; Antonietti, M. *Advanced Materials* **1998**, *10*, 195.

(51) Brinker, C. J.; Lu, Y.; Sellinger, A.; Fan, H. *Advanced Materials* **1999**, *11*, 579.

(52) Sanchez, C.; Boissière, C.; Grosso, D.; Laberty, C.; Nicole, L. *Chemistry of Materials* **2008**, *20*, 682.

(53) Grosso, D.; Cagnol, F.; Soler-Illia, G. d. A.; Crepaldi, E. L.; Amenitsch, H.; Brunet-Bruneau, A.; Bourgeois, A.; Sanchez, C. *Advanced Functional Materials* **2004**, *14*, 309.

(54) Choi, S. Y.; Mamak, M.; Coombs, N.; Chopra, N.; Ozin, G. A. *Advanced Functional Materials* **2004**, *14*, 335.

(55) Fattakhova-Rohlfing, D.; Wark, M.; Brezesinski, T.; Smarsly, B. M.; Rathouský, J. *Advanced Functional Materials* **2006**, *17*, 123.

(56) Zukalova, M.; Zukal, A.; Kavan, L.; Nazeeruddin, M. K.; Liska, P.; Grätzel, M. *Nano letters* **2005**, *5*, 1789.

(57) Greenwood, N. N.; Earnshaw, A. *Chemistry of the Elements*; Pergamon: Oxford, 1984.

(58) Zhang, H.; F. Banfield, J. *Journal of Materials Chemistry* **1998**, *8*, 2073.

(59) Kloepfer, H.; Patent, G., Ed. 1942; Vol. DE 762723.

(60) Kriechbaum, G. W.; Kleinschmit, P. *Angewandte Chemie* **1989**, *101*, 1446.

(61) O'Regan, B.; Gratzel, M. *Nature* **1991**, *353*, 737.

(62) Zhigang, Z.; Jinhua, Y.; Kazuhiro, S.; Hironori, A. *Nature* **2001**, *414*, 625.

(63) http://en.wikipedia.org/wiki/File:Anatase-unit-cell-3D-balls.png, 30.04.2013.

(64) Amatucci, G. G.; Badway, F.; Du Pasquier, A.; Zheng, T. *Journal of the Electrochemical Society* **2001**, *148*, A930.

(65) Ohzuku, T.; Ueda, A.; Yamamoto, N. *Journal of the Electrochemical Society* **1995**, *142*, 1431.

(66) Wagemaker, M.; van Eck, E. R.; Kentgens, A. P.; Mulder, F. M. *The Journal of Physical Chemistry B* **2008**, *113*, 224.

(67) Haetge, J.; Hartmann, P.; Brezesinski, K.; Janek, J.; Brezesinski, T. *Chemistry of Materials* **2011**, *23*, 4384.

(68) Borghols, W.; Wagemaker, M.; Lafont, U.; Kelder, E.; Mulder, F. *Journal of the American Chemical Society* **2009**, *131*, 17786.

(69) Kim, S. H.; Lee, K. H.; Seong, B. S.; Kim, G.-H.; Kim, J. S.; Yoon, Y. S. *Korean Journal of Chemical Engineering* **2006**, *23*, 961.

(70) Zhu, G.-N.; Liu, H.-J.; Zhuang, J.-H.; Wang, C.-X.; Wang, Y.-G.; Xia, Y.-Y. *Energy & Environmental Science* **2011**, *4*, 4016.

(71) Plitz, I.; DuPasquier, A.; Badway, F.; Gural, J.; Pereira, N.; Gmitter, A.; Amatucci, G. *Applied Physics A* **2006**, *82*, 615.

(72) Wang, Y.; Liu, H.; Wang, K.; Eiji, H.; Wang, Y.; Zhou, H. *Journal of Materials Chemistry* **2009**, *19*, 6789.

(73) Tang, Y.; Yang, L.; Qiu, Z.; Huang, J. *Journal of Materials Chemistry* **2009**, *19*, 5980.

(74) Kavan, L.; Grätzel, M. *Electrochemical and Solid-State Letters* **2002**, *5*, A39.

(75) Ghosh, M.; Biswas, K.; Sundaresan, A.; Rao, C. *J. Mater. Chem.* **2005**, *16*, 106.

(76) Avasthi, D.; Mehta, G. *Swift Heavy Ions for Materials Engineering and Nanostructuring* **2011**, 142.

(77) Liu, H.; Wang, G.; Liu, J.; Qiao, S.; Ahn, H. *Journal of Materials Chemistry* **2011**, *21*, 3046.

(78) Xing, W.; Li, F.; Yan, Z.-f.; Lu, G. *Journal of power sources* **2004**, *134*, 324.

(79) Nattestad, A.; Mozer, A.; Fischer, M. K.; Cheng, Y.-B.; Mishra, A.; Bäuerle, P.; Bach, U. *Nature materials* **2009**, *9*, 31.

(80) Hoa, N. D.; El-Safty, S. A. *Chemistry-A European Journal* **2011**, *17*, 12896.

(81) Shulga, J.; Kisand, V.; Kink, I.; Reedo, V.; Matisen, L.; Saar, A. In *Journal of Physics: Conference Series*; IOP Publishing: **2007**; *93*, 012006.

(82) http://staff.aist.go.jp/nomura-k/common/STRUCIMAGES/NiO.gif, 30.04.2013.

(83) Wang, X.; Song, J.; Gao, L.; Jin, J.; Zheng, H.; Zhang, Z. *Nanotechnology* **2004**, *16*, 37.

(84) Wuled Lenggoro, I.; Itoh, Y.; Iida, N.; Okuyama, K. *Materials research bulletin* **2003**, *38*, 1819.

(85) Qiao, H.; Wei, Z.; Yang, H.; Zhu, L.; Yan, X. *Journal of Nanomaterials* **2009**, *2009*, 2.

(86) Thota, S.; Kumar, J. *Journal of Physics and Chemistry of Solids* **2007**, *68*, 1951.

(87) Sue, K.; Kawasaki, S.-i.; Suzuki, M.; Hakuta, Y.; Hayashi, H.; Arai, K.; Takebayashi, Y.; Yoda, S.; Furuya, T. *Chemical Engineering Journal* **2011**, *166*, 947.

(88) Beach, E. R.; Shqau, K.; Brown, S. E.; Rozeveld, S. J.; Morris, P. A. *Materials Chemistry and Physics* **2009**, *115*, 371.

(89) Cornell, R. M.; Schwertmann, U. *The iron oxides: structure, properties, reactions, occurrences and uses*; Wiley-vch, **2003**.

(90) Sivula, K.; Zboril, R.; Le Formal, F.; Robert, R.; Weidenkaff, A.; Tucek, J.; Frydrych, J.; Gratzel, M. *Journal of the American Chemical Society* **2010**, *132*, 7436.

(91) Sivula, K.; Le Formal, F.; Grätzel, M. *ChemSusChem* **2011**, *4*, 432.

(92) Ahmed, S.; Leduc, J.; Haller, S. *The Journal of Physical Chemistry* **1988**, *92*, 6655.

(93) van de Krol, R.; Liang, Y.; Schoonman, J. *Journal of Materials Chemistry* **2008**, *18*, 2311.

(94) Smith, W. L.; Hobson, A. D. *Acta Crystallographica Section B* **1973**, *29*, 362.

(95) Bailie, J.; Rochester, C.; Hutching, G. *J Chem Soc Faraday Trans* **1997**, *93*, 2331.

(96) Schmidtszalowski, K.; Krawczyk, K.; Petryk, J. *Appl Catal A* **1998**, *175*, 147.

(97) Li, W.; Xu, L.; Chen, J. *Adv Funct Mater* **2005**, *15*, 851.

(98) Shin, C.; Manuel, J.; Kim, D.-S.; Ryu, H.-S.; Ahn, H.-J.; Ahn, J.-H. *Nanoscale Research Letters* **2012**, *7*, 73.

(99) Maruyama, T.; Arai, S. *J Electrochem Soc* **1996**, *143*, 1383.

(100) Nozik, A. *Physica E* **2002**, *14*, 115.

(101) Makhlouf, S. *J Magn Magn Mater* **2002**, *246*, 184.

(102) Matijevic, E. *Chem Mater* **1993**, *5*, 412.

(103) Xi, L.; Tran, P. D.; Chiam, S. Y.; Bassi, P. S.; Mak, W. F.; Mulmudi, H. K.; Batabyal, S. K.; Barber, J.; Loo, J. S. C.; Wong, L. H. *The Journal of Physical Chemistry C* **2012**, *116*, 13884.

(104) Osterloh, F. E. *Chemistry of Materials* **2007**, *20*, 35.

(105) http://en.wikipedia.org/wiki/File:Cobalt%28II, 30.04.2013.

(106) Singh, R.; Koenig, J.; Chartier, P. *J Electrochem Soc* **1990**, *137*, 1408.

(107) Fu, Z.; Wang, Y.; Zhang, Y.; Qin, Q. *Solid State Ionics* **2004**, *170*, 105.

(108) Jiang, Y.; Wu, Y.; Xie, B.; Xie, Y.; Qian, Y. *Mater Chem Phys* **2002**, *74*, 234.

(109) Baydi, M.; Poillerat, G.; Rehspringer, J.; Gautier, J.; Koenig, J.; Chartier, P. *J Solid State Chem* **1994**, *109*, 281.

(110) Gratzel, M. *Nature* **2001**, *414*, 338.

(111) Grätzel, M. *Inorganic Chemistry* **2005**, *44*, 6841.

(112) Kawashima, T.; Ezure, T.; Okada, K.; Matsui, H.; Goto, K.; Tanabe, N. *Journal of Photochemistry and Photobiology A: Chemistry* **2004**, *164*, 199.

(113) Tennakone, K.; Perera, V.; Kottegoda, I.; Kumara, G. *Journal of Physics D: Applied Physics* **1999**, *32*, 374.

(114) Sayama, K.; Sugihara, H.; Arakawa, H. *Chemistry of Materials* **1998**, *10*, 3825.

(115) Zukalová, M.; Zukal, A.; Kavan, L.; Nazeeruddin, M. K.; Liska, P.; Grätzel, M. *Nano Letters* **2005**, *5*, 1789.

(116) Nazeeruddin, M.; Kay, A.; Rodicio, R.; Miiller, E.; Liska, P. *J. Am. Chem. Soc* **1993**, *115*, 6382.

(117) Nusbaumer, H.; Moser, J.-E.; Zakeeruddin, S. M.; Nazeeruddin, M. K.; Grätzel, M. *The Journal of Physical Chemistry B* **2001**, *105*, 10461.

(118) Wang, P.; Klein, C.; Humphry-Baker, R.; Zakeeruddin, S. M.; Gratzel, M. *Applied Physics Letters* **2005**, *86*, 123508.

(119) Yella, A.; Lee, H.-W.; Tsao, H. N.; Yi, C.; Chandiran, A. K.; Nazeeruddin, M. K.; Diau, E. W.G.; Yeh, C.-Y.; Zakeeruddin, S. M.; Grätzel, M. *Science* **2011**, *334*, 629.

(120) Itzhaik, Y.; Niitsoo, O.; Page, M.; Hodes, G. *The Journal of Physical Chemistry C* **2009**, *113*, 4254.

(121) Plass, R.; Pelet, S.; Krueger, J.; Grätzel, M.; Bach, U. *The Journal of Physical Chemistry B* **2002**, *106*, 7578.

(122) Lee, M. M.; Teuscher, J.; Miyasaka, T.; Murakami, T. N.; Snaith, H. J. *Science* **2012**, *338*, 643.

(123) Grätzel, M. *Progress in photovoltaics: research and applications* **2000**, *8*, 171.

(124) Hardin, B. E.; Hoke, E. T.; Armstrong, P. B.; Yum, J.-H.; Comte, P.; Torres, T.; Fréchet, J. M.; Nazeeruddin, M. K.; Grätzel, M.; McGehee, M. D. *Nature photonics* **2009**, *3*, 406.

(125) Ishwara, T.; Bradley, D.; Nelson, J.; Ravirajan, P.; Vanseveren, I.; Cleij, T.; Vanderzande, D.; Lutsen, L.; Tierney, S.; Heeney, M. *Applied Physics Letters* **2008**, *92*, 053308.

(126) http://www.mpoweruk.com/solar_power.htm, 30.04.2013.

(127) Liu, C.; Li, F.; Ma, L. P.; Cheng, H. M. *Advanced Materials* **2010**, *22*, E28.

(128) Winter, M.; Brodd, R. J. *Chemical Reviews* **2004**, *104*, 4245.

(129) Zhang, Q.; Uchaker, E.; Candelaria, S. L.; Cao, G. *Chemical Society Reviews* **2013**, *42*, 3127.

(130) Kraytsberg, A.; Ein-Eli, Y. *Journal of Power Sources* **2011**, *196*, 886.

(131) Besenhard, J.; Eichinger, G. *Journal of Electroanalytical Chemistry and Interfacial Electrochemistry* **1976**, *68*, 1.

(132) Whittingham, M. S. *Chemical Reviews-Columbus* **2004**, *104*, 4271.

(133) Padhi, A. K.; Nanjundaswamy, K.; Goodenough, J. B. d. *Journal of The Electrochemical Society* **1997**, *144*, 1188.

(134) Scrosati, B. *Electrochimica Acta* **2000**, *45*, 2461.

(135) Ferg, E.; Gummow, R.; De Kock, A.; Thackeray, M. *Journal of The Electrochemical Society* **1994**, *141*, L147.

(136) Besenhard, J.; Yang, J.; Winter, M. *Journal of Power Sources* **1997**, *68*, 87.

(137) Chan, C. K.; Peng, H.; Liu, G.; McIlwrath, K.; Zhang, X. F.; Huggins, R. A.; Cui, Y. *Nature nanotechnology* **2007**, *3*, 31.

(138) Aurbach, D.; Talyosef, Y.; Markovsky, B.; Markevich, E.; Zinigrad, E.; Asraf, L.; Gnanaraj, J. S.; Kim, H.-J. *Electrochimica Acta* **2004**, *50*, 247.

(139) Arora, P.; Zhang, Z. *Chemical Reviews-Columbus* **2004**, *104*, 4419.

(140) Augustin, S.; Hennige, V.; Hörpel, G.; Hying, C. *Desalination* **2002**, *146*, 23.

(141) Walter, M. G.; Warren, E. L.; McKone, J. R.; Boettcher, S. W.; Mi, Q.; Santori, E. A.; Lewis, N. S. *Chemical Reviews* **2010**, *110*, 6446.

(142) Lewis, N. S. *science* **2007**, *315*, 798.

(143) Styring, S. *Faraday Discussions* **2012**, *155*, 357.

(144) Kudo, A.; Miseki, Y. *Chemical Society Reviews* **2009**, *38*, 253.

(145) Lubitz, W.; Reijerse, E. J.; Messinger, J. *Energy & Environmental Science* **2008**, *1*, 15.

(146) Bolton, J. R.; Strickler, S. J.; Connolly, J. S. *Nature* **1985**, *316*, 495.

(147) Fujishima, A.; Honda, K. *Nature* **1972**, *238*, 37.

(148) Asahi, R.; Morikawa, T.; Ohwaki, T.; Aoki, K.; Taga, Y. *Science* **2001**, *293*, 269.

(149) Goossens, A.; Maloney, E. L.; Schoonman, J. *Chemical Vapor Deposition* **1998**, *4*, 109.

(150) Mavroides, J. G.; Kafalas, J. A.; Kolesar, D. F. *Applied Physics Letters* **1976**, *28*, 241.

(151) Hardee, K. L.; Bard, A. J. *Journal of the Electrochemical Society* **1976**, *123*, 1024.

(152) Hamann, T. W. *Dalton Transactions* **2012**, *41*, 7830.

(153) Kay, A.; Cesar, I.; Grätzel, M. *Journal of the American Chemical Society* **2006**, *128*, 15714.

(154) Brillet, J.; Cornuz, M.; Formal, F. L.; Yum, J.-H.; Grätzel, M.; Sivula, K. *Journal of Materials Research* **2010**, *25*, 17.

(155) Wang, H.; Deutsch, T.; Turner, J. A. *Journal of The Electrochemical Society* **2008**, *155*, F91.

(156) Kennedy, J. H.; Frese, K. W. *Journal of the Electrochemical Society* **1978**, *125*, 709.

(157) Liao, P.; Toroker, M. C.; Carter, E. A. *Nano Letters* **2011**, *11*, 1775.

(158) Kennedy, J. H.; Anderman, M.; Shinar, R. *Journal of The Electrochemical Society* **1981**, *128*, 2371.

(159) Kumar, P.; Sharma, P.; Shrivastav, R.; Dass, S.; Satsangi, V. R. *International Journal of Hydrogen Energy* **2011**, *36*, 2777.

(160) Shinar, R.; Kennedy, J. H. *Solar Energy Materials* **1982**, *6*, 323.

(161) Glasscock, J. A.; Barnes, P. R. F.; Plumb, I. C.; Savvides, N. *The Journal of Physical Chemistry C* **2007**, *111*, 16477.

(162) Bjoerksten, U.; Moser, J.; Graetzel, M. *Chemistry of Materials* **1994**, *6*, 858.

(163) Tilley, S. D.; Cornuz, M.; Sivula, K.; Grätzel, M. *Angewandte Chemie International Edition* **2010**, *49*, 6405.

(164) Cummings, C. Y.; Marken, F.; Peter, L. M.; Tahir, A. A.; Wijayantha, K. G. U. *Chemical Communications* **2012**, *48*, 2027.

(165) Gamelin, D. R. *Nat Chem* **2012**, *4*, 965.

(166) Klahr, B.; Gimenez, S.; Fabregat-Santiago, F.; Bisquert, J.; Hamann, T. W. *Journal of the American Chemical Society* **2012**, *134*, 16693.

(167) Barroso, M.; Cowan, A. J.; Pendlebury, S. R.; Grätzel, M.; Klug, D. R.; Durrant, J. R. *Journal of the American Chemical Society* **2011**, *133*, 14868.

(168) Zhong, D. K.; Gamelin, D. R. *Journal of the American Chemical Society* **2010**, *132*, 4202.

2 Characterization

Nanoparticles and porous materials constructed thereof can be characterized by using a variety of different techniques usually applied in materials science. The nanoparticle composition and properties are commonly assessed by electron microscopy (TEM and SEM), dynamic light scattering (DLS), powder X-ray diffraction (XRD) and vibrational spectroscopy (Raman). Porous materials can be visualized by electron microscopy, but additionally physisorption plays a very important role in the estimation of the porosity and the pore size. Finally, depending on the materials properties, the performance of these can be analyzed in the corresponding applications, such as dye-sensitized solar cells, batteries and photoelectrochemical water splitting.

2.1 X-Ray diffraction (XRD)

X-ray diffraction (XRD) is a very useful non-destructive analytical method that gives information on the phase composition and crystallinity of a specimen. Additionally, XRD can be used for the characterization of periodically ordered mesostructures. The physical principle of X-ray diffraction is the elastic scattering of X-rays by atoms in a periodic three-dimensional structure having a periodicity similar to the X-ray wavelengths. If the material is periodically structured, the scattered X-rays interfere constructively and give the diffraction pattern (Figure 2-1). The relationship between the scattering angle and the distance of lattice planes or pore walls is given by Bragg's law:

$$n\lambda = 2d \sin\theta \tag{2-1}$$

n: Order of interference

λ: Wavelength of utilized X-rays (for Cu K_α: λ = 1.540562 Å)

d: Lattice spacing

θ: Angle of incidence

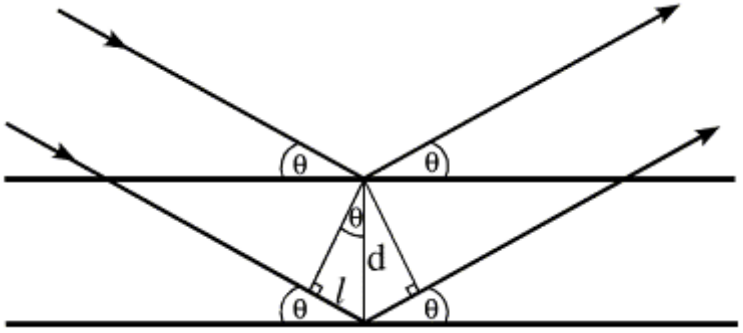

Figure 2-1: Derivation of Bragg's relation.

Wide angle X-ray scattering (WAXS) is measured at angles from 10° to about 100° 2θ and allows for the analysis of the phase composition and the crystallinity of the material. The full width at half maximum (FWHM) of the reflections is correlated to the peak broadening which is used to determine the average size of the crystallite domains with the Scherrer Equation:

$$D = \frac{k\lambda}{\beta \cos\theta} \tag{2-2}$$

k: Shape-dependent proportionality factor

λ: Wavelength of X-rays

β: Full width at half maximum of the reflection (FWHM)

θ: Scattering angle

For spherical particles the shape-dependent proportionality factor is usually around 0.9 and the FWHM is corrected for the intrinsic instrumental broadening.

Small angle X-ray scattering (SAXS) is typically measured at 2θ angles below 10° and with this method periodic structures on the nanoscale as in ordered mesoporous films for example can be characterized. In this way, the pore-to-pore distance can be calculated by using Bragg's equation.

X-ray diffraction analysis was carried out in reflection mode using a Bruker D8 Discover with Ni-filtered Cu-K_α-radiation and a position-sensitive semiconductor detector (LynxEye). Measurements in transmission mode were carried out on a STOE powder diffractometer in transmission geometry (Cu-$K_{\alpha1}$, λ = 1.5406 Å) equipped with a position-sensitive Mythen-1K detector.

2.2 Raman spectroscopy

Raman spectroscopy is a non-destructive and quantitative method for the characterization of materials and allows for determining properties such as the presence of certain chemical moieties or phases in the specimen. In Raman spectroscopy vibrational, rotational and low-frequency modes are monitored to give information about the molecules or crystalline materials. In general, a monochromatic light source, most commonly a laser, is used to interact with the electron cloud or bonds in a molecule to excite the material from the ground state into a virtual energy state. This excitation is different from absorption processes in which the excitation leads to discrete excited states. From the excited state the molecule relaxes and a photon is emitted in the course of this process. The incident light can either be scattered elastically (Rayleigh scattering) which means that the energy of the emitted compared to the absorbed photon is unchanged, or it can be scattered inelastically where the energy of the emitted photon is different from the excitation energy (Figure 2-2). The observation of this shift in energy is called Raman effect and was observed for the first time in 1928 by Sir C.V. Raman.[1] The difference of the energy of the incident and emitted light is due to the relaxation into a vibrational or rotational state different from the initial state. There are two possibilities for the inelastic scattering and therefore different energy shifts: In the so-called Stokes Raman scattering the molecule which is excited is initially in its ground state and it can relax into a vibrational or rotational state with higher energy leading to the emission of photons with a longer wavelength. In Anti-Stokes Raman scattering the molecule is initially in an excited vibrational state and relaxes into a state with lower energy leading to the emission of photons with higher energy than the excitation energy.

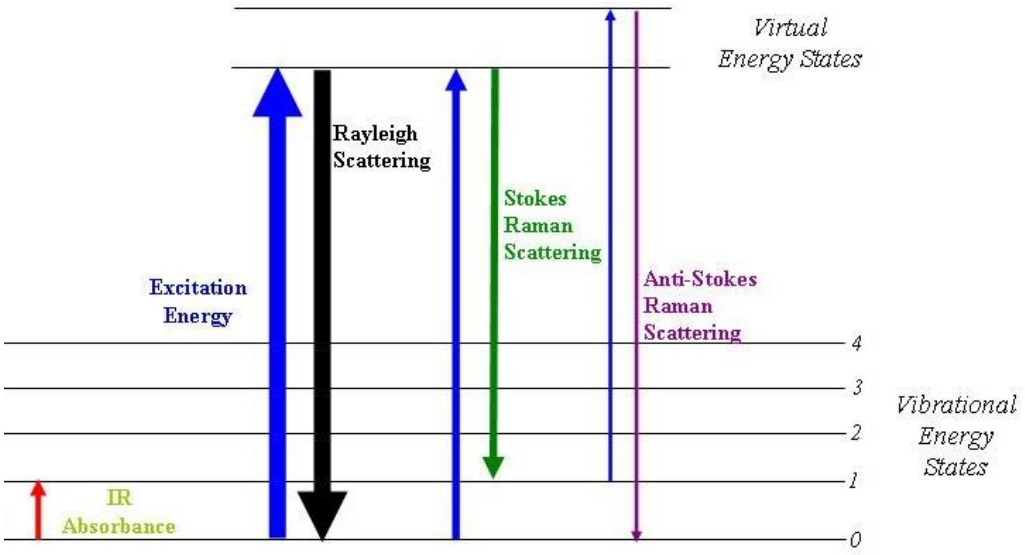

Figure 2-2: Energy levels and transition processes in Raman spectroscopy with the Rayleigh-, Stokes-, and anti-Stokes scattering.[2]

In general, the intensity of the Stokes lines is much higher than for Anti-Stokes scattering, due to the low occupation of excited states at room temperature.

Raman spectra were recorded with a LabRAM HR UV-VIS (Horiba Jobin Yvon) Raman microscope (Olympus BX41) with a Symphony CCD detection system using a HeNe laser at 632.8 nm.

2.3 Dynamic light scattering

Dynamic light scattering (DLS), also called photon correlation spectroscopy, is a non-destructive and fast method to determine the size distribution of particles in suspension or of polymers in solution.[3,4] Additionally it can be used to monitor the agglomeration behavior of nanoparticles over a certain time scale depending on the surrounding conditions such as the pH value for example.[5] A suitable light source for the measurements is a laser due to its monochromatic and coherent radiation. If the size of the particles is small compared to the wavelength of the light source, Rayleigh scattering occurs equally in all directions. A time-dependent fluctuation of the detected signal results from the Brownian motion of the

nanoparticles. The constructive and destructive interference of the scattered light gives intensity fluctuations, a so-called speckle pattern, which contains information about the movement of the scatterers. Since this is also dependent on the hydrodynamic shell of these species, the detected size is always the hydrodynamic radius rather than the real size of the objects. The changes in the speckle pattern are analyzed with the help of a digital correlator and the fluctuations in intensity are correlated over time with a second order autocorrelation function:

$$g^2\,(q;\tau) = \frac{\langle I(t)I(t+\tau)\rangle}{\langle I(\tau)\rangle^2} \qquad (2\text{-}3)$$

q: Wave detector

τ: Delay time

I: Intensity

This function decays exponentially towards long delay times and can be related to a first order autocorrelation function g^1:

$$g^2\,(q;\tau) = 1 + \beta[g^1(q;\tau)]^2 \qquad (2\text{-}4)$$

q: Wave detector

τ: Delay time

β: Correction factor

The diffusion coefficient D can be obtained from a single exponential function when assuming a monodisperse dilute dispersion of nanoparticles:

$$g^1\,(q;\tau) = e^{-q^2 D\tau} \tag{2-5}$$

D: Diffusion coefficient

The Stokes-Einstein equation gives the relation between this diffusion coefficient and the hydrodynamic diameter of spherical particles:

$$D = \frac{kT}{3\pi\eta d} \tag{2-6}$$

k: Boltzmann constant

T: Temperature

η: Solvent viscosity

d: Hydrodynamic diameter

Due to the usually non-monodisperse nature of nanoparticles, size distribution effects have to be taken into account by the application of Mie theory or Rayleigh scattering. While Mie Theory describes the scattering from larger particles, Rayleigh scattering is used to describe the elastic interaction of unpolarized light with particles smaller than the wavelength of the light:

$$I = I_0 \frac{1 + \cos^2\theta}{2\,R^2} \left(\frac{2\pi}{\lambda}\right)^4 \left(\frac{n^2 - 1}{n^2 + 2}\right)^2 \left(\frac{d}{2}\right)^6 \quad (2\text{-}7)$$

I_0: Intensity of incoming light

θ: Scattering angle

R: Distance to the particle

λ: Wavelength of incoming light

n: Refractive index of the material

d: Diameter of particles

Since the scattering intensity is proportional to d^6, big particles contribute much more to the scattering intensity as compared to small ones. This effect leads to an over-estimation of the size in polydisperse samples and thus needs to be considered in data evaluation. To solve this issue, the intensity-based measurement data of the DLS can also be presented as volume-weighted (d^3) or number-weighted (d) distributions, giving the real size distribution of polydisperse samples. Dynamic light scattering (DLS) measurements were carried out on diluted suspensions using a Malvern Zetasizer-Nano instrument with a 4 mW He-Ne laser (λ = 633 nm) and an avalanche photo detector.

2.4 UV/Vis spectroscopy

UV/Vis spectroscopy is used to quantitatively determine the light absorption behavior of molecules in solution or solid materials. For this purpose, the sample is illuminated with light in the ultraviolet and visible region, which can interact with valence electrons and excite them

to higher energy orbitals. The energy of the absorbed photons corresponds to the energy difference of the orbitals and can give information about the compounds. Beer-Lamberts law allows determining the concentration of an absorbing species with this equation:[1]

$$A = -log\frac{I}{I_0} = \varepsilon cL \tag{2-8}$$

A: Detected absorbance

I_0: Intensity of incident light

I: Intensity of transmitted light

ε: Extinction coefficient

L: Path length of light through sample

The setup of UV/Vis spectrophotometers usually consists of a light source, a monochromator, a sample holder and a detector. Different light sources are applied to ensure a continuous spectrum, such as a deuterium arc lamp for the UV region and a tungsten filament or a xenon arc lamp for the visible region. The monochromator separates the different wavelengths from each other and allows the measurement of a wavelength resolved spectrum. The detector is typically a photodiode array or a charge-coupled device (CCD).

UV-Vis measurements were performed on a Hitachi U3501 or a Perkin Elmer Lambda 1050 spectrophotometer.

2.5 Electron microscopy

Electron microscopy is a very important technique to characterize materials in detail concerning their structure and composition on the nanoscale. Contrary to usual light

microscopes the resolution is not limited to about 200 nm and therefore images can be obtained on the atomic scale due to the shorter wavelength of the utilized electrons in the range of picometers.[6] The electron beam can be generated by either a heated tungsten filament or a field emission gun and is accelerated with a potential difference of about 4 to 1000 keV. The electron beam is then focused on the sample with electromagnetic or electrostatic lenses with a spot size of typically a few nanometers (Figure 2-3). The interaction of these high energy electrons with matter is much stronger than that of X-rays or light and the resulting primary electrons can be classified as following: No interaction with the sample, no change in direction and no energy loss can be detected for transmitted electrons which are important for the imaging of the structure of a sample. The fraction of transmitted electrons is depending on the elemental composition, the density or porosity of the material and mainly on the thickness of a sample, which needs to be prepared thinner than about 100 nm with elaborate sample preparation techniques. Diffracted and backscattered electrons are scattered elastically with both still having a high energy but occurring at different diffraction angles. When the high energy primary electrons hit and strike out electrons of the sample, secondary electrons can be emitted. Due to the rather low energy of these electrons, only those generated close to the surface of a sample can emerge and be detected which makes them very important for surface probing techniques. When electrons of the sample are removed from the inner shell, the generated vacancies are filled by electrons from a higher shell. This energy difference is either released by the emission of characteristic X-rays or of an Auger electron from an outer shell.

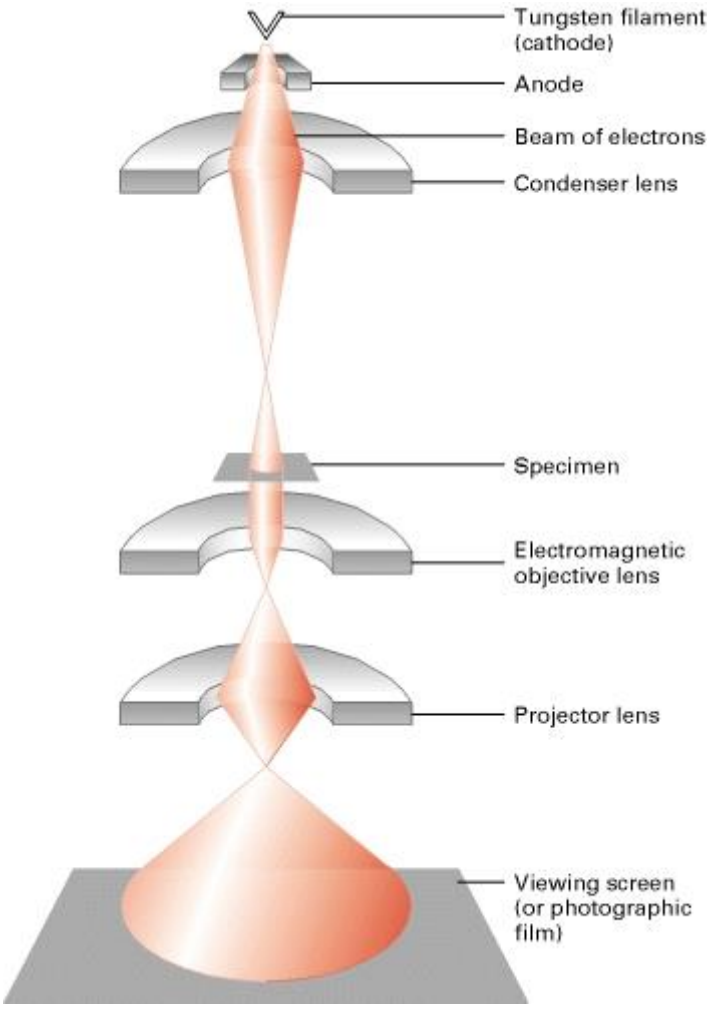

Figure 2-3: Optical pathway in a transmission electron microscope.[5]

Electron microscopy can be mainly divided into three different techniques: Scanning electron microscopy (SEM) is used to investigate the surface of a sample by scanning it with a beam of focused electrons in a grid pattern. The resulting signal of each sample spot is collected and the information is put together to produce an image of the surface. In contrast, transmission electron microscopy (TEM) is used to obtain information on the internal structure of a sample by detecting the transmitted electrons on a fluorescent screen or by a CCD camera. When obtaining the image in TEM with a strongly focused electron beam that scans the sample in a grid-like pattern like in SEM, this special technique is called scanning transmission electron microscopy (STEM). With a circular detector arranged around the optical axis of the microscope, images with a very high mass contrast can be obtained due to the collection of

only high angle diffracted electrons. This technique is called high angle annular dark field mode (HAADF).

Scanning electron microscopy (SEM) was performed on a JEOL JSM-6500F scanning electron microscope equipped with a field emission gun operated at 4 – 10 kV depending on the sample. High Resolution Transmission Electron Microscopy (HRTEM) and Scanning Transmission Electron Microscopy in High Angle Annular Dark Field mode (STEM-HAADF) were performed using a FEI Titan 80-300 equipped with a field emission gun operated at 300 kV.

2.6 Sorption

Sorption measurements are a versatile method for the characterization of porous systems regarding the pore characteristics and the surface area.[7] Sorption isotherms are measured at a constant temperature and the amount of adsorbed species is plotted versus varying pressures for the adsorption and the desorption processes. The interactions of the adsorbed species with the surface are mainly weak van-der-Waals forces, so they can be classified as physisorption processes. Various models with different assumptions are used to describe those interactions and one of the most common ones is the Brunauer-Emmett-Teller (BET) theory.[8] Two assumptions are made: There is no interaction of the adsorbed species among each other in a layer and the adsorption enthalpy of the first monolayer is different from that for multilayer formation. The BET method allows determining the surface area of a sample by analyzing the monolayer formation at low partial pressures in the isotherm and multiplying it with the adsorption area of the adsorptive molecules.

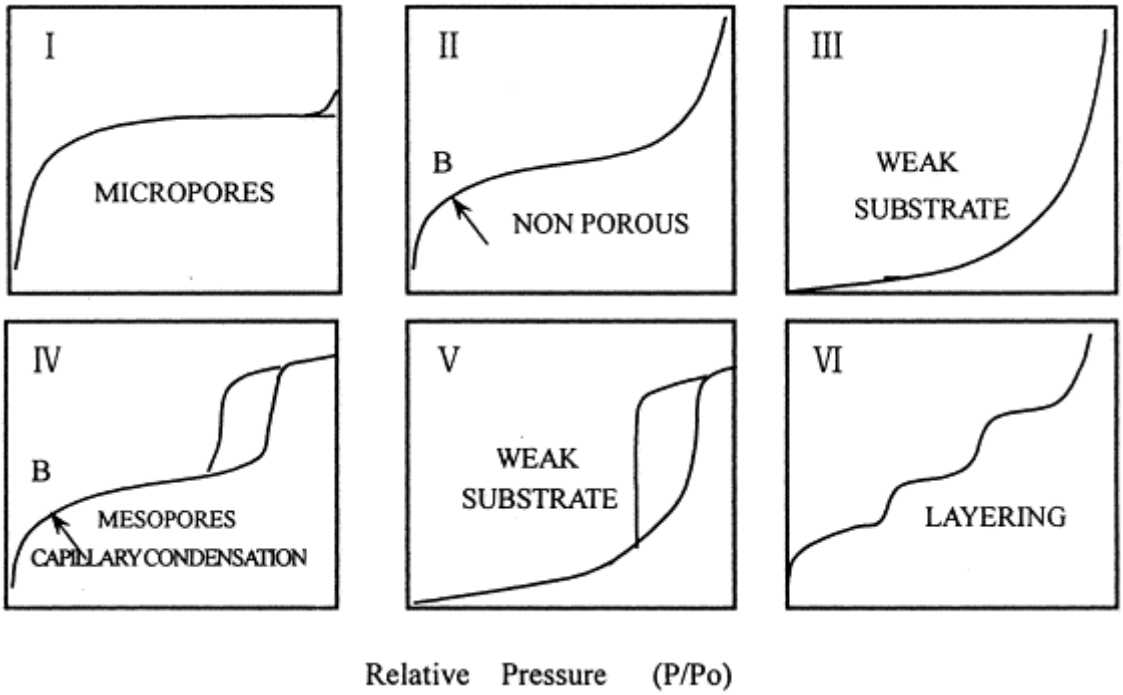

Figure 2-4: The six types of gas sorption isotherms as classified by IUPAC.[9]

Sorption isotherms can be classified in 6 different basic types (I – VI) depending on the structure and size of the pore systems and interaction strength of the adsorptive with the adsorbent (Figure 2-4). Type IV isotherms are typical for mesoporous samples exhibiting a monolayer adsorption with the subsequent multilayer formation at low partial pressures and a typical hysteresis loop of the adsorption and desorption branch which is ascribed to capillary condensation of adsorptive in the mesopores and the hindered desorption therefrom.[10] The further adsorption at higher partial pressures is caused by adsorption at the external surface or in textural porosity.

Nitrogen gas is usually used as adsorptive for sorption measurements on porous powder samples. The measurements are carried out at the boiling point of liquid nitrogen, i.e. 77 K. Structure characteristics of porous materials, such as surface area and pore volume can be obtained from classical thermodynamic calculations whereas for the calculation of the pore size distribution approaches such as the Barrett-Joyner-Halenda (BJH) theory, non-local density functional theory (NLDFT) or Monte-Carlo simulations (MC) have to be employed.

Nitrogen sorption is not applicable to materials with a very small specific surface area, for example thin mesoporous films. In this case, Krypton sorption measurements can be conducted alternatively to determine surface areas down to a few cm^2.[11] Krypton sorption is also measured at 77 K where it is solid and therefore has a lower saturation vapor pressure than nitrogen. However, due to its physical properties, the theory for other liquid adsorptives cannot be applied and the surface area and pore size have to be determined indirectly by calibration measurements of standards.

For the characterization of mesoporous titania films assembled from the ultra-small titania nanocrystals, all Kr sorption measurements were performed and evaluated by Dr. Jiri Rathouský at the J. Heyrovský Institute of Physical Chemistry in Prague. The analysis of adsorption isotherms of Kr at the boiling point of liquid nitrogen (approx. 77 K) gave the porosity of the thin films. An ASAP 2010 apparatus (Micromeritics) was used to obtain the isotherms. For the determination of textural properties of the samples, the shape of the hysteresis loop and the limiting adsorption at saturation pressure of the krypton sorption isotherms was compared with reference materials (anatase powders) characterized by nitrogen sorption. The pore size distribution was obtained from comparison plots that were based on the differentiation of these plots for each sample.

Nitrogen sorption measurements were performed on a Quantachrome Instruments Nova 4000e or an Autosorb-1 by Quantachrome Instruments at 77 K and the samples were degassed for 12 h at 150 °C.

2.7 Quartz crystal microbalance

The Quartz Crystal Microbalance (QCM) is an ultrafine balance system that measures very small changes in mass through the change in resonance frequency of a piezoelectric quartz crystal. This method is based on the inverse piezoelectric effect in which a mechanical deformation results from the application of an electric field and the Sauerbrey equation gives the relation of the change in mass Δm with a change in frequency Δf:[12]

$$\Delta f = -\frac{2f_0^2 \Delta m}{A\sqrt{\rho_q \mu_q}} \tag{2-9}$$

f_0: Resonant frequency

A: Active area of the crystal

ρ_q: Density of quartz

μ_q: Shear modulus of quartz

The frequency change results from a modified vibration frequency of the piezoelectric chip due to a changed mass loading. This allows to measure very small amounts of mass deposited on the chip and can therefore be used for the determination of the mass of very thin porous films. For example, for a 10 MHz crystal a frequency change of 1 Hz corresponds to a mass loading of $4.42 \cdot 10^{-9}$ g on an active surface area on the chip of 1 cm^2. This high sensitivity is especially useful for electrochemical measurements, since the capacity of an electrode material is usually given in electric charge (Ah) per mass (g) and the usual balances are not sensitive enough to determine the mass of very thin electrodes. The application of these chips as electrodes in electrochemical measurements allows a direct determination of the active mass deposited on the electrodes (Figure 2-5).

Figure 2-5: Image of a QCM chip.

Alternatively, the very high gravimetric sensitivity of the quartz crystal microbalance can be employed for gravimetric sorption measurements. The mesoporous films are usually prepared by spin-coating and subsequent calcination on the QCM chips. Adsorptives can be gases or solvent vapors. However, the models for nitrogen gas sorption are difficult to adapt to the interaction of solvent molecules with porous metal oxide surfaces.

QCM measurements were carried out using a self-built Quartz Crystal Microbalance (QCM) system. The mesoporous films were produced by spin-coating of a precursor solution on KVG 10 MHz QCM devices with gold electrodes (from Quartz Crystal Technology GmbH) and subsequent calcination.

2.8 Thermogravimetric analysis

Thermogravimetric analysis (TGA) is a method to detect a change in the mass of a sample with temperature and time. The sample is placed in an inert crucible, such as platinum or corundum, which is coupled to a microbalance. The heating process with a constant heat rate can be conducted in different gas atmospheres such as argon, nitrogen or synthetic air. This

allows distinguishing evaporation and desorption of solvent molecules, for example from oxidative decomposition processes.[13] By calculating the total mass loss after heating the sample to 900 °C in an oxidative atmosphere, the total content of inorganic material in metal oxide nanoparticles can be determined and compared to the initial weight including solvent molecules and surface-bound organic ligands. Additionally, the enthalpy of those processes can be determined with differential scanning calorimetry (DSC) measuring the difference of energy needed for heating the sample compared to an inert reference. The nature of the processes can be assessed from the information gained in these measurements, for example combustion (exothermic) can be distinguished from phase transformation and evaporation (endothermic) processes.

Thermogravimetric analyses of the samples were performed on a Netzsch STA 440 C TG/DSC.

2.9 Electrochemical lithium insertion

High-performance battery materials are very important not only for the implementation in personal mobile devices but will also play a decisive role in the conversion from fossil fuel based transportation to a low carbon dioxide footprint electrical transportation based on renewable energy sources. In this work two nanostructured anode materials for lithium ion batteries were prepared, TiO_2 and the highly stable $Li_4Ti_5O_{12}$. The electrochemical equations for the charging reactions are as follows:

$$x\ Li^+ + x\ e^- + TiO_2 \rightarrow Li_xTiO_2 \qquad (2\text{-}10)$$

$$Li_4Ti_5O_{12} + 3\ Li^+ + 3\ e^- \rightarrow Li_7Ti_5O_{12} \qquad (2\text{-}11)$$

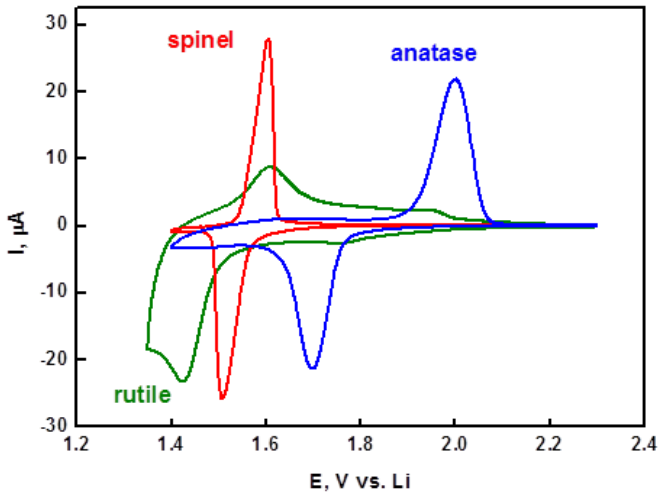

Figure 2-6: Cyclic voltammogram (CV) of an electrochemical lithium insertion experiment in the TiO_2 phases rutile and anatase and $Li_4Ti_5O_{12}$ spinel with the corresponding distinct insertion and extraction peaks. A broad hysteresis of the baseline curve is mainly attributed to capacitive (faradaic and non-faradaic) charging as well as electrochemical contributions of amorphous titania phases.

In both cases Ti(IV) is reduced to Ti(III) and lithium ions are inserted into the structures to compensate the charge. The formal potentials at which this lithium insertion takes place depend on the phases of the material, and they are 1.85 V and 1.55 V vs. lithium for TiO_2 in its anatase phase and lithium titanate, respectively (Figure 2-6). The maximum theoretical capacities for both materials at full lithium insertion are 168 mAh g^{-1} and 175 mAh g^{-1}, corresponding to $Li_{0.5}TiO_2$ and $Li_7Ti_5O_{12}$, respectively. This total capacity can be attributed to mainly two different contributions, i.e. the faradaic insertion of lithium into the bulk of the materials and charge-storage on the surface of the nanomaterials which can either be a capacitive process (non-faradaic) or of faradaic nature (pseudo-capacitive) in which redox reactions at the surface take place. The kinetics of such reactions are usually very different from each other since the bulk diffusion of lithium ions is rather slow. Hence, when increasing the surface area of the electrodes the capacitive and pseudo-capacitive contributions can be drastically increased leading to a shortened charging time of the devices.

In our studies we used a method to quantify the amount contributed from the different charge storage mechanisms in which the contributions can be distinguished by determining the current response depending on the sweep rates in cyclic voltammetry (CV).[14-16] In cyclic voltammetry the applied potential is varied linearly over time with a certain sweep rate and the resulting current is detected.[17] When reaching a certain set potential the potential ramp is inverted and applied until the initial potential is reached. The oxidation and reduction reactions take place at characteristic potentials for the materials and the potential is varied in a certain region usually defined by the decomposition reactions of the utilized electrolyte. Cyclic voltammetry is a versatile method to characterize electrochemically active compounds usually in a three-electrode setup with a working electrode, a counter electrode and a reference electrode. The total gravimetric lithium insertion capacities can be determined by the integration of the area under CV curve upon reduction (charging) and oxidation (discharging) of the TiO_2 and $Li_4Ti_5O_{12}$ and normalizing the obtained charge to the mass of the electrode.

For $Li_4Ti_5O_{12}$ mainly galvanostatic lithium insertion experiments were conducted in which a constant current is applied and the resulting change in potential is monitored until a cut-off potential is reached. This method allows a very fast and simple determination of the capacity of the tested electrodes by simply normalizing the charge plotted on the x-axis to the electrode mass. The electrochemical insertion and extraction reactions can be inverted by applying the same current with a negative sign and vice versa. Depending on the amount of current applied compared to the active electrode mass, charging and discharging rates can be specified. This is usually expressed as the C-rate, which is defined as a factor of charge over time. Charging or discharging a battery in 1 hour to its full capacity is defined as 1 C and doing this in half an hour would lead to a C-rate of 2 C, for example. The kinetics of the nanostructured electrodes can be characterized by performing the measurements at various C-rates, and to assess the

stability of the materials cycling experiments have been conducted by repeating the measurements up to 1000 times. The contributions from pseudo-capacitive and bulk-diffusion limited processes were deconvoluted by the analysis of cyclic voltammograms at different scan rates. This is described in detail in Chapter 7.

Electrochemical measurements were carried out using a Parstat 2273 potentiostat (Princeton Applied Research). The measurements were performed in a 1 M LiN-$(SO_2CF_3)_2$ solution in a mixture of ethylenecarbonate (EC) and 1,2-dimethoxyethane (DME) (1:1 by weight). Li wires were used as both the auxiliary and the reference electrodes.

2.10 Photovoltaic characterization

The dye-sensitized solar cells were assembled from the mesoporous titania films and were mainly characterized by measuring current-voltage (I-V) curves on a potentiostat with and without illumination of the sample. The current was collected at altering externally applied potentials with scan rates slow enough to a avoid capacitive charging on the high surface area of the titania films.[18] The standard performance characteristics of the solar cells such as the short-circuit current I_{SC}, the open circuit potential V_{OC}, the fill factor FF and the power conversion efficiency η can be extracted from the I-V-curves as described in the introduction (Chapter 1.5).

An AM 1.5 solar simulator (Solar light Co.) was used for the characterization of solar cells. The light intensity was monitored by a pyranometer (PMA2100, Solar light Co.). Current density-voltage measurements were performed with a Zahner IM6ex impedance measurement unit with a scan speed of 10 mV s^{-1}.

2.11 Photo-electrochemical water splitting characterization

For the characterization of hematite photo-electrodes in photo-electrochemical water splitting, several measurements were conducted. The current-voltage characteristics of the masked films were obtained by scanning from negative to positive potentials in the dark or under illumination, with a 20 mV s^{-1} sweep rate. For external quantum efficiency (EQE) measurements, chopped monochromatic light (chopping frequency 2 Hz) was provided by a 150 W Xenon lamp in combination with a monochromator and order-sorting filters. The cell was biased to 1.23 V vs. RHE under simulated solar irradiation to ensure realistic operating conditions. Current transients were used to determine the transfer efficiency of holes to the solution phase.[19] The high power light emitting diode (LED) was switched on and off every 500 ms. The hematite electrodes were held at a given potential, and transient current was sampled at 0.1 ms intervals. This fast sampling allowed the instantaneous current to be determined. In cases where the current transient had not reached a steady state value after 500 ms, additional photocurrent transients were recorded with 5 s on/off times, sampled at 1 ms intervals.

All electrochemical measurements were carried out in a 0.1 M NaOH aqueous electrolyte in glass or quartz cells using a μ-Autolab III potentiostat equipped with a FRA2 impedance analyzer connected to a saturated Ag/AgCl (or a Hg/HgO) reference electrode and a Pt mesh counter electrode. Illumination was either provided by a power LED (Thorlabs, 455 nm), or a simulated AM1.5 solar simulator (Solar Light Model 16S) at 100 mW cm^{-2}, and was incident through the substrate (SI) or the electrolyte (EI). The light intensity was measured inside the cells using a 4 mm^2 photodiode, which had been calibrated against a certified Fraunhofer ISE silicon reference cell equipped with a KG5 filter.

2.12 References

(1) Atkins, P. W. *Physikalische Chemie*; John Wiley & Sons, **2002**.

(2) http://commons.wikimedia.org/wiki/File:Raman_energy_levels.jpg, 30.04.2013.

(3) Burchard, W. In *Light Scattering from Polymers*; Springer Berlin Heidelberg: **1983**; Vol. 48, p 1.

(4) Pecora, R. *Journal of Nanoparticle Research* **2000**, *2*, 123.

(5) Murphy, R. J.; Pristinski, D.; Migler, K.; Douglas, J. F.; Prabhu, V. M. *The Journal of Chemical Physics* **2010**, *132*, 194903.

(6) Williams, D. B.; Carter, C. B. *The Transmission Electron Microscope*; Springer, **1996**.

(7) Lowell, S.; Shields, J. E.; Thomas, M. A.; Thommes, M. *Characterization of porous solids and powders: surface area, pore size and density*; Springer, **2006**; Vol. 16.

(8) Brunauer, S.; Emmett, P. H.; Teller, E. *Journal of the American Chemical Society* **1938**, *60*, 309.

(9) Ryu, Z.; Zheng, J.; Wang, M.; Zhang, B. *Carbon* **1999**, *37*, 1257.

(10) Rouquerol, J.; Rouquerol, F.; Sing, K. S. W. *Adsorption by Powders and Porous Solids*; Elsevier Science, **1998**.

(11) Beebe, R. A.; Beckwith, J. B.; Honig, J. M. *Journal of the American Chemical Society* **1945**, *67*, 1554.

(12) Sauerbrey, G. *Zeitschrift für Physik* **1959**, *155*, 206.

(13) Pang, L. S. K.; Saxby, J. D.; Chatfield, S. P. *The Journal of Physical Chemistry* **1993**, *97*, 6941.

(14) Brezesinski, T.; Wang, J.; Polleux, J.; Dunn, B.; Tolbert, S. H. *Journal of the American Chemical Society* **2009**, *131*, 1802.

(15) Wang, J.; Polleux, J.; Lim, J.; Dunn, B. *The Journal of Physical Chemistry C* **2007**, *111*, 14925.

(16) Conway, B. E.; Birss, V.; Wojtowicz, J. *Journal of Power Sources* **1997**, *66*, 1.

(17) Heinze, J. *Angewandte Chemie* **1984**, *96*, 823.

(18) Hagfeldt, A.; Boschloo, G.; Sun, L.; Kloo, L.; Pettersson, H. *Chemical Reviews* **2010**, *110*, 6595.

(19) Peter, L. M.; Wijayantha, K. G. U.; Tahir, A. *Faraday Discussions* **2011**.

3 Ultrasmall titania nanocrystals and their direct assembly into mesoporous structures showing fast lithium insertion

This chapter is based on the following publication:

Johann M. Szeifert, Johann M. Feckl, Dina Fattakhova-Rohlfing, Yujing Liu, Vit Kalousek, Jiri Rathouský, Thomas Bein, *Journal of the American Chemical Society* **2010**, *132*, 12605 – 12611.

3.1 Introduction

Mesoporous crystalline metal oxide layers have been in the focus of extensive research activities in the last decade.[1-5] The crystallinity of a metal oxide scaffold in combination with a high interfacial surface area and a periodic ordering on the nanoscale are of special interest in applications involving interfacial charge transfer and bulk charge transport processes such as solar cells,[6-8] sensors[9] and energy storage devices.[10,11] The basic approach to manufacturing such layers is the self-assembly of metal oxide building units assisted by a suitable structure-directing agent.[1,12] The critical point here is the amorphous character of the common metal oxide precursors, which usually emanate from sol-gel synthesis and require crystallization at elevated temperatures, often resulting in the collapse of the mesostructure.[13] This limitation motivates the search for largely crystalline building units that could convert to the final crystalline periodic scaffolds at mild conditions and low temperatures.[14] To make such an approach successful, the building blocks need to be extremely small in order to be compatible with the size of the structure-directing agents, and they should be dispersible in the required solvents without agglomeration.[15] Hydrothermal synthesis methods are often unsuitable for this purpose due to the fast reaction rates, resulting in highly agglomerated nanoparticles with

a wide distribution of particle size and shape. On the contrary, non-aqueous solvothermal routes usually provide much better control over the size, crystallinity and agglomeration behavior of the nanoparticles.[16] Among the large number of organic solvents examined in this context, benzyl alcohol has received much attention, as it enables the synthesis of a large variety of metal oxide nanoparticles with high crystallinity, a low degree of agglomeration and tunable particle size.[17,18] However, it is difficult to prepare extremely small particles with this approach, and surface-modifying ligands are needed for stabilization. Another issue with the benzyl alcohol synthesis is the presence of benzyl alcoholate residues on the particles' surface, which influence physical and chemical properties of the interface and can be removed only by harsh oxidative treatment or at temperatures above 450 °C.[19,20] An accessible and ligand-free surface is, however, of great importance for charge transfer processes across the interfaces. This issue can be solved when non-aromatic solvents are used as reaction medium.[21] Thus, polyols enable the preparation of monodisperse crystalline nanoparticles with good interface properties, however, again it is difficult to prepare very small nanoparticles with this approach.[22,23] Aliphatic alcohols usually require higher reaction temperatures and typically do not provide homodispersed non-agglomerated nanocrystals.[24-27] Crystalline nanoparticles can also be prepared in other non-aqueous solvents such as ketones or aldehydes.[28]

Aiming to prepare metal oxide nanoparticles of small size, enhanced crystallinity and good dispersibility without the need of additional stabilizing ligands, we explored *tert*-butanol as a novel reaction medium. Similar to other small aliphatic alcohols, this solvent can be easily removed due to its low boiling point of 83 °C. The unique reactivity of *tert*-butanol resulting from a strong inductive stabilization of an intermediate carbocation is supposed to result in a different mechanism of particle formation compared to that of other aliphatic alcohols, thus

leading to particles with different properties and morphology.[29] As a metal oxide system we selected titanium dioxide, which is of great interest for applications in solar cells, catalysis and energy storage.[30]

Here we describe the use of *tert*-butanol as a new solvent and reactant in a non-aqueous sol-gel protocol leading to highly dispersible and nanocrystalline titania particles without the need for additional ligands or surfactants. Ultrasmall anatase nanoparticles of high crystallinity were obtained by a special microwave-based heating procedure that allows the crystal formation within several minutes. Additionally, this new approach permits the direct application of the as-synthesized particles in combination with a commercial polymer template for the preparation of mesoporous titanium dioxide films without the need for particle separation or chemical processing. The crystalline nature of the films and their use as electrode material for Li-ion batteries is shown by electrochemical lithium insertion. In this method, the high surface to bulk ratio of the nanocrystals, and the easily accessible mesoporous structures with extremely thin walls lead to a drastic acceleration of the Li insertion and high maximum capacitance. This fast synthetic strategy leading to highly dispersible and crystalline nanoparticles represents a versatile alternative for the preparation of periodically ordered mesostructures, and should be applicable to other metal oxides and mixed oxides.

The following experiments have been performed by Johann M. Feckl and Johann M. Szeifert in the group of Prof. Dr. Thomas Bein. Vit Kalousek and Dr. Jiri Rathouský contributed by measuring and evaluating krypton sorption isotherms.

3.2 Results and Discussion

In a typical procedure for the preparation of titanium dioxide nanoparticles, a solution of titanium tetrachloride in toluene was added to water-free *tert*-butanol at 25 °C and subjected to different temperature treatments. In a conventional synthesis, the reaction mixture was put into an oven at 60 °C for 24 hours until it turned into a colorless but turbid and highly viscous suspension (assigned further as T60). After cooling to room temperature, the nanoparticles were separated by centrifugation for further characterization. The particles were highly dispersible in ethanol, and wide-angle X-ray scattering (WAXS) of the material showed the formation of partially crystalline TiO_2 anatase particles of about 4 nm in size and the presence of a relatively large amount of amorphous phase (Figure 3-1a).

In an attempt to shorten the reaction time, microwave-based heating was examined for this reaction mixture, as it had been reported for other systems to significantly accelerate certain reactions.[31] After only one hour at 50 °C under microwave irradiation, the solution turned colorless and transparent, and formation of anatase particles of only 3.1 nm was observed by dynamic light scattering (DLS) and WAXS (Sample MW50, Figure 3-1a). The broad background in the WAXS pattern still indicates the presence of amorphous material, but at much lower relative ratios than for samples prepared by conventional heating. Microwave syntheses at higher temperatures led to a significant increase in crystallinity, but also to larger particle sizes and precipitation of the particles from the solution, thus decreasing their dispersibility.

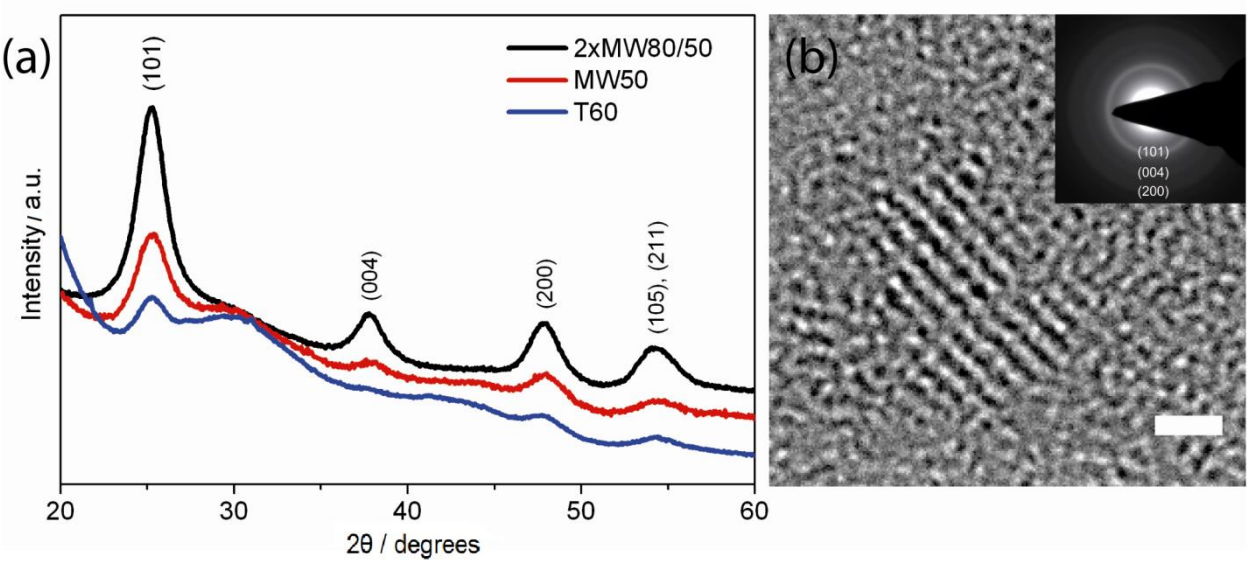

Figure 3-1: Crystallinity and morphology of the TiO_2 nanoparticles obtained using *tert*-BuOH as the reaction medium after different synthesis conditions: WAXS patterns of samples T60 (blue), MW50 (red) and 2xMW80/50 (black) (a); high resolution TEM image (HRTEM) and SAED pattern (inset) of the MW50 particles (b). The scale bar corresponds to a distance of 1.0 nm.

Using microwave irradiation, we aimed to maximize the yield of crystalline material in the product and simultaneously to prevent further particle growth and agglomeration. For this purpose, we combined a fast ramp to a higher temperature such as 80 °C for an initial burst of nucleation, directly followed by a cooling period and a longer dwell time at lower temperatures (50 °C) for subsequent particle growth (sample MW80/50). This procedure leads to the formation of very small and crystalline particles without visible agglomeration, as demonstrated by the DLS data of the particles in solution (Figure 3-3), and the transmission electron microscopy (TEM) images of dried particles on a carbon-coated copper grid (Figure 3-1b). Although DLS data show the formation of small particles of less than 3 nm in size, the yellow color of the reaction solution still indicates the presence of titanium-chloro complexes and thus incompletely reacted molecular precursors. It was found that after two cycles of this heat treatment a colorless and slightly turbid solution can be obtained (sample 2xMW80/50), from which nanoscale titanium dioxide could be flocculated using n-heptane. TGA data of this sample show weight loss to above 400 °C, suggesting the presence of organic material on

the surface of the nanoparticles (Figure 3-2). The WAXS pattern of particles made this way shows much reduced amorphous phase, and the peak broadening corresponds to nanocrystals of 3.8 nm in size (Figure 3-1a). This is in good agreement with the HRTEM micrographs (Figure 3-1b) that show particles of the same size exhibiting lattice fringes and the typical d-spacings and electron diffraction pattern of anatase.

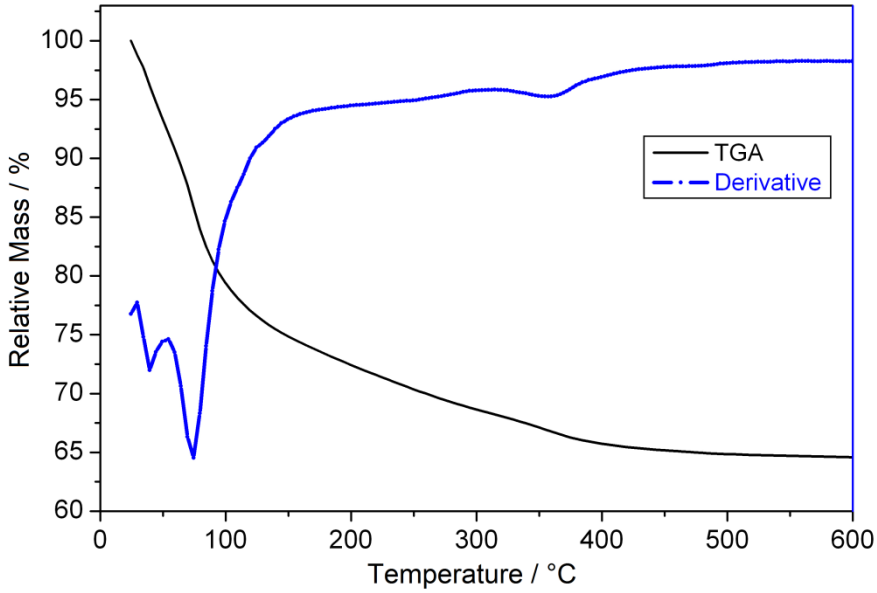

Figure 3-2: TGA of TiO_2 nanoparticles from a *tert*-BuOH synthesis (sample 2xMW80/50, prior to measurement powder was dried at 60 °C over night). The initial weight losses below 100 °C correspond to the evaporation of remaining solvent molecules.

The dispersibility of the particles in *tert*-butanol and ethanol was proven by DLS, showing monodisperse particles with hydrodynamic radii of 3 to 4 nm (Figure 3-3b).

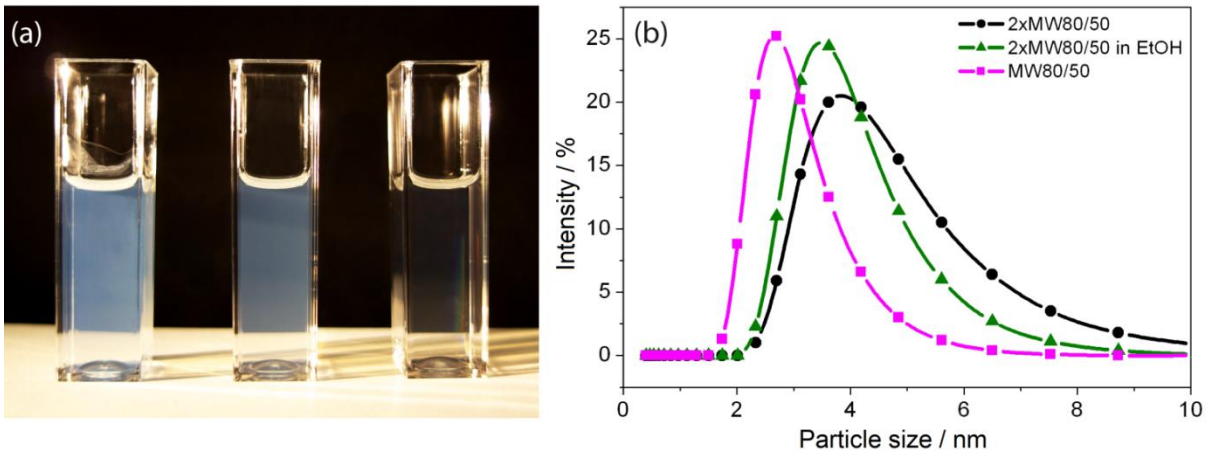

Figure 3-3: (a) Picture of 2xMW80/50 particle solutions: in *tert*-butanol/toluene (3:1 volume ratio, 3.3 wt% TiO_2, left), after flocculation with heptane, centrifugation and redispersion in ethanol (3.3 wt%, middle), and further diluted in ethanol (0.7 wt%, right). (b) DLS data of dispersions of particles prepared by microwave treatment in tBuOH (magenta: MW80/50, black: 2xMW80/50), and of 2xMW80/50 in EtOH (green).

The excellent dispersibility of the *tert*-butanol-based nanoparticles in both ethanol and *tert*-butanol can be exploited for the preparation of mesoporous films using the as-synthesized nanocrystals as metal oxide building blocks. The special advantages of *tert*-butanol are, first, that due to its low boiling point of only 83 °C, unlike benzyl alcohol, it is a suitably volatile solvent for evaporation-induced self-assembly (EISA) in thin films. Second, it is a good solvent for the polymers of the Pluronic family, which are commonly used as templates for mesostructure formation.[3,30] In this way, the reaction mixture containing the nanoparticles can be used directly, and the effort needed for the additional steps of particle separation and redispersion in other solvents suitable for the EISA process can be avoided. Using this direct coating technique, mesoporous titanium dioxide films were produced from solutions containing Pluronic P123 in *tert*-butanol that were treated with either one cycle of microwave irradiation, or two microwave cycles and thus containing fully crystalline titania particles. For comparison, films were also prepared without any heat treatment of the coating solution from a sol-gel precursor in *tert*-butanol (sample tBuOH-SG).

A TEM investigation of very thin films was performed to get insights into how the particles arrange around the pores forming the network. The contrast variations in the walls around the mesopores in Figure 3-4 b and c prove that for both microwave-heated samples, the pore walls consist of many small particles, whereas for the untreated solution, the walls surrounding the pores show uniform density which indicates the presence of homogeneous but amorphous titanium dioxide (Figure 3-4a). The tBuOH-SG sample also exhibits a worm-like pore structure, which only converts to an open porous phase at higher temperatures as observed by SEM after calcination at 300 °C (Figure 3-4d).

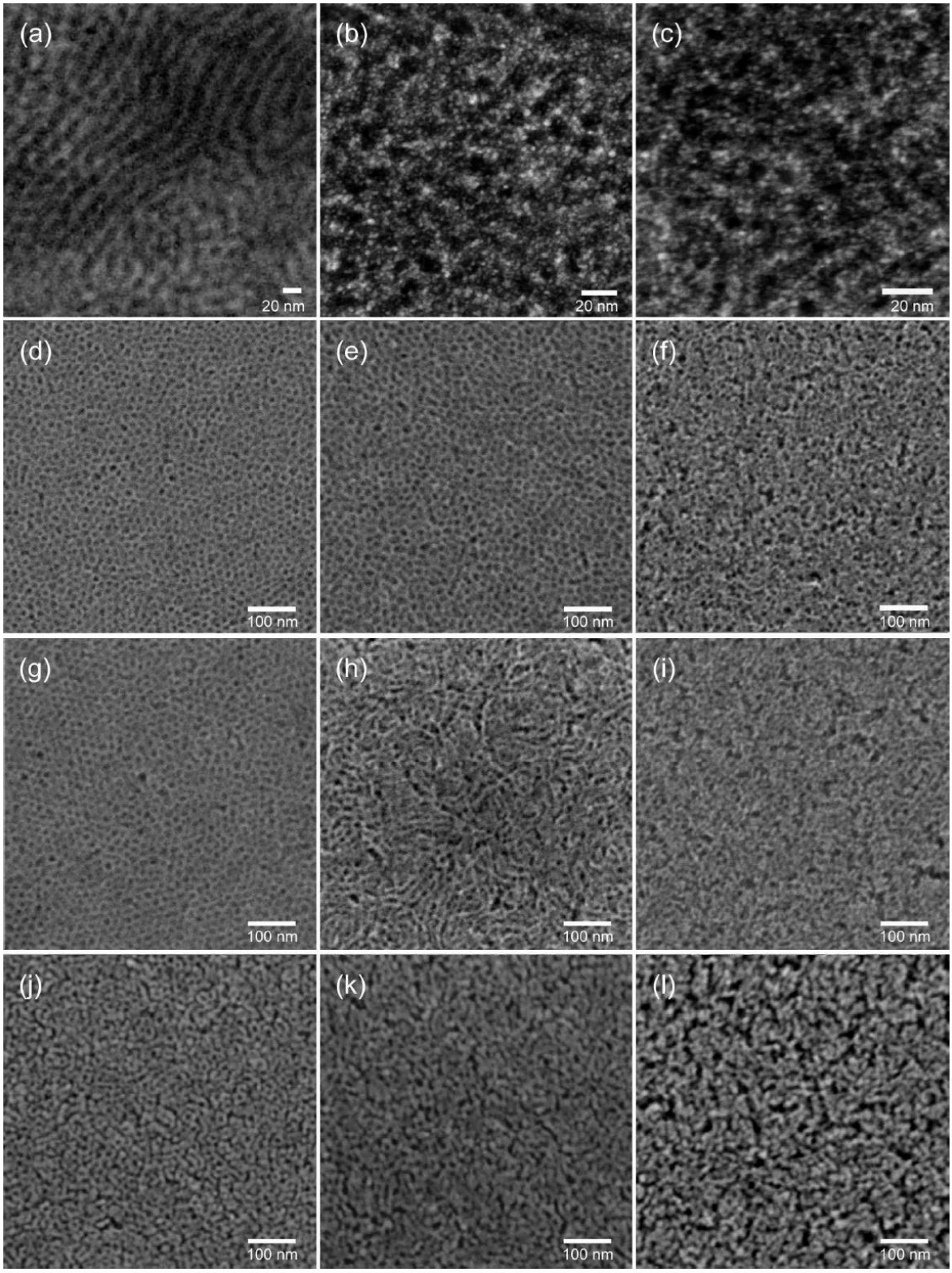

Figure 3-4: Mesoporous titanium dioxide films assembled from different building blocks: *tert*-butanol titania sol-gel (tBuOH-SG) (a, d), MW80/50 (b, e) and 2xMW80/50 (c, f). The first row (a-c) shows STEM-HAADF images of the films directly after coating, and the second row (d-f) SEM images (top view) of the same films after calcination at 300 °C, 450 °C (g-i), and 600 °C (j-l).

All of the layers prepared from different types of reaction mixtures and calcined at 300 °C show mesoporous structures with a regular, wormlike pore system. The reference sample prepared from non-treated sol-gel titania precursor (Figure 3-4d) exhibits the highest degree of periodicity, the biggest size of periodic domains and the smallest mesostructure spacing of 14 nm. The MW80/50 particle solution results in a structure with slightly smaller periodic domains and a larger pore spacing of about 20 nm (Figure 3-4e), while the use of a solution with the more crystalline 2xMW80/50 particles leads to a much less periodic structure on the film surface (Figure 3-4f). Still, pores of the same size that are open to the surface can be observed.

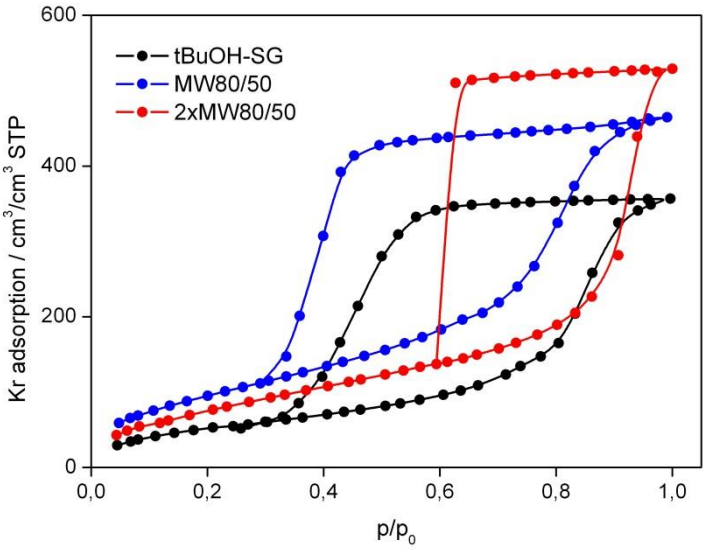

Figure 3-5: Isotherms of Krypton adsorption on the titania layers assembled from different building blocks: tBuOH-SG (black), MW80/50 (blue), 2xMW80/50 (red). The BET surface areas of these films are 116 $m^2 g^{-1}$ (tBuOH-SG), 294 $m^2 g^{-1}$ (MW80/50), and 297 $m^2 g^{-1}$ (2xMW80/50). The films were calcined at 300 °C.

The mesoporous nature of the pore system after the template combustion was also investigated using Kr adsorption (Figure 3-5 and Figure 3-6). The isotherms of all layers exhibit the typical shape of mesoporous materials with a large surface area, high pore volume

and the open and accessible character of porosity. The highest surface area of about 300 $m^2 g^{-1}$ is exhibited by the layers assembled from the MW80/50 and 2xMW80/50 particles. The use of more crystalline 2xMW80/50 particles leads to mesoporous layers with increased pore size and pore volume.

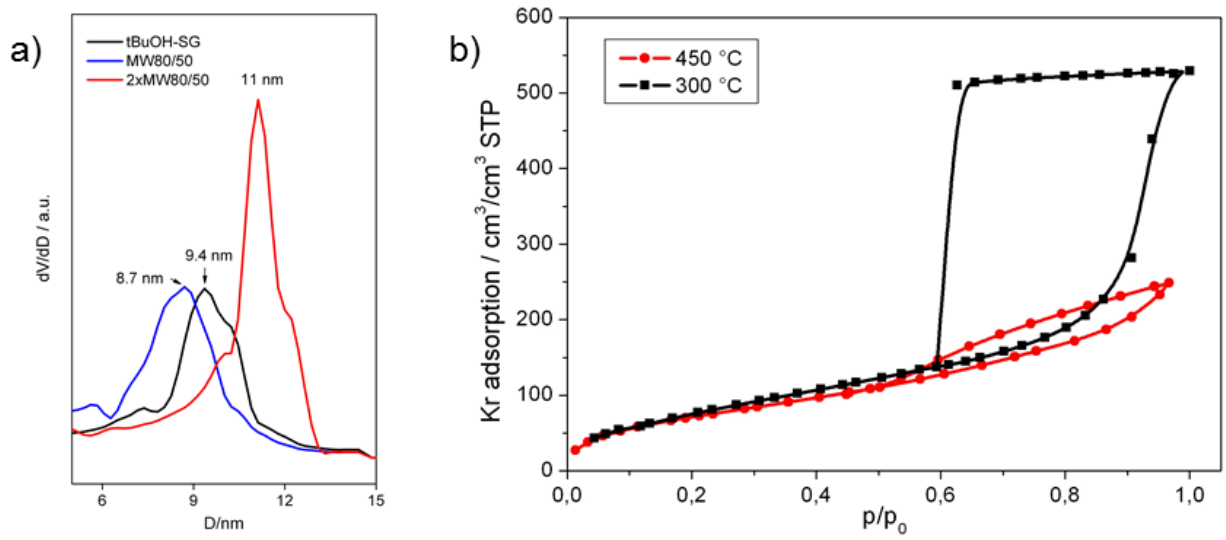

Figure 3-6: Textural properties from Kr sorption of samples after calcination at different temperatures. (a): Pore diameters for samples after calcination at 300 °C for samples tBuOH-SG, MW80/50, and 2xMW80/50 (sample names given in the figure). (b): Comparison of isotherms of sample 2xMW80/50 after calcination at 300 °C and 450 °C; these data show the preservation of the surface area (228 $m^2 g^{-1}$ for the sample 2xMW80/50 after calcination at 450 °C) and a change in the textural porosity upon heating to the higher temperature.

The periodicity of the mesostructure after treatment at high temperatures was confirmed by the existence of reflections in small angle X-ray scattering (SAXS, Figure 3-7) from samples calcined at different temperatures. At room temperature, the samples exhibited the typical reflection of Pluronic P123-templated titania corresponding to d-spacings of 10 to 12 nm. After calcination at 450 °C, this peak was shifted to higher angles and gradually disappeared at higher temperatures due to rather strong contraction of the mesostructure in the direction perpendicular to the substrate.[32,33] At the same time, other reflections became visible close to the lower detection limit of the SAXS at 0.6 to 0.7° 2θ and remained at the same position

upon further heating. This proves the existence of periodically repeating structural features after heating up to 600 °C, and indicates structural changes upon thermal treatment.

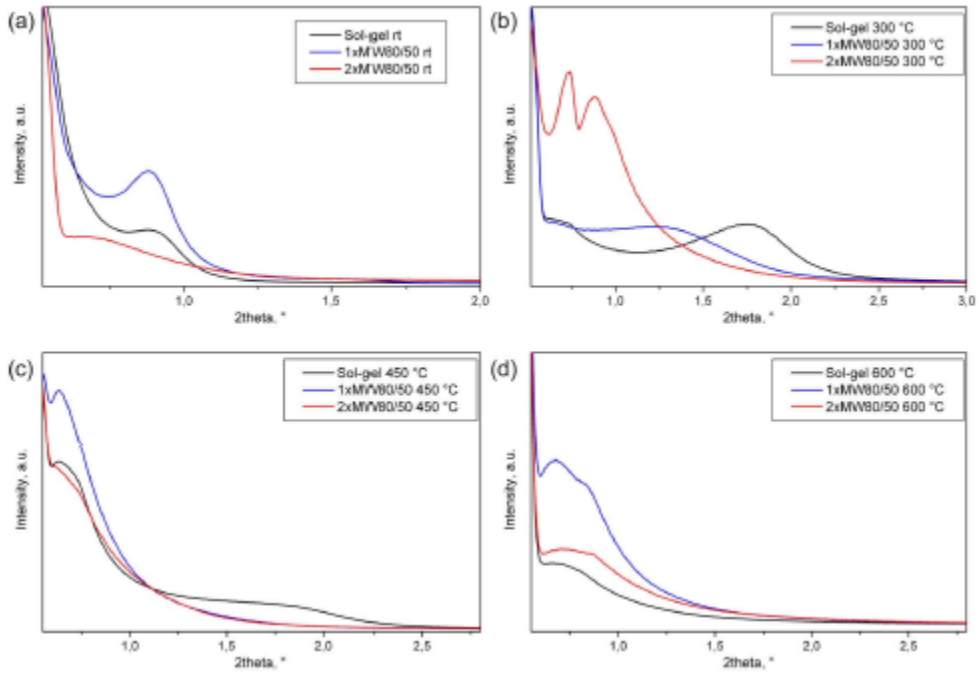

Figure 3-7: SAXS patterns of films before and after calcination at different temperatures (a): room temperature, (b): 300 °C, (c): 450 °C, (d): 600 °C. Black: *t*BuOH-SG, blue: MW80/50, red: 2xMW80/50.

The crystallization behavior upon heating was also monitored by evaluating the peak broadening in wide angle X-ray scattering (WAXS). In the sol-gel sample (tBuOH-SG), first traces of anatase nanoparticles of about 4.7 nm could be detected only after heating to 450 °C (Figure 3-8).[33,34] At even higher temperatures, the nanocrystals in the *tert*-butanol sol-gel sample grow rapidly and almost triple their size when heated to 600 °C. The microwave-treated nanoparticulate precursor, however, exhibits a more steady controllable crystallization, and the particles of originally 4 nm grow to only about 6 nm at 300 °C, to 8 nm at 500 °C, and finally to 11 to 13 nm at 600 °C. Summarizing, at 450 °C the nanoparticulate systems show both crystallinity and templated mesoporosity, while the sol-gel derived systems show only

low crystallinity with templated mesoporosity. On heating to 600 °C, both systems have lost the templated mesoporosity due to further crystal growth.

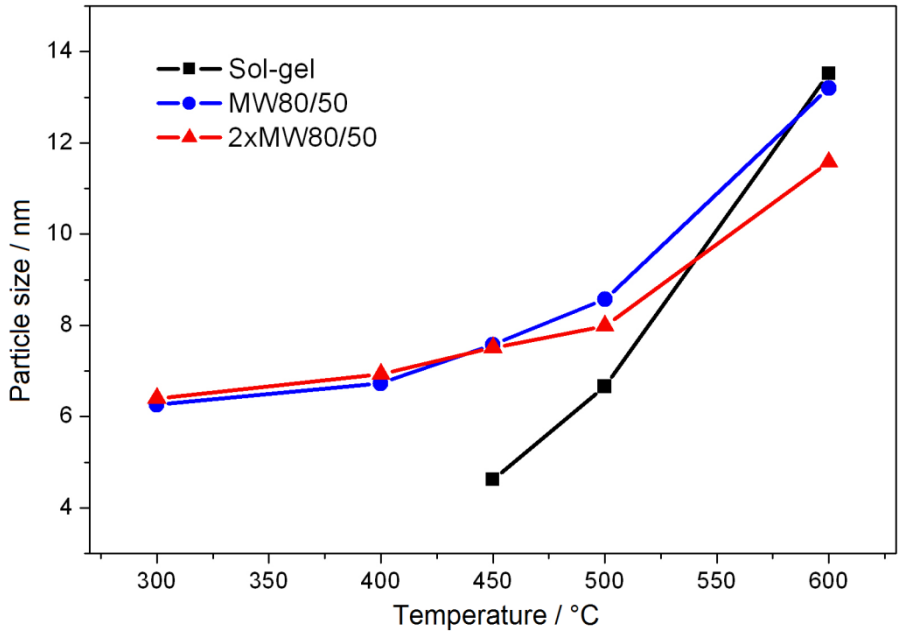

Figure 3-8: Development of crystal size from broadening of the (101) anatase reflection in wide-angle X-ray scattering upon heating. Black: tBuOH-SG, blue: MW80/50, red: 2xMW80/50 (film data below 300 °C were not recorded due to their low scattering intensity).

Electrochemical lithium insertion was performed for the determination of the relative amounts of crystalline and amorphous phase in the films assembled from different precursors, and to examine their applicability as electrode materials for Li-ion batteries.[35,36] The layers were calcined at 300 °C in order to combust the template and to open the pores, and at 450 °C to induce further crystallization of the networks. Cyclic voltammograms of the films prepared from the untreated solution exhibit only the broad insertion/extraction features of the amorphous phase even after calcination at 450 °C (Figure 3-9). The films prepared from the MW80/50 nanoparticles show the insertion behavior of an amorphous titania phase after calcination at 300 °C and, after calcination at 450 °C, clearly feature the characteristic quasireversible insertion/extraction anatase-based peaks around 1.85 V vs. Li. Finally, the

films assembled from 2xMW80/50 particles show the presence of anatase already after calcination at 300 °C. The amount of crystalline anatase phase doubles after heating the films at 450 °C, and only small traces of TiO_2(B) are observable.

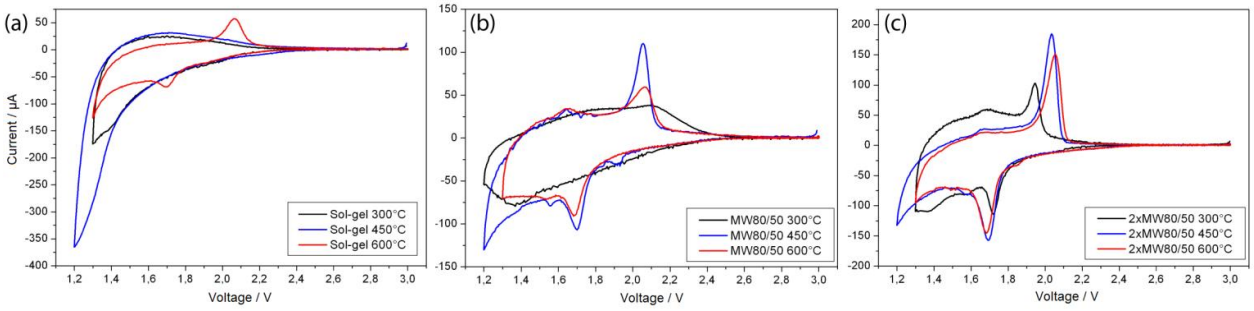

Figure 3-9: Cyclic voltammograms (scan rate 0.5 mV s^{-1}) from Li insertion of the mesoporous TiO_2 films after calcination at different temperatures: tBuOH-SG (a), MW80/50 (b), and 2xMW80/50 (c). Black: 300 °C; blue: 450 °C; red: 600 °C.

We conclude that the microwave irradiation of the titanium tetrachloride solution in *tert*-butanol leads to the formation of ultrasmall crystalline nanoparticulate seeds, which after film preparation can induce crystallization of the surrounding network at elevated temperatures by lowering the activation energy.

The films from solutions employing two cycles of the burst of nucleation profile (sample 2xMW80/50) show a capacity for lithium insertion at 1.7 V (end of the first plateau corresponding to insertion into anatase phase) of 143 mAh g^{-1} after calcination at 450 °C, which is a high level for this temperature considering the maximum theoretical Li insertion capacity of anatase of 167 mAh g^{-1}.[35] Furthermore, the material shows good cycling stability, which is comparable to other recently reported nanostructured titania systems (Figure 3-10).[36,37]

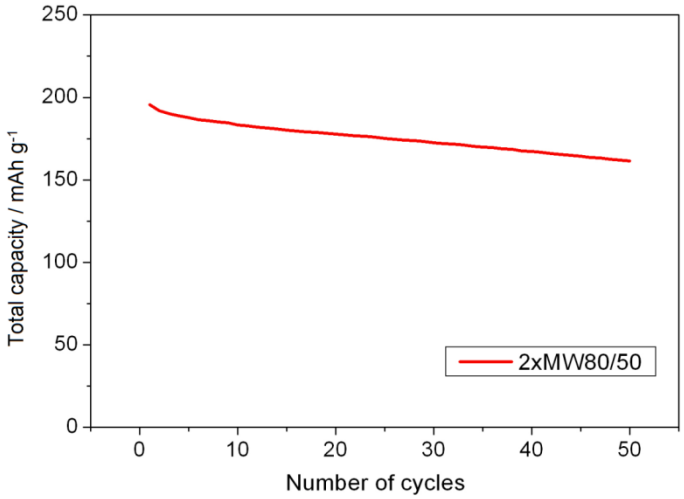

Figure 3-10: Total discharge capacity of the sample 2xMW80/50 after calcination at 450 °C upon multiple lithium insertion cycles in the potential range from 3.0 to 1.3 V vs. Li (scan rate 10 mV s^{-1}).

In addition to the high capacitance, the nanocrystalline and mesoporous nature of the films also leads to a significant increase in the insertion/extraction rate of Li ions (Figure 3-11 and Figure 3-12). During a charging time of only 150 s, the microwave treated samples reach over 80 % of their maximum insertion capacity, whereas reference films assembled from 20 nm anatase particles take approximately 10 times longer to reach that level. Similar accelerated kinetics were also described for films assembled from crystalline anatase nanoparticles[36,38] and were attributed to a significant contribution of pseudocapacitive processes in the total electrochemical Li insertion due to the large surface area of the nanoparticles. The small crystal size comparable to a maximum penetration depth for Li ions, the good connectivity of the crystals providing a continuous pathway for the ion/electron diffusion in the titania scaffold, and the excellent accessibility of the pore system for the Li ions in the electrolyte also contribute to fast insertion kinetics of the prepared films.[38] The high insertion capacity and the fast insertion kinetics in combination with a fast and facile preparation procedure make the described mesoporous films promising electrode materials for thin layer Li ion batteries and supercapacitors.

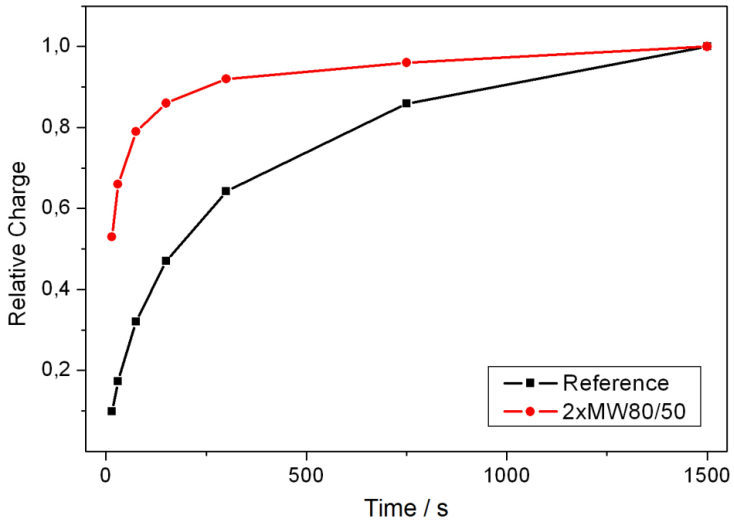

Figure 3-11: Comparison of charging rates for reaching maximum Li insertion into TiO_2 films assembled from different titania precursors. The relative charge was calculated as the ratio of measured charge over the maximum charge at the lowest scan rate. Black: Standard reference film made from 20 nm anatase particles, red: 2xMW80/50.

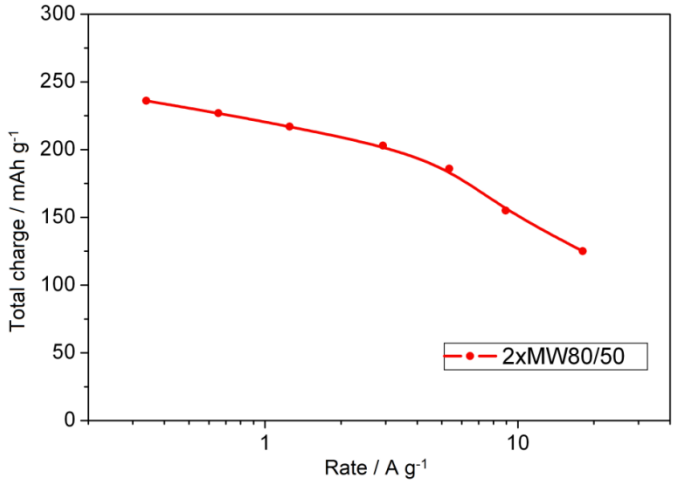

Figure 3-12: Rate dependence of the total charge in Li insertion experiments of the sample 2xMW80/50 after calcination at 450 °C in the potential range from 3.0 to 1.3 V vs. Li.

3.3 Conclusion

Non-aqueous sol-gel procedures using benzyl alcohol have been successfully employed for the preparation of crystalline metal oxide nanoparticles. However, for titania nanoparticles obtained with this method the dispersibility in organic solvents is limited and very small particle sizes are not accessible. Here we show that the combination of the new reaction medium *tert*-butanol and microwave irradiation using very short reaction times provides an effective synthesis protocol for the preparation of stable, dispersible, and ultrasmall anatase nanoparticles. Additionally, due to the low boiling point of *tert*-butanol and the high solubility of Pluronic template in this solvent, it was possible to develop a direct coating technique for the preparation of mesoporous films from nanocrystalline particles, omitting the time-consuming steps of centrifugation and redispersion of nanoparticles in a different solvent. The use of these ultrasmall and highly dispersible particles allowed the production of mesoporous layers from nanoparticulate precursors using commercial Pluronic templates in an efficient one-pot procedure, and the films exhibit uniform mesoporous networks with a very high surface area. The microwave-treated titanium dioxide films can be converted, contrary to untreated *tert*-butanol sol-gel derived films, into anatase upon calcination at 450 °C due to a seeding effect of the previously formed crystalline nanoparticles. Finally, electrochemical lithium insertion in these films shows the advantages of the microwave treatment regarding the retention of mesoporosity and crystallinity, leading to high insertion capacities and remarkably fast charging rates. The efficient preparation of the ultrasmall nanoparticles and their applicability in the direct preparation of mesoporous titanium dioxide make this *tert*-butanol system an attractive alternative to other non-aqueous sol-gel strategies.

3.4 Experimental

Titanium dioxide nanoparticles were synthesized using a non-aqueous sol-gel route in *tert*-butyl alcohol under microwave irradiation. All chemicals were purchased from Sigma-Aldrich and used as received. *tert*-Butyl alcohol was dried over 4 Å molecular sieve at 28 °C and filtered prior to use.

For all syntheses, titanium tetrachloride (1.5 mL, 13.7 mmol) was dissolved in toluene (10 mL) and added to *tert*-butyl alcohol (30 mL, 320 mmol) under continuous stirring. This solution was directly used as metal oxide precursor for the sample tBuOH-SG. For the sample T60, this solution was kept at 60 °C for 24 hours. Microwave heating was performed in microwave autoclaves with an initial heating power of 1200 W (Synthos 3000, Anton Paar). MW50 was heated to 50 °C within one minute and kept at this temperature for one hour. MW80/50 was heated to 80 °C within one minute, and then kept at 50 °C for 20 minutes resulting in a slightly yellow, transparent solution of nanoparticles.

To obtain the nanoparticles as a solid, this heating procedure had to be repeated one more time after a cooling period to room temperature (2xMW80/50). The solution was then colorless, and titanium dioxide could be flocculated by the addition of n-heptane (n-heptane:t-butanol/toluene 1:1 volume ratio) and separated by centrifugation at 50000 rcf for 15 minutes. The content of TiO_2 of the resulting solid was determined to be 73 wt% by thermogravimetric analysis (Netzsch STA 440 C TG/DSC).

One-pot coating solutions were made by mixing the reaction mixtures with Pluronic P123 (1.4 g, 0.24 mmol) after microwave heating. Coatings with the nanocrystalline solid as TiO_2 source were made by dissolving the amount of 0.2 g nanoparticles in ethanol (2 mL) and mixing this solution with Pluronic P123 (0.2 g, 0.04 mmol) in THF (2 mL). Films of

mesoporous TiO_2 were prepared on glass, FTO, or silicon by spin-coating with 1000 rpm at (23 ± 2) °C and a relative humidity of (45 ± 10) %.

Scanning electron microscopy (SEM) was performed on a JEOL JSM-6500F scanning electron microscope equipped with a field emission gun, at 4 kV. High Resolution Transmission Electron Microscopy (HRTEM) and Scanning Transmission Electron Microscopy in High Angle Annular Dark Field mode (STEM-HAADF) were performed using a FEI Titan 80-300 equipped with a field emission gun operated at 300 kV. The particulate samples were prepared by evaporating a drop of a diluted dispersion of particles with small amounts of Pluronic P123 in THF on a Plano holey carbon coated copper grid. HRTEM of films was carried out by scraping the thin-film samples off the substrate onto a holey carbon coated copper grid or by direct spin-coating of the dilute solution on a non-holey carbon coated copper grid.

The porosity of the films was determined by the analysis of adsorption isotherms of Kr at the boiling point of liquid nitrogen (approx. 77 K) using an ASAP 2010 apparatus (Micromeritics). Textural data were obtained by comparing the shape of the hysteresis loop and the limiting adsorption at saturation pressure of the Krypton sorption isotherms with reference materials (anatase powders) characterized by Nitrogen sorption. Comparison plots were constructed for each sample, and the differentiation of these plots provided the basis for the pore size distribution.

X-ray diffraction analysis was carried out in reflection mode using a Scintag XDS 2000 (Scintag Inc.) and a Bruker D8 Discover with Ni-filtered Cu K_α-radiation and a position-sensitive detector (Vantec). The thermal development of the XRD diffraction patterns was monitored either by ex situ heating or in in-situ measurements using a DHS-1100 heating chamber with a graphite dome (Anton Parr).

Dynamic light scattering (DLS) was performed using a Malvern Zetasizer-Nano equipped with a 4 mW He-Ne laser (633 nm) and an avalanche photodiode detector. The scattering data were weighted based on particle number. Prior to DLS measurements, the viscosity of the solvent mixture was measured using a Bohlin rotational rheometer (Malvern).

For lithium insertion, the mesoporous films were coated on conductive ITO glass and subjected to cyclic voltammetry using a Parstat 2273 potentiostat (Princeton Applied Research). The measurements were performed in a 1 M solution of $LiN(SO_2CF_3)_2$ in a 1:1 w/w mixture of ethylenecarbonate and 1,2-dimethoxyethane. The solution preparation and cell assembly were carried out in an Ar-filled glove box with a water and oxygen content of less than 20 ppm. The electrolyte solution was dried over 4 Å molecular sieve. Li wire was used as both the auxiliary and the reference electrode. The working electrode was masked with a silicone resin to precisely define the exposed surface area. Electrochemical measurements were taken in a potential range from 3.0 to 1.3 V. The scan rate in cyclic voltammetry measurements was chosen as 1 mVs^{-1}. The weight of the titania layers was calculated using the thickness of the films and their density, which can be obtained by multiplying the density of anatase (3.9 g cm^{-3}) with the porosity determined by Kr sorption experiments. The accuracy of this method was confirmed by weighing 10 films of the same samples on larger substrates with similar film thicknesses. The reference sample for Li insertion was made as described elsewhere.[39] In brief, anatase nanoparticles of 20 nm size were synthesized hydrothermally, and were mixed with cellulose binders. Porous films on FTO substrates were obtained using the doctor blade technique (Zehntner ZAA2300) and calcination at 450 °C for 30 min (1 °C min^{-1} ramp).

3.5 References

(1) Yang, P.; Zhao, D.; Margolese, D. I.; Chmelka, B. F.; Stucky, G. D. *Nature* **1998**, *396*, 152.

(2) Lee, J.; Orilall, C. M.; Warren, S. C.; Kamperman, M.; DiSalvo, F. J.; Wiesner, U. *Nature Materials* **2008**, *7*, 222.

(3) Boettcher, S. W.; Fan, J.; Tsung, C.-K.; Shi, Q.; Stucky, G. D. *Accounts of Chemical Research* **2007**, *40*, 784.

(4) Wan, Y.; Yang, H.; Zhao, D. *Accounts of Chemical Research* **2006**, *39*, 423.

(5) Sanchez, C.; Boissière, C.; Grosso, D.; Laberty, C.; Nicole, L. *Chemistry of Materials* **2008**, *20*, 682.

(6) O'Regan, B.; Gratzel, M. *Nature* **1991**, *353*, 737.

(7) Qifeng, Z.; Tammy , P. C.; Bryan, R.; Samson , A. J.; Guozhong, C. *Angewandte Chemie International Edition* **2008**, *47*, 2402.

(8) Rajan, J.; Velmurugan, T.; Seeram, R. *Journal of the American Ceramic Society* **2009**, *92*, 289.

(9) Pinna, N.; Neri, G.; Antonietti, M.; Niederberger, M. *Angewandte Chemie International Edition* **2004**, *43*, 4345.

(10) Li, H.; Balaya, P.; Maier, J. *Journal of The Electrochemical Society* **2004**, *151*, A1878.

(11) Poizot, P.; Laruelle, S.; Grugeon, S.; Dupont, L.; Tarascon, J. M. *Nature* **2000**, *407*, 496.

(12) Grosso, D.; Cagnol, F.; Soler-Illia, G. J. de A. A.; Crepaldi, E. L.; Amenitsch, H.; Brunet-Bruneau, A.; Bourgeois, A.; Sanchez, C. *Advanced Functional Materials* **2004**, *14*, 309.

(13) Yang, P.; Zhao, D.; Margolese, D. I.; Chmelka, B. F.; Stucky, G. D. *Chemistry of Materials* **1999**, *11*, 2813.

(14) Szeifert, J. M.; Fattakhova-Rohlfing, D.; Georgiadou, D.; Kalousek, V.; Rathousky, J.; Kuang, D.; Wenger, S.; Zakeeruddin, S. M.; Gratzel, M.; Bein, T. *Chemistry of Materials* **2009**, *21*, 1260.

(15) Fattakhova-Rohlfing, D.; Szeifert, J. M.; Yu, Q.; Kalousek, V.; Rathousky, J.; Bein, T. *Chemistry of Materials* **2009**, *21*, 2410.

(16) Niederberger, M.; Garnweitner, G. *Chem. Eur. J.* **2006**, *12*, 7282.

(17) Niederberger, M.; Bartl, M. H.; Stucky, G. D. *Chemistry of Materials* **2002**, *14*, 4364.

(18) Niederberger, M.; Bartl, M. H.; Stucky, G. D. *Journal of the American Chemical Society* **2002**, *124*, 13642.

(19) Niederberger, M.; Garnweitner, G.; Krumeich, F.; Nesper, R.; Colfen, H.; Antonietti, M. *Chemistry of Materials* **2004**, *16*, 1202.

(20) Kotsokechagia, T.; Cellesi, F.; Thomas, A.; Niederberger, M.; Tirelli, N. *Langmuir* **2008**, *24*, 6988.

(21) Pinna, N.; Niederberger, M. *Angewandte Chemie International Edition* **2008**, *47*, 5292.

(22) Feldmann, C.; Jungk, H.-O. *Angewandte Chemie International Edition* **2001**, *40*, 359.

(23) Feldmann, C. *Advanced Functional Materials* **2003**, *13*, 101.

(24) Wang, C.; Deng, Z.-X.; Zhang, G.; Fan, S.; Li, Y. *Powder Technology* **2002**, *125*, 39.

(25) Xianfeng, Y.; Hiromi, K.; Huifang, X.; Mingmei, W. *European Journal of Inorganic Chemistry* **2006**, *2006*, 2229.

(26) Li, G.; Li, L.; Boerio-Goates, J.; Woodfield, B. F. *Journal of the American Chemical Society* **2005**, *127*, 8659.

(27) Wang, C.; Deng, Z.-X.; Li, Y. *Inorganic Chemistry* **2001**, *40*, 5210.

(28) Garnweitner, G.; Antonietti, M.; Niederberger, M. *Chem. Commun.* **2005**, 397.

(29) Kominami, H.; Kato, J.; Takada, Y.; Doushi, Y.; Ohtani, B.; Nishimoto, S.; Inoue, M.; Inui, T.; Kera, Y. *Catalysis Letters* **1997**, *46*, 235.

(30) Bartl, M. H.; Boettcher, S. W.; Frindell, K. L.; Stucky, G. D. *Accounts of Chemical Research* **2005**, *38*, 263.

(31) Bilecka, I.; Djerdj, I.; Niederberger, M. *Chem. Commun.* **2008**, 886.

(32) Grosso, D.; Soler-Illia, G. J. d. A. A.; Crepaldi, E. L.; Cagnol, F.; Sinturel, C.; Bourgeois, A.; Brunet-Bruneau, A.; Amenitsch, H.; Albouy, P. A.; Sanchez, C. *Chemistry of Materials* **2003**, *15*, 4562.

(33) Crepaldi, E. L.; Soler-Illia, G. J. d. A. A.; Grosso, D.; Cagnol, F.; Ribot, F.; Sanchez, C. *Journal of the American Chemical Society* **2003**, *125*, 9770.

(34) Sung Yeun, C.; Marc, M.; Scott, S.; Naveen, C.; Geoffrey , A. O. *Small* **2005**, *1*, 226.

(35) Fattakhova-Rohlfing, D.; Wark, M.; Brezesinski, T.; Smarsly, B. M.; Rathouský, J. *Advanced Functional Materials* **2007**, *17*, 123.

(36) Brezesinski, T.; Wang, J.; Polleux, J.; Dunn, B.; Tolbert, S. H. *Journal of the American Chemical Society* **2009**, *131*, 1802.

(37) Ren, Y.; Hardwick, L. J.; Bruce, P. G. *Angew. Chem. Int. Ed*. **2010**, *49*, 2570.

(38) Wang, J.; Polleux, J.; Lim, J.; Dunn, B. *J. Phys. Chem. C* **2007**, *111*, 14925.

(39) Ito, S.; Murakami, T. N.; Comte, P.; Liska, P.; Grätzel, C.; Nazeeruddin, M. K.; Grätzel, M. *Thin Solid Films* **2008**, *516*, 4613.

4 Titania electrodes assembled from ultrasmall titania nanoparticles for dye-sensitized solar cells

4.1 Introduction

Since the discovery of dye sensitized solar cells (DSCs) in 1991 by Michael Grätzel and his co-workers much research has been conducted in this field.[1,2] Significant progress was achieved in enhancing the solar cell conversion efficiency by optimizing all the individual components of the DSCs and the better synchronization of their functions in the complete device. New sensitizer dyes aim at optimization of the light absorption and injection efficiency into the semiconducting electrodes,[3] and the iodide/triiodide redox electrolyte was optimized with additives regarding the adjustment of the redox potential to a value compatible with the utilized sensitizer dye and to optimize the dye/electrolyte interaction.[4,5] The porous semiconducting titania absorber layer was also the target of several detailed studies.[6,7] The standard electrodes are usually manufactured in a doctor-blading process from nanoparticles which are prepared in a hydrothermal hydrolysis reaction.[8] After a heat treatment at high temperatures the porogens are removed and the titania nanocrystals are sintered together to produce transparent, highly crystalline porous films with a surface area of approximately 70 $m^2 g^{-1}$. In order to improve the performance of these films several studies were addressing the issue of the low surface area of porous titania layers with the development of templated sol-gel procedures.[9-11] In these experiments, a surfactant (usually an amphiphilic polymer) is added to the inorganic precursor solution to enable the formation of periodically structured materials in a so-called evaporation induced self-assembly (EISA) process.[12] The periodic structures formed by self-assembled surfactant micelles act as a template for the mesoporous titania, with the voids being filled by the inorganic precursor. The template is then removed

by thermal decomposition yielding porous titania films with a very high surface area and an accessible pore system. Mesoporous titania morphologies with a uniform regular porosity are shown to be among the most active anodes in DSCs, demonstrating one of the highest light conversion efficiencies per thickness ratio.[13,14] A large accessible surface area providing a high dye loading capability in combination with the relatively large uniform pore size is highly beneficial for the filling with electrolyte and the non-restricted diffusion thereof.

This synthesis pathway however is limited by certain factors. The deposition is only possible from solutions or dispersions of the inorganic precursors with a rather low concentration of the deposition solutions, thus leading to only very thin solid films. Removal of the template and the crystallization of the inorganic material are often accompanied by large changes in density, leading to severe cracking or delamination of the films deposited as thicker coatings. The thick films needed for sufficient surface area and thus dye density and light absorption usually cannot be deposited in one step; their fabrication requires a multiple deposition of thin coatings accompanied by an intermediate calcination of each deposited layer. Thus, Zukalova et al. have produced thin transparent organized mesoporous films by templating an amorphous titania sol-gel with a Pluronic di-block-copolymer.[13] These films show a roughness factor which is 5 times higher than that of randomly oriented 12 nm sized TiO_2 particles. The resulting higher dye loading produces an increased short-circuit photocurrent of the DSCs and a 50 % better ratio of photo-conversion efficiency to thickness compared to the nanoparticulate samples. Although the films had a thickness below 1 µm they were prepared in 3 coating steps, each involving a time consuming ageing step for 30 h and subsequent calcination. Additionally, sorption data indicate a deterioration of the porous system for multi-layered films as the pore diameter shrinks for thicker films. This shrinkage occurs upon densification of the initially amorphous precursor.

One approach to overcome this challenge is the so-called 'brick and mortar' strategy.[14] It allows the formation of mesoporous crystalline materials by the combination of preformed titania nanocrystals with surfactant-templated sol-gel titania. The similar chemical composition of the nanocrystalline and the sol-gel titania leads to an induced crystallization of the amorphous precursor by the crystalline seeds and allows for crystallization at mild conditions. Additionally, less shrinkage is observed during the crystallization and densification of the material leading to films of typically about 700 nm thickness. Although the 'brick and mortar' films can be made much thicker than the sol-gel ones, the thickness of the films obtained in one coating and with it the effective surface area are still not sufficient for a high performance of these electrodes in DSCs. Thicker films can be made by stacking several layers of porous titania on top of each other by a sequential coating and calcination process.[15] In contrast to the sol-gel films whose porous morphology deteriorates after a few subsequent coatings, the porosity and surface area of the 'brick and mortar' films scale up linearly with the number of coatings. However, a desirable thickness of about 10 µm still requires up to 15 time-consuming subsequent coatings followed by intermediate calcination steps.

Therefore, in this study we have focused on a possibility to fabricate thick mesoporous titania coatings in a much simpler way, which could make this promising morphology more suitable for large-scale applications. Mesoporous surfactant-templated films were prepared in an EISA process by using the as-prepared reaction solution of ultra-small titania nanoparticles which were synthesized in a non-aqueous solvothermal microwave-assisted reaction in *tert*-butanol and mixed with Pluronic P123 as a templating agent. The films exhibit a very high surface area of around 300 $m^2 g^{-1}$,[16] which can be of great value for the adsorption of dye molecules on the titania surface in dye sensitized solar cells.

We demonstrate the preparation of mesoporous titania films that show a high efficiency to thickness ratio when applied as electrodes in DSCs. One of the key points in order to increase the film thickness and with it the efficiency, is the addition of ethyl cellulose to a modified coating solution containing Pluronic F127. This modified coating solution exhibits a higher titania content and an increased viscosity leading to an effective thickness of a single layer obtained after calcination of approximately 2 µm. The addition of ethyl cellulose does not only affect the thickness of the films but also the structure of the pore system, which can be described as a bimodal system with an interpenetrating macropore system. This pore system can be found throughout the whole film and enables a fast mass transport in the redox electrolyte. The smaller mesopores resulting from Pluronic F127 exhibit a high surface area and therefore increase the adsorption of the sensitizing dye leading to increased photocurrents. The preparation of multi-layer films by a sequential spin-coating and calcination procedure enables the production of films with an overall thickness of up to 10 µm in only 5 steps. In this way, it was possible to increase the photo-conversion efficiency of the manufactured devices by a factor of 2.5 compared to a single layer and to obtain comparable efficiencies as for the 15 layer 10 µm brick and mortar films.

4.2 Results and Discussion

Ultra-small titania nanoparticles were synthesized as described in a previous study.[16] The 3 nm sized crystalline titania nanoparticles are perfectly dispersed in the reaction solution and non-agglomerated. In this way the as-prepared solutions can be directly utilized for the preparation of mesostructured films via spin-coating on conductive transparent oxide coated glass substrates after adding a structure directing agent such as the triblock copolymer Pluronic P123. The titania content of the resulting solution is about 27 mg TiO_2/mL solvent

(3.5 wt-%) if a 100 % reaction yield is assumed. The films are calcined at 450 °C to remove the template and to fully crystallize the scaffold. This procedure is very simple, but leads to individual layers of only around 300 nm thickness after calcination. This is due to a limited concentration of the nanoparticles in the as-prepared synthesis solution, as the ultra-small titania nanoparticles are obtained only at certain precursor concentrations. To increase the concentration of nanoparticles, the dispersion was concentrated by evaporation of around 40 % of the initial solvent volume, thus leading to a titania content of the resulting solution of about 45 mg TiO_2/mL solvent (5.8 wt-%). Films prepared with this concentrated solution exhibit a film thickness of around 700 nm after calcination, as determined by profilometry. The films are transparent and the porous system is highly accessible from the surface as depicted in the SEM image in Figure 4-1, left. The structure of the mesoporous films can be described as a not periodically ordered worm-like structure with an open porous system. The application of such a film as a photoanode in a DSC with N719 as sensitizer leads to a very high photo-conversion efficiency of 3.2 % for such a thin film. Additionally, the open circuit voltage of 850 mV is relatively high compared to other films prepared from slightly bigger nanoparticles synthesized in benzyl alcohol.[14] This could be due to different surface composition of the nanoparticles, as in the latter case the products of the non-complete combustion of aromatic benzyl alcohol groups could remain on the surface even after calcination. Additionally, the very small size of the ultra-small nanoparticles could lead to a better sintering of the particles upon calcination in the mesostructure and therefore to enhanced electronic properties of the resulting films.

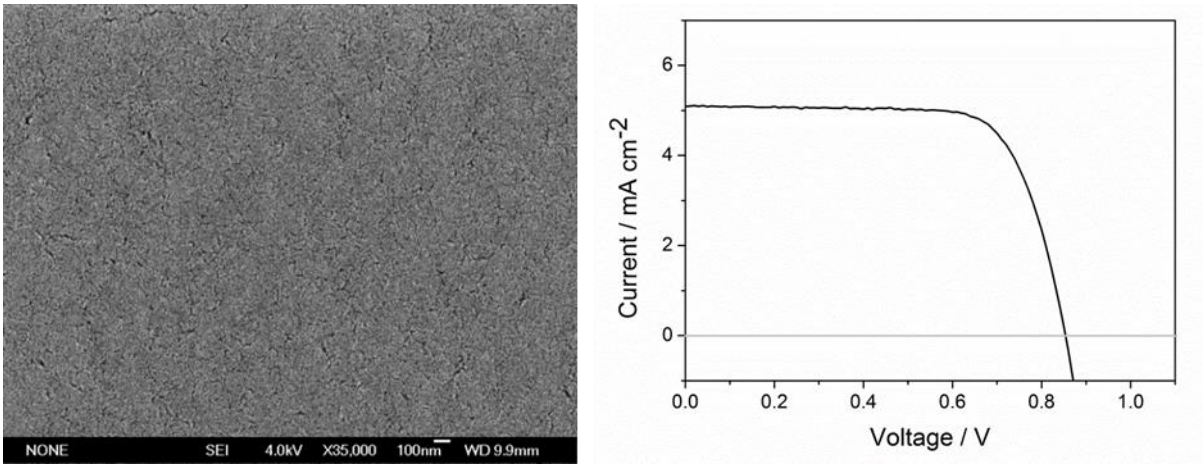

Figure 4-1: Left: Top-view SEM image of a 700 nm thin mesoporous titania film prepared from the concentrated solution of ultra-small titania nanoparticles and calcined at 450 °C. Right: Photocurrent-voltage curve of a DSC constructed with the film shown in the SEM image, N719 sensitizer and volatile I^-/I_3^- electrolyte. The photovoltaic performance was measured at air mass 1.5 (100 mW cm^{-2}) full sunlight illumination. The active cell area was 0.196 cm^2.

Powder XRD patterns of scratched off films that had been calcined at 425 °C show pure anatase with a crystallite size calculated from the peak broadening of the 101 reflection to be 10 nm (Figure 4-2). Compared to the initial size of the crystallites of 3 nm this accounts for a growth of 340 % indicating a good interconnection of the mesoporous scaffold. The obtained high short circuit current of 5.09 mA cm^{-2} compared to the film thickness of only 700 nm can be attributed to the high surface area of the film which is proportional to the dye loading and therefore the generated current (Figure 4-1, right). The fill factor of 73.8 % is in a usual range for this type of DSCs.

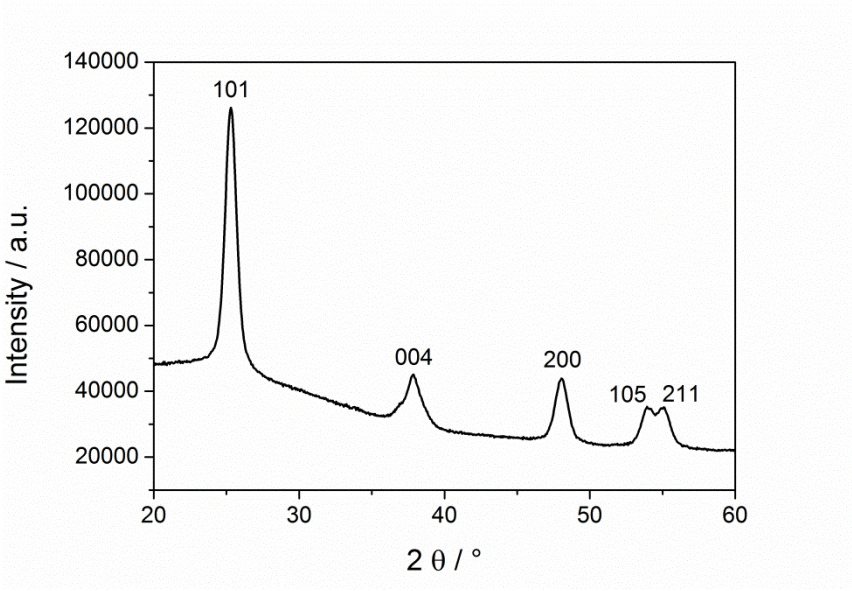

Figure 4-2: XRD pattern of anatase material obtained from films calcined at 425 °C. The average crystallite size was determined to be 10 nm calculated with the Scherrer equation from the broadening of the 101 reflection.

In order to achieve higher efficiencies, a procedure to obtain films with increased thickness was developed, in which the coating solution had to be prepared in a different way compared to the procedure described above for the 700 nm film. First of all, the ultra-small titania nanoparticles were separated from the reaction solution by flocculation with the apolar solvent heptane (2:1 heptane : reaction solution) and subsequent centrifugation. The obtained pellet was quickly redispersed in absolute ethanol and the surfactant Pluronic F127 was added and dissolved under stirring and heating to 60 °C. Afterwards a 10 weight-% solution of ethyl cellulose was added and the resulting solution was used for spin-coating to produce films of up to 2 µm thickness after calcination at 425 °C. This increase in film thickness per layer is attributed to the higher viscosity of the coating solution after the addition of ethyl cellulose and the increased titania content of the dispersion (107 mg TiO_2/mL solvent, 13.6 wt-%) by over a factor of 2 compared to the concentrated solution without ethyl cellulose. This leads to a higher amount of titania remaining on the substrate during the spin-coating process. The addition of ethyl cellulose also causes a morphological change compared to films prepared

without it. Additionally to the small pores formed from the template Pluronic F127, bigger pores of over 60 nm caused by ethyl cellulose can be observed (Figure 4-3).

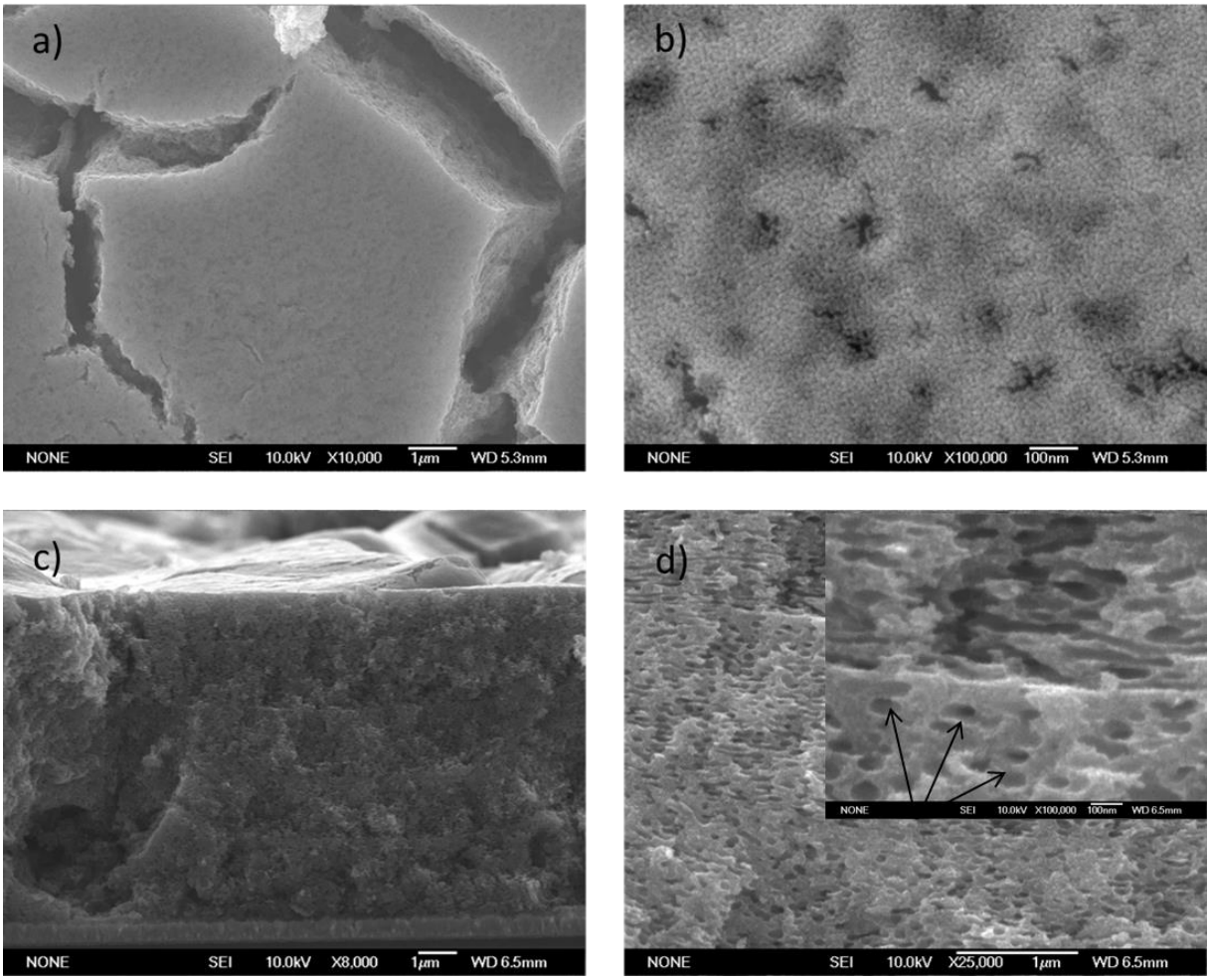

Figure 4-3: Top-view SEM images of a 8 µm 4-layer titania film prepared with the addition of ethyl cellulose and calcined at 425 °C (a, b). Cross-sectional images of the films (c,d). Some ethyl cellulose-derived pores are marked with arrows in the inset in d.

The cross-sectional SEM image shows a homogeneous distribution of the smaller and bigger pores throughout the whole film, resulting in a bimodal pore system with pores of around 8 nm resulting from the template Pluronic F127 and pores of around 60 – 100 nm from the ethyl cellulose (Figure 4-3, c,d). This bimodal pore system with its bigger pores from the ethyl cellulose can be advantageous for electrolyte diffusion resulting in good mobilities and possibly less recombination. Additionally, the cracks perpendicular to the FTO substrate

could be advantageous channels for a fast mass transport in the electrolyte, especially combined with the large pore system of the ethyl cellulose that connects the smaller pores resulting from the F127 template. In this way, a high surface area of 130 m^2 g^{-1} is successfully combined with an accessible pore system (Figure 4-4). For the preparation of thicker films, the complete procedure of film formation was repeated with fresh coating solutions until the desired film thickness was obtained. The evolution of film thickness follows a linear trend as depicted in Figure 4-5 (left), flattening off for higher film thicknesses. Films prepared in this way are not completely crack-free (Figure 4-3a) and therefore appear light-scattering and white, but look homogeneous, are stable and do not peel off the substrates (Figure 4-5, right).

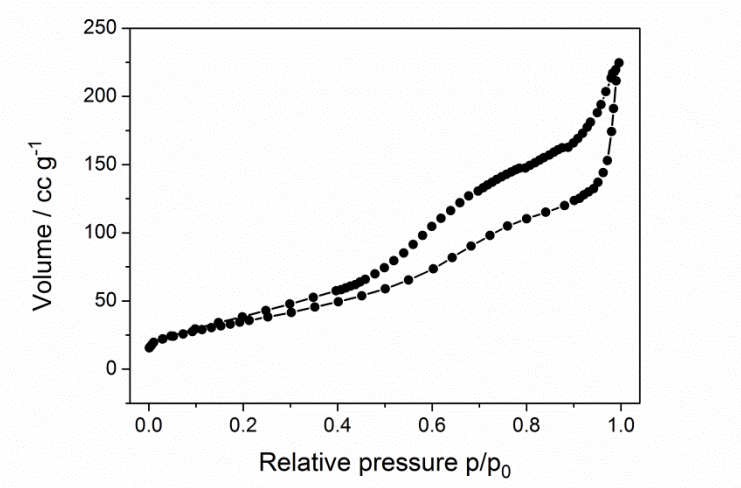

Figure 4-4: Nitrogen sorption isotherm of a scratched-off powder from 3-layer films prepared with ethyl cellulose. The BET surface area is 130 m^2 g^{-1}.

The photograph of the film which was reduced to a suitable size (by scratching) for the manufacturing of DSCs and immersed in a solution of N719 dye for 3 days shows the intense color indicating a desirable high light absorption caused by the high surface area and therefore the high dye adsorption capability of these films (Figure 4-5, right).

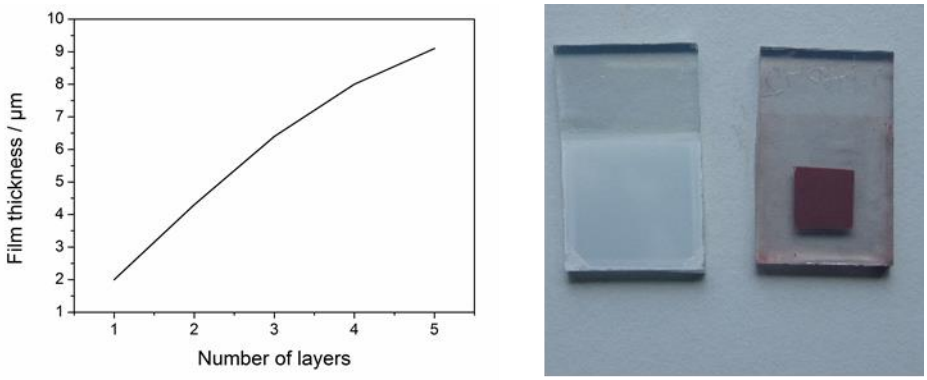

Figure 4-5: Left: Evolution of film thickness of multi-layered films prepared with ethyl cellulose and intermediate calcinations steps at 425 °C. Right: Image of films prepared with ethyl cellulose after calcination at 425 °C (left) and after immersion of the scratched film in the dye-solution for 3 days (right).

Since the current injected into the titania scaffold is approximately proportional to the dye loading, it can explain the trend of the increasing short circuit current for increasing film thickness (Figure 4-6, right). The decline in photocurrent for very thick films can be ascribed to a higher recombination in thicker films since the pathways for the electrons are longer. In the same way, the power conversion efficiency rises up to 7.7 % for a thickness of 8.0 µm and drops off for even thicker films (Figure 4-6). The maximum can be explained by an optimum in both light absorption (resulting from a combination of high surface area and sufficient film thickness) and efficient charge extraction. Additionally, all samples show a high open circuit potential for this system of up to 874 mV. These observations are attributed to the high accessibility of the thin-walled bimodal pore system and the crystallinity of the films. The characteristics of the solar cells are summarized in Table 4-1.

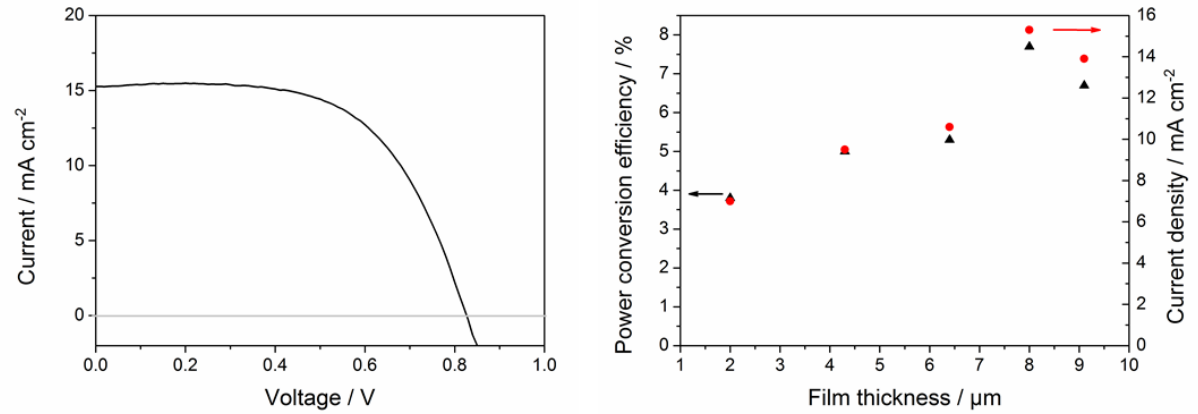

Figure 4-6: Left: Photocurrent-voltage curve of the best-performing DSC constructed with an 8 µm thick film prepared with ethyl cellulose and multi-layering, N719 sensitizer and volatile I^-/I_3^- electrolyte. The photovoltaic performance was measured at air mass 1.5 (100 mW cm^{-2}) full sunlight illumination. The active cell area was 0.196 cm^2. Right: Power conversion efficiency (black triangles) and current density at short circuit conditions (red circles) depending on the thickness of the films prepared with ethyl cellulose.

Table 4-1: Photovoltaic performance of DSCs made using Pluronic F127 and ethyl cellulose templated mesoporous TiO_2 electrodes with varying thickness, and employing N719 dye with a volatile electrolyte under 1 sun illumination:

Number of layers	Thickness [µm]	V_{OC} [mV]	I_{SC} [mA cm^{-2}]	FF [%]	Efficiency [%]
1	2.0	874	7.0	61.0	3.8
2	3.9	812	9.1	61.2	4.5
2	4.3	838	9.5	62.4	5.0
3	5.4	795	9.7	62.0	4.8
3	6.4	795	10.6	62.3	5.3
4	8.0	827	15.3	60.7	7.7
4	8.3	862	14.3	61.2	7.5
5	9.0	852	12.2	59.4	6.2
5	9.1	852	13.9	56.5	6.7

4.3 Conclusion

In conclusion, this study shows an efficient method for the preparation of mesoporous titania films from preformed ultra-small titania nanoparticles as electrodes for dye-sensitized solar cells. The addition of ethyl cellulose to the spin-coating solution leads to the formation of films with around 2 µm per single layer exhibiting a bimodal pore system induced by the structure-directing agent Pluronic F127 and ethyl cellulose. A multi-layering technique allows for preparing mesoporous films of up to 10 µm in a short time and few steps. Concerning the application of the films in DSCs, it was found that the efficiency rises for increasing film thickness and reaches a maximum of 7.7 % at around 8 µm. These highly performing mesoporous films would also be attractive candidates for application as photoanodes in other types of solar cells with alternative hole conductors.

4.4 Experimental

Ultra-small titania nanoparticles were synthesized using a *tert*-butanol microwave procedure. Titanium tetrachloride (0.7 mL, 6.9 mmol) was added to dry toluene (5 mL) under stirring in a 10 mL glass vial. The resulting orange solution was added under stirring to dry *tert*-butanol (15 mL) in a 20 mL glass vial, which formed a yellow solution. The *tert*-butanol was dried over 4 Å molecular sieve at 28 °C and filtered through a syringe filter prior to use. The mixture was then heated with microwave radiation to 80 °C in 1 minute and then held at 50 °C for 20 min (Synthos 3000, Anton Paar). After cooling to room temperature the same microwave procedure was repeated 20 hours later to complete the NP synthesis, giving a very faint yellow, transparent solution.

For the preparation of the 700 nm film, 4 mL of the as-prepared nanoparticle dispersion as described earlier was added to 0.132 g Pluronic P123 and this solution was kept at room temperature for 24 h to remove approximately 40 % of the solvent *tert*-butanol. This concentrated solution was then used for spin-coating at 2000 rpm for 30 s by applying 120 µL of this solution onto the scotch-tape masked FTO coated glass substrates (TEC-7 from Pilkington) with a sintered coating (~70 nm) of a TEOT blocking layer, leaving 1.5 x 1.5 cm^2 accessible surface.

For the preparation of thicker films the nanoparticles were separated from the reaction solution by flocculation with the apolar solvent *n*-heptane (2:1 heptane : reaction solution) and subsequent centrifugation at 20500 rpm (49000 rcf) for 20 minutes (Sorvall Evolution RC, Thermo Scientific). The obtained pellet was quickly redispersed in absolute ethanol in the ratio of 0.3 g nanoparticles per 1 mL ethanol. To this dispersion 0.07 g per mL of the surfactant Pluronic F127 was added and dissolved under stirring and heating to 60 °C for several minutes in a drying oven. Afterwards 0.4 mL/mL of a 10 weight-% solution of ethyl cellulose was added and 120 µL of the solution was used for spin-coating at 800 rpm for 30 s as described above. The resulting films were calcined at 425 °C (with a ramp of 0.6 °C min^{-1}) for 30 minutes in a laboratory oven.

The sintered films were scratched off of the edges of the glass so that only a square in the middle with sides slightly larger than 0.5 cm in length remained. This was done to reduce both lateral electron percolation and the amount of dye adsorbed on film not used in the DSC. The films were then cleaned of water and organics by being heated on a hot plate for 30 min at 120 °C under two UV lamps (254 nm and 365 nm). The films were completely immersed in ruthenium-based polypyridyl dye N719 (0.592 mg) in a 1:1 ratio of acetonitrile : *tert*-butanol solution (1 mL) for 3 days.

To create the blocking layer solution, concentrated HCl (0.37 mL, 4.4 mmol) and TEOT (0.55 mL, 2.6 mmol) were added in a 10 mL glass vial. THF (7 mL) was then added, and the solution was stirred for at least 5 min. FTO-coated glass was cleaned for 15 min by ultrasonication in a 1:1 solution of ethanol : acetone. The glass was wiped with a Kimwipe and then plasma cleaned in oxygen plasma for 5 min at 50 % power to remove the remaining organic residues (Femto UHP, Diener Electronic). The blocking layer solution was spin coated onto the FTO glass at 4000 rpm for 30 s (WS-400B-6NPP/LITE, Laurell). The coated glass was sintered with a ramp of 11 hours to 450 °C, holding this temperature for 30 min.

Counter Electrode: The counter electrodes were prepared by first drilling a 1 mm hole into FTO coated glass. The glass was then cleaned by ultrasonication for 15 min in a 1:1 solution of water : ethanol and a drop of soap. After rinsing in ethanol, the drilled glass was ultrasonicated twice more for 15 minutes in ethanol. The counter electrodes were wiped with a Kimwipe and then plasma cleaned for 5 min at 50 % power to remove the remaining organic residues (Femto UHP, Diener Electronic). The Pt catalyst was applied by spreading a drop of a solution of H_2PtCl_6 (2 mg, 4.8 µmol) in ethanol (1 mL). The Pt-coated glass was slowly heated on a hot plate to 400 ºC in increments of 50 ºC every 10 min.

Electrolyte: The electrolyte solution was prepared by mixing together 1-butyl-3-methylimidazolium iodide (0.536 mL, 60 mmol), iodine (0.038 g, 1.5 mmol), guanidinium thiocyanate (0.059 g, 10 mmol), 4-*tert*-butylpyridine (0.37 mL, 50 mmol), acetonitrile (4.25 mL), and valeronitrile (0.75 mL) in a 20 mL glass vial.

For the assembly of DSCs the films were removed from the dye solution and rinsed with acetonitrile. A 60 µm surlyn plastic insert with a 0.196 cm^2 hole was sandwiched between the mesoporous film electrode and the platinum-covered counter electrode. The DSC was placed

on a hot plate at 150 ºC for 30 s to melt the plastic enough to adhere the two electrodes together. The electrolyte was then injected into the DSC by vacuum backfilling through a pre-drilled hole in the counter electrode. After the hole in the plastic insert was completely filled with the electrolyte, the DSC was sealed with tape. The outside of the DSC was cleaned with ethanol to complete the assembly.

The photovoltaic characterization of solar cells was performed on an AM 1.5 solar simulator (Solar light Co.). The measurements were conducted under one sun illumination, and the light intensity was monitored by a pyranometer (PMA2100, Solar light Co.). Current density-voltage measurements were performed with a Zahner IM6ex impedance measurement unit.

4.5 References

(1) O'Regan, B.; Gratzel, M. *Nature* **1991**, *353*, 737.

(2) Grätzel, M. *Accounts of Chemical Research* **2009**, *42*, 1788.

(3) Grätzel, M. *Inorganic Chemistry* **2005**, *44*, 6841.

(4) Kuang, D.; Klein, C.; Ito, S.; Moser, J. E.; Humphry-Baker, R.; Evans, N.; Duriaux, F.; Grätzel, C.; Zakeeruddin, S. M.; Grätzel, M. *Advanced Materials* **2007**, *19*, 1133.

(5) Boschloo, G.; Hagfeldt, A. *Accounts of Chemical Research* **2009**, *42*, 1819.

(6) Chen, X.; Mao, S. S. *Chemical Reviews* **2007**, *107*, 2891.

(7) Hagfeldt, A.; Boschloo, G.; Sun, L.; Kloo, L.; Pettersson, H. *Chemical Reviews* **2010**, *110*, 6595.

(8) Wang, P.; Zakeeruddin, S. M.; Comte, P.; Charvet, R.; Humphry-Baker, R.; Grätzel, M. *The Journal of Physical Chemistry B* **2003**, *107*, 14336.

(9) Choi, S. Y.; Lee, B.; Carew, D. B.; Mamak, M.; Peiris, F. C.; Speakman, S.; Chopra, N.; Ozin, G. A. *Advanced Functional Materials* **2006**, *16*, 1731.

(10) Crepaldi, E. L.; Soler-Illia, G. J. d. A. A.; Grosso, D.; Cagnol, F.; Ribot, F.; Sanchez, C. *Journal of the American Chemical Society* **2003**, *125*, 9770.

(11) Sanchez, C.; Boissière, C.; Grosso, D.; Laberty, C.; Nicole, L. *Chemistry of Materials* **2008**, *20*, 682.

(12) Brinker, C. J.; Lu, Y.; Sellinger, A.; Fan, H. *Advanced Materials* **1999**, *11*, 579.

(13) Zukalová, M.; Zukal, A.; Kavan, L.; Nazeeruddin, M. K.; Liska, P.; Grätzel, M. *Nano Letters* **2005**, *5*, 1789.

(14) Szeifert, J. M.; Fattakhova-Rohlfing, D.; Georgiadou, D.; Kalousek, V.; Rathouský, J.; Kuang, D.; Wenger, S.; Zakeeruddin, S. M.; Grätzel, M.; Bein, T. *Chemistry of Materials* **2009**, *21*, 1260.

(15) Szeifert, J. M.; Fattakhova-Rohlfing, D.; Rathouský, J.; Bein, T. *Chemistry of Materials* **2012**, *24*, 659.

(16) Szeifert, J. M.; Feckl, J. M.; Fattakhova-Rohlfing, D.; Liu, Y.; Kalousek, V.; Rathousky, J.; Bein, T. *Journal of the American Chemical Society* **2010**, *132*, 12605.

5 One-dimensional metal-organic framework photonic crystals used as platforms for vapor sorption

This chapter demonstrates the applicability of mesoporous titania as high refractive-index layers in Bragg stacks and is based on the following publication:

Florian M. Hinterholzinger, Annekathrin Ranft, Johann M. Feckl, Bastian Rühle, Thomas Bein and Bettina V. Lotsch, *Journal of Materials Chemistry* **2012**, *22*, 10356 – 10362.

5.1 Introduction

Metal–organic frameworks represent a class of hybrid materials with promising properties for various applications.[1,2,3-5] In particular, the modular tailorability, the rich host–guest interactions, and the widely tunable sorption behavior make MOFs attractive candidates for chemical sensing.[6,7] However, only a few reports are dealing with MOF-based sensors,[8,9] in which the intrinsic framework luminescence[10-14] or the refractive index modulation of Fabry–Pérot interference peaks have been explored for signal transduction.[15] The tunability of the effective refractive index (RI) of MOFs *via* adsorption of guests inspired us to correlate these properties with the underlying optics of photonic crystals (PCs), which are composed of alternating dielectric layers featuring periodic changes in their effective refractive indices.[16-18]

One-dimensional assemblies, which represent the structurally simplest form of photonic crystals, are also known as Bragg stacks (BS) or Bragg mirrors. 1D-PC multilayer structures interacting with visible light require layer thicknesses corresponding to optical wavelengths.[19] As a consequence of the periodicity in the dielectric function, specific wavelengths are efficiently reflected due to diffraction and interference of incident light at each interface of the periodically stacked composite.[20] Enhanced reflectivity is achieved by increasing the number

of bilayers or by choosing dielectric materials featuring a high refractive index contrast (Scheme 5-1).[21]

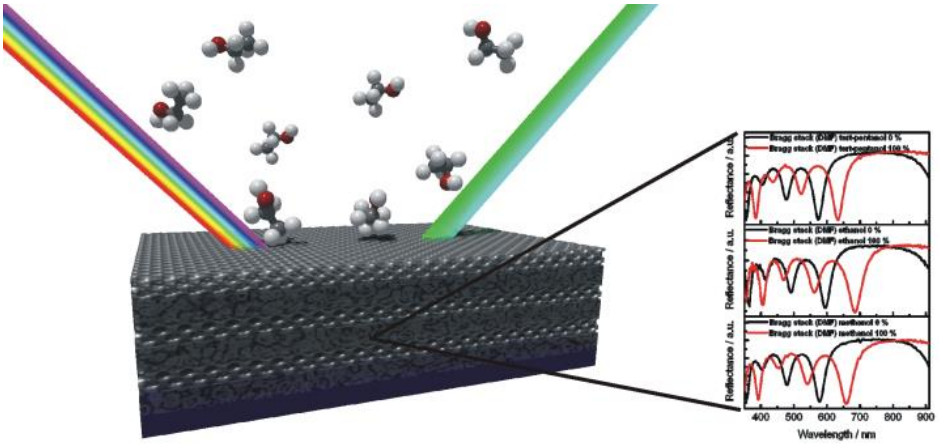

Scheme 5-1: Schematic representation of a multilayered photonic crystal architecture illustrating the structure- and angle-dependent reflection of incident light as well as the optical response upon exposure to external stimuli.

Currently, intensive research efforts are focused on the development of tunable optical sensors with a label-free operation and compact set-up. There are several approaches ranging from plasmonic noble metal nanotubes[22] or field effect transistors based on reduced graphene[23] to Bragg stacks built up from an alternating polymer architecture,[24] which deal with the implementation of these materials as tunable and label-free sensors. In particular, detection platforms based on Bragg stacks can be realized by translating stimuli-induced optical thickness changes of the constituent materials into a color change of the multilayer photonic structure. So far, several studies are dealing with tailor-made inorganic or hybrid materials to implement functionality within one-dimensional photonic crystals.[25] While there are several examples of versatile SiO_2–TiO_2 systems,[26-28] including both dense and porous morphologies as well as nanoparticle-based Bragg stacks,[29,30] smart hybrid photonic materials with intrinsic functionality are still rare.

In principle, a Bragg stack offers a versatile platform for the detection of molecular interactions and the development of chemical sensors, whereas the realization of chemical selectivity in sensors remains a great challenge. Very recently, several groups reported a new transduction scheme based on the fabrication of MOF-containing ordered 3D photonic structures.[31,32] The selectivity issue is addressed by integrating metal–organic frameworks into three-dimensional inverse opal structures. While Wu *et al.*[32] employed a colloidal crystal templating approach using a polystyrene opaline ‘‘mold’’, the group of J. Hupp[31] deposited MOF crystals onto a silica template to obtain hybrid MOF–silica colloidal crystal (MOF–SCC) films. The authors have shown that the introduction of an ordered porous structure imparts useful optical features to HKUST-1 and ZIF-8. For MOF–SCC an optical signal displayed by distinct stop band shifts upon analyte sorption is readily observed.

Contrary to 3D photonic materials, we introduce herein a one-dimensional photonic architecture based on a microporous metal–organic framework and titanium dioxide. Thus, an optical transducer system is built, which is used to efficiently convert molecular adsorption into an optical response. As a microporous material, the intensively studied zeolitic imidazolate framework ZIF-8[33] was chosen; this is expected to impart size- and chemoselectivity and, thus, functionality to the 1D-MOF PC. Complementary material properties in one single platform, such as hydrophobicity/hydrophilicity, dual pore-size regimes, and high refractive index contrast, can be additionally integrated by our combined assembly approach.

Ultimately, the presented results are expected to extend the toolbox for designing nanoporous and at the same time highly selective photonic crystals, to promote our understanding of molecular interactions in porous materials, and to provide novel concepts for label-free chemo-optical sensors.

The following experiments have been performed by Florian M. Hinterholzinger, Bastian Rühle and Johann M. Feckl in the group of Thomas Bein and by Annekathrin Ranft in the group of Bettina V. Lotsch. The ellipsometric sorption measurements were conducted by Florian M. Hinterholzinger.

5.2 Experimental

All chemicals (zinc nitrate hexahydrate, 2-methylimidazole; nitric acid (0.1 M), titanium(IV) ethoxide, titanium tetrachloride) as well as solvents are commercially available and were used as received. *Tert*-butyl alcohol was dried over a 4 Å molecular sieve at 28 °C and filtered prior to use.

Route A

Preparation of dense ZIF-8 films

ZIF-8 thin films were prepared on silicon wafers, similar to the approach reported in ref. 14 and 15. The substrates were pre-cleaned in piranha solution (H_2SO_4/H_2O_2, 70:30 (v/v)) at 70 °C for 30 minutes, rinsed with distilled water and dried under nitrogen flow.

For ZIF-8 thin film preparation, 500 mL methanolic stock solutions of $Zn(NO_3)_2 \cdot 6H_2O$ (25 mM, 99 %, *Aldrich*) as well as of 2-methylimidazole (*mIm*) (50 mM, 99 %, *Aldrich*) were prepared. A ZIF-8 thin film was obtained by immersing the cleaned substrates in a fresh mixture of 10 mL $Zn(NO_3)_2$ stock solution and 10 mL *mIm* stock solution for 30 minutes at room temperature. For optimization of homogeneity and to enhance surface smoothness, two different strategies were employed. The beakers were either put in an ultrasonic bath or fixed on a shaker during film growth. The as-prepared ZIF-8 thin film was washed with methanol

and dried under nitrogen flow. Thicker films could be obtained by simply repeating the process with fresh solutions.

Synthesis of ultrasmall titanium dioxide nanoparticles and film preparation

Titanium dioxide nanoparticles were synthesized as described earlier.[34] In brief, a non-aqueous sol-gel route in *tert*-butyl alcohol under microwave irradiation was used to yield ultrasmall (3 nm), crystalline (anatase), non-agglomerated and highly dispersible nanoparticles.

For all syntheses, titanium tetrachloride (0.7 mL, 6.4 mmol, 99.995 %, *Aldrich*) was dissolved in toluene (5 mL) and added to *tert*-butyl alcohol (15 mL, 160 mmol, *Aldrich*) under continuous stirring. Microwave heating was performed in microwave autoclaves with an initial heating power of 1200 W (Synthos 3000, Anton Paar). The solution was heated to 80 °C within 1 min and then kept at 50 °C for 20 min resulting in a slightly yellow, transparent solution of nanoparticles. To obtain the fully crystalline nanoparticles, this heating procedure was repeated one more time after a cooling period to room temperature. The solution was then colorless and titanium dioxide could be flocculated by the addition of *n*-heptane (*n*-heptane:*tert*-butanol/toluene 2:1 volume ratio; Sigma) and separated by centrifugation at 50000 rcf for 15 min.

For the preparation of the mesoporous (mp) titania films the nanoparticle pellet (0.4 g) was redispersed in ethanol (8.3 mL) and Pluronic F127 (0.1 g, *BASF*) was added as structure directing agent (SDA).

Fabrication of Bragg stack 1 (BS-1)

For the fabrication of Bragg stack 1 (**BS-1**) thoroughly washed and dense ZIF-8 thin films were coated with a fresh colloidal suspension of redispersed ultrasmall titanium dioxide

nanoparticles. The films were deposited by spin-coating using a Laurell WS-400B-6NPP-Lite-AS spin-coater at a speed of 5000 rpm to give a film thickness of ~50 nm. To remove the SDA, the films were first heated to 100 °C (3 h ramp, 1 h dwell time) to increase the film stability followed by an extraction of the SDA with ethanol under reflux for 1 h.

The complete removal was confirmed by reflection absorption infrared (RAIR) spectroscopy in addition to scanning electron microscopy (SEM) (Figure 5-1 and Figure 5-2). The whole procedure was repeated 3 times to obtain multiple alternating ZIF-8/mp-TiO_2 architectures.

Route B

Synthesis of ZIF-8 nanoparticles

ZIF-8 nanoparticles were prepared by a modified literature synthesis.[35] In a typical experiment, $Zn(NO_3)_2 \cdot 6\ H_2O$ (1.03 g, 3.45 mmol, 99 %, *Grüssing*) was dissolved in methanol (70 mL, puriss, *Sigma*) and rapidly added to a pre-cooled (0 °C) solution of 2-methylimidazole (2.27 g, 27.7 mmol, 99 %, *Aldrich*) in methanol (70.0 mL). The mixture was stirred and cooled constantly throughout the reaction until the solution slowly turned turbid. After 30 min, the nanocrystals were separated from the solvent by centrifugation. Colloidal suspensions of ZIF-8 were obtained by redispersing the particles after centrifugation in DMF (or methanol) (670 mg ZIF-8 / 1 mL DMF).

Synthesis of titania nanoparticles

Titania nanoparticles were synthesized according to the literature.[36] In a typical procedure, $Ti(OEt)_4$ (6.25 mL, *Aldrich*) was slowly added to HNO_3 (0.1 M, 37.5 mL, puriss., *Acros*) under stirring and heated to 80 °C for 8 h. After cooling to room temperature, the opalescent mixture was sonicated for at least 3 h in order to break up agglomerates. Colloidal

suspensions of titania in a solvent sufficiently volatile for spin-coating were obtained by repeated collection of the particles by centrifugation and redispersion in DMF (or methanol) (130 mg TiO_2 / 1 mL DMF).

Fabrication of Bragg stack 2 (BS-2)

Silicon wafers were used as substrates for the film deposition by spin-coating. The substrates were pre-cleaned with soap and water and subsequently treated with Piranha solution (H_2SO_4/H_2O_2, 2:1). After thoroughly rinsing with deionized water, the wafers were dried under nitrogen flow and stored in ethanol. Before film deposition, the substrates were plasma-cleaned and rinsed with ethanol under spinning for 5 s. The preparation of the Bragg reflector was performed by spin-coating alternatingly colloidal suspensions of ZIF-8 and titania onto the substrate at a speed of 4000 rpm (1500 acceleration) for 60 s, starting with ZIF-8. The film thickness was adjusted by the particle concentration in the suspensions and by multiple coating steps. After each deposition, the film was annealed at 200 °C for 30 min.

5.3 Characterization

X-ray diffraction (XRD) measurements of powders and thin films were performed using a Bruker D8 (Cu-Kα_1 = 1.5406 Å; Cu-Kα_2 = 1.5444 Å) in *theta-theta* geometry. The films were measured between 5° and 20° *two theta*, with a step-size of 0.05° *two theta* and a scan-speed of 0.3° min^{-1}. The data of the powder samples were collected between 5° and 45° *two theta* with a step-size of 0.05° *two theta* and a scan-speed of 3° min^{-1}.

SEM micrographs of **BS-1** were recorded with a JEOL JSM-6500F scanning electron microscope (SEM) equipped with an Oxford EDX analysis system; those of **BS-2** with a Merlin (Zeiss) FE-SEM. Ellipsometry measurements were performed with a Woollam

M2000D at an angle of 75° in the spectral range of 190 – 1000 nm. The data were fitted between 350 and 1000 nm using a Cauchy-type material as model layer. Reflectance measurements were recorded with the same ellipsometer using *s*-polarized light at an incident angle of 75°.

The recording of isotherms was performed at ambient temperature using a home-made Labview-controlled gas mixer. Digital mass flow controllers (W-101A-110-P, F-201C, Bronkhorst High-Tech) ensured the accurate dosing of the carrier gas nitrogen and the liquid analyte, which was vaporized in a controlled evaporation and mixing element (W-101A, Bronkhorst High-Tech). Partial pressures (p) were calculated using the van der Waals equation.[28,37] The relative pressure $p\ p_0^{-1}$ relates to the saturation pressure p_0.

5.4 Results and Discussion

Bragg stack preparation and structural properties

Two different strategies were employed for the fabrication of 1D-MOF photonic crystals consisting of either dense or porous ZIF-8 layers, and differently sized mesoporous titanium dioxide nanoparticle derived films. Stability, pore accessibility as well as high optical quality multilayer films are key requirements for the fabrication of analyte-responsive transducer systems. Those features were addressed by the choice of suitable deposition and post-treatment parameters. For the mp-TiO_2 deposition in **BS-1**, both a complete removal of the template (Figure 5-1 and Figure 5-2) as well as minimum etching of the ZIF-8 underlayer had to be achieved.

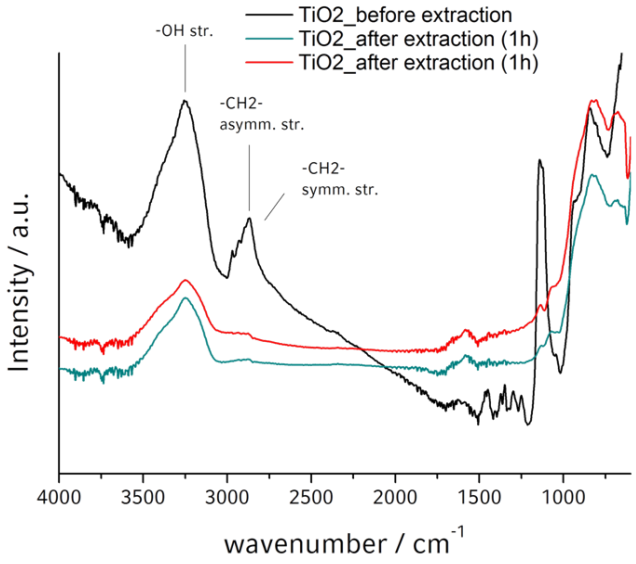

Figure 5-1: RAIR spectra of a TiO_2 thin film before and after the ethanol extraction procedure.

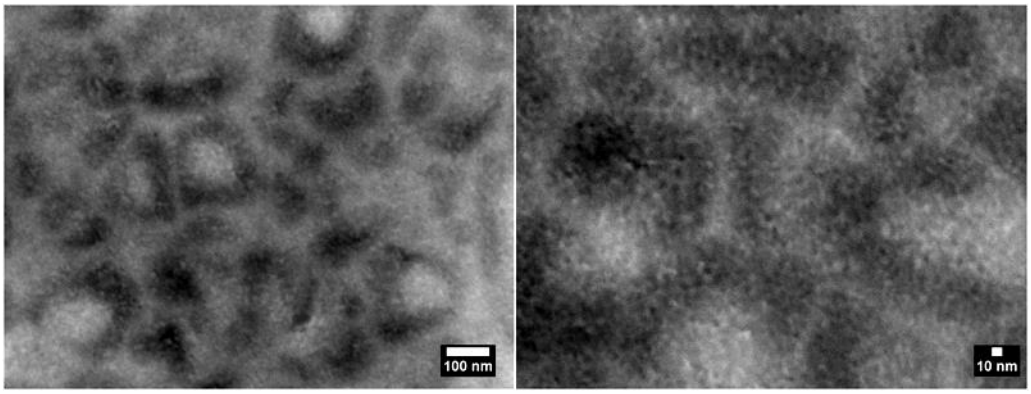

Figure 5-2: SEM micrographs demonstrating the mesoporous structure of a thin TiO_2 film after ethanol extraction (magnification: x100.000 (left); x250.000 (right)).

In Figure 5-3 the X-ray diffraction patterns of both 3-bilayer Bragg stacks (photographs shown in Figure 5-6) are depicted and compared to simulated data. The mild annealing temperatures employed in either case, in addition to the solvent extraction carried out under non-acidic conditions (**BS-1**), retain the crystallinity and stability of the ZIF-8 layers. The diffraction patterns of the multilayered ZIF-8–TiO_2 composites show excellent agreement with the simulated ZIF-8 data, apart from peak broadening, indicating a slightly smaller grain size of the ZIF-8 crystals within the BSs.

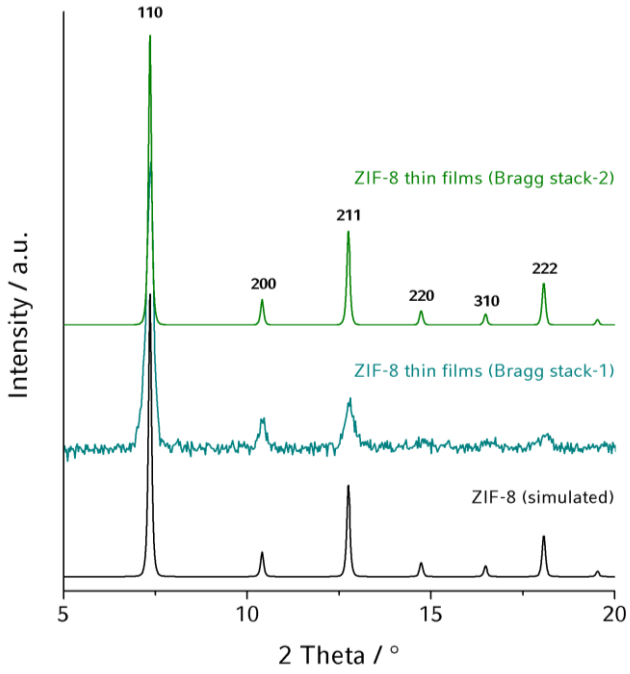

Figure 5-3: X-ray diffraction patterns (background corrected) of the 3-bilayer Bragg stack 1 (middle) as well as of Bragg stack 2 (top) after temperature treatment and complete removal of the structure-directing agent (F127), compared to simulated data (bottom line).

In contrast to **BS-1**, which features dense ZIF-8 layers, **BS-2** is composed of ZIF-8 nanocrystals (approx. 50 nm diameter, see Figure 5-4), forming uniform layers, and nanoparticle-based TiO_2 layers with TiO_2 particles around 10 – 15 nm in diameter. Therefore, we expect **BS-2** to exhibit a fairly high degree of textural mesoporosity in both layers, in addition to the intrinsic microporosity provided by the ZIF-8 crystals.

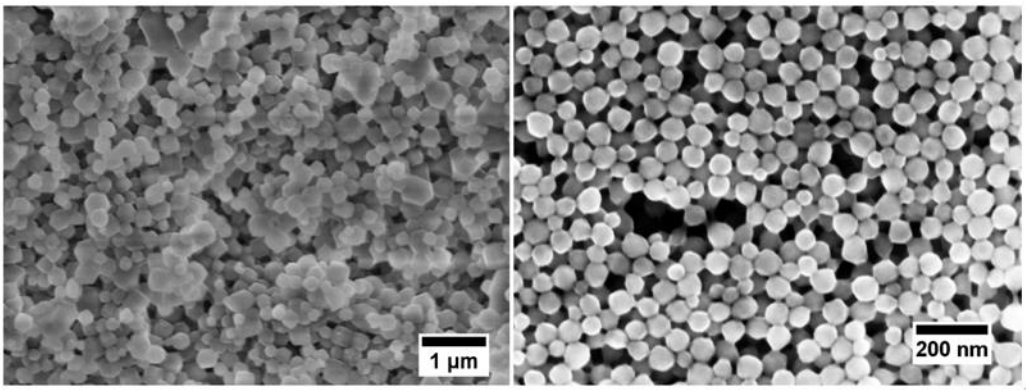

Figure 5-4: Scanning electron microscopy (SEM) images showing a bulk ZIF-8 powder sample obtained from the mixture solution used for the fabrication of BS-1 (left) as well as ZIF-8 nanoparticles used for the preparation of BS-2 (right).

The coexistence of both materials embedded in the 1D-MOF PC structure is confirmed by scanning electron microscopy (SEM). In Figure 5-5 representative 3-bilayer Bragg stacks composed of alternating microporous ZIF-8 layers and porous titania layers deposited on a silicon substrate are depicted.

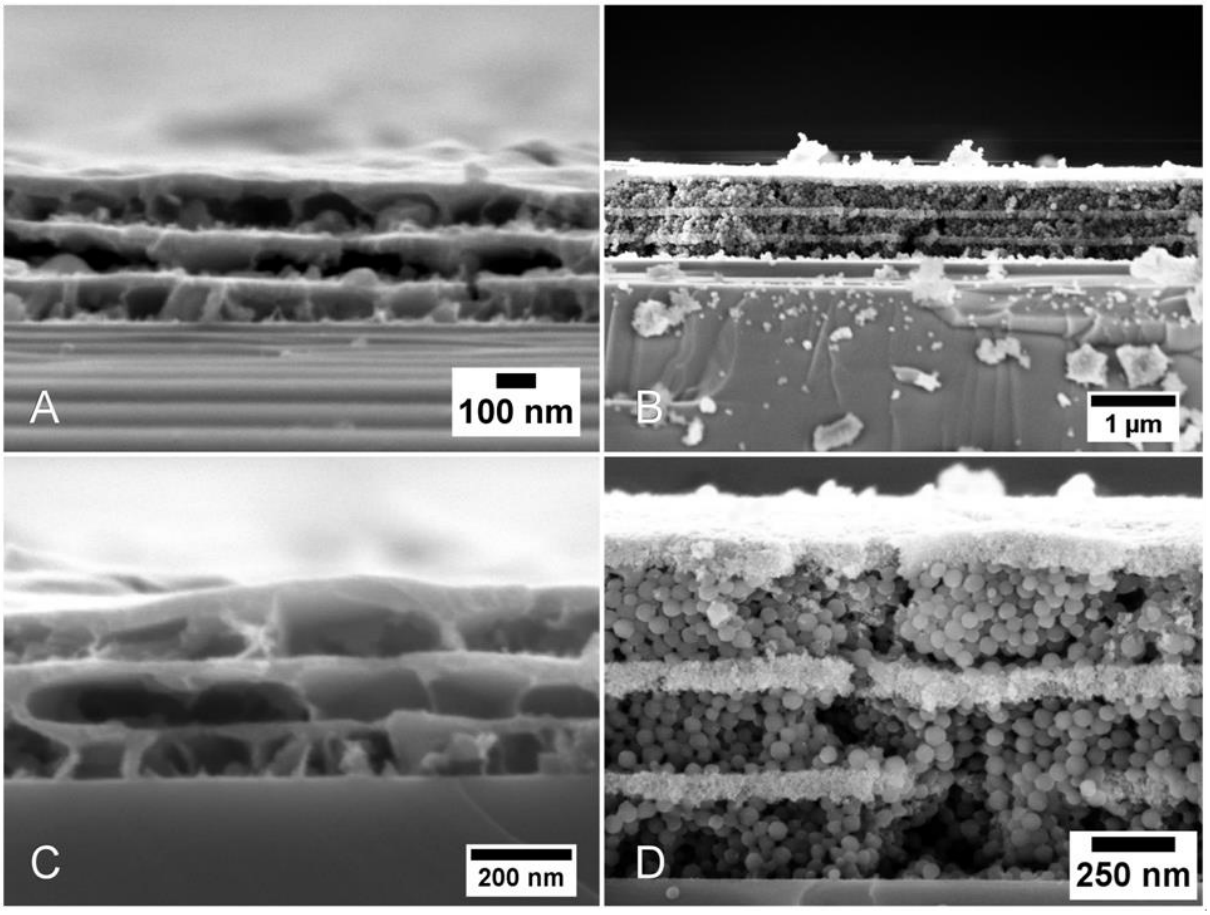

Figure 5-5: Scanning electron micrographs showing cross-sections of both 3-bilayer Bragg stacks with an average film thickness of ~ 50 nm for each titania layer and ~ 70 nm for each ZIF-8 layer for BS-1 (A and C) as well as for BS-2 (DMF, B and D) exhibiting a layer thickness of ~ 50 nm for each titania layer and ~ 200 nm for ZIF-8 layers, respectively. ZIF-8–TiO_2-BSs are depicted for different magnifications.

The differently prepared Bragg stacks exhibit a ZIF-8 layer thickness of approximately 70 nm in **BS-1** and about 200 nm in **BS-2**, respectively. TiO_2 layers deposited on each ZIF-8 film have a thickness of about 50 nm in both Bragg stacks. The cross-sectional SEM micrographs reveal that both fabrication methods yield fairly uniform layer thicknesses throughout the entire architecture. Figure 5-5 also demonstrates the alteration of both materials seen by the differences in material contrast. While the dark layers represent the ZIF-8 material exhibiting a lower electron density, the brighter thin films consist of TiO_2 nanoparticles. Not only the deposition of ZIF-8 layers on silicon, as already shown by several groups,[15,38] but also adhesion between ZIF-8 and mesoporous/nanoparticle titania layers was achieved using our

dual assembly approach. In contrast to the deposition of MOF material on inverse opal structures,[31,32] no surface modification is necessary when preparing ZIF-8-based one-dimensional photonic structures. Regarding the stability and crystallinity of the multilayered Bragg stacks, no delamination or amorphization upon heating, extraction or adsorption of volatile species is observed, which is consistent with the corresponding XRD results (see Figure 5-3). In conclusion, robust, uniform and high-optical quality multilayered photonic crystals composed of two different materials with varying morphologies can reproducibly be fabricated and thus provide the basis for chemical sensing studies.

Vapor adsorption and optical sensing

The combination of a microporous MOF material with mesoporous metal oxide layers is supposed to endow the material with a unique combination of size-selectivity and analyte sensitivity. The integration of both morphologies within one photonic structure is expected to act as a molecular sieving platform, readily adsorbing analyte molecules with small kinetic diameters in both layers, whereas the access of larger guests is exclusively possible into the mesoporous titania layers. Essentials such as high specific surface areas, pore accessibility, efficient diffusion and molecular sieving abilities are all addressed by our highly porous 1D-MOF photonic crystals.

Figure 5-6: Photographs of 3-bilayer Bragg stack 1 (left) and Bragg stack 2 (right) on a 5 x 2.5 cm^2 Si substrate in air.

The optical response of the 1D-MOF PCs to guest adsorption was investigated by performing sorption experiments of volatile analyte molecules. According to the optical Bragg equation, sorption of volatile species into the porous layers influences the effective refractive index of a bilayer by which analyte-induced color changes can be efficiently monitored. Figure 5-7 the reflectance spectra of both Bragg stacks are demonstrated.

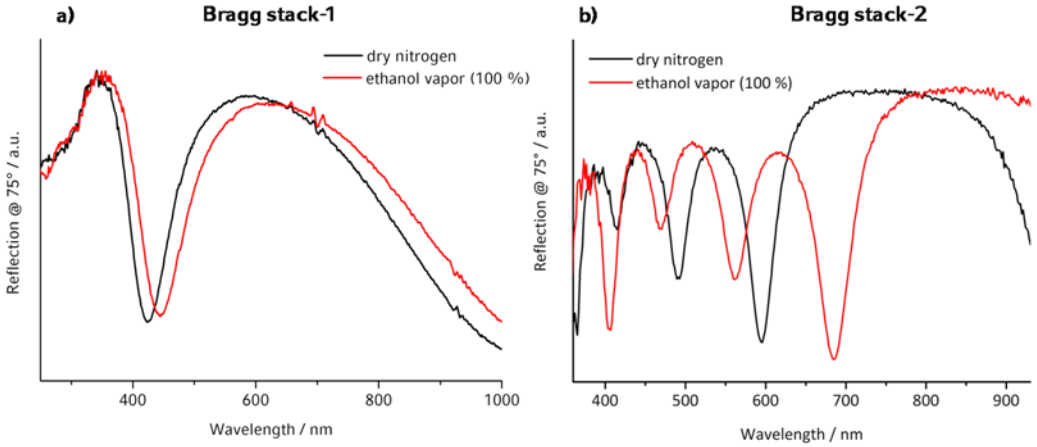

Figure 5-7: Reflectance spectra of Bragg stack 1 (a) and Bragg stack 2 (DMF) (b) illustrating the optical shift upon ethanol exposure recorded at the highest partial pressure ($p/p_0 \approx 1.0$).

Here, the optical response is triggered by the adsorption of ethanol vapor at the highest partial pressure ($p/p_0 \approx 1.0$), which entails pronounced red-shifts of the Fabry–Pérot fringe of **BS-1** from $\lambda \approx 585$ to $\lambda \approx 630$ nm as well as of the stop band of **BS-2**, derived from nanoparticles redispersed in DMF, from $\lambda \approx 740$ to $\lambda \approx 840$ nm, respectively. We attribute the significantly larger optical shift of **BS-2** to the thicker ZIF-8 layers and amplified external surface area (and hence accessibility), which underlines the enhanced contribution of the ‘‘active’’ component to the observed overall optical shift of the BS.[39] Compared to the 3D-MOF (HKUST-1) hybrid photonic crystals recently reported by the groups of J. Hupp and G. Li,[31,32] which show optical shifts of 9 nm and 16 nm upon ethanol sorption, respectively, a significant increase with respect to the optical response can be monitored in our system. However, when

infiltrating 30 mm thick polystyrene template films with ZIF-8, Wu *et al.* observed a distinct shift of about 75 nm upon methanol adsorption.[32] Compared to the inherently smaller absolute shifts observed with **BS-1,** which are presumed to result from the significantly smaller thickness of the ZIF-8 films, an even higher sensitivity upon sorption of organic vapors can be deduced from the reflectance spectrum of **BS-2** (Figure 5-7). Note that only a short heating period of 15 minutes at 200 °C was applied to **BS-2** prior to the sorption experiments compared to the activation procedure reported by Wu *et al.*[32] The samples were additionally subjected to a high-rate flow of dry nitrogen (Varian Chrompack Gas-clean Moisture Filter CP 17971, outlet concentration <0.1 ppm), which highlights the facile analyte uptake and release during a series of sorption measurements.

Analyte-induced variations of the optical thickness give rise to distinct optical shifts not only for ethanol and methanol but also for other larger analytes such as isobutanol and *tert*-pentanol. Adsorption isotherms monitoring the optical shift as a function of relative vapor pressure were recorded for **BS-2** (Figure 5-8c) as well as for the dense and porous ZIF-8 films as reference (Figure 5-8a and b). The latter show that the smaller alcohols are readily adsorbed by this MOF, including analyte molecules with larger kinetic diameters compared to the aperture size of ZIF-8 (3.4 Å).[33] These results are consistent with literature data, as it was previously shown that molecules such as ethanol or isobutanol exhibiting kinetic diameters of 4.5 Å (ref. 40) and 5 Å (ref. 41) are readily adsorbed owing to the flexibility of the pore apertures in ZIF-8.[40-42] Hence, *tert*-pentanol (2-methyl-1-propanol) was chosen as a sterically demanding analyte molecule with a kinetic diameter larger than 5 Å.[43] The dense ZIF-8 reference film only shows a minute optical shift of 4 nm, which is consistent with the almost complete exclusion of *tert*-pentanol from the ZIF-8 pore system (Figure 5-8a). The nanoparticle-based ZIF-8 film shows a larger optical shift of about 30 nm at the highest partial

pressure (p/p_0 = 1.0, Figure 5-8b), which is in agreement with the presence of a significant degree of textural mesoporosity.

In order to probe the host–guest interactions within the comparatively more complex Bragg stack environment, optical adsorption isotherms were recorded exemplarily for **BS-2**, as depicted in Figure 5-8c. Specifically, the initial stages during adsorption of alcohol vapors and the expected pore size-specific adsorption isotherms achieved through the incorporation of different porosities are of key interest.

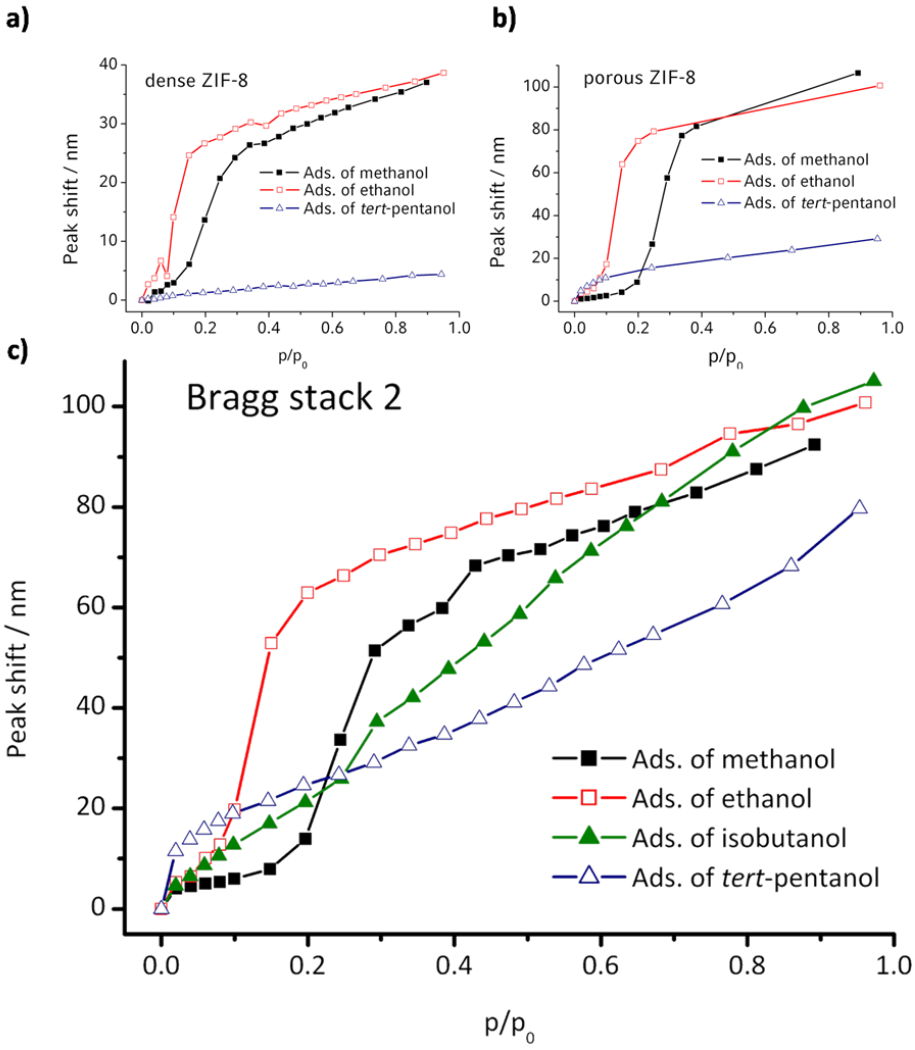

Figure 5-8: Optical vapor sorption isotherms demonstrating the adsorption performance of (a) dense and (b) nanoparticulate ZIF-8 reference samples as well as of (c) BS-2 (DMF) during exposure to a series of alcohol vapors.

During the first two dosing steps the 1D-MOF Bragg stack rapidly responds to all analyte molecules, indicated by varying red-shifts ranging from 5 to 15 nm (Figure 5-8c). At a partial pressure of p/p_0 = 0.1 and p/p_0 = 0.2, respectively, a steep increase in the methanol and ethanol isotherms is observed. However, a larger optical shift is recorded for ethanol, which is attributed to more beneficial interactions between ethanol and ZIF-8 owing to the larger hydrophobicity of ethanol compared to that of methanol. At the respective threshold pressures, pronounced optical shifts of about 50 – 60 nm are recorded, which gradually increase up to saturation pressure. The S-shaped isotherms upon methanol and ethanol adsorption recorded for both the single ZIF-8 films and for **BS-2** are in good agreement with the results obtained by Remi *et al.*[44] The authors attribute the S-shaped isotherms to changes in the framework triggered by interactions with guest-molecules, which was additionally confirmed and described elsewhere.[42] In contrast to the distinct S-shaped isotherms, isobutanol sorption experiments yield an almost linearly increasing adsorption behavior with an absolute shift of about 100 nm at the highest partial pressure. In contrast, the adsorption isotherm of *tert*-pentanol exhibits a convex shape featuring the highest uptake during the first dosing steps, which we attribute to the textural porosity of both ZIF-8 and titania layers arising from the nanoparticle architecture, as seen also for the porous ZIF-8 film (Figure 5-8b). However, this analyte exhibits the smallest overall uptake, which is consistent with the exclusion of *tert*-pentanol from the ZIF-8 pores, as demonstrated also for the individual ZIF-8 films. In contrast, the smaller analytes (methanol, ethanol, isobutanol) are more readily adsorbed owing to their smaller kinetic diameters.

As discussed above, an important finding is the fact that distinctly shaped isotherms are obtained for each of the four analytes over the entire relative pressure range, as additionally

demonstrated by reproduced sorption experiments using Bragg stacks derived from two different synthesis batches (Figure 5-9).

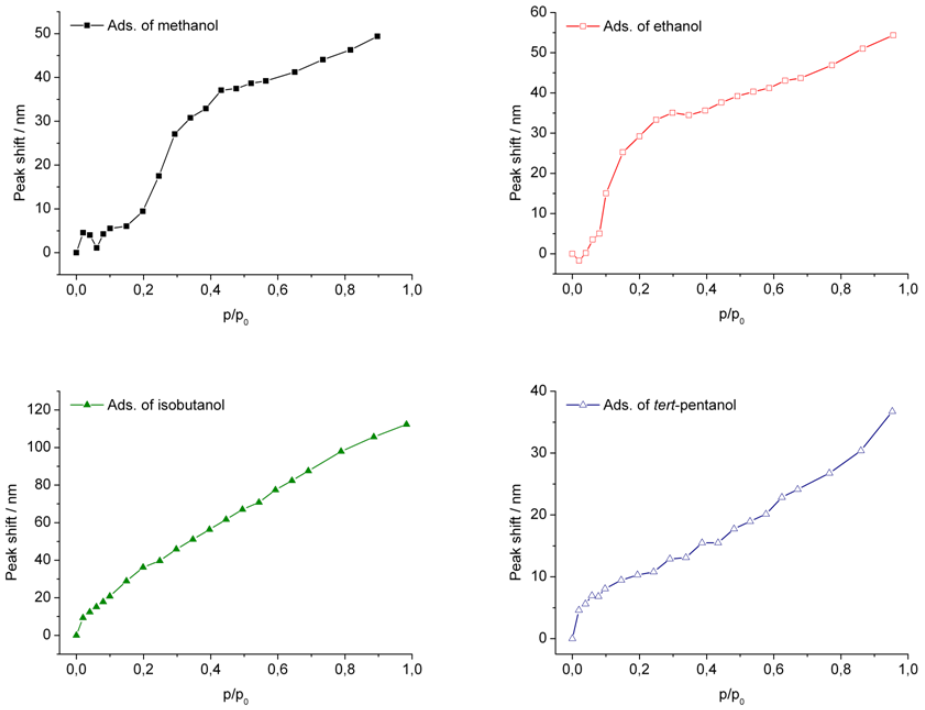

Figure 5-9: Reproduced optical vapor sorption isotherms demonstrating the adsorption of methanol, ethanol and *tert*-pentanol performed with Bragg stack 2 which was fabricated by redispersing the ZIF-8 nanoparticles in methanol (BS-2 (MeOH), see Experimental) as well as the adsorption of isobutanol into BS-2 prepared with nanoparticles redispersed in DMF (BS-2 (DMF)).

Owing to the different fabrication methods and the resulting differences in the ZIF-8 layer thicknesses, less pronounced absolute shifts of about 50 nm are recorded using the **BS-2** (MeOH) as compared to **BS-2** (DMF) used in Figure 5-8c and for isobutanol adsorption (Figure 5-9). Therefore, the optical shift for isobutanol agrees well with the results obtained with **BS-2** (DMF) shown in Figure 5-8c, whereas the absolute shifts for the other solvent vapors are smaller. Nevertheless, note that the shapes of all four optical isotherms are in good agreement with the isotherms shown in Figure 5-8, indicating the same host-guest interactions as in **BS-2** and thus, the same analyte selectivity to operate.

The characteristic sorption behavior indicates a high degree of chemical selectivity inherent to the MOF-BS, which is especially noticeable at low relative pressures. Comparison of the shapes of the isotherms for the BS and the individual ZIF-8 thin films (Figure 5-8) confirms that the optical response is dominated by ZIF-8.

5.5 Conclusions

In summary, a one-dimensional MOF-based photonic crystal heterostructure with embedded micro- and mesoporosity is presented. The fabrication of the 1D-MOF PC was achieved *via* two different inexpensive bottom-up synthesis approaches. The strategy of combining a microporous MOF material with mesoporous titanium dioxide layers provides the basis for a highly sensitive signal transduction scheme with an amplified overall optical response, while maintaining high chemical specificity. Hence, molecular recognition is translated into a readable optical signal without the use of any reporter systems.

The concept of MOF-based one-dimensional photonic crystal structures extends the scope of chemoselective optical signal transducer systems. We anticipate a generalization of the assembly of 1D photonic materials in terms of the large variety and tunability of MOFs or related materials. Thus, we believe that the above proof-of-concept experiments provide a basis for the design of highly sensitive and chemically selective optical sensors.

5.6 References

(1) Yaghi, O. M.; O'Keeffe, M.; Ockwig, N. W.; Chae, H. K.; Eddaoudi, M.; Kim, J. *Nature* **2003**, *423*, 705.

(2) Ferey, G. *Chem. Soc. Rev.* **2008**, *37*, 191.

(3) Mueller, U.; Schubert, M.; Teich, F.; Puetter, H.; Schierle-Arndt, K.; Pastre, J. *J. Mater. Chem.* **2006**, *16*, 626.

(4) Li, J. R.; Kuppler, R. J.; Zhou, H. C. *Chem. Soc. Rev.* **2009**, *38*, 1477.

(5) Meek, S. T.; Greathouse, J. A.; Allendorf, M. D. *Adv. Mater.* **2011**, *23*, 249.

(6) Scherb, C.; Williams, J. J.; Hinterholzinger, F.; Bauer, S.; Stock, N.; Bein, T. *J. Mater. Chem.* **2011**, *21*, 14849.

(7) Shekhah, O.; Liu, J.; Fischer, R. A.; Woll, C. *Chem. Soc. Rev.* **2011**, *40*, 1081.

(8) Allendorf, M. D.; Bauer, C. A.; Bhakta, R. K.; Houk, R. J. T. *Chem. Soc. Rev.* **2009**, *38*, 1330.

(9) Kreno, L. E.; Leong, K.; Farha, O. K.; Allendorf, M.; Van Duyne, R. P.; Hupp, J. T. *Chem. Rev.* **2011**, *112*, 1105.

(10) Xu, H.; Liu, F.; Cui, Y.; Chen, B.; Qian, G. *Chem. Commun.* **2011**, *47*, 3153.

(11) Chen, B.; Wang, L.; Xiao, Y.; Fronczek, F. R.; Xue, M.; Cui, Y.; Qian, G. *Angew. Chem., Int. Ed.* **2009**, *121*, 508.

(12) Gole, B.; Bar, A. K.; Mukherjee, P. S. *Chem. Commun.* **2011**, *47*, 12137.

(13) Stylianou, K. C.; Heck, R.; Chong, S. Y.; Bacsa, J.; Jones, J. T. A.; Khimyak, Y. Z.; Bradshaw, D.; Rosseinsky, M. J. *J. Am. Chem. Soc.* **2010**, *132*, 4119.

(14) Takashima, Y.; Martínez, V. M.; Furukawa, S.; Kondo, M.; Shimomura, S.; Uehara, H.; Nakahama, M.; Sugimoto, K.; Kitagawa, S. *Nat. Commun.* **2011**, *2*, 168.

(15) Lu, G.; Hupp, J. T. *J. Am. Chem. Soc.* **2010**, *132*, 7832.

(16) Bonifacio, L. D.; Lotsch, B. V.; Puzzo, D. P.; Scotognella, F.; Ozin, G. A. *Adv. Mater.* **2009**, *21*, 1641.

(17) John, S. *Phys. Rev. Lett.* **1987**, *58*, 2486.

(18) Arsenault, A.; Fournier-Bidoz, S.; Hatton, B.; Miguez, H.; Tetreault, N.; Vekris, E.; Wong, S.; Ming Yang, S.; Kitaev, V.; Ozin, G. A. *J. Mater. Chem.* **2004**, *14*, 781.

(19) Joannopoulos, J. D.; Villeneuve, P. R.; Fan, S. *Nature* **1997**, *386*, 143.

(20) Lee, H. *J. Appl. Phys.* **2003**, *93*, 819.

(21) Bardosova, M. *Appl. Phys. Lett.* **2006**, *89*, 093116.

(22) McPhillips, J.; Murphy, A.; Jonsson, M. P.; Hendren, W. R.; Atkinson, R.; Höök, F.; Zayats, A. V.; Pollard, R. J. *ACS Nano* **2010**, *4*, 2210.

(23) Stine, R.; Robinson, J. T.; Sheehan, P. E.; Tamanaha, C. R. *Adv. Mater.* **2010**, *22*, 5297.

(24) Wang, Z.; Zhang, J.; Xie, J.; Wang, Z.; Yin, Y.; Li, J.; Li, Y.; Liang, S.; Zhang, L.; Cui, L.; Zhang, H.; Yang, B. *J. Mater. Chem.* **2012**, *22*, 7887.

(25) Khartsev, S. I. *Appl. Phys. Lett.* **2005**, *87*, 122504.

(26) Fuertes, M. C.; López-Alcaraz, F. J.; Marchi, M. C.; Troiani, H. E.; Luca, V.; Míguez, H.; Soler-Illia, G. J. A. A. *Adv. Funct. Mater.* **2007**, *17*, 1247.

(27) Choi, S. Y.; Mamak, M.; von Freymann, G.; Chopra, N.; Ozin, G. A. *Nano Letters* **2006**, *6*, 2456.

(28) Kobler, J.; Lotsch, B. V.; Ozin, G. A.; Bein, T. *ACS Nano* **2009**, *3*, 1669.

(29) Lee, D.; Rubner, M. F.; Cohen, R. E. *Nano Letters* **2006**, *6*, 2305.

(30) Colodrero, S.; Ocaña, M.; González-Elipe, A. R.; Míguez, H. *Langmuir* **2008**, *24*, 9135.

(31) Lu, G.; Farha, O. K.; Kreno, L. E.; Schoenecker, P. M.; Walton, K. S.; Van Duyne, R. P.; Hupp, J. T. *Adv. Mater.* **2011**, *23*, 4449.

(32) Wu, Y.-n.; Li, F.; Zhu, W.; Cui, J.; Tao, C.-a.; Lin, C.; Hannam, P. M.; Li, G. *Angew. Chem., Int. Ed.* **2011**, *50*, 12518.

(33) Park, K. S.; Ni, Z.; Côté, A. P.; Choi, J. Y.; Huang, R.; Uribe-Romo, F. J.; Chae, H. K.; O'Keeffe, M.; Yaghi, O. M. *Proc. Natl. Acad. Sci.* **2006**, *103*, 10186.

(34) Szeifert, J. M.; Feckl, J. M.; Fattakhova-Rohlfing, D.; Liu, Y.; Kalousek, V.; Rathousky, J.; Bein, T. *J. Am. Chem. Soc.* **2010**, *132*, 12605.

(35) Cravillon, J.; Münzer, S.; Lohmeier, S.-J.; Feldhoff, A.; Huber, K.; Wiebcke, M. *Chem. Mater.* **2009**, *21*, 1410.

(36) Lotsch, B. V.; Scotognella, F.; Moeller, K.; Bein, T.; Ozin, G. A. *Proc. SPIE* **2010**, *7713*, 7713V.

(37) Scherb, C.; Koehn, R.; Bein, T. *J. Mater. Chem.* **2010**, *20*, 3046.

(38) Demessence, A.; Boissiere, C.; Grosso, D.; Horcajada, P.; Serre, C.; Ferey, G.; Soler-Illia, G. J. A. A.; Sanchez, C. *J. Mater. Chem.* **2010**, *20*, 7676.

(39) Allendorf, M. D.; Houk, R. J. T.; Andruszkiewicz, L.; Talin, A. A.; Pikarsky, J.; Choudhury, A.; Gall, K. A.; Hesketh, P. J. *J. Am. Chem. Soc.* **2008**, *130*, 14404.

(40) Zhu, G.; Li, Y.; Zhou, H.; Liu, J.; Yang, W. *Mater. Lett.* **2008**, *62*, 4357.

(41) Liu, X.-L.; Li, Y.-S.; Zhu, G.-Q.; Ban, Y.-J.; Xu, L.-Y.; Yang, W.-S. *Angew. Chem., Int. Ed.* **2011**, *50*, 10636.

(42) Fairen-Jimenez, D.; Moggach, S. A.; Wharmby, M. T.; Wright, P. A.; Parsons, S.; Düren, T. *J. Am. Chem. Soc.* **2011**, *133*, 8900.

(43) Kodaka, M. *J. Phys. Chem. B* **2003**, *108*, 1160.

(44) Cousin Saint Remi, J.; Rémy, T.; Van Hunskerken, V.; van de Perre, S.; Duerinck, T.; Maes, M.; De Vos, D.; Gobechiya, E.; Kirschhock, C. E. A.; Baron, G. V.; Denayer, J. F. M. *ChemSusChem* **2011**, *4*, 1074.

6 Niobium doped titania nanoparticles: synthesis, assembly into mesoporous films and electrical conductivity

This chapter is based on the following publication:

Yujing Liu, Johann M. Szeifert, Johann M. Feckl, Benjamin Mandlmeier, Jiri Rathousky, Oliver Hayden, Dina Fattakhova-Rohlfing and Thomas Bein. *ACS Nano*, **2010,** *4*, 5373 – 5381.

6.1 Introduction

Transparent conducting oxides (TCO) with a regular mesoporous architecture have recently attracted attention owing to their ability to accommodate functional guest molecules in photovoltaic, electrochromic and chemical sensing applications, where the access of both photons and charge carriers to a high-surface area interface is of key importance.[1-3] However, the range of compounds that simultaneously feature electrical conductivity and optical transparency in the visible spectrum is limited.[4] TCOs usually consist of doped indium, tin, zinc or cadmium oxides; of these only tin-doped indium oxide (ITO) and antimony-doped tin oxide (ATO) have been prepared with a periodic porous morphology.[1-3,5] The synthesis of mesoporous electrodes from other classes of TCOs is of great interest, as it could substantially extend the library of available transparent conducting nanoarchitectures meeting the requirements of different optoelectronic applications.

In 2005, Furubayashi et al.[6,7] reported a metallic type conductivity of Nb doped anatase titania (NTO) films. Thin films, epitaxially grown by pulsed laser deposition, exhibit a conductivity of 10^3 – 10^4 S cm^{-1} and high optical transmittance in visible light, which makes them

comparable with the much more expensive ITO. The conductivity mechanism was explained by the formation of an impurity band overlapping with the conduction band of anatase, and corroborated by first-principles band calculations showing that Nb doping does not change band dispersions except for filling the conduction band, implying that Nb atoms do not generate in-gap states.[8]

The idea to synthesize mesoporous transparent titania-based electrodes is appealing, as titania films with controlled mesoporous structure can be easily prepared. An increase in electrical conductivity of the existing mesostructures due to doping with Nb atoms could open a way to inexpensive nanostructured TCO materials with controlled porosity. Moreover, the already known applications of titania, such as in photovoltaics, photocatalysis and charge storage, could greatly benefit from an increased electrical conductivity of the titania framework. This has recently been demonstrated by Huang *et al.*, who reported that higher conductivity of a TiO_2 electrode by Nb doping leads to enhanced photovoltaic performance.[9]

Fabrication of periodic mesoporous Nb-doped titania films has been reported by Sanchez *et al*[10] and Wu *et al*,[14] however, the electrical conductivity of those materials was not investigated. Disordered porous NTO powders[11, 13, 15] and films[12] have also been reported, but these materials were studied regarding their photocatalytic and electrocatalytic behavior. Additional studies dealing with the preparation of conducting titania materials usually involve physical processes or high temperature solid state reactions, which are not conducive for the fabrication of periodic porous nanostructures.[16-29]

Periodic mesoporous titania films with controlled porous structure can be prepared by the self-assembly of amorphous titania sols, crystalline nanoparticles or a combination of both in the presence of surfactants acting as structure-directing agents.[9,30-32] It was recently

demonstrated for mesoporous thin films of antimony-doped tin oxide (ATO) that TCO nanocrystals can also serve as building blocks for the assembly of nanostructured transparent electrodes.[33] The doping level and thus the electrical conductivity can be precisely adjusted, because composition can be controlled in the particle synthesis. Due to the intrinsic crystallinity of the building blocks, crystalline mesostructures can be obtained already at moderate temperatures. However, the use of nanoparticles as the primary units for the assembly of mesoporous conducting films implies certain requirements to their properties. The particles should be just a few nanometers in size with a narrow particle size distribution, feature crystallinity and electrical conductivity, and should be dispersible in various solvents to form stable colloidal solutions. Synthesis of Nb-doped titania nanoparticles meeting those criteria has not been reported so far. Recently, we have reported that *tert*-butanol can be used as a novel reaction medium for the solvothermal synthesis of ultrasmall and highly dispersible nanoparticles.[34] The use of *tert*-butanol in microwave-assisted synthesis provides monodispersed nanosized particles of titania, whose size and crystallinity could be easily controlled by the variation of reaction temperature and time.

Here we describe the solvothermal synthesis of crystalline monodispersed niobium doped titania nanoparticles using *tert*-butanol as a reaction medium and an oxide source. Furthermore, the ability of the obtained nanocrystals to self-assemble into complex 3D mesoporous nanostructures, and the electrical conductivity of the nanoparticles and mesoporous films are investigated.

6.2 Results

Synthesis of Nb-doped TiO_2 nanoparticles and their assembly into mesoporous films

For the preparation of niobium doped titania nanoparticles, titanium tetrachloride and niobium(V) ethoxide were dissolved in *tert*-butanol. The particles with different Nb content are designated as NPX, where X is the Nb/(Nb+Ti) molar ratio in percent. The clear solution was kept at different temperatures and different times in a laboratory oven in a Teflon-sealed autoclave. The solution turned turbid when the nanoparticles were formed. The particle size and crystallinity strongly depend on the reaction temperature. At 60 °C the particles are still completely amorphous, and an increase in the reaction temperature to 100 °C is necessary to obtain a crystalline phase (Figure 6-1). A further increase in the reaction temperature leads to larger crystalline particles. Thus, the size of the NP0 particles obtained after 12 hours of reaction at 100 °C and 150 °C is 10 nm and 14 nm, respectively.

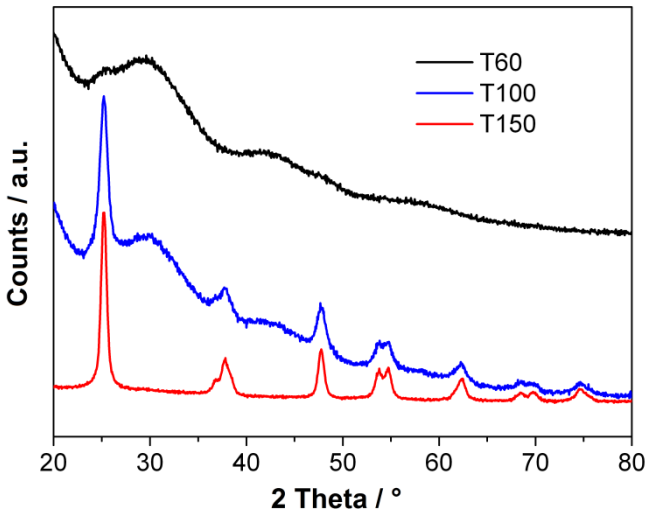

Figure 6-1: XRD patterns of as-produced NP0 TiO_2 particles prepared by solvothermal reaction in *tert*-BuOH at different reaction temperatures (reaction time 12 hours).

An increase in the concentration of Nb leads to a delayed formation of particles. For the particles prepared at 100 °C the onset of crystallization was observed (by XRD) after 1.5, 3 and 4 hours for NP0, NP10 and NP20, respectively. This effect – also reported for other synthesis procedures[13,15,35] – is attributed to the suppression of particle crystallization due to Nb doping. Furthermore, the particle size at the same reaction temperature can be varied by changing the reaction time. While NP20 particles synthesized at 100 °C for 4 hours are only 4 nm in size, prolonging the reaction time to 20 hours increases the particle size to 13 nm (Figure 6-2b).

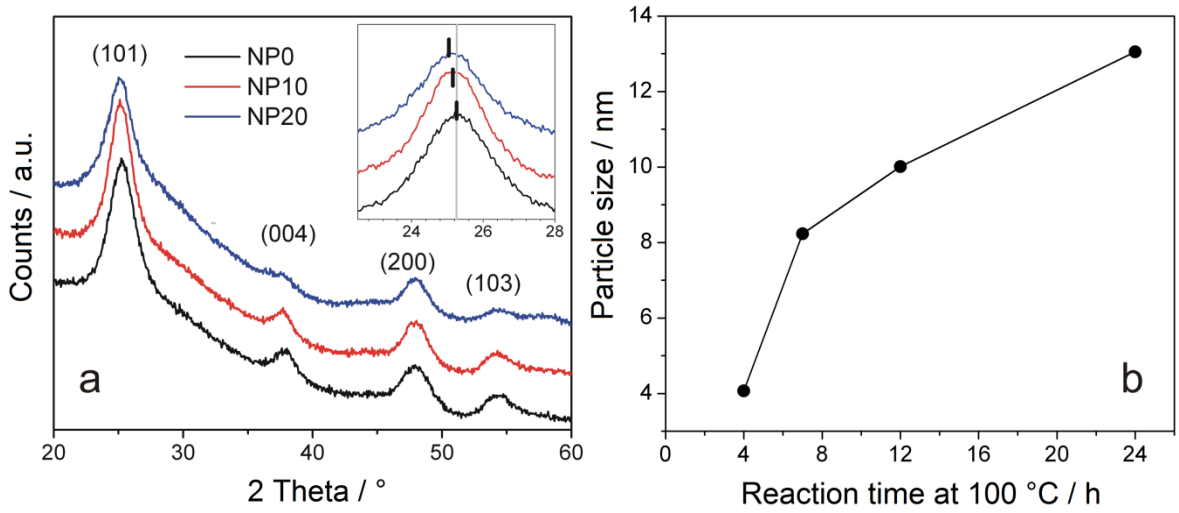

Figure 6-2: (a) XRD patterns of as prepared 0 %, 10 % and 20 % Nb-doped TiO_2 nanoparticles synthesized by a solvothermal reaction in *tert*-butanol at 100 °C for 1.5, 3 and 4 hours, respectively. The inset shows the position of the (101) reflection. (b) Variation of the size of NP20 nanoparticles during synthesis in *tert*-BuOH at 100 °C with the reaction time. The particle size was derived from the peak broadening in the XRD patterns according to the Scherrer equation.

As we aimed at the preparation of crystalline nanoparticles as small as possible, the reaction at 100 °C was stopped just after the onset of crystallization. The NTO nanoparticles with different Nb content prepared this way are crystalline and average 4 – 5 nm in size (Table 6-1), as shown by HRTEM images (Figure 6-3) and XRD patterns (Figure 6-2a). The XRD

patterns of both pure and doped nanoparticles with up to 20 mol% titania show only one crystalline phase, either anatase or a phase structurally closely related to anatase (Figure 6-2a). An increase in the Nb content leads to a shift of the (101) and (200) reflections to lower angles corresponding to the unit cell expansion by about 5 % due to the replacement of Ti^{4+} ions (radius 60.5 pm) by slightly larger Nb^{5+} ions (radius 64 pm) according to Vegard's law. The same changes in d-spacing with increasing Nb content were observed in the HR-TEM images of doped particles.

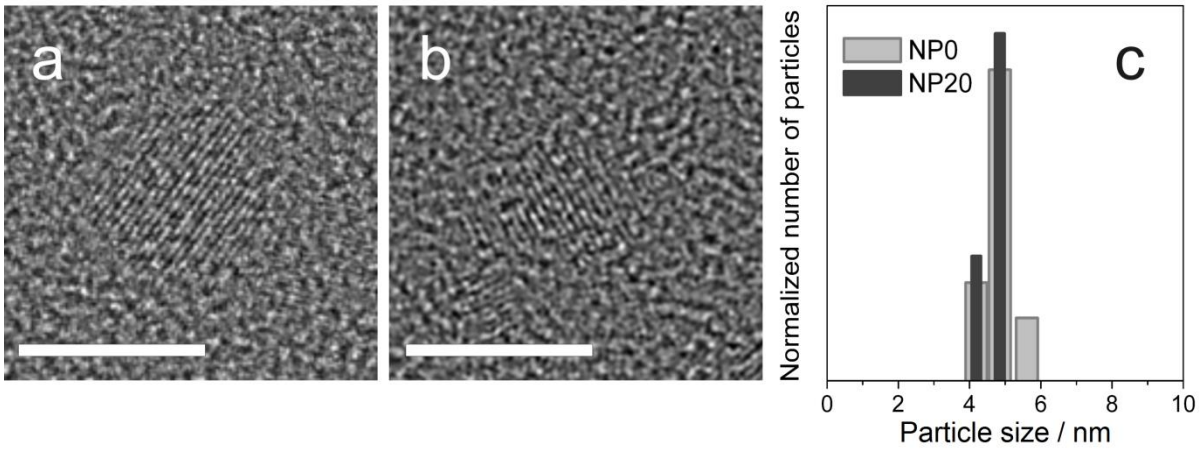

Figure 6-3: HR-TEM images of as-made NP0 (a) and NP20 (b) nanoparticles synthesized at 100 °C (scale bar corresponds to 5 nm), and the particle size distribution determined by DLS in tetrahydrofurane (c).

Table 6-1: Size of NTO nanoparticles prepared by a solvothermal reaction in tert-butanol at 100 °C determined by DLS, XRD (size calculated from the Scherrer equation) and TEM (statistical evaluation of about 100 particles).

Particle size	DLS	XRD	TEM
NP0	4.6 nm	4 nm	4.1nm
NP10	4.6 nm	4.1nm	-------
NP20	4.4 nm	4 nm	4 nm

All the nanoparticles can be dispersed easily in tetrahydrofurane (THF) at concentrations of more than 5 wt % of NTO in the presence of small amounts of hydrochloric acid, forming stable transparent colloidal dispersions. The particle size distributions obtained by DLS (Figure 6-3c) are in a good agreement with those obtained from X-ray diffractograms.

To sum up, the undoped as well as Nb-doped titania nanoparticles prepared by the solvothermal synthesis in *tert*-butanol are crystalline, nanosized and dispersible, which makes them suitable building blocks for the assembly of nanostructured materials. We have examined the applicability of the as-synthesized nanoparticles for the assembly of mesoporous films using the commercial Pluronic F127 polymer as a structure-directing agent. Thin films designated as MS0, MS10 and MS20 were prepared from NP0, NP10 and NP20 nanoparticles, respectively. The synthesis times for the different samples were chosen such that the particle size of all samples was about 4 nm, in order to make the particles compatible with the surfactant-assisted self-assembly. In order to remove the template and to sinter the nanoparticles, the films were heated in air at 300 °C for 2 hours, because this is the lowest temperature sufficient for the removal of the Pluronic copolymer and the complete removal of organic residues from the interior of the pores in the thin films.[32-34]

The SEM images (Figure 6-4) show the surface of the mesoporous structures assembled from nanoparticles with varying Nb content. Depending on the composition of the nanoparticles used, the character of the mesostructure of the films differs significantly. The assembly of the undoped NP0 nanoparticles gives a worm-like open mesostructure with a homogeneous pore distribution. The films assembled from NP10 nanoparticles feature a channel-type mesostructure similar to that assembled from antimony doped tin oxide nanoparticles.[33] Finally, the NP20 particles provide films with a higher degree of pore ordering, resembling a

cubic mesostructure with a d-spacing of about 17 nm. The thickness of the films assembled from particles with different doping levels is around 200 nm.

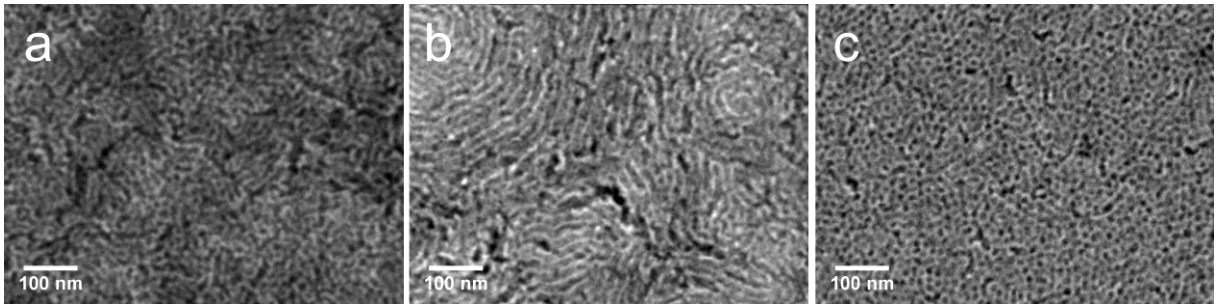

Figure 6-4: SEM images (top view) of MS0 (a), MS10 (b), and MS20 (c) films calcined in air at 300 °C.

The highly porous morphology of the films assembled from nanoparticles is also apparent in TEM images (Figure 6-5). The Fourier transforms of the TEM images show a ring corresponding to a mesostructure periodicity of 16±1 nm. Similar information about the mesostructure ordering is provided by the small angle XRD patterns (Figure 6-6), which exhibit a clearly distinguishable reflection for the MS10 and MS20 samples and a broad shoulder for a less ordered MS0 film.

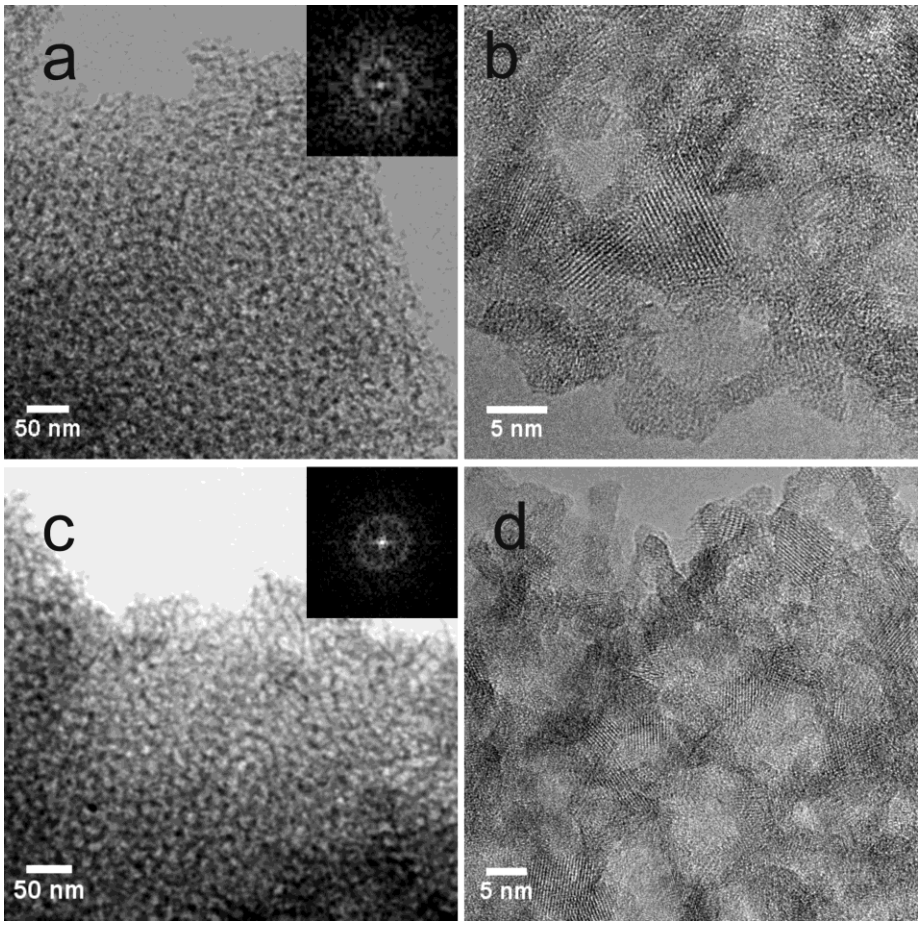

Figure 6-5: TEM (a,c) and HR-TEM (b, d) images of MS10 (first row) and MS20 (second row) samples calcined at 300 °C. The insets in (a, c) show the Fourier transforms of the images.

The HR-TEM images show that the pore walls are composed of crystalline nanoparticles (Figure 6-5b, d). The high crystallinity of the films calcined at 300 °C was also proven by wide angle X-ray diffraction (Figure 6-7). The crystalline domain size calculated from the (101) reflection of the corresponding XRD patterns is about 7.5 nm and 6.5 nm for MS0 and MS20 films, respectively. This illustrates that the crystal size increases after calcination at 300 °C compared to the size of nanoparticles used for the films assembly.

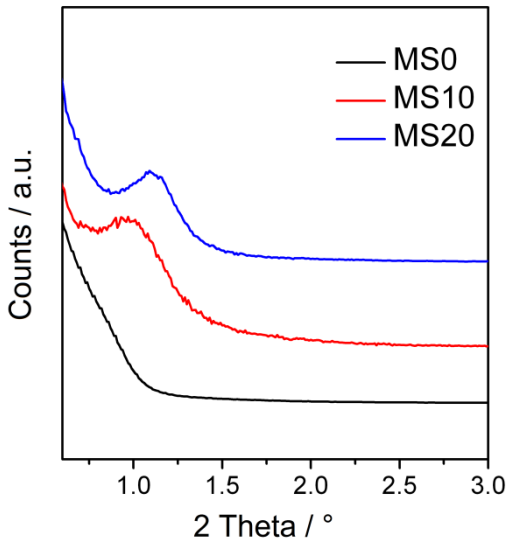

Figure 6-6: Small angle XRD pattern of mesostructured films MS0, MS10 and MS20 assembled from the corresponding nanoparticles after calcination at 300 °C.

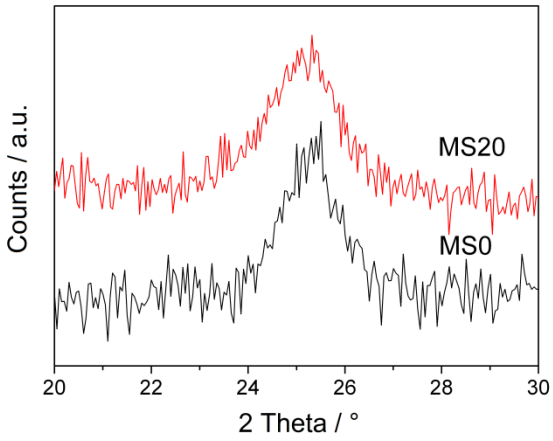

Figure 6-7: Wide angle XRD patterns of mesostructured films MS0 and MS20 after calcination at 300 °C ((101) reflection).

The textural properties and the accessibility of the internal surface of the thin films were studied by krypton adsorption at 77 K (Figure 6-8). The samples assembled from nanoparticles are characterized by an open porous structure without pore blocking. The use of particles with a higher Nb content provides films exhibiting a larger pore volume and surface area, in combination with a higher degree of periodicity of the mesostructure as could be seen in electron microscopy. The MS20 films feature the largest pore volume and a porosity of

43 %, with a surface area of 190 m^2 cm^{-3}. The pore size determined from the Kr isotherm is 9 – 10 nm with narrow pore size distribution, as evidenced by the very steep adsorption and desorption branches. The isotherms of samples MS10 and MS0 are flatter, their pore size distribution is broader and the surface area is smaller (163 and 90 m^2 cm^{-3}, respectively).

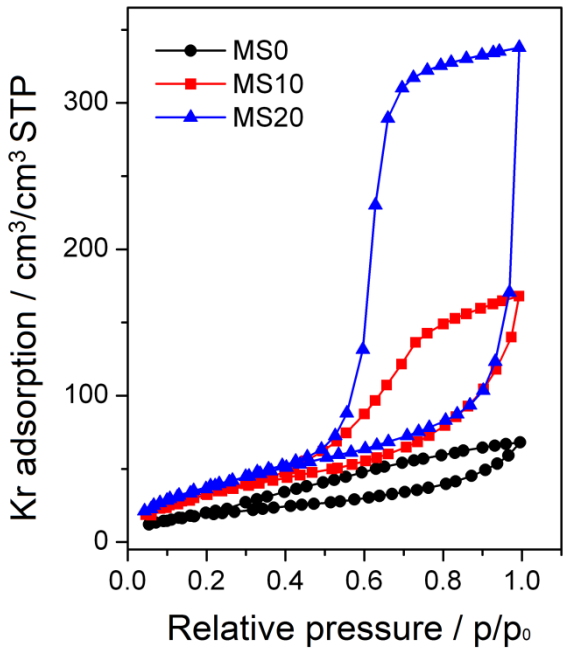

Figure 6-8: Kr adsorption isotherms at 77 K of templated mesoporous films assembled from nanoparticles with different Nb content: MS0 (black, circles), MS10 (red, squares) and MS20 (blue, triangles). All the films were calcined at 300 °C.

Electrical conductivity of Nb-doped TiO_2 nanoparticles

The valence state of the metal atoms in the Nb-doped titania lattice is an important indication of successful doping with regard to the electric conductivity, which is directly related to the specific defects formed in the doping process.[36] The valence state of the Ti and Nb in the nanoparticles containing 20 % of Nb prepared in *tert*-BuOH at 100 °C was investigated using X-ray photoelectron spectroscopy (XPS) (Figure 6-9), which shows the peaks corresponding to oxygen, titanium and niobium. About 20 mol% of both titanium and niobium is found in their reduced states, Ti^{3+} and Nb^{4+} or lower,[15] respectively, which is consistent with the Nb

doping level of 20 %. As each added Nb atom causes one extra electron that can reside in the form of reduced valence states of Ti or Nb, we assume that the extra electrons are not compensated by other easily formed defects such as Ti vacancies or oxygen interstitials. Therefore, the introduction of Nb^{5+} ions into the titania lattice leads to the donation of electrons into the conduction band and thus an increase in the charge carrier concentration. The presence of the reduced species due to the Nb doping is also reflected in the particle color. The as-prepared Nb-doped nanoparticles are bluish-green after pressing them into a pellet, the color being more intensive for the larger particles, while the undoped TiO_2 particles remain white.

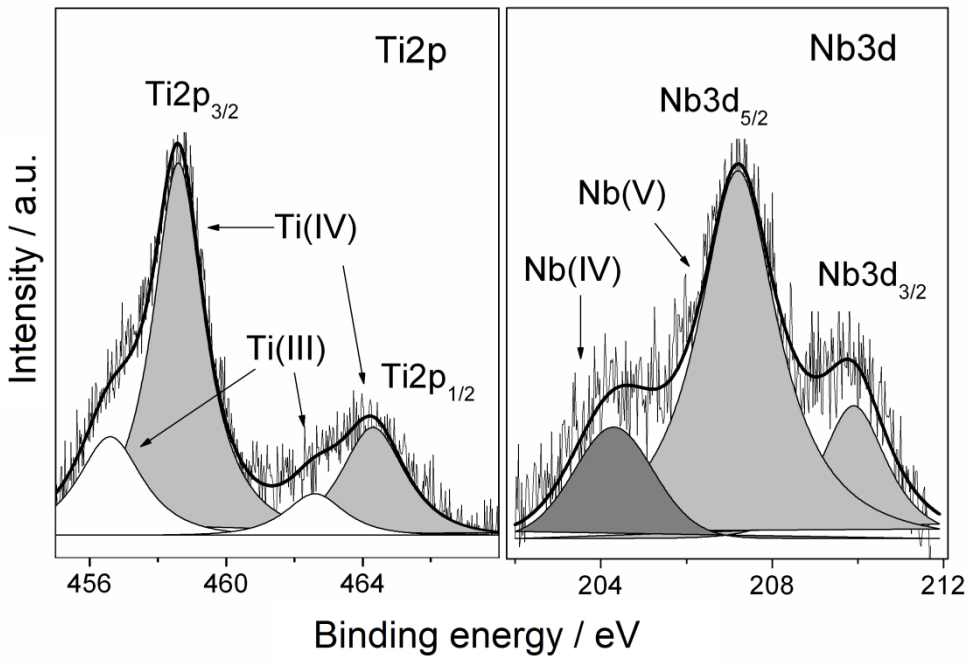

Figure 6-9: XPS spectra of as-prepared NP20 nanoparticles synthesized in *tert*-BuOH at 100 °C. The peaks were assigned according to refs.[26, 37, 38, 39]

In spite of the presence of Ti in the reduced state, the room temperature electrical *dc*-conductivity of the crystalline nanoparticles prepared at 100 °C is still quite low, *ca.* $1 \cdot 10^{-6}$ S cm^{-1} for undoped and $2 \cdot 10^{-5}$ S cm^{-1} for the 20 % doped nanoparticles, which is

comparable with the data reported by Huang *et al.*[9] for the pressed NTO nanoparticles prepared by hydrothermal synthesis. This could be due to a strong localization of the free electrons and their low mobility. To further improve the electrical conductivity, the as-produced NTO nanoparticles have to be heated in non-oxidizing atmosphere such as nitrogen at 400 – 600 °C (Figure 6-10). Heating in air leads to an irreversible loss of conductivity, which is also indicated by the change in the particle color to deep-blue or white after heating in N_2 or air, respectively. The change in conductivity with Nb content was found to be nonlinear. The introduction of Nb in the anatase lattice drastically increases the conductivity by several orders of magnitude, the highest conductivity being found for the 20 % Nb sample, for which the conductivity and the carrier concentration obtained from Hall effect measurements were 0.25 S cm^{-1} and 10^{20} cm^{-3}, respectively. A further increase in the Nb content does not lead to further improvement. The maximum conductivity was obtained for a much higher Nb concentration than for materials prepared by physical methods, for which the highest conductivity is observed already at 3 % of Nb.[40]

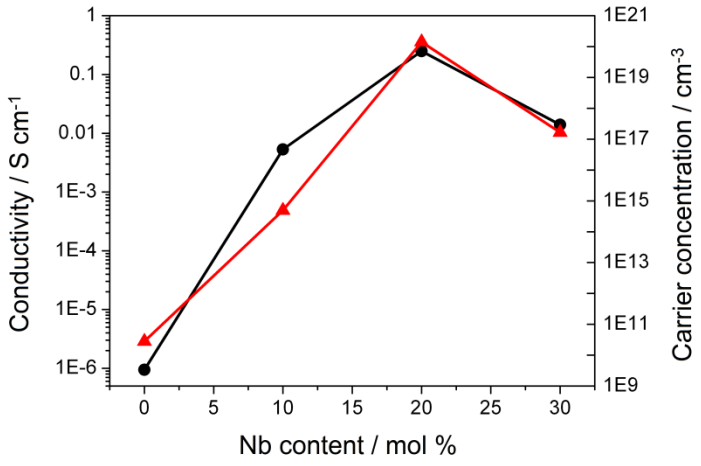

Figure 6-10: Specific conductivity (black, circles) and charge carrier concentration (red, triangles) of the pellets pressed from Nb-doped nanoparticles and heated at 600 °C in N_2, as a function of Nb content. The axes are shown in logarithmic scale.

XPS measurements at different depths from the particle surface performed after polishing the particles with argon ions reveal that the surface composition of the particles after heating in N_2 at 600 °C differs from that of the bulk. As the niobium content reaches 30.0 % at the surface and 19.8 % in the bulk, respectively, the particle surface is enriched with niobium. At the surface, both titanium and niobium are in their highest oxidization states (Figure 6-11). On the contrary, in the particle core a part of the titanium atoms is also present as Ti^{3+} cations, their fraction (16 %) being similar to the amount of Nb^{5+} cations introduced in the synthesis (about 20 %). This indicates that most of the extra electrons generated by Nb doping are released into the conduction band of TiO_2, leading to the formation of Ti^{3+} and resulting in the high conductivity.[8]

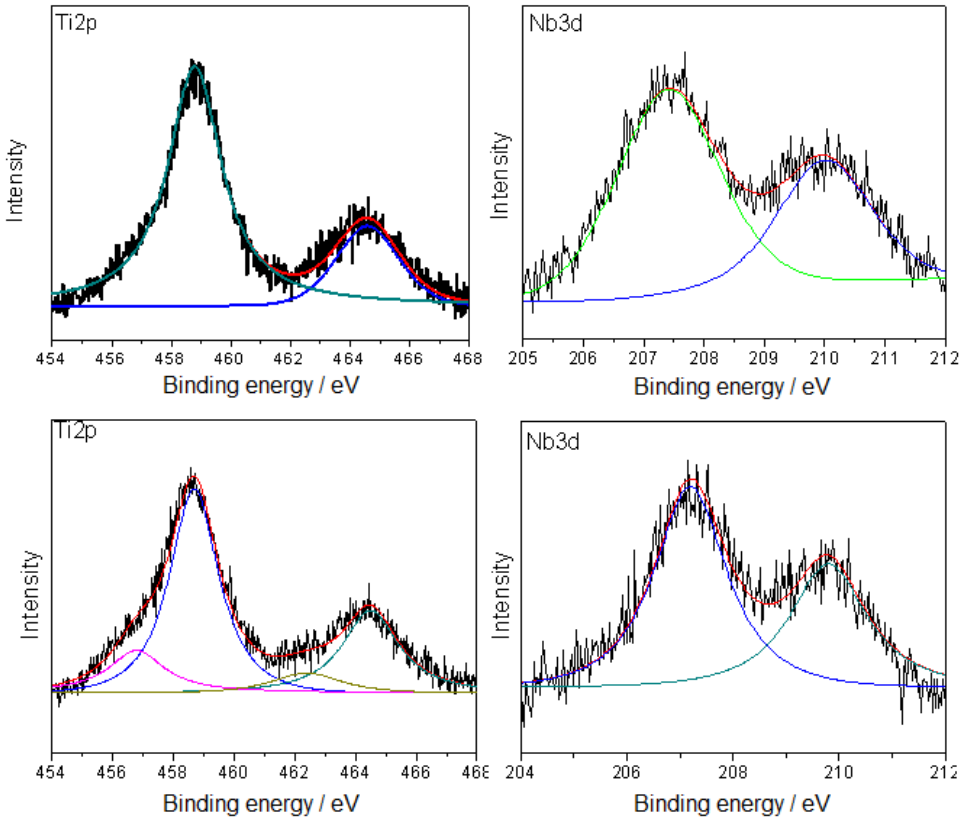

Figure 6-11: XPS of NTO particles prepared in *tert*-butyl alcohol at 60 °C and heated in N_2 at 600 °C after Ar^+ polishing for 5 min (first row) and for 30 min (second row). Argon polishing was performed at 1500 eV.

The electrical conductivity of mesoporous thin films assembled from different types of nanoparticles is much lower than that of the heated particles and shows much smaller variation with the Nb content. Thus, the conductivity of the doped MS20 films (10^{-4} S cm^{-1}) is only about two times larger than that of the pure titania film.

6.3 Discussion

The results above show that *tert*-butanol is a suitable reaction medium for the fabrication of crystalline monodispersed nanoparticles. The reaction in *tert*-butanol can be carried out both using microwave heating, as described in our previous publication,[34] and solvothermally at mild temperatures, leading to highly dispersible nanoparticles. The size of the particles and their degree of crystallinity can be controlled by reaction temperature and reaction time, thus enabling the preparation of particles 4 – 15 nm in size. Besides the pristine oxides, the solvothermal reaction in *tert*-butanol is suitable for the preparation of doped nanoparticles with homogeneously distributed dopant within the host lattice (before heat treatment, as the latter can lead to surface enrichment as was shown above by the XPS data) Following this synthesis route, the anatase lattice can incorporate more than 20 % of Nb ions. The incorporation of the guest impurities slows down the crystallization rate and leads to some expansion of the anatase lattice.

In contrast to the titania particles prepared by the well-established solvothermal synthesis in benzyl alcohol,[41] the particles of similar size and crystallinity synthesized in *tert*-butanol can be easily dispersed up to high concentrations in THF to form stable colloidal dispersions. This can be attributed to their different surface chemistry. The different surface properties of nanoparticles synthesized either in aromatic or aliphatic alcohols are the reason for their different ability to self-organize into periodic mesoscopic structures directed by the block

copolymers of the poly-alkylene oxide type. The particles prepared using *tert*-butanol assemble into regular mesostructures directed by the Pluronic templates, while those obtained using benzyl alcohol provide only disordered structures with these templates.[32] The films assembled from doped titania nanoparticles exhibit a higher degree of mesostructure ordering than those prepared from undoped ones, which may be due to the different surface properties of nanoparticles with varying Nb content. A similar behavior was observed for the ATO nanoparticle system.[2,33] Generally, the assembly of mesoporous films from particles has a beneficial effect on the porosity in comparison with sol-gel films, especially regarding the open nature of the porous system and as a result the better accessibility of the inner surface.[32] Doping with niobium leads to an enhancement of the mesostructure periodicity, the surface area and the pore volume.

The incorporation of Nb drastically increases the electrical conductivity of the nanoparticles. The maximum conductivity at room temperature of the 20 % Nb-doped sample, reaching 0.25 S cm^{-1}, is remarkably high for the wide band gap semiconductor titania. It supports the assumption that a considerable increase in the electrical conductivity of the anatase lattice is possible due to extrinsic doping with niobium ions. The only other study published to date on the chemical preparation of conducting Nb-doped titania nanoparticles by Huang *et al*[9] gives similar values of conductivity of as-produced nanoparticles and thus an additional support to the suitability of chemical routes for the preparation of conducting titania particles. Their conductivity is, however, still much lower than the range of 10^3 – 10^4 S cm^{-1} reported by Furubayashi *et al*[6,17,8] for epitaxially grown NTO films. It appears to be a general feature of the polycrystalline TCO systems prepared by chemical methods[1,33] that their DC conductivity is lower than the conductivity of analogous materials prepared by physical deposition techniques such as evaporation or magnetron sputtering. This difference is attributed

primarily to grain boundary scattering in the polycrystalline material and the larger amount of defects and imperfections in the nanosized crystals. Moreover, for the Nb-doped titania the situation is even more complicated due to the specific properties of this system. In contrast to the conventionally used indium or tin oxides, which can form solid solutions with various dopants causing only limited distortion of the host crystalline lattice,[4] incorporation of Nb into the anatase lattice can cause a noticeable lattice expansion or lattice deformation reported also by other authors,[39] which generally leads to the decreased electron mobility.[4] Moreover, donated electrons are susceptible to compensation by easily formed defects, such as Ti vacancies or oxygen interstitials.[26, 42]

Further improvement of the electrical conductivity requires an optimization of the reaction conditions. It appears that at least two factors are important for obtaining a niobium doped titania degenerate semiconductor. First, doped Nb atoms must be homogeneously distributed within the anatase lattice. Second, the formation of other defects except for the replacement of tetravalent Ti with pentavalent Nb should be avoided, as the extra electrons caused by Nb doping and existing in the form of Ti^{3+} and/or Nb^{4+} are easily compensated by titanium vacancies or oxygen interstitials. The conductivity of the as-prepared nanoparticles is rather low and can be substantially increased by a treatment at elevated temperatures in non-oxidizing atmosphere. The reasons that can contribute to the greatly enhanced conductivity of the pressed particle pellets after thermal treatment are particle growth, particle sintering and combustion of the organic residues acting as an insulator. However, such a treatment can lead to the undesired partial surface segregation of Nb due to a “self-purification” process described for NTO as well as for other doped oxides due to the size mismatch of the metal cations.[26, 43, 44]

The mesoporous layers assembled from the Nb-doped titania nanoparticles show very good structural properties such as the periodicity of the porous system, a uniform pore size, a high pore volume, a large surface area and crystallinity of the walls. However, the increase in conductivity due to Nb doping is much less pronounced for the mesoporous films than for the similarly treated particles. We tentatively attribute this (i) to the much smaller size of the crystals in the walls of the mesoporous films compared to that of the pressed pellets after heating (7 nm and 22 nm, respectively) due to the confining effect of the template, and (ii) the oxidation of a surface layer by adsorbed oxygen molecules upon exposure to air due to the high surface area of the films.

Now that the concept has been proven to be successful for making periodic porous conducting architectures on the basis of Nb-doped titania, future efforts should be aimed at the improvement of the conductivity of the mesoporous films. One of the ways to increase the conductivity can be the use of bigger crystals for the mesostructure assembly, which would require larger amphiphilic polymers.[45] Further optimization of non-oxidizing processing methods for particle sintering is also necessary. In this respect, a "brick and mortar" approach which has been used successfully for the preparation of highly crystalline mesoporous titania films[32] could be one of the possibilities to sinter the crystals at lower temperatures and thus to minimize the surface segregation.

6.4 Conclusions

The solvothermal procedure developed in this study enables the preparation of crystalline doped and undoped non-agglomerated dispersible titania nanoparticles with a narrow particle size distribution and homogeneous incorporation of doping atoms within the host lattice. The particle size and crystallinity can be controlled by the reaction temperature and time.

Substitutional doping with niobium ions drastically increases the electrical conductivity of the titania particles. In contrast to the titania particles prepared by a solvothermal synthesis in benzyl alcohol, those of similar size and crystallinity synthesized in *tert*-butanol can be easily dispersed at high concentrations in THF to form stable colloidal dispersions, which can be attributed to different surface chemistry. The Nb-doped titania nanoparticles can be assembled into regular three-dimensional mesoporous structures with a narrow pore size distribution and high surface area.

6.5 Experimental

All chemicals were purchased from Sigma-Aldrich and used as received. *tert*-Butanol and benzyl alcohol were dried over 4 Å molecular sieve at 28 °C and filtered prior to use. Pluronic F127 ($EO_{106}PO_{70}EO_{106}$, where EO is ethylene oxide, PO is propylene oxide) was purchased from Sigma-Aldrich.

For the synthesis of niobium-doped titania nanoparticles with different Nb contents, $TiCl_4$ and $Nb(OEt)_5$ were added to *tert*-butanol (12 mL, 1.8 mmol) under continuous stirring. The particles with different Nb content are designated as NPX, where X is the Nb/(Nb+Ti) molar ratio in per cent. As an example for the preparation of NP20 nanoparticles, 0.16 ml (1.44 mmol) of $TiCl_4$ and 0.09 ml (0.36 mol) of $Nb(OEt)_5$ were used. The clear solution was kept at 100 °C in a laboratory oven in a Teflon-sealed autoclave. The reaction time was 1.5 h, 3 h and 4 h for NP0, NP10 and NP20 nanoparticles, respectively. The resulting nanoparticles were separated by centrifugation at 50000 rcf for 15 minutes. The particles separated this way contain 25 – 50 % of organic residues as determined by thermogravimetric analysis (Netzsch STA 440 C TG/DSC).

For the fabrication of mesostructured films, a solution of Pluronic F127 (0.07 g, 0.006 mmol) in THF (2 mL) was added to 0.2 g of non-washed particles previously separated by centrifugation (metal oxide content was 1.75 mmol as determined by TGA analysis), and stirred until the particles were homogeneously redispersed. Concentrated HCl (0.2 ml) was added to obtain a clear transparent solution. The mesoporous films were fabricated by dip coating of prepared solutions on various substrates (Si wafer, glass) at a relative humidity of 50 % – 60 % and 25 °C. The films were heated in air at 300 °C for 2 hours and/or in N_2 at 500 °C for 2 hours, with a ramp speed of 0.5 °C min^{-1} for each heating step. The average thickness of the films after heating is around 200 nm.

Wide angle X-ray diffraction analysis was carried out in reflection mode using a Bruker D8 Discover diffractometer with Ni-filtered CuK_α-radiation (λ = 1.5406 Å), and equipped with a Vantec-1 position-sensitive detector. The crystal lattice d spacing and particle size calculation were based on the Bragg equation and Scherrer equation. The dispersion behavior of nanoparticles was studied by dynamic light scattering using a Malvern Zetasizer-Nano equipped with a 4 mW He-Ne laser (633 nm) and an avalanche photodiode detector.

High Resolution Transmission Electron Microscopy (HRTEM) was performed using a FEI Titan 80-300 instrument equipped with a field emission gun operated at 300 kV. The particulate samples were prepared by evaporating a drop of a diluted suspension of particles in THF on a Plano holey carbon coated copper grid. HRTEM of films was carried out by removing the thin-film samples from the substrate and transferring them onto a holey carbon coated copper grid. Scanning electron microscopy (SEM) was performed on a JEOL JSM-6500F scanning electron microscope equipped with a field emission gun, at 4 kV.

Small angle X-ray diffraction was carried out using a Scintag XDS 2000 diffractometer (Scintag Inc.), with a Ni-filtered Cu K_α-radiation (λ = 1.5406 Å) with theta/theta geometry and a scintillation detector operated at 40 kV and 30 mA. The textural properties of mesostructured films were analyzed with Kr adsorption/desorption measurements at 77 K using an ASAP 2010 apparatus (Micromeritics).

Electrical conductivity measurements on NTO nanoparticles were performed on pellets prepared by pressing finely ground nanoparticles under a pressure of 10 tons cm^{-2}. To further improve conductivity, thermal treatment under a nitrogen atmosphere was performed at 600 °C for 2 hours, with the ramp of 5 °C min^{-1}. The Hall mobility, charge carrier density and conductivity were measured by the Hall method (ECOPIA HMS 3000) using a magnetic field of 0.55 T.

X-ray photoelectron spectroscopy (XPS) analysis of the particles on a silicon substrate was performed using a VSW HA 100 electron analyzer and the K_α radiation provided by a non monochromatized magnesium anode system (Mg K_α = 1253.6 eV). Ar ion polishing was done at 1500 eV. The recorded elemental peaks were fitted by Gaussian-Lorentzian profiles and the elemental ratios were calculated by the equation $\frac{X_A}{X_B} = \frac{I_A / S_A}{I_B / S_B}$, where I_A/I_B is the ratio of fitted areas, and S is the sensitivity factor.[38]

6.6 References

(1) Fattakhova-Rohfing, D.; Brezesinski, T.; Rathousky, J.; Feldhoff, A.; Oekermann, T.; Wark, M.; Smarsly, B. *Adv. Mater.* **2006**, *18*, 2980 – 2983.

(2) Muller, V.; Rasp, M.; Stefanic, G.; Ba, J. H.; Gunther, S.; Rathousky, J.; Niederberger, M.; Fattakhova-Rohlfing, D. *Chem. Mater.* **2009**, *21*, 5229 – 5236.

(3) Hou, K.; Puzzo, D.; Helander, M. G.; Lo, S. S.; Bonifacio, L. D.; Wang, W. D.; Lu, Z. H.; Scholes, G. D.; Ozin, G. A. *Adv. Mater.* **2009**, *21*, 2492 – 2496.

(4) Chopra, K. L.; Major, S.; Pandya, D. K. *Thin Solid Films* **1983**, *102*, 1 – 46.

(5) Wang, Y. D.; Brezesinski, T.; Antonietti, M.; Smarsly, B. *ACS Nano* **2009**, *3*, 1373 – 1378.

(6) Furubayashi, Y.; Hitosugi, T.; Yamamoto, Y.; Inaba, K.; Kinoda, G.; Hirose, Y.; Shimada, T.; Hasegawa, T. A. *Appl. Phys. Lett.* **2005**, *86*, 252101 – 3.

(7) Emeline, A. V.; Furubayashi, Y.; Zhang, X. T.; Jin, M.; Murakami, T.; Fujishima, A. *J. Phys. Chem. B* **2005**, *109*, 24441 – 24444.

(8) Hitosugi, T.; Kamisaka, H.; Yamashita, K.; Nogawa, H.; Furubayashi, Y.; Nakao, S.; Yamada, N.; Chikamatsu, A.; Kumigashira, H.; Oshima, M.; Hirose, Y.; Shimada, T.; Hasegawa, T. *Appl. Phys. Expr.* **2008**, *1*, 111 – 203.

(9) Lu, X. J.; Mou, X. L.; Wu, J. J.; Zhang, D. W.; Zhang, L. L.; Huang, F. Q.; Xu, F. F.; Huang, S. M. *Adv. Funct. Mater.* **2010**, *20*, 509 – 515.

(10) Dros, A. B.; Grosso, D.; Boissiere, C.; Soler-Lia, G.; Albouy, P. A.; Amenitsch, H.; Sanchez, C. *Micropor. Mesopor. Mater.* **2006**, *94*, 208 – 213.

(11) Hirano, M.; Matsushima, K. *J. Amer. Ceram. Soc.* **2006**, *89*, 110 – 117.

(12) Mattsson, A.; Leideborg, M.; Larsson, K.; Westin, G.; Osterlund, L. *J. Phys. Chem. B* **2006**, *110*, 1210 – 1220.

(13) Ruiz, A. M.; Dezanneau, G.; Arbiol, J.; Cornet, A.; Morante, J. R. *Chem. Mater.* **2004**, *16*, 862 – 871.

(14) Hasin, P.; Alpuche-Aviles, M. A.; Li, Y.; Wu, Y. *J. Phys. Chem. C* **2009**, *113*, 7456 – 7460.

(15) De Koninck, M.; Manseau, P.; Marsan, B. *J. Electroanal. Chem.* **2007**, *611*, 67 – 79.

(16) Furubayashi, Y.; Hitosugi, T.; Yamamoto, Y.; Hirose, Y.; Kinoda, G.; Inaba, K.; Shimada, T.; Hasegawa, T. *Thin Solid Films* **2006**, *496*, 157 – 159.

(17) Furubayashi, Y.; Yamada, N.; Hirose, Y.; Yamamoto, Y.; Otani, M.; Hitosugi, T.; Shimada, T.; Hasegawa, T. *J. Appl. Phys.* **2007**, *101*, 212106 – 212108.

(18) Haosugi, T.; Ueda, A.; Nakao, S.; Yamada, N.; Furubayashi, Y.; Hirose, Y.; Konuma, S.; Shimada, T.; Hasegawa, T. *Thin Solid Films* **2008**, *516*, 5750 - 5753.

(19) Hitosugi, T.; Ueda, A.; Furubayashi, Y.; Hirose, Y.; Konuma, S.; Shimada, T.; Hasegawa, T. *Japan. J. Appl. Phys. 2* **2007**, *46*, L86 – L88.

(20) Hitosugi, T.; Ueda, A.; Nakao, S.; Yamada, N.; Furubayashi, Y.; Hirose, Y.; Shimada, T.; Hasegawa, T. *Appl. Phys. Lett.* **2007**, *90*, 212106.

(21) Neumann, B.; Bierau, F.; Johnson, B.; Kaufmann, C. A.; Ellmer, K.; Tributsch, H. *Phys. Stat. Solidi B* **2008**, *245*, 1849 – 1857.

(22) Yamada, N.; Hitosugi, T.; Hoang, N. L. H.; Furubayashi, Y.; Hirose, Y.; Konuma, S.; Shimada, T.; Hasegawa, T. *Thin Solid Films* **2008**, *516*, 5754 – 5757.

(23) Zhang, S. X.; Kundaliya, D. C.; Yu, W.; Dhar, S.; Young, S. Y.; Salamanca-Riba, L. G.; Ogale, S. B.; Vispute, R. D.; Venkatesan, T. *J. Appl. Phys.* **2007**, *102*, 013701.

(24) Zhang, S. X.; Dhar, S.; Yu, W.; Xu, H.; Ogale, S. B.; Venkatesan, T. *Appl. Phys. Lett.* **2007**, *91*, 112113.

(25) Noh, J. H.; Lee, S.; Kim, J. Y.; Lee, J. K.; Han, H. S.; Cho, C. M.; Cho, I. S.; Jung, H. S.; Hong, K. S. *J. Phys. Chem. C* **2009**, *113*, 1083 – 1087.

(26) Morris, D.; Dou, Y.; Rebane, J.; Mitchell, C. E. J.; Egdell, R. G.; Law, D. S. L.; Vittadini, A.; Casarin, M. *Phys. Rev. B* **2000**, *61*, 13445 – 13457.

(27) Sheppard, L.; Bak, T.; Nowotny, J.; Sorrell, C. C.; Kumar, S.; Gerson, A. R.; Barnes, M. C.; Ball, C. *Thin Solid Films* **2006**, *510*, 119 – 124.

(28) Sheppard, L. R.; Bak, T.; Nowotny, J. *J. Phys. Chem. B* **2006**, *110*, 22447 – 22454.

(29) Sheppard, L. R.; Bak, T.; Nowotny, J. *J. Phys. Chem. B* **2006**, *110*, 22455 – 22461.

(30) Grosso, D.; Soler-Illia, G.; Babonneau, F.; Sanchez, C.; Albouy, P. A.; Brunet-Bruneau, A.; Balkenende, A. R. *Adv. Mater.* **2001**, *13*, 1085 – 1090.

(31) Hwang, Y. K.; Lee, K. C.; Kwon, Y. U. *Chem. Comm.* **2001**, 1738 – 1739.

(32) Szeifert, J. M.; Fattakhova-Rohlfing, D.; Georgiadou, D.; Kalousek, V.; Rathousky, J.; Kuang, D.; Wenger, S.; Zakeeruddin, S. M.; Gratzel, M.; Bein, T. *Chem. Mater.* **2009**, *21*, 1260 – 1265.

(33) Müller, V.; Rasp, M.; Rathouský, J.; Schütz, B.; Niederberger, M.; Fattakhova-Rohlfing, D. *Small* **2010**, *6*, 633 – 637.

(34) Szeifert, J. M.; Feckl, J. M.; Fattakhova-Rohlfing, D.; Liu, Y.; Kalousek, V.; Rathousky, J.; Bein, T. *J. Am. Chem. Soc.*, **2010**, *132* (36), 12605 – 12611.

(35) Arbiol, J.; Cerda, J.; Dezanneau, G.; Cirera, A.; Peiro, F.; Cornet, A.; Morante, J. R. *J. Appl. Phys.* **2002**, *92*, 853 – 861.

(36) Di Valentin, C.; Pacchioni, G.; Selloni, A. *J. Phys. Chem. C* **2009**, *113*, 20543 – 20552.

(37) Atashbar, M. Z.; Sun, H. T.; Gong, B.; Wlodarski, W.; Lamb, R. *Thin Solid Films* **1998**, *326*, 238 – 244.

(38) Dacca, A.; Gemme, G.; Mattera, L.; Parodi, R. *Appl. Surf. Sci.* **1998**, *126*, 219 – 230.

(39) Kubacka, A.; Colon, G.; Fernandez-Garcia, M. *Catal. Today* **2009**, *143*, 286 – 292.

(40) Hitosugi, T.; Kinoda, G.; Yamamoto, Y.; Furubayashi, Y.; Inaba, K.; Hirose, Y.; Nakajima, K.; Chikyow, T.; Shimada, T.; Hasegawa, T. *J. Appl. Phys.* **2006**, *99*, 08M121.

(41) Niederberger, M. *Acc. Chem. Res.* **2007**, *40*, 793 – 800.

(42) Zunger, A. *Appl. Phys. Letters* **2003**, *83*, 57 – 59.

(43) Norris, D. J.; Efros, A. L.; Erwin, S. C. *Science* **2008**, *319*, 1776 – 1779.

(44) Mikulec, F. V.; Kuno, M.; Bennati, M.; Hall, D. A.; Griffin, R. G.; Bawendi, M. G. *J. Amer. Chem. Soc.* **2000**, *122*, 2532 – 2540.

(45) Grosso, D.; Boissiere, C.; Smarsly, B.; Brezesinski, T.; Pinna, N.; Albouy, P. A.; Amenitsch, H.; Antonietti, M.; Sanchez, C. *Nat. Mater.* **2004**, *3*, 787 – 792.

7 Nanoscale porous framework of lithium titanate for ultrafast lithium insertion

This chapter is based on the following publication:

Nanoscale porous framework of lithium titanate for ultrafast lithium insertion, Feckl, J. M., Fominykh, K., Döblinger, M., Fattakhova-Rohlfing, D. & Bein, T., Angew. Chemie, **2012**, *51*, 7459.

7.1 Introduction

The rapidly growing demand for electric vehicles and mobile electronics urgently requires the development of electrochemical energy storage systems with both high energy density and high power.[1]. Supercapacitors[2] can deliver very high powers, but their attainable energy densities are far lower than those of batteries.[3] "Closing the gap" between the two main technologies requires the development of materials that can incorporate or liberate a large amount of charge in a very short time. Here we report the synthesis of fully crystalline interconnected porous frameworks composed of ultrasmall lithium titanate spinel nanocrystals of a few nm in size. These frameworks feature a gravimetric capacity of about 175 mAh g^{-1} at rates of 1 – 50 C (0.17 – 8.7 A g^{-1}) and can deliver up to 73 % of their maximum capacity at unprecedented high rates of up to 800 C or 140 A g^{-1} (corresponding to only 4.5 sec of charge/discharge) without deterioration up to a thousand cycles. This is the fastest ever-reported titanate morphology for lithium insertion.

A key to this performance is the design of a fully crystalline interconnected porous framework composed of ultrasmall spinel nanocrystals of a few nm in size. The assembly of nanoscale

building blocks into interconnected porous frameworks is a promising strategy to maximize the rate performance and to enhance the power density, and is also possible for materials not accessible by electrodeposition. Nanoscaling greatly increases the interface leading to enhanced charge transfer, and drastically shortens the ion/electron diffusion pathways by decreasing the grain size of the bulk material.[1b, 4-5] Lithium titanate $Li_4Ti_5O_{12}$ (LTO) is widely used as an active material in commercial lithium ion batteries and hybrid electrochemical storage devices[6] due to its suitable potential, relatively high capacity and robustness. Although the lithium insertion rate in bulk LTO is intrinsically low due to its low conductivity, recent reports have demonstrated that it can be substantially increased by decreasing the crystal size to the nanometer scale,[6-7] and several approaches were developed to obtain nanoscaled material. The reported strategies include flash annealing[6] or solid-state reactions of nanosized titania,[7a] which however lead to relatively large crystals of over 30 nm. Lithium titanate with much smaller crystalline domains and enhanced insertion rates can be obtained by solvothermal[7b] and sol-gel reactions.[7c-f, 7i, 8] However, the power density and especially the cycling stability still need to be improved. High rate capability in combination with excellent cycling stability was achieved for hybrid materials composed of a few nanometer-sized crystals anchored on a conducting carbon matrix, although at the expense of significantly decreased gravimetric and volumetric capacities due to a high content of the conducting support.[9-10] A non-supported nanosized and fully crystalline LTO with extremely high insertion/extraction rates and high cycling stability was not reported yet.

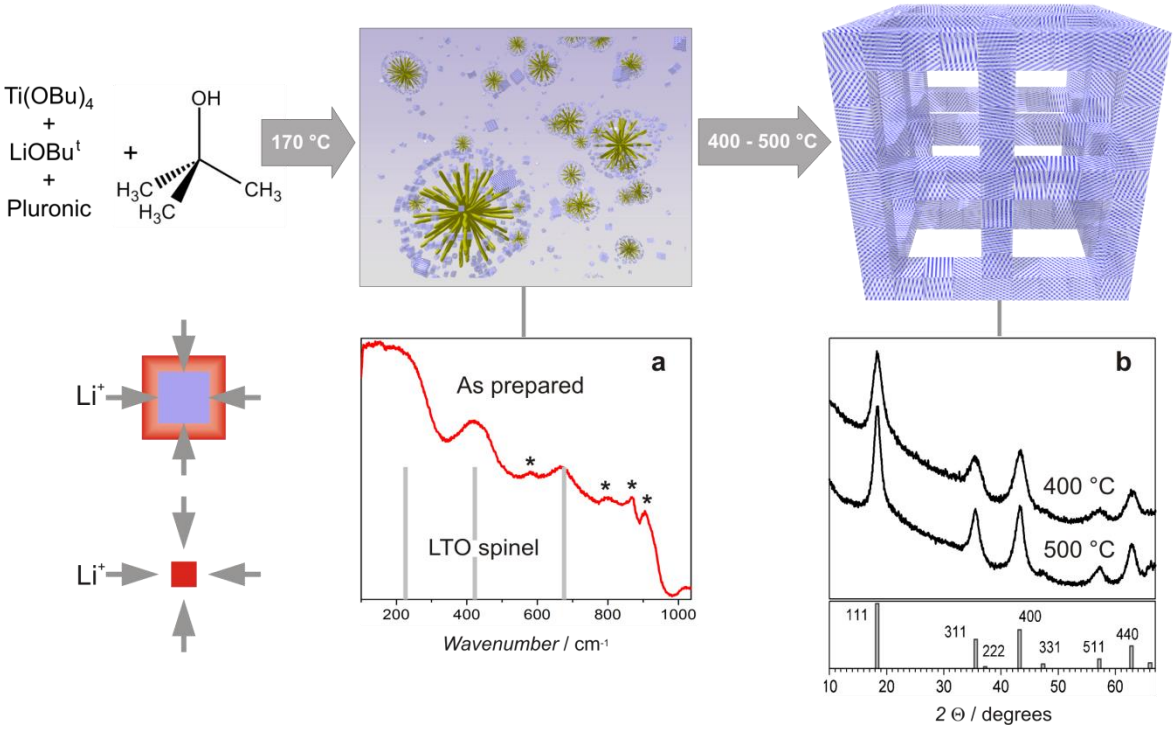

Figure 7-1: Formation of the lithium titanate LTO via solvothermal reaction in *tert*-butanol: a**, Raman spectrum of the as-prepared material demonstrating formation of the spinel nuclei after solvothermal reaction (the grey bars mark the Raman bands of crystalline $Li_4Ti_5O_{12}$, the remaining bands are associated with the Pluronic polymer), and** b**, powder XRD patterns of the LTO obtained after thermal treatment of as-prepared material at 400 °C and 500 °C and the JCPSD card 26-1198 for the $Li_4Ti_5O_{12}$ spinel. A scheme (bottom left) illustrates the depth of Li diffusion (red) into large (top) and small (bottom) crystals.**

7.2 Results and Discussion

To create ultrasmall building blocks for a porous spinel framework, we have developed a solvothermal reaction in *tert*-butanol in the absence of water for the LTO synthesis. We have recently shown that *tert*-butanol is an excellent reaction medium for the synthesis of ultrasmall undoped and Nb-doped anatase titania crystals.[5c, 11] In a reaction of appropriate molecular metal oxide precursors (see below) with *tert*-butanol, the spinel nuclei are formed already at a low reaction temperature of 170 °C. Although the materials obtained at this temperature appear X-ray amorphous, the formation of nuclei with the spinel symmetry can be detected by Raman spectroscopy (Figure 7-1a). The formed nuclei are subsequently crystallized in a controlled way by a thermal treatment of the dried reaction mixture at 400 –

500 °C (the material appears X-ray amorphous at lower temperatures). Screening of different precursor combinations demonstrates that a similar reactivity of the precursors in the solvothermal reaction is required for the formation of a pure spinel phase (Figure 7-2). The choice of $LiOBu^t$ and $Ti(OBu)_4$ as the metal sources, and the presence of amphiphilic Pluronic polymer (P123) in the reaction mixture were found to be essential for the formation of the phase-pure porous spinel framework. Moreover, considering that the single-phase LTO is formed only when the polymer is added (Figure 7-2) we can propose that it also influences the crystallization process, possibly due to its coordination to metal precursors and modulating their reactivity.

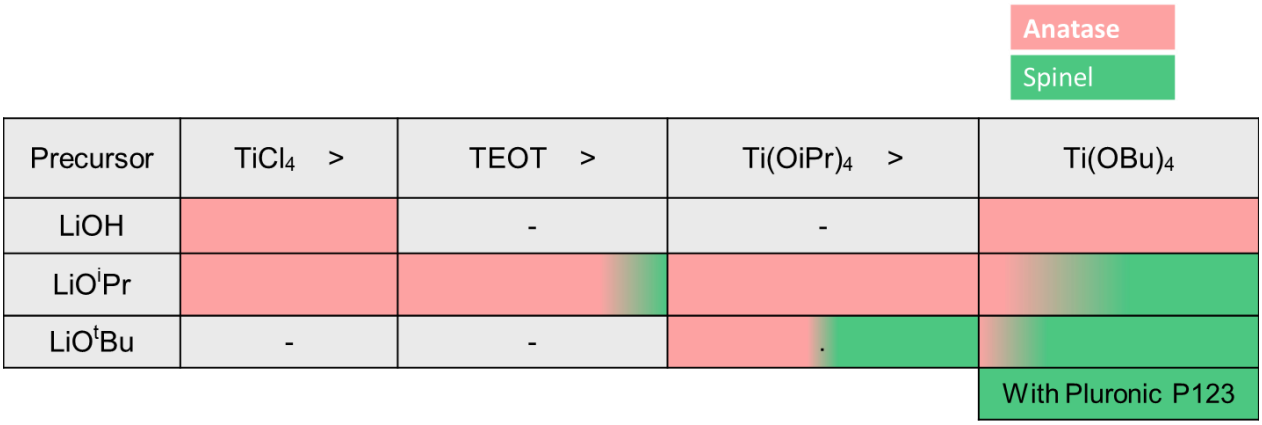

Figure 7-2: Screening of different precursor combinations in a solvothermal reaction in *tert*-butanol. The color bars represent the fraction of the titanate phases (approximately estimated from the powder XRD measurements) formed after heating of the reaction products at 400 °C. The titanium(IV) precursors are ordered with respect to their reactivity in hydrolysis reactions.

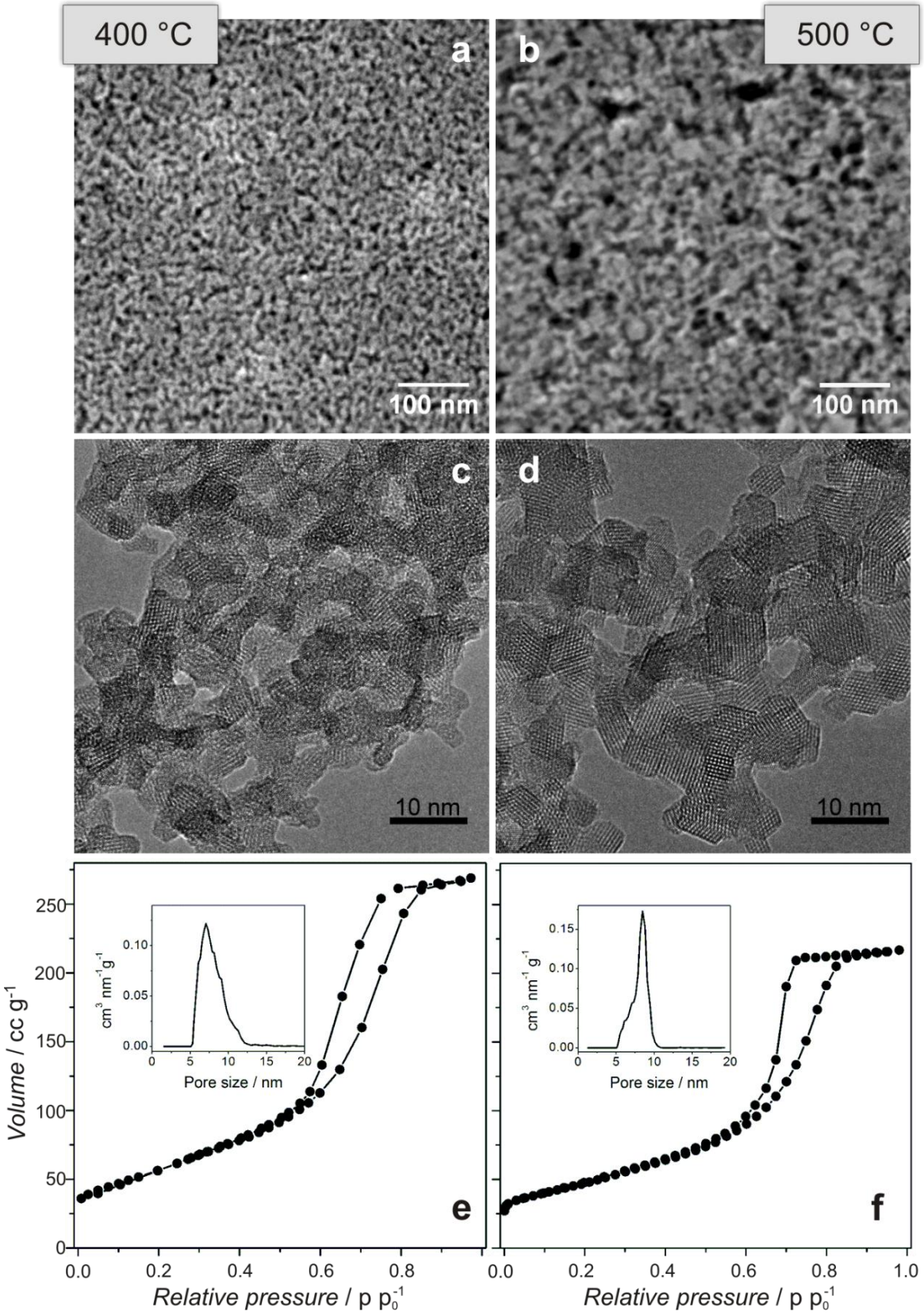

Figure 7-3: Morphology and crystallinity of nanosized spinel lithium titanate heated at 400 °C (a, c, e) and 500 °C (b, d, f): First row, SEM top view of the films on the FTO substrate; second row, HR-TEM images; third row, nitrogen sorption isotherms with pore size distribution.

Heating the reaction mixture in air at 400 °C leads to the formation of a highly porous single-phase $Li_4Ti_5O_{12}$ spinel framework (named nano-LTO-400) with a very small size of the crystalline domains (3 – 4 nm), as derived from the peak broadening in the XRD patterns (Figure 7-1b) and from transmission electron microscopy (Figure 7-3c). The heating time at this temperature does not markedly influence the crystallinity, as we did not observe any significant differences in the crystallinity of the material heated at 4 h and 12 h, respectively. Heating at 500 °C for 10 min (reached with a 2 h ramp) leads to material (named nano-LTO-500) with slightly larger crystalline domains between 4 nm and 7 nm in diameter, but the highly porous character of the LTO framework remains preserved (Figure 7-1b and Figure 7-3b,d). Electron microscopy confirms that the materials obtained at both temperatures are homogenous and that, in spite of the very small size of the crystals, the samples appear to be fully crystalline, being composed of spinel nanocrystals interconnected into a porous scaffold (Figure 7-3, SEM and TEM). Furthermore, gas adsorption studies show that the LTO samples obtained at 400 °C and at 500 °C feature highly porous morphologies with high surface areas of 205 $m^2 g^{-1}$ and 170 $m^2 g^{-1}$ and a uniform pore size of 7 nm and 8 nm (Figure 7-3), respectively. The latter correspond to the pores usually formed by Pluronic P123. Heating the as-prepared reaction mixture at 600 °C results in the formation of larger spinel crystals (around 35 – 55 nm) in addition to smaller crystals of 15 ± 5 nm in size, and in the formation of some fraction of larger TiO_2 anatase crystals (even for annealing times as short as 10 min, Figure 7-4). The crystal growth at 600 °C is accompanied by the collapse of porosity and a decrease of surface area to 25 $m^2 g^{-1}$. These findings show that heating at 400 – 500 °C constitutes the optimum thermal treatment conditions for the nanoscale spinel materials using the above reaction protocol.

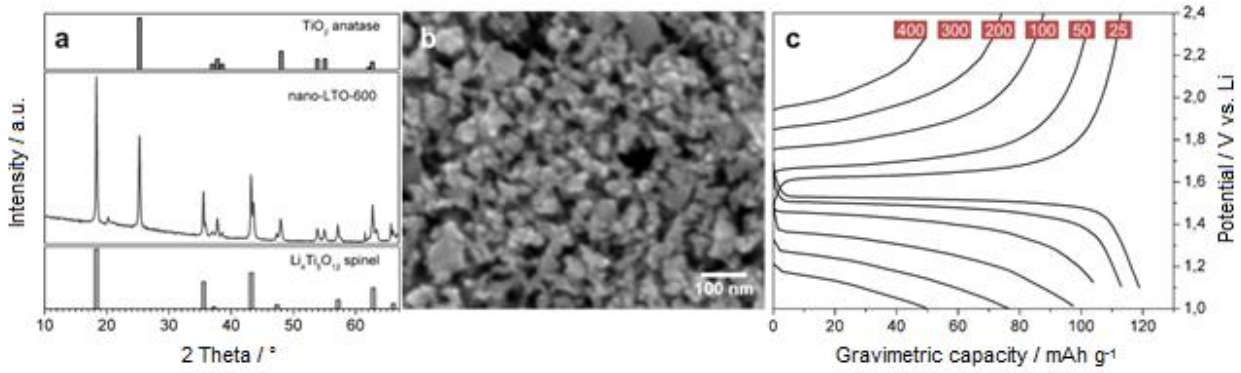

Figure 7-4: Morphology, crystallinity and the electrochemical performance of the nano-LTO-600 spinel heated at 600 °C: (a), powder XRD pattern of the LTO obtained after thermal treatment of as-prepared material at 600 °C and the JCPSD cards 26-1198 for the $Li_4Ti_5O_{12}$ spinel and 21-1272 for TiO_2 anatase; (b), SEM top view of the film on the FTO substrate, and (c), galvanostatic charge/discharge curves shown at different rates (corresponding to X C, with X shown in the corresponding labels).

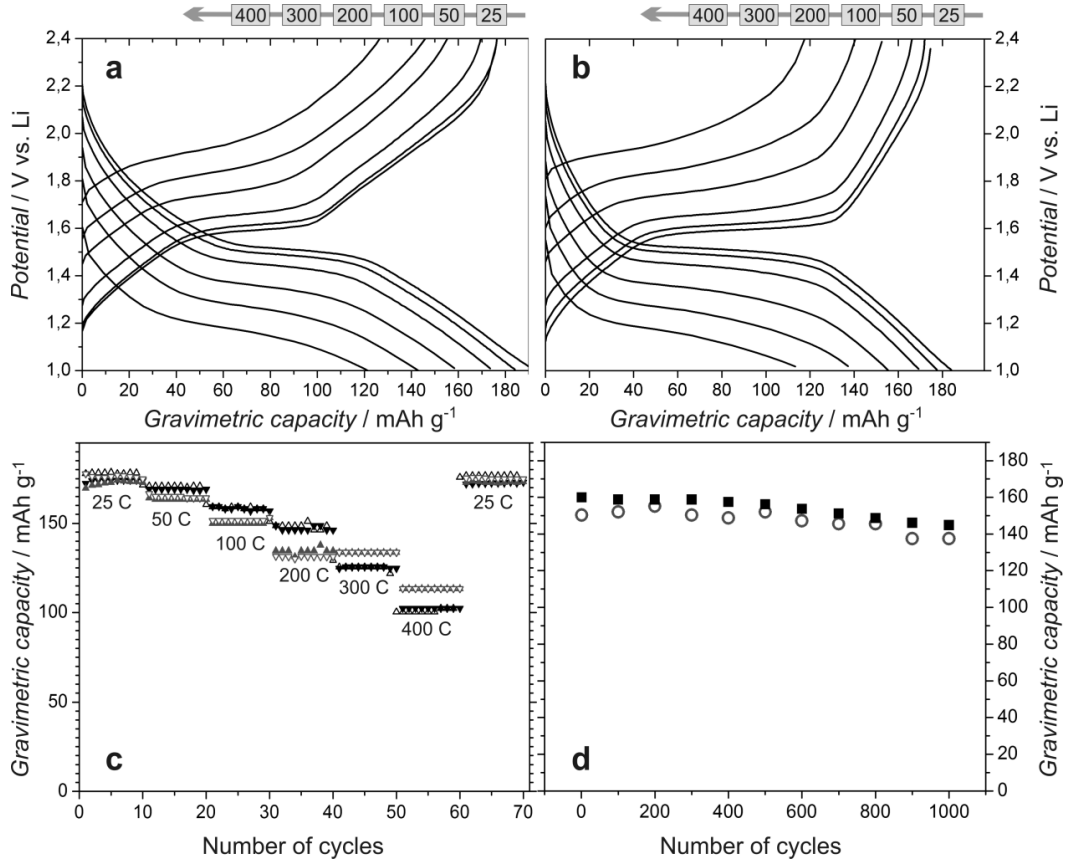

Figure 7-5: Electrochemical Li insertion/extraction with LTO spinel heated at 400 °C (a) and at 500 °C (b); galvanostatic charge/discharge shown at different rates (corresponding to X C, with X shown in the corresponding label). (c) Multicycling stability at different rates (ten cycles each are shown), (d) multicycling stability at the rate 100 C (the capacity corresponds to the extraction process). The grey and black symbols correspond to the nano-LTO-400 and nano-LTO-500 spinel, respectively. The open and the filled symbols correspond to charge and discharge cycles, respectively. The cut-off potentials were 1.0 V and 2.4 V vs. Li. The thickness of the films is about 0.5 µm (corresponding to a loading of about 0.14 mg cm^{-2}).

Coating of the synthesis solutions on conducting substrates followed by heating in air at temperatures beyond 400 °C leads to the formation of homogeneous films, whose thickness can be varied from 150 to 500 nm. The thickest films heated at 400 °C (nano-LTO-400) show a reversible electrochemical Li uptake of 176 mAh g^{-1}, which is practically equal to the theoretical insertion capacity for $Li_4Ti_5O_{12}$ spinel (Figure 7-5a; the capacitive contribution from the FTO substrate can be practically neglected, Figure 7-6). The maximum theoretical capacity was achieved already at a rate of 50 C or 8.6 A g^{-1} (meaning complete charging or discharging of the total storage capacity in 1/50 hour or 1.2 min), and 96 % of the maximum capacity were still achieved at the rate of 100 C or 17 A g^{-1} (36 sec). At the rate of 300 C, up to 82 % of the maximum capacity could still be obtained, and even at the very high rate of 400 C or 68 A g^{-1} (9 sec) about 72 % of the total capacity were still available (Figure 7-5a).

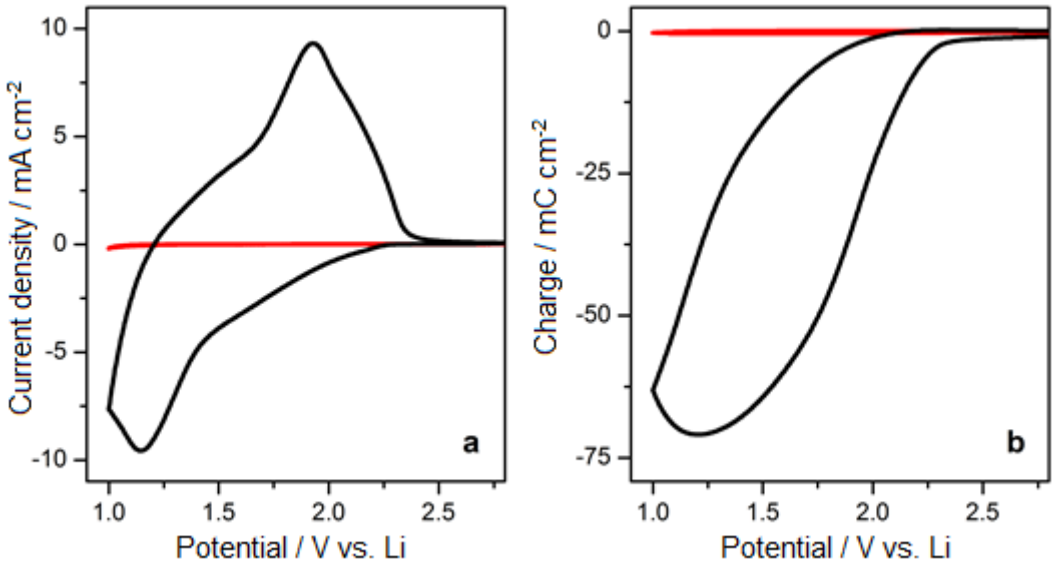

Figure 7-6: Cyclic voltammograms of the nano-LTO-400 spinel film on the FTO substrate (black) and the bare FTO substrate of the same area (red) taken at 100 mV s^{-1}: a, current - potential curves, b, charge - potential curves: The electrode was heated at 400 °C; the thickness of the film is about 0.5 µm (corresponding to a loading of about 0.14 mg cm^{-2}).

Even higher insertion/extraction rates can be achieved for the thinner films. The film of about 150 nm in thickness can be charged/discharged to 85 % of its full capacity at the rate of 400 C, and deliver up to 73 % of the theoretical capacity at the rate of 800 C or 136 A g^{-1} (4.5 sec) (Figure 7-7). We attribute this extremely high rate of insertion/extraction processes to the very small size of the crystalline domains and the very large electrode-electrolyte interface. The nanoscale morphology of the LTO spinel is also reflected in its potential profiles during charging (Li insertion) and discharging (Li extraction).

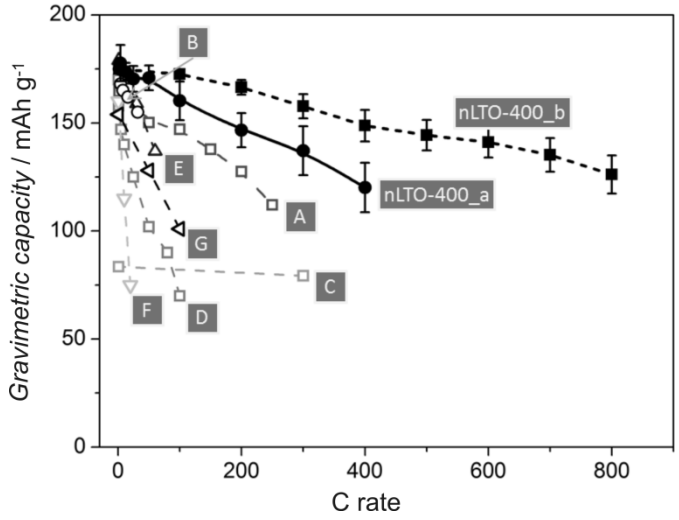

Figure 7-7: Rate capability of the nano-LTO-400 sample in comparison to fast LTO materials reported in the literature: mesoporous LTO A[7c] (grey open squares) and B[8] (black open circles), composite LTO – carbon nanofiber material C[7h] (grey open squares; the gravimetric capacity is calculated per total mass of the electrode material containing about 50 % carbon), LTO nanoparticles synthesized by the combustion method D[15] (grey open squares), LTO prepared by a solvothermal method E[7f] (black open triangles), surface-modified LTO nanoparticles F[7a] (grey open triangles), LTO/reduced graphite oxide nano-hybrid material G[10] (black open triangles). Samples nLTO-400_a and nLTO-400_b denote the films with thickness of about 500 nm and 150 nm, respectively.

Bulk $Li_4Ti_5O_{12}$ spinel exhibits an extended potential plateau due to a well-defined two-phase insertion mechanism.[12] In contrast, the nano-LTO-400 spinel shows curved voltage profiles with reduced length of the potential plateau region. This feature, which is characteristic for different nanosized materials, is usually attributed to a dominant role of surface-associated insertion processes in the very small crystals.[12b, 13] The latter involve a changed potential distribution in the near-surface area,[12b] as well as pseudocapacitive surface storage processes

which become very significant for large surface area materials. Analysis of cyclic voltammograms of the nano-LTO-400 spinel performed according to the procedure described by Conway *et al.*[14a] and Dunn *et al.*[14b] reveals that the pseudocapacitive storage contributes to about 55 – 60 % of the total charge, which can explain the unusually high rate performance of the nano-LTO electrodes (Figure 7-8).

The deconvolution of the pseudocapacitive and bulk diffusion-limited contributions to the total charge storage was performed by the analysis of cyclic voltammograms at different scan rates. The proposed method is based on the different character of current - scan rate dependence for the different mechanisms of the charge storage. The current in CVA can be generally described as $i(\upsilon) = a\upsilon^b$, where υ is the scan rate and *a* is the proportionality coefficient containing electrode surface area and concentration of the active material. The value of the parameter *b* depends on the kinetic limitations of the electrochemical process. The parameter *b*, which can be found from the slope of the plot of log I vs. log υ is equal to 1 for a surface-confined (pseudocapacitive) process and equal to 0.5 for a diffusion-controlled process (bulk solid state diffusion in case of insertion materials). Analysis of the current – scan rate dependencies enables determination of the type of dominating charge storage mechanism at any point of the insertion/extraction process. Assuming that both mechanisms contribute – to a different degree – to the total charge storage, the current at any given potential can be expressed as $i(\upsilon) = k_1\upsilon + k_2\upsilon^{1/2}$ for the pseudocapacitive and the insertion contributions, respectively, which enables quantitative determination of the different contributions. For the latter purpose, the expression for current is rearranged as $i(\upsilon)/\upsilon^{1/2} = k_1\upsilon^{1/2} + k_2$ and the normalized contributions of the pseudocapacitive (k_1) and the insertion (k_2) mechanisms are determined as the slope and the intercept, respectively, of the dependence of $i(\upsilon)/\upsilon^{1/2}$ on $\upsilon^{1/2}$ at the chosen potentials.

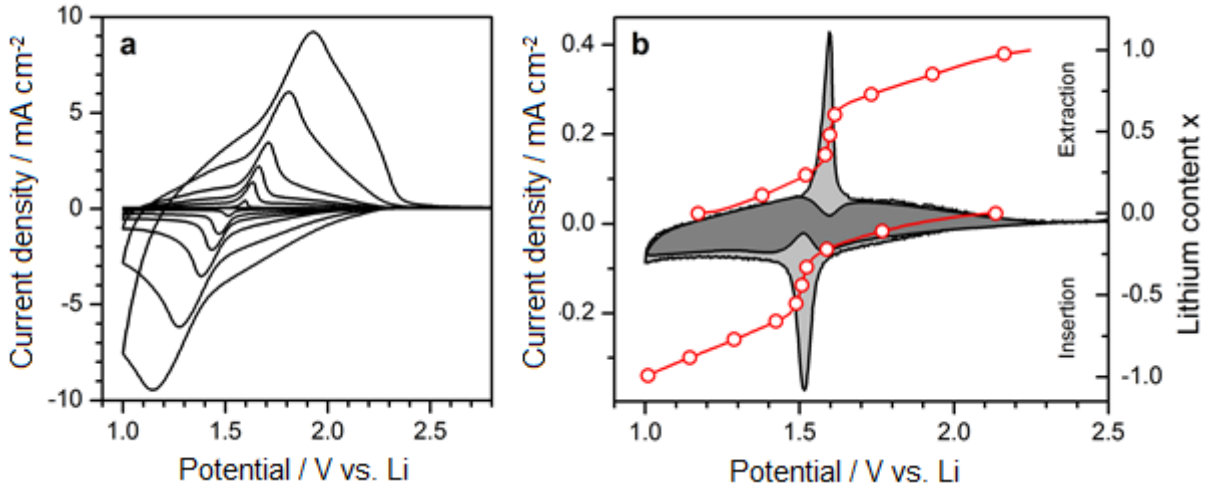

Figure 7-8: Electrochemical Li insertion/extraction with the nano-LTO-400 spinel heated at 400 °C: a, Cyclic voltammograms taken at the scan rates 1 mV s^{-1}, 2 mV s^{-1}, 5 mV s^{-1}, 10 mV s^{-1}, 20 mV s^{-1}, 50 mV s^{-1} and 100 mV s^{-1} (from bottom to top). b, Deconvolution of the pseudocapacitive (dark grey) and the bulk lithium insertion (light grey) contributions to the total lithium storage performed according to the procedure described by Conway *et al.* and Dunn *et al.* at different potentials (corrected for the potential shift for the higher scan rates). The cyclic voltammogram was taken at the scan rate 1 mV s^{-1}. The red curves correspond to the galvanostatic charge/discharge curves taken at the rate 25 C for the same electrode. The thickness of the film is about 0.5 µm (corresponding to a loading of about 0.14 mg cm^{-2}).

Another feature of the nanocrystallinity is the additional insertion process at low potentials, which was also observed for other nanoscale spinel materials.[12b] For the samples nano-LTO-400 and nano-LTO-500, this effect was observed for insertion rates below 25 C (4.3 A g^{-1}) at potentials below 1.2 V; this process is irreversible (Figure 7-9). At high insertion rates the insertion/extraction process in the nanosized spinel is perfectly reversible up to 1 V vs. Li, and the electrode can be charged/discharged several hundreds of cycles with only a minor capacity loss (the capacity retention is 98 % after 500 cycles and 89 % after 1000 cycles at the rate 100 °C, Figure 7-5c).

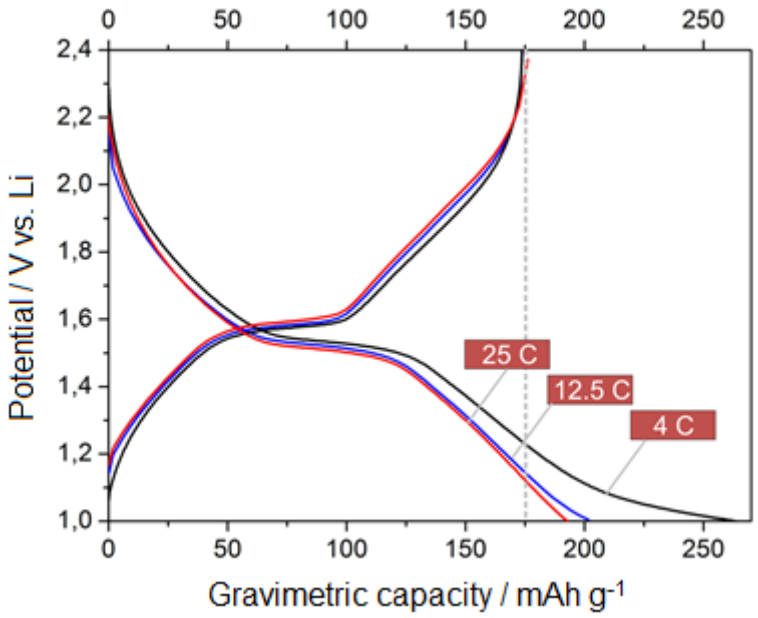

Figure 7-9: Galvanostatic charge/discharge curves of nano-LTO-400 spinel heated at 400 °C, taken at the rates of 25 C (4.3 A g^{-1}, red), 12.5 C (2.2 A g^{-1}, blue) and 4 C (0.7 A g^{-1}, black).

The lithium insertion behavior of the LTO annealed at 500 °C is similar to that of nano-LTO-400. Due to the slightly increased crystal size (about 6 nm compared to about 3 nm for nano-LTO-400) the insertion/extraction rate in nano-LTO-500 is slightly slower compared to nano-LTO-400 but still extremely fast, such that 66 % of the maximum insertion capacity is retained at the rate 400 C (68 A g^{-1}) and 80 % at the rate 300 C (51 A g^{-1}), respectively, for about 0.5 µm thick films. The lower surface area of the nano-LTO-500 material and the slightly larger crystal size are reflected in the increase of the plateau region (Figure 7-5b). The nano-LTO-500 spinel is also perfectly stable in multiple insertion/extraction processes (Figure 7-5c,d), the capacity retention being 98 and 91 % after 500 and 1000 cycles, respectively. We note that the high stability of these systems - even after 1000 cycles at 100 C (17 A g^{-1}) - is reflected in unchanged nano-morphology as illustrated by the electron micrographs in Figure 7-10. The advantages of the small crystal size for the lithium insertion rates are highlighted by comparing the electrochemical performance of the materials obtained after heating at 400 °C

and 500 °C to that heated at 600 °C. In the latter, the presence of larger crystals in addition to the smaller ones as well as the anatase impurity substantially decrease the insertion capacity already at low insertion rates to about 70 % of the theoretical, and results in slower insertion kinetics (Figure 7-4).

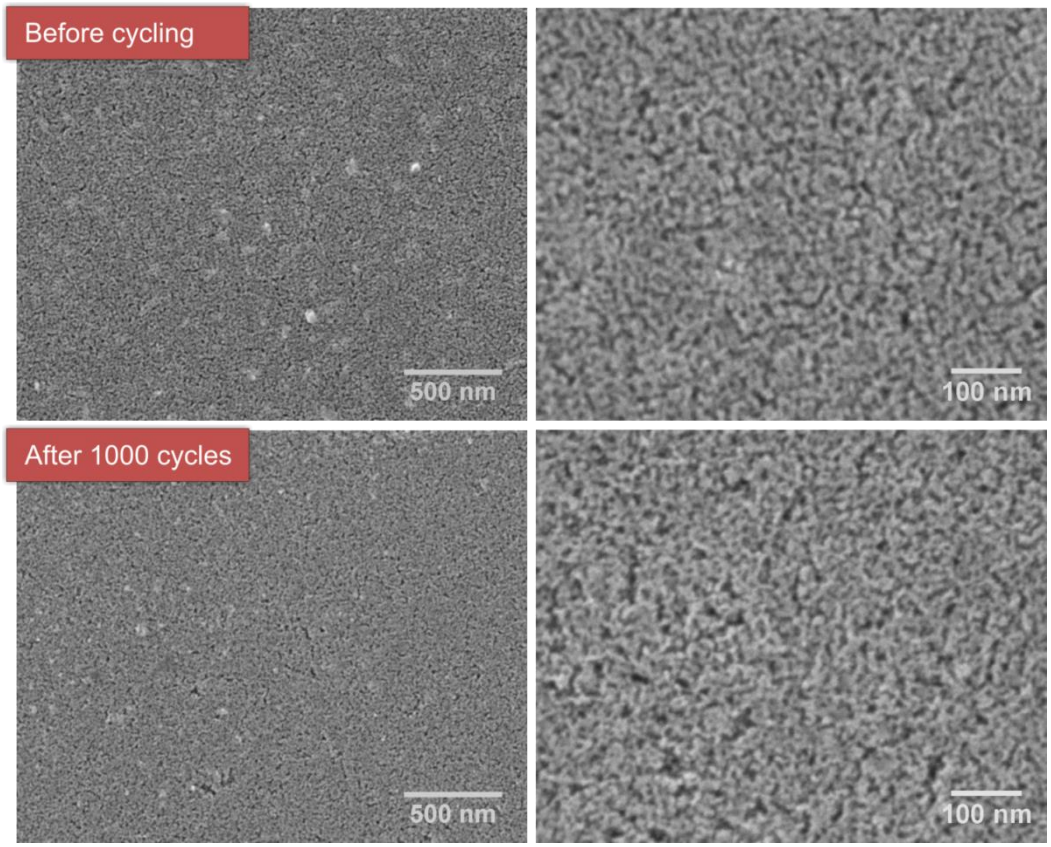

Figure 7-10: Stability of the mesoporous LTO framework in the multiple insertion/extraction experiments: scanning electron microscopy images at two different magnifications of the nano-LTO-400 layer on the FTO substrate before (first row) and after (second row) 1000 cycles at the rate 100 C in the potential range from 2.4 V to 1.1 V vs. Li.

To the best of our knowledge, the nano-LTO spinel obtained via our novel *tert*-butanol route is by far the fastest spinel lithium titanate morphology for lithium insertion reported to date. It compares favorably with the porous nanocrystalline LTO spinel obtained via sol-gel methods,[7c, 8] composed of crystals greater than 11 nm (Figure 7-7). Our nano-LTO spinel also has a much higher insertion rate than porous $Li_4Ti_5O_{12}$ obtained by solution-combustion synthesis[15] and carbon-coated nanocrystalline spinel,[7g] and a higher available gravimetric

capacity compared to hybrid materials.[9-10] It is also significantly faster than the nanocrystalline TiO_2 (B) morphology that can deliver about 120 mAh g^{-1} at the rate of 20 A g^{-1} (60 C), which was recently reported to be the fastest titania material.[16]

7.3 Conclusions

The novel non-aqueous synthesis in *tert*-butanol described here enables the formation of extremely small crystalline nanoparticles of LTO whose size can be tuned by the heating temperature. We have shown that these particles can be used to construct crystalline lithium titanate spinel frameworks with extremely high surface areas already at the mild temperature of 400 °C. The combination of these features in the LTO framework leads to drastically enhanced kinetic behavior at high cycle stability. This way we have created materials with combined properties typical for both batteries (high energy density) and for supercapacitors (high power densities). The nano-LTO spinel can be charged very fast to almost its full capacity, and then discharged at much slower rates (Figure 7-11). Such materials are of great interest for applications in electrical vehicles or mobile electronic devices, where very short charging times are highly desirable and enabling for many envisioned applications. In combination with emerging fast nanostructured cathode materials,[4, 17] the ultrafast LTO anodes should have great potential for the development of Li-ion batteries and supercapacitors that can operate both at high energy density and high power.

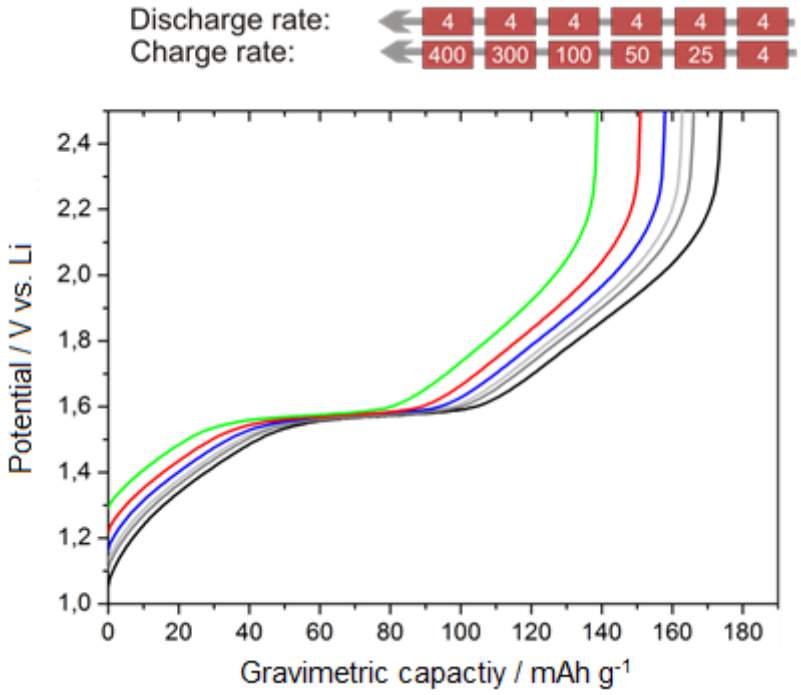

Figure 7-11: Galvanostatic discharge curves of the nano-LTO-400 obtained at different charge rates varying from 4 C to 400 C (indicated in labels) and a constant discharge rate of 4 C.

7.4 Experimental

Tert-butanol was utilized as reaction medium in a non-aqueous sol-gel synthesis to prepare 3–6 nm $Li_4Ti_5O_{12}$ spinel nanocrystals. All chemicals were purchased from Sigma-Aldrich and used as received. *Tert*-butanol was dried over 4 Å molecular sieve at 28 °C and filtered prior to use. For the synthesis of nanocrystalline mesoporous LTO, stoichiometric amounts of titanium(IV) butoxide (2.04 g, 5.99 mmol) and lithium *tert*-butoxide (0.381 g, 4.76 mmol) were dissolved in 19 mL *tert*-butanol containing 0.5 g of Pluronic P123 and 1 ml benzyl alcohol. The resulting solution was placed in a Teflon-lined steel autoclave and heated in a laboratory oven at 170 °C for 20 h. The presence of small amounts of benzyl alcohol does not influence the properties of the reaction product, but improves the wetting ability of the reaction mixture for film fabrication. For the preparation of mesoporous powders for Raman, XRD, TEM and sorption analysis, the reaction solution was cast as thin layers on glass substrates, dried and then calcined on the substrate at various temperatures (nano-LTO-400:

2 h ramp to 400 °C followed by 10 h dwell time; nano-LTO-500: 2 h ramp to 500 °C followed by 10 min dwell time; nano-LTO-600: 1 h ramp to 600 °C followed by 10 min dwell time). For the powder preparation the films were scraped off the substrate and ground in a mortar.

Electrode preparation

Mesoporous films for SEM analysis and electrochemical measurements were prepared by drop-casting or by spin-coating of the reacted synthesis solutions on the FTO-coated glass substrate.

For preparation of drop-cast films, 5.0 µL of the reacted synthesis solution was distributed over about 1 cm^2 of FTO-coated glass substrate and afterwards spun at the rotation speed of 500 rpm at 23 ± 2 °C and a relative humidity of 35 ± 10 % to improve the homogeneity of the coating. At such a low speed no material is removed from the substrate and the deposition is practically quantitative. The transparent films were heated in air using the heating procedures described above. The amount of LTO spinel in the drop-cast films is 0.138 mg cm^{-2}, which was calculated on the basis of the precursor concentration and confirmed by TGA experiments by determination of the rest mass (Figure 7-12). For the TGA measurements, 15 times 5 µL = 75 µL of the reacted synthesis solution was placed into the tared crucible and heated to 900 °C with a ramp of 10 °C min^{-1} in air. The solution volume was taken with the same adjustable 5 µL micropipette which was used for the electrode preparation. By heating to the high temperature all organic residues (solvents, by-products and precursors) are decomposed and LTO remains. The mass of the LTO in the volume used was determined from the residual mass at 900 °C which was 1.9528 mg, which corresponds to 1.9528 mg/15 = 0.130 mg LTO in 5 µL of the reaction mixture. The determined mass is in a good agreement with the theoretically calculated concentration of LTO in the solution.

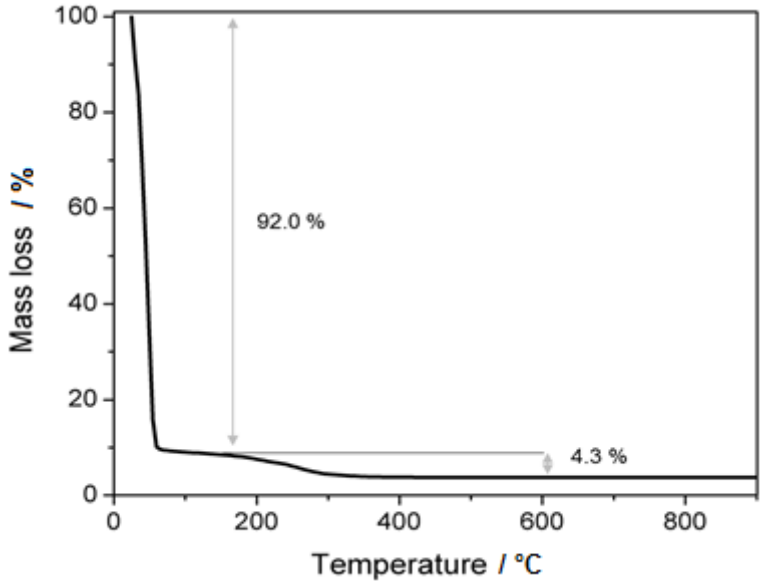

Figure 7-12: TGA curve of 75 µL of the reacted synthesis solution measured with a ramp of 10 °C min^{-1} in air. The mass losses at 25 – 180 °C and at 180 – 350 °C correspond to evaporation of solvent and to decomposition of Pluronic P123, respectively. The residual mass at 900 °C is 1.9528 mg, which corresponds to 0.130 mg LTO in 5 µL of the reaction mixture.

The thickness of the films obtained in this way was about 500 nm, as measured by profilometry (Dektak). Measurements on more than one hundred electrodes prepared in the same way prove the good reproducibility of the electrode deposition procedure. The gravimetric capacity of such electrodes obtained from the charge of the extraction process and the calculated mass of the resulting LTO is very close to or even exactly matches the theoretical capacity of 175 mAh g^{-1} of $Li_4Ti_5O_{12}$ and therefore proves the quantitative deposition of the drop-cast films.

In addition, classical spin-coating was used for the controlled variation of the film thickness. For that purpose, 100 µL of the as-prepared synthesis solution was distributed on 1.0 cm^2 open surface of the masked FTO substrate and then spun at speeds of 500 – 2000 rpm. Although the amount of the LTO on such electrodes after heating can be estimated from the film volume (the film thickness can be accurately measured by profilometry) and the known porosity determined by gas sorption, we do not claim quantitative deposition for this film preparation technique. The amount of the material on such electrodes was calculated from the

charge passed through the electrode at low rates from the extraction branch. The thickness of the films can be varied from about 150 nm to about 500 nm by changing the rotation speed. The largest thickness of the films prepared by both methods is about 500 nm (corresponding to a loading of about 0.14 mg cm^{-2}). A linear dependence between the electrode capacity and the film thickness for the spin-coated films was observed (Figure 7-13).

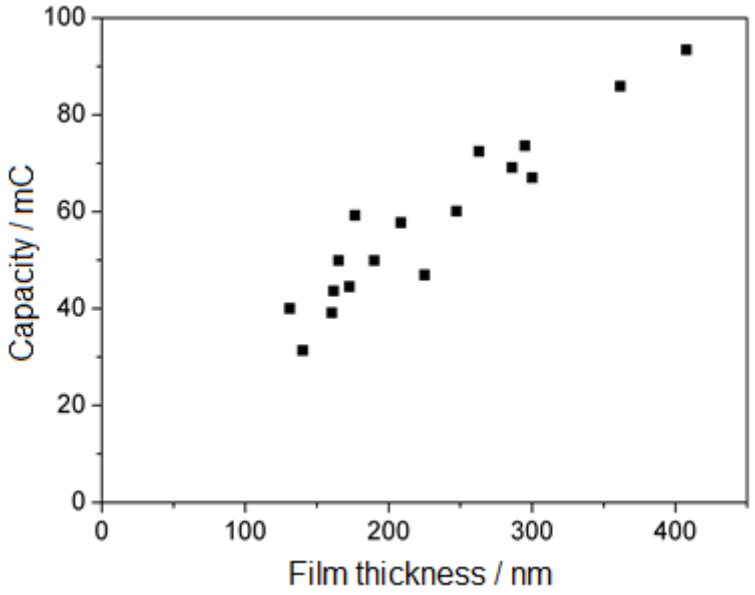

Figure 7-13: Capacity of thin film nano-LTO-400 electrodes prepared by spin-coating at different rotation speeds. The capacity was measured from the galvanostatic discharge curves at the rate 5 C.

Characterization

Thermogravimetric analysis (TGA) was performed on a Netzsch STA 440 C TG/DSC instrument (heating rate of 10 K min^{-1} in a stream of synthetic air of about 25 mL min^{-1}). Scanning electron microscopy (SEM) was performed on a JEOL JSM-6500F scanning electron microscope equipped with a field emission gun. High Resolution Transmission Electron Microscopy (HR-TEM) was performed using a FEI Titan 80-300 equipped with a field emission gun operated at 300 kV. TEM samples were prepared by dispersion of the

calcined materials in ethanol and evaporation of one drop of this dispersion on a Plano holey carbon coated copper grid.

The surface area of the calcined powders was determined by the analysis of sorption isotherms of N_2 at the boiling point of liquid nitrogen (approx. 77 K) using a Quantachrome Instruments NOVA 4000e apparatus. Samples were degassed for 12 h at 150 °C. The pore size distribution was calculated from the adsorption branch using the NLDFT adsorption branch model for silica, with cylindrical pores. X-ray diffraction analysis of the powders on silicon wafers was carried out in reflection mode using a Bruker D8 Discover with Ni-filtered CuK_α-radiation and a position-sensitive detector (Vantec). Raman spectra were recorded on a Jobin Yvon Horiba HR800 UV Raman microscope using a HeNe laser emitting at 632.8 nm.

Electrochemical measurements were carried out using a Parstat 2273 potentiostat (Princeton Applied Research) with PowerSuite software for collection and analysis of the data. The measurements were performed in 1 M $LiN(SO_2CF_3)_2$ solution in a 1 : 1 by weight mixture of ethylenecarbonate (EC) and 1,2-dimethoxyethane (DME). The solution preparation and cell assembly were carried out in an Ar-filled glove box with a water and oxygen content of less than 5 ppm. The electrolyte solution was dried over a 4 Å molecular sieve. Li wires were used as both the auxiliary and the reference electrodes. Electrochemical measurements were taken in a potential range from 2.4 to 1.0 V vs. Li. Galvanostatic measurements for the determination of the cycle stability of nano-LTO were performed at 100 C (17 A g^{-1}) with cut-off potentials of 1.1 V for the lithium insertion process and 2.4 V for the extraction process. The measurements were performed on about 100 films; the reported data correspond to the mean values with the corresponding error bars.

7.5 References

(1) a) Z. Yang, J. Zhang, M. C. W. Kintner-Meyer, X. Lu, D. Choi, J. P. Lemmon, J. Liu, *Chem. Rev.* **2011**, *111*, 3577-3613; b) V. Etacheri, R. Marom, R. Elazari, G. Salitra, D. Aurbach, *Energy Environ. Sci.* **2011**, *4*, 3243–3262; c) M. Contestabile, G. J. Offer, R. Slade, F. Jaeger, M. Thoennes, *Energy Environ. Sci.* **2011**, *4*, 3754–3772.

(2) J. R. Miller, P. Simon, *Science* **2008**, *321*, 651-652.

(3) R. J. Brodd, K. R. Bullock, R. A. Leising, R. L. Middaugh, J. R. Miller, E. Takeuchi, *J. Electrochem. Soc.* **2004**, *151*, K1-K11.

(4) H. Zhang, X. Yu, P. V. Braun, *Nature Nanotech.* **2011**, *6*, 277-281.

(5) a) A. S. Arico, P. Bruce, B. Scrosati, J. M. Tarascon, W. Van Schalkwijk, *Nature Mater.* **2005**, *4*, 366-377; b) F. Cheng, J. Liang, Z. Tao, J. Chen, *Adv. Mat.* **2011**, *23*, 1695-1715; c) J. M. Szeifert, J. M. Feckl, D. Fattakhova-Rohlfing, Y. Liu, V. Kalousek, J. Rathousky, T. Bein, *J. Am. Chem. Soc.* **2010**, *132*, 12605-12611.

(6) I. Plitz, A. DuPasquier, F. Badway, J. Gural, N. Pereira, A. Gmitter, G. G. Amatucci, *Appl. Phys. A* **2006**, *82*, 615-626.

(7) a) Y. Wang, H. Liu, K. Wang, H. Eiji, Y. Wang, H. Zhou, *J. Mater. Chem.* **2009**, *19*, 6789-6795; b) Y. Tang, L. Yang, Z. Qiu, J. Huang, *J. Mater. Chem.* **2009**, *19*, 5980-5984; c) L. Kavan, M. Gratzel, *Electrochem. Solid State Lett.* **2002**, *5*, A39-A42; d) M. Kalbac, M. Zukalova, L. Kavan, *J. Solid State Electrochem.* **2003**, *8*, 2-6; e) S.-H. Yu, A. Pucci, T. Herntrich, M.-G. Willinger, S.-H. Baek, Y.-E. Sung, N. Pinna, *J. Mater. Chem.* **2011**, *21*, 806-810; f) J. Lim, E. Choi, V. Mathew, D. Kim, D. Ahn, J. Gim, S.-H. Kang, J. Kim, *J. Electrochem. Soc.* **2011**, *158*, A275-A280; g) G.-N. Zhu, H.-J. Liu, J.-H. Zhuang, C.-X. Wang, Y.-G. Wang, Y.-Y. Xia, *Energy Environ. Sci.* **2011**; h) K. Naoi, *Fuel Cells* **2010**, *10*, 825-833.

(8) J. Haetge, P. Hartmann, K. Brezesinski, J. Janek, T. Brezesinski, *Chem. Mat.* **2011**, 23, 4384–4393.

(9) K. Naoi, S. Ishimoto, Y. Isobe, S. Aoyagi, *J. Power Sources* **2010**, *195*, 6250-6254.

(10) H.-K. Kim, S.-M. Bak, K.-B. Kim, *Electrochem. Comm.* **2010**, *12*, 1768-1771.

(11) Y. Liu, J. M. Szeifert, J. M. Feckl, B. Mandlmeier, J. Rathousky, O. Hayden, D. Fattakhova-Rohlfing, T. Bein, *ACS Nano* **2010**, *4*, 5373-5381.

(12) a) N. Takami, K. Hoshina, H. Inagaki, *J. Electrochem. Soc.* **2011**, *158*, A725-A730; b) W. J. H. Borghols, M. Wagemaker, U. Lafont, E. M. Kelder, F. M. Mulder, *J. Am. Chem. Soc.* **2009**, *131*, 17786–17792.

(13) a) Y. G. Guo, Y. S. Hu, J. Maier, *Chem. Comm.* **2006**, 2783-2785; b) Y. S. Hu, L. Kienle, Y. G. Guo, J. Maier, *Adv. Mater.* **2006**, *18*, 1421-1426.

(14) A. S. Prakash, P. Manikandan, K. Ramesha, M. Sathiya, J. M. Tarascon, A. K. Shukla, *Chem. Mater.* **2010**, *22*, 2857-2863.

(15) a) Y. Ren, Z. Liu, F. Pourpoint, A. R. Armstrong, C. P. Grey, P. G. Bruce, *Angew. Chem. Int. Ed.* **2012**, *51,* DOI: 10.1002/anie.201108300; b) H. Liu, Z. Bi, X.-G. Sun, R. R. Unocic, M. P. Paranthaman, S. Dai, G. M. Brown, *Adv. Mater.* **2011**, *23*, 3450-3454.

(16) H.-W. Lee, P. Muralidharan, R. Ruffo, C. M. Mari, Y. Cui, D. K. Kim, *Nano Lett.* **2010**, *10*, 3852-3856.

8 Ultrasmall dispersible crystalline nickel oxide nanoparticles as high performance catalysts for electrochemical water splitting

This chapter is based on the following publication:

Ksenia Fominykh*, Johann M. Feckl*, Markus Döblinger, Sebastian Böcklein, Jürgen Ziegler, Jiri Rathousky, Laurie Peter, Thomas Bein, Dina Fattakhova-Rohlfing, to be submitted

*these authors contributed equally

8.1 Introduction

Nickel(II) oxide NiO is an abundant and technologically important semiconducting oxide. The main applications of nickel oxide, such as catalysis,[1,2] batteries,[3,4] supercapacitors,[5,6] electrochromics[7] and many others can often benefit from nanostructuring and reducing the crystal size down to the nanometer scale. Due to a largely increased interface and drastically reduced dimensions relative to the bulk, the numerous reported nickel oxide nanomorphologies such as nanoflowers,[8,9] porous spheres,[10] nanowires[11] or nanotubes[12] demonstrate a superior performance in applications involving charge transfer and charge transport processes.[13] An additional attractive nickel oxide nanomorphology is realized by crystalline non-agglomerated dispersible nanoparticles. The colloidal nanocrystal dispersions are advantageous for a controlled electrodeposition of crystalline nickel oxide at room temperature,[14,15] or for the fabrication of hole transporting layers in polymer solar cells.[16,17] Furthermore, a reduction in the crystal size to only a few nanometers is expected to modulate

the electronic, optical and magnetic characteristics of the nanocrystals as well as their surface properties.[18]

Although colloidal non-agglomerated nanocrystals can be obtained for several metal oxides, [19,20] nickel oxide in this form was not available so far. It can be easily prepared in different ways including chemical or electrochemical oxidation of metallic nickel, microemulsion,[21] precipitation,[22] microwave irradiation,[23] low pressure spray pyrolysis,[24] the anodic arc plasma method[25] and thermal decomposition of nickel compounds.[26-29] However, practically all the reaction pathways require a thermal treatment at elevated temperatures to obtain a crystalline material, thus resulting in an irreversible agglomeration of the nanoparticles. Sol-gel,[30] hydrothermal,[31] and solvothermal[32] approaches provide a better control over the size, shape and agglomeration of nanoparticles, enabling fabrication of smaller nanoparticles down to 4 – 5 nm in size. Still, the reported NiO nanoparticles exhibit a broad particle size distribution, formation of intergrown or agglomerated crystals and a lack of dispersibility.

The following experiments have been performed as a joint project: The nickel oxide nanoparticle synthesis and characterization was performed by Ksenia Fominykh and Johann M. Feckl. The electrochemical measurements were performed by Dina Fattakhova-Rohlfing. XPS characterization was done by Sebastian Böcklein and Jürgen Ziegler. TEM images were recorded by Markus Döblinger.

8.2 Results and Discussion

In order to overcome the previous limitations and to obtain single ultrasmall colloidal NiO nanocrystals, we have developed a solvothermal approach in *tert*-butanol leading to a direct formation of crystalline nanoparticles via a chemical reaction with the solvent. The suitability

of this reaction pathway for the fabrication of ultrasmall dispersible nanocrystals was demonstrated by us earlier for several titanate systems,[33-35] but the *tert*-butanol approach was not tested yet for other metal oxide systems. The formation of NiO nanocrystals via this pathway takes place in a narrow range of reaction conditions and is sensitive to the precursor concentration, the reaction temperature and the reaction time. The choice of NiO precursors is decisive for the formation of nanoparticles. Nickel hydroxide, nickel chloride and nickel oxalate remain unreacted in all examined conditions. The use of nickel(II) acetate leads to the formation of phase-pure NiO nanoparticles with crystalline domain sizes of about 5 nm (Figure 8-1a, D). Smaller particles, however, are not available with this precursor, and the nanoparticles obtained in this way are not dispersible.

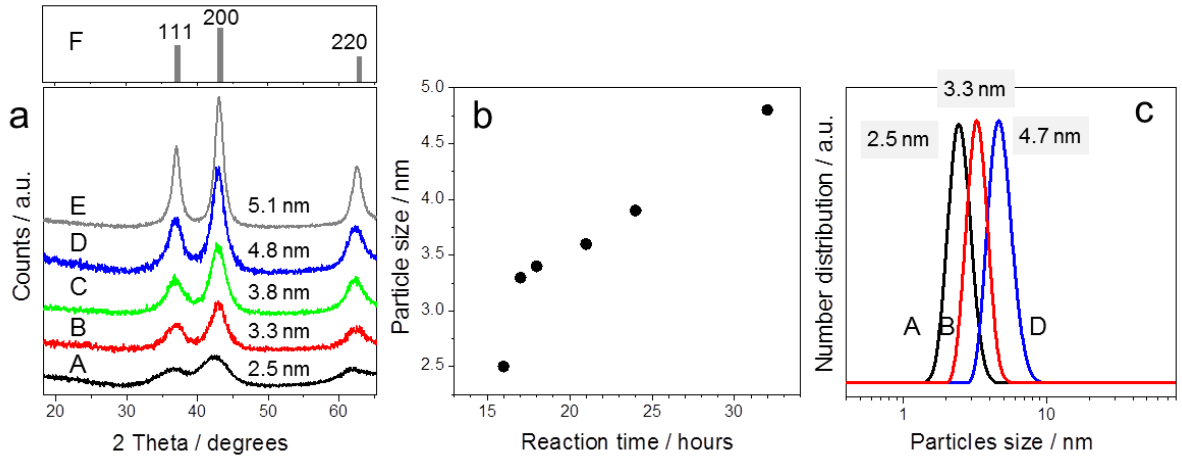

Figure 8-1: Size of the NiO nanoparticles prepared from the reaction of $Ni(acac)_2$ (0.036 mol L^{-1}) in *tert*-BuOH at 200 °C after different reaction times: 16 h (A; sample code for further discussion in the text: NP-2.5), 17 h (B; NP-3.3), 24 h (C; NP-3.8) and 33 h (D, NP-4.8); sample E was prepared from $Ni(OAc)_2 \cdot 4H_2O$: (a) Powder XRD patterns of the dried NiO nanoparticles (F corresponds to the ICDD card number 01-071-1179), (b) Crystalline domain size after different reaction times calculated from the XRD patterns for the most intensive NiO signal at 2θ = 43° using the Scherrer equation, (c) Dynamic light scattering (DLS) analysis of ethanolic dispersions of NiO nanoparticles.

Screening of various commercially available Ni(II) compounds as precursors revealed that nickel(II) acetylacetonate ($Ni(acac)_2$) is the most suitable precursor for dispersible crystalline NiO nanoparticles in this reaction. We found that the concentration of $Ni(acac)_2$ should not

exceed 0.036 mmol mL^{-1}, otherwise the precursor remains largely unreacted. Formation of NiO from $Ni(acac)_2$ in *tert*-butanol requires a reaction temperature of 200 °C; no product formation was observed at lower temperatures. The discussion below therefore refers to NiO nanoparticles obtained from the reaction of $Ni(acac)_2$ in *tert*-butanol at 200 °C. Formation of nickel oxide starts only after 12 h of reaction (Figure 8-2).

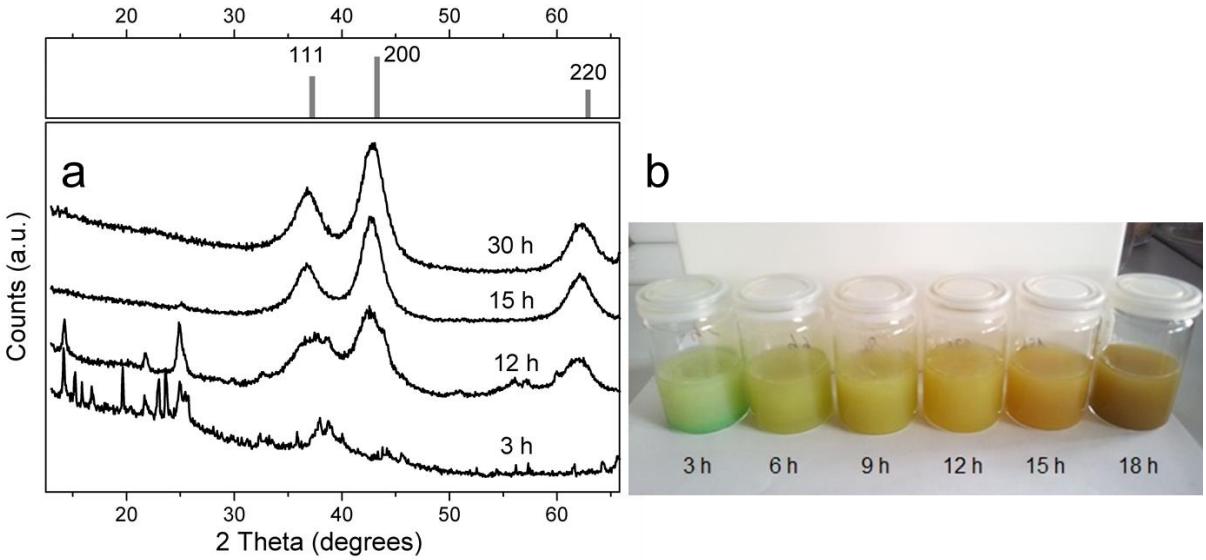

Figure 8-2: XRD patterns (a) and photograph (b) of the reaction products obtained after reaction of (0.036 mol L^{-1}) $Ni(acac)_2$ in *tert*-BuOH for different reaction times at 200 °C.

Reactions carried out for 12 h to 15 h show broadened NiO reflections with increasing intensity in the course of the reaction. This indicates the formation of small crystalline particles, but still some amounts of non-reacted $Ni(acac)_2$ precursor remain. For reaction times longer than 16 h exclusively NiO reflections are observed in the XRD patterns (Figure 8-1a). The reaction progress is also clearly noticeable in the appearance of the reaction mixture, which changes its color from light green for the precursor solution to brown after 18 h of reaction (Figure 8-2b).

The size of the phase-pure NiO nanocrystals calculated from the line broadening in the XRD corresponds to 2.5 nm after 16 h reaction time at 200 °C. For further discussion in the text the sample labeling NP-x.y will be used with x.y being the particle size determined from XRD. The particle size increases almost linearly from 3.3±0.1 nm (NP-3.3) to 4.8±0.1 nm (NP-4.8) with reaction times between 17 h and 33 h, respectively (Figure 8-1a,b). Dried NiO nanoparticles are perfectly dispersible in ethanol after the addition of very small amounts of acetic acid. Dynamic light scattering (DLS) measurements of these transparent colloidal dispersions reveal narrow size distributions centered at 2.5 nm (NP-2.5), 3.3 nm (NP-3.3) and 4.7 nm (NP-4.8), respectively (Figure 8-1c). The particle size in DLS agrees well with the particle size calculated from the XRD patterns and determined from TEM images (see below). The dispersions proved to be stable, as DLS measurements showed the same particle size after several weeks.

Transmission electron microscopy (TEM) images of the NiO nanoparticles NP-3.3 show non-agglomerated, defined particles with a narrow particle size distribution (Figure 8-3a, b). The presence of lattice fringes (Figure 8-3b) indicates a crystalline structure of NiO, which is also confirmed by electron diffraction (Figure 8-3c) and which correlates with the XRD pattern.

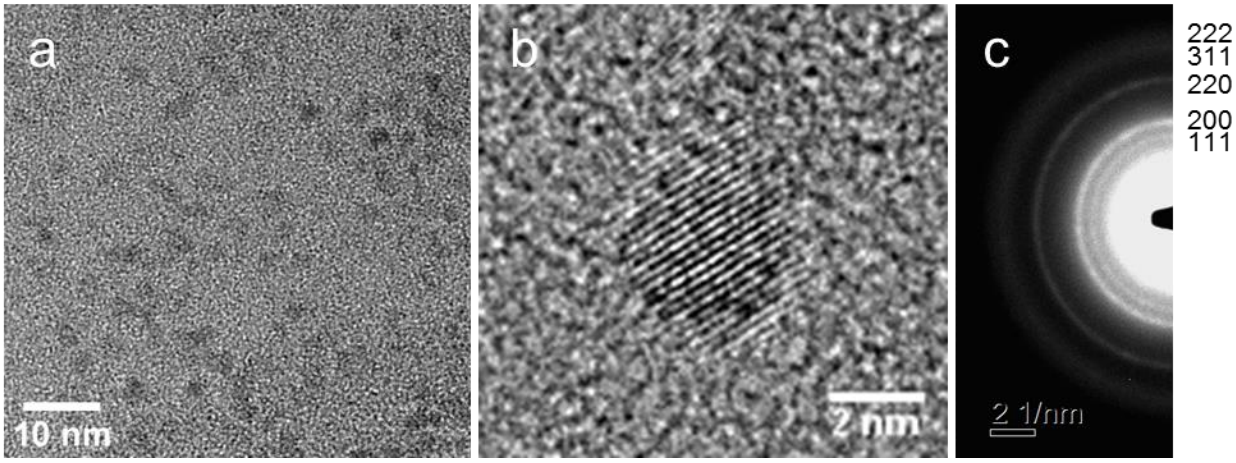

Figure 8-3: TEM images of the NiO nanoparticles NP-3.3: a) overview of the nanoparticles dispersed on the TEM grid; b) HRTEM image of a single NiO nanoparticle. c) Electron diffraction pattern of the NiO nanoparticles. The corresponding d-values are 2.4 (111), 2.08 (200), 1.47 (220) 1.26 (311) and 1.2 Å(222).

The average particle size from the TEM images, measured and calculated over 30 particles, is 3.3 nm which is also in good agreement with the size calculated from the XRD pattern (3.3 nm, NP-3.3). When more concentrated dispersions of NiO nanoparticles were used for TEM sample preparation, we observed the formation of hexagonal supercrystals assembled from nanoparticles (Figure 8-4). The presence of such supercrystalline assemblies is indicative for the monodisperse shape and size of the nanoparticles.[36]

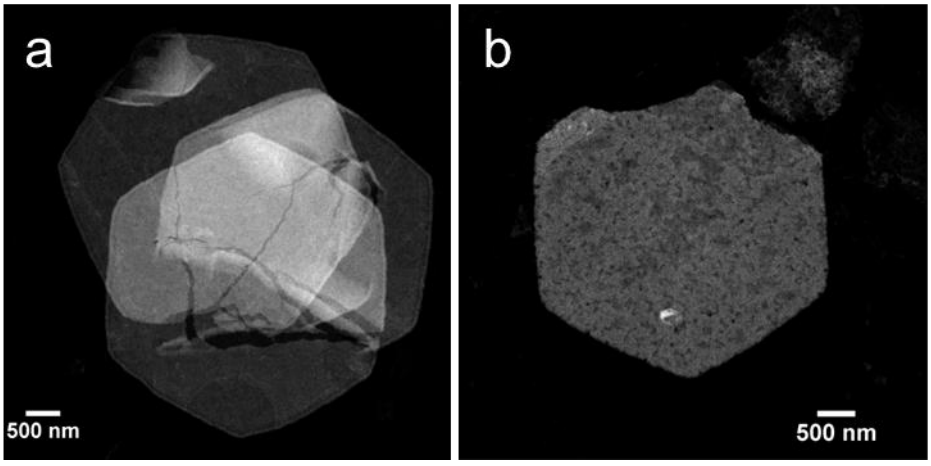

Figure 8-4: STEM image of the hexagonal supercrystals assembled from the NiO nanoparticles obtained from the reaction of $Ni(acac)_2$ after 18 h.

Raman spectra of the as-prepared dry NiO powders (NP-3.3) show the presence of aliphatic organic groups corresponding to *tert*-BuOH solvent residues, which practically vanish after heating the samples at 100 °C. The Raman spectra of NiO powders heated at 100 – 240 °C show only one broad phonon vibration peak at ca. 500 – 600 cm^{-1} typical for NiO[35] and similar to the spectrum of commercial NiO nanopowder (Figure 8-5a). Temperature treatment up to 300 °C does not influence the size of the NiO nanoparticles; they only start to grow at temperatures above 350 °C (Figure 8-5b).

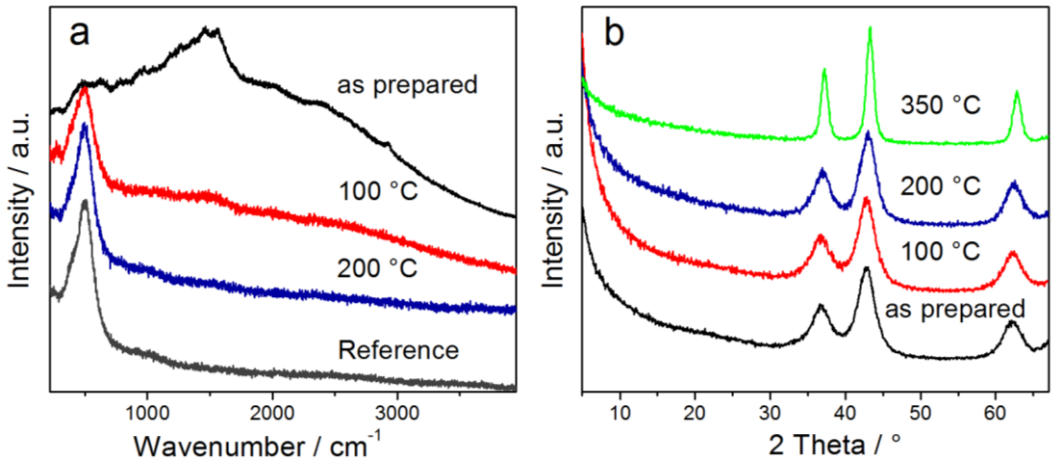

Figure 8-5: (a) Raman spectra of as-prepared NiO nanopowders (NP-3.3) and after heating at 100 °C and 200 °C. The bottom spectrum corresponds to the commercial NiO nanopowders (Sigma-Aldrich, 99.8 % trace metal basis, < 50 nm). (b) XRD powder patterns of the as-prepared NiO nanoparticles (NP-3.3) and after heating to 100 °C – 350 °C.

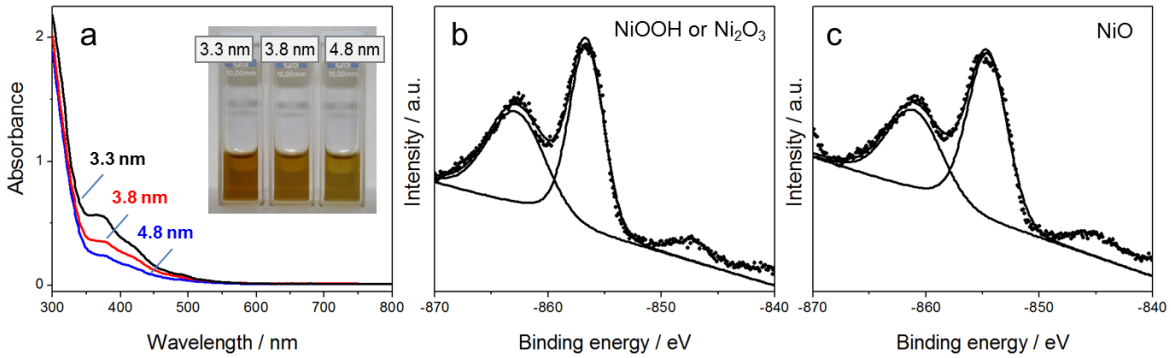

Figure 8-6: (a) UV-Vis absorption spectra of dispersions of NiO nanoparticles in ethanol with sizes of 3.3 nm (black, NP-3.3), 3.8 nm (red, NP-3.8) and 4.8 nm (blue, NP-4.8), and the photographs of the corresponding dispersions in an inset (5 mM concentration). X-ray photoelectron spectra (XPS) of as prepared (b) and argon polished (c) NiO nanoparticles (NP-3.3). The XPS spectra show the energy region between 840 and 870 eV corresponding to the Ni $2p_{3/2}$ doublet. The points correspond to the experimental spectra, and the lines are the fitted curves and the Gaussian individual peak fits, respectively.

Figure 8-6 shows the UV-visible spectra of nickel oxide nanocrystals of various sizes dispersed in ethanol with the same concentration for each sample. The distinct absorption peak around 375 nm in the UV region, as well as the weaker absorption features around 425 and 480 nm are attributed to d-d transitions of Ni(III).[38] It can be seen that smaller particles with a higher ratio of surface atoms show a stronger absorption in this region, which results in a stronger brown coloration of the dispersions (see inset in Figure 8-6). This suggests that the absorption arises from Ni(III) states at the surface of the nanoparticles that are probably present in the form of NiOOH or Ni(III) oxide moieties.[39] The steep absorption in the UV region below 350 nm is attributed to the band gap absorption in NiO.[40] The so-called Tauc plot in Figure 8-7b shows a linear relation in the energy range around 3.8 to 4.1 eV for n = 2, (see UV-Vis characterization in the experimental part) indicating a direct transition as often reported for the semiconducting NiO nanoparticles.[18,41] This is supported by the observation that the absorption coefficients of the NiO nanoparticle dispersions in this region are in the range of 10^4 – 10^5 cm^{-1}, also indicating a direct transition (Figure 8-7a).

Extrapolation of the linear portion of the high energy part of the plots yields band gap values of 3.73, 3.78 and 3.79 eV for NP-3.3, NP-3.8and NP-4.8, respectively (Figure 8-7b).

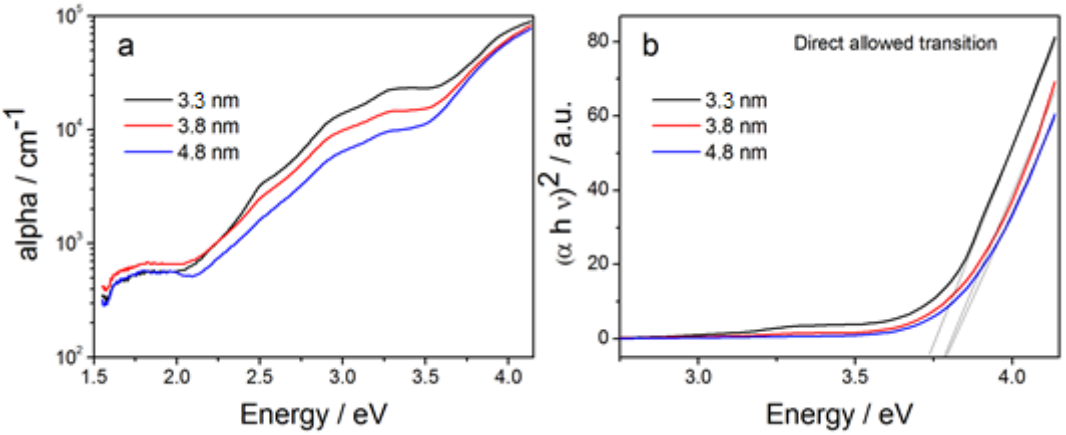

Figure 8-7: (a) Absorption coefficient alpha of the NiO nanoparticles with various sizes. (b) Tauc plot for the determination of the band gap of NiO.

These findings, indicating that nickel(III) states occupy the surface of the particles, are also supported by XPS analysis (Figure 8-6b,c). The measurements show signals for nickel(III) states,[42] which could be in the form of Ni_2O_3, NiOOH or *tert*-butoxide groups attached to the surface of NiO. Quantification of the elements in the XPS measurements show a ratio of Ni to O atoms of nearly 1:2, which suggests that Ni(III) states are present in the form of NiOOH on the surface of the nanoparticles (Table 8-1). When sputtering the surface with argon ions, the spectra only show NiO. Quantification of the elements for the sputtered sample is closer to the 1:1 atomic ratio of pure NiO. This is also in good agreement with the non-surface selective XRD measurements which only show a signal for NiO. In conclusion, the combination of the results of XRD, XPS and UV-Vis absorption indicates that the as-synthesized nanoparticles have a core of NiO and some form of nickel(III) states on their surface.

Table 8-1: Atomic proportions from the quantification of XPS spectra.

Sample	C 1s %	Ni 2p %	O 1s %
NiO untreated	21.3[a]	24.8	48.8
NiO sputtered	7.5	39.6	48.3

[a]The high carbon content for the untreated nanoparticles is typical for samples prepared ex-situ and which were exposed to ambient conditions, but could also be an indication for surface bound *tert*-butoxide groups originating from the chemical synthesis of the nanoparticles in *tert*-butanol.

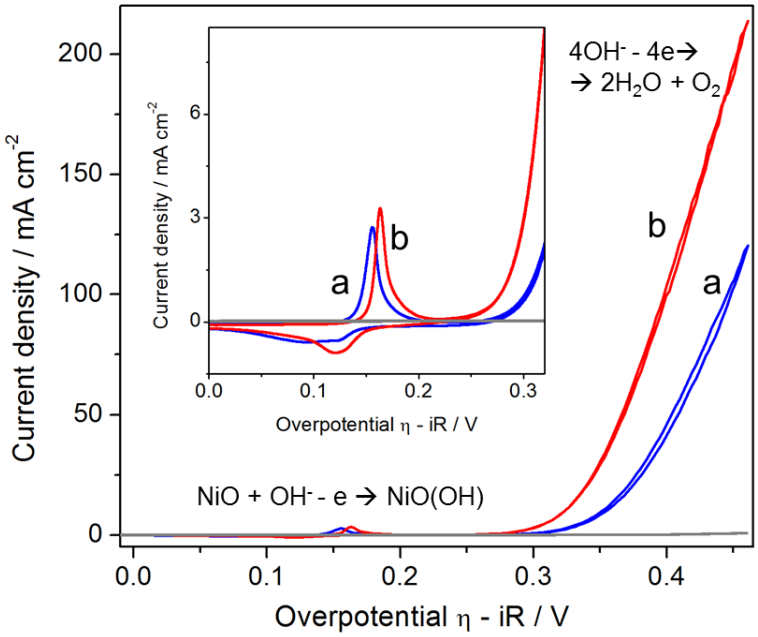

Figure 8-8: Cyclic voltammograms of NiO nanoparticles (NP-3.3) on Au-coated QCM electrodes in 0.5 M KOH: pre-conditioned by cycling 30 times from 0.1 to 0.7 V vs. sat. Ag/AgCl electrode with a scan rate *v* = 20 mV s^{-1} (blue line, a), and electrochemically aged by applying a constant current of 7.5 mA cm^{-2} for 2.5 h (red line, b). The gray line corresponds to a voltammogram taken on the bare Au electrode aged at the same conditions as (b). The voltammograms were taken at a scan rate of 20 mV s^{-1}.

As Ni(III) states are usually associated with the electrocatalytic activity of nickel compounds,[43,44] we have tested our NiO nanoparticles as catalysts for the electrochemical oxidation of water. For that purpose, NiO nanoparticles NP-3.3 were deposited as thin films on Au-coated QCM crystals. The use of QCM crystals enables an accurate determination of the NiO mass loading, which was 20±0.8 µg cm^{-2} for the thinnest films. Cyclic

voltammograms (CVA) taken in 0.5 M KOH show the typical behavior for NiO in basic media. The CVAs feature a pair of anodic and cathodic peaks centered around 0.370 V vs. Ag/AgCl corresponding to a redox reaction of NiO ($NiO + OH^- - 1e^- \rightarrow NiOOH$), followed by a current due to O_2 evolution (Figure 8-8). It should be noted that only a very low current was measured on the bare Au electrode under the same conditions (see grey line in Figure 8-8). The current increases during the first few cycles and reaches a stable value after 30 scans, after which it remains stable and does not change anymore with prolonged cycling. The electrodes pre-conditioned in this way show a narrow anodic and a broad cathodic peak in the reversed scan, corresponding to the redox reaction of NiO. The charge obtained from the integration of the cathodic peak corresponds to about 2.7 mC cm^{-2}, which is only about 10±2 % of the deposited NiO, independent of the mass loading on the electrode. The same fraction of electrochemically active Ni atoms was obtained for electrodes with about 2.5-times (6.0 mC cm^{-2}) and about 4.5-times (9.9 mC cm^{-2}) higher mass loadings. The measured charge closely agrees with the theoretical surface charge value corresponding to the particle surface, which can be calculated assuming that only surface Ni atoms are electrochemically active. Using the specific surface area of the NP-3.3 NiO nanoparticles of 210 $m^2 g^{-1}$ determined by Kr sorption (Figure 8-9), the real surface area (roughness factor) of the electrodes with a mass loading of 20 μg cm^{-2} is equal to 42 $cm^2 cm^{-2}$. This leads to a surface charge value of 2.76 mC cm^{-2} using the estimated surface density of Ni atoms of $4.08 \cdot 10^{14}$ cm^{-2} for a 110 plane. This good agreement with the electrochemically obtained charge (2.7 mC cm^{-2}) indicates that indeed surface Ni atoms are preferentially electrochemically active and that the surface of the NiO nanoparticles is also electrochemically accessible for the thicker films. Unlike the previously reported ultrathin NiO films that completely transform to layered $Ni(OH)_2$ after prolonged electrochemical treatment,[43] the NiO electrodes assembled from our nanoparticles obtained by the *tert*-butanol route keep their integrity. The amount of Ni atoms

involved in the electrochemical reaction practically does not change after prolonged cycling, as determined from the charge obtained by integration of the corresponding peaks. The integrated charge remains practically unchanged even after electrochemical aging of the electrodes, which was performed galvanostatically by applying 7.5 mA cm^{-2} current for 2.5 h. However, the aging leads to a shift of the NiO redox potential to more positive values (from 0.370+0.001 V to 0.385+0.002 V vs. Ag/AgCl, respectively). The positive shift in the redox potential is usually assigned to a phase transformation of the OH-terminated Ni atoms, which spontaneously form on the NiO surface in basic media, from a disordered α-modification to a more ordered and more catalytically active β-modification.[43] The shift in the peak in our case is accompanied by a decrease in the overpotential of the OER process. The overpotential required for 1 mA cm^{-2} OER current changes from 305 mV for the conditioned electrode to 280 mV for the aged electrode, respectively.

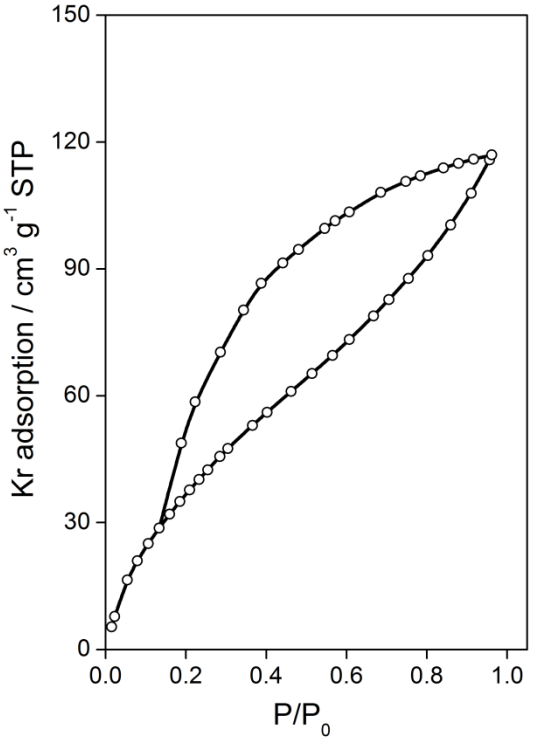

Figure 8-9: Kr sorption isotherm (measured at 77 K) on NiO nanoparticles (NP-3.3) which were tempered at 240 °C. The BET surface area corresponds to 210 $m^2 g^{-1}$. The isotherm demonstrates a hysteresis due to the textural porosity between the nanoparticles. The particle size was calculated from the BET surface area and NiO density of 6.67 g cm^{-3} using a spherical model corresponding to around 4 nm particle diameter.

The electrodes prepared from our NiO nanoparticles show high turnover frequencies (TOF, defined as number of O_2 molecules formed per active metal site per second) at relatively low overpotentials. The TOF calculated per active Ni atoms (determined from the real surface area of the electrodes) for the aged electrodes described above is 0.293 s^{-1} at an overpotential of η = 300 mV. This value is much higher than the reported TOF value of 0.009 s^{-1} at the same overpotential for IrO_x thin film electrodes that are known as some of the most active OER catalysts. The TOF value for our ultrasmall NiO particles is also higher than that of 0.21 s^{-1} for Fe-doped ultrathin NiO layers which was the highest reported value so far.[45] This makes our NiO nanoparticles very promising catalysts for electrochemical water splitting.

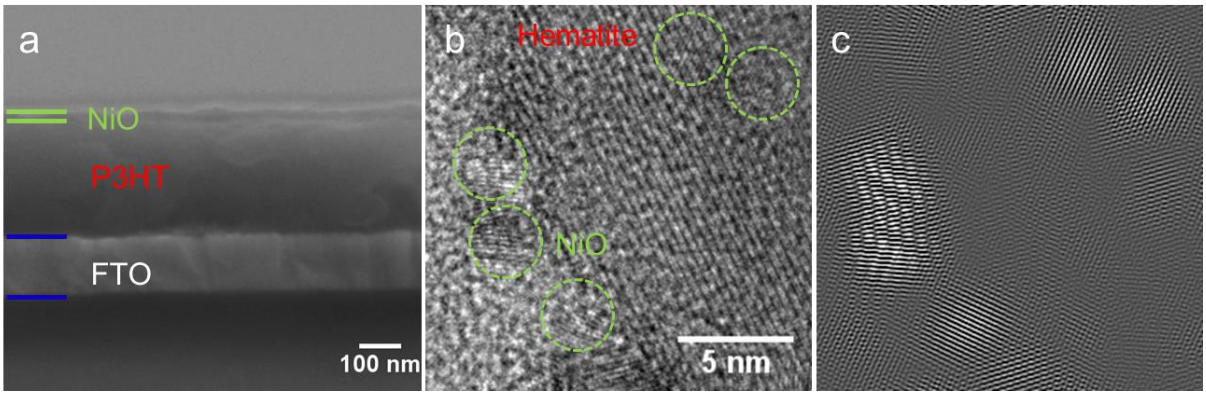

Figure 8-10: Deposition of NiO nanoparticles from ethanolic dispersions on different substrates: (a) as thin compact films on the top of a P3HT polymer layer (SEM image, cross-section), and as single non-agglomerated nanoparticles on crystalline mesoporous Fe_2O_3 hematite: top-view HR-TEM image (b) and its inverse FFT image (c).

The unique features of the obtained NiO nanoparticles, such as the high crystallinity and dispersibility, allow for a controlled deposition of the NiO nanocrystals on various flat and porous substrates. The deposition of thin, compact crystalline films of nickel oxide is particularly interesting for manufacturing organic/inorganic polymer solar cells. The colloidal dispersion can be easily processed in a large-scale compatible spin-coating deposition procedure and the films do not require further temperature treatment steps for crystallization. This enables the deposition on temperature sensitive polymers or other organic materials. Figure 8-10a shows a cross-sectional SEM image of a P3HT polymer layer with a compact NiO overlayer with a thickness of around 7 nm. This p-type layer can act as a hole selective layer in the hybrid solar cells, increasing the charge extraction and thereby reducing recombination processes. Furthermore, the high dispersibility and the very small size of the nickel oxide nanoparticles allow us to distribute them homogeneously not only on flat substrates but also on high surface area porous host materials for possible catalytic applications. This is demonstrated in Figure 8-10b and c, which shows the homogeneous distribution of the individual non-agglomerated NiO nanoparticles on a mesoporous hematite host, which is an interesting material for photoelectrochemical water splitting (see Chapter 9).

8.3 Conclusions

In conclusion, we describe for the first time the preparation of ultrasmall, crystalline and dispersible NiO nanoparticles, which have a high potential as catalysts for electrochemical oxygen generation. Using a solvothermal reaction in *tert*-butanol, very small nickel oxide nanocrystals can be prepared with sizes tunable from 2.5 to 6 nm and a narrow particle size distribution. The crystals are perfectly dispersible in ethanol even after drying, giving stable transparent colloidal dispersions. The nanoparticles dried at room temperature contain ca. 50 % of organics, which can be completely removed at about 100 °C leaving an aromatics-free surface. Besides the decreasing particles dimensions and increasing the surface area, the nanoscaling in our synthesis leads to a changed stoichiometry of the surface compared to the bulk. Our data demonstrate that although the crystalline structure of the obtained nanocrystals corresponds to a phase-pure stoichiometric nickel(II) oxide, the particle surface exhibits Ni(III) states. The presence of these surface states can be beneficial in many cases, especially for surface-related applications such as catalysis. The partially oxidized surface of NiO nanoparticles could explain the efficient catalytic behavior of the material in electrochemical water splitting experiments. The nanoparticles of 3.3 nm in size demonstrate very high turn-over frequencies of $0.293\ s^{-1}$ at an overpotential of $\eta = 300$ mV, even outperforming expensive rare earth iridium oxide catalysts. Additionally, their unique features such as the high crystallinity and dispersibility allow for the deposition of crystalline NiO layers on temperature sensitive substrates such as polymers, without the necessity of a subsequent heat treatment for crystallization. This would enable the preparation of hybrid organic/inorganic devices such as polymer solar cells. We believe that the unique features of these NiO nanocrystals provide a great potential for the preparation of numerous composite materials with applications in fields such as catalytic water splitting.

8.4 Experimental

Synthesis of NiO nanoparticles

Nickel(II) acetylacetonate was purchased from Alfa Aaesar (95 % purity). Nickel(II) acetate tetrahydrate was purchased from Aldrich (98 % purity), *tert*-butanol was purchased from Sigma-Aldrich (puriss. p.a., ACS reagent, ≥99.7 %). All chemicals were used as received. *tert*-butanol was dried over 4 Å molecular sieve at 28 °C and filtered prior to use.

For the synthesis of nickel oxide nanoparticles with different size, 0.13 g (0.50 mmol) of nickel(II) acetylacetonate ($Ni(acac)_2$) was added to 14 mL of *tert*-butanol (0.147 mol) at ambient conditions forming a turbid light green suspension. The reaction mixture was stirred for 10 min, then transferred into a Teflon autoclave liner and subsequently hermetically sealed. The autoclaves were kept at 200 °C in a laboratory oven for different reaction durations. The as-prepared powders were dried in air at 60 °C in a laboratory oven. The reproducibility of the reaction is very sensitive to the mass transfer conditions in the autoclave reactors, which are strongly influenced by the geometry of the autoclave and the stirring conditions. The most reproducible results were achieved for 20 mL cylindrical autoclaves (5.3 cm x 8 cm) that were rotated in the oven with a rate of ca. 250 rpm. For these conditions, about 2.5 nm (NP-2.5), 3.3 nm (NP-3.3), 3.8 nm (NP-3.8) and 4.8 nm (NP-4.8) phase-pure NiO nanoparticles were obtained after 16 h, 17 h, 24 h and 33 h reaction time, respectively.

Preparation of NiO dispersions

Dispersions of the NiO nanoparticles were prepared in ethanol by the addition of concentrated acetic acid. In a typical procedure, 2.4 mg of the dried NiO powder was covered with 4 µL of

acetic acid and afterwards dispersed in 1 mL of ethanol to obtain a colloidal dispersion with a NiO concentration of 0.03 mol L^{-1}.

Fabrication of thin films on FTO and polymer layers and deposition of NiO nanoparticles on mesoporous hematite layers

The NiO nanoparticle dispersions (0.03 mol L^{-1}) were used for the fabrication of thin films by spin coating on fluorine-doped tin oxide coated glass (FTO) and on polymer layers of poly(3-hexylthiophene-2,5-diyl) (P3HT) deposited on FTO. 40 µL of the dispersion was cast onto the substrate with a size of 1.5 x 1.5 cm and spun at 2000 rpm for 30 s. With this method thin films with a thickness of approximately 7 nm are obtained (Figure 8-10a).

For the deposition of the NiO nanoparticles on mesoporous hematite layers 5 µL of the NiO dispersions were drop-cast onto the hematite substrate with dimensions of 1 cm^2 and dried at room temperature.

Characterization

Wide angle X-ray diffraction analysis was carried out in reflection mode using a Bruker D8 Discover diffractometer with Ni-filtered CuK_α-radiation (λ = 1.5406 Å) equipped with a LynxEye position sensitive detector. Powder XRD patterns of the samples were collected in a 2θ range from 5° to 67° with a step of 0.5° and fixed counting time of 0.1 second per step. The size of the crystalline domains was calculated from the XRD patterns for the most intensive NiO signal at $2\theta = 43°$ using the Scherrer equation.

Dynamic light scattering measurements were performed on a MALVERN Zetasizer-Nano instrument equipped with a 4 mW He-Ne laser (633 nm) and an avalanche photodiode detector.

TEM measurements were carried out using a FEI Titan 80-300 equipped with a field emission gun operated at 300 kV. For the sample preparation a drop of a strongly diluted dispersion of a sample in ethanol was placed on a holey carbon coated copper grid and evaporated.

SEM images were obtained with a JEOL JSM-6500F scanning electron microscope equipped with a field emission gun operated at 4 kV. The films were prepared on silicon substrates and glued onto a brass sample holder with silver lacquer.

Raman spectroscopy measurements were carried out using a LabRAM HR UV-Vis (HORIBA JOBIN YVON) Raman Microscope (OLYMPUS BX41) with a SYMPHONY CCD detection system and a He-Ne laser (λ = 633 nm). Spectra were recorded using a lens with a 100-fold magnification.

Thermogravimetric analysis of the samples was performed on a NETZSCH STA 440 C TG/DSC (heating rate of 10 K min^{-1} in a stream of synthetic air of about 25 mL min^{-1}).

X-ray photoelectron spectroscopy (XPS) analysis of the particles on a silicon substrate was performed using a VSW HA 100 electron analyzer and the K_α radiation provided by a non monochromatized magnesium anode system (Mg K_α = 1253.6 eV). Ar ion polishing was done at 1500 eV for 10 minutes. The recorded elemental peaks were fitted by Gaussian-Lorentzian profiles and the elemental ratios were calculated by the equation

$$\frac{X_A}{X_B} = \frac{I_A / S_A}{I_B / S_B} \tag{8-1}$$

where I_A/I_B is the ratio of fitted areas, and S is the sensitivity factor.

UV-Vis characterization

The UV-visible spectra of the samples were measured with a Perkin Elmer Lambda 1050 spectrophotometer equipped with an integrating sphere.

The bandgap E_g of NiO was determined from the measured spectra using the equation:

$$h\nu - E_g \propto (\alpha h\nu)^n \tag{8-2}$$

where $h\nu$ is the photon energy, α (alpha) is the absorption coefficient, and the exponential factor n being either 2 for a direct allowed transition or ½ for an indirect allowed transition. The absorption coefficient alpha was calculated from the absorbance with the following equations:

$$A = -\log_{10}\frac{I_t}{I_0} = \varepsilon c_{solid} l \tag{8-3}$$

where A is the absorbance, I_0 is the incident light, I_t is the transmitted light, ε is the molar absorption coefficient, c is the concentration of nickel oxide in the dispersion (5 mM), and l is the optical path length (1 cm).

$$-ln\frac{I_t}{I_0} = \alpha l = -2.303\log_{10}\frac{I_t}{I_0} = \varepsilon c_{solid} l \tag{8-4}$$

$$\alpha = 2.303\varepsilon c_{solid} \tag{8-5}$$

The concentration c_{solid} of the solid NiO was calculated from the molar volume V_m that is given by the molar mass M_{NiO} (74.69 g mol^{-1}) and the density ρ_{NiO} (6.67 g cm^{-3}) of NiO:

$$c_{solid} = \frac{1}{V_M} = \frac{\rho}{M} = 89.3\frac{mol}{dm^3} = 89.3\ M \tag{8-6}$$

ε was calculated from the concentration of nickel oxide in the dispersion (5 mM):

$$\varepsilon = \frac{A}{c_{dispersion} l} = \frac{A}{5 * 10^{-3}} \quad (8\text{-}7)$$

$$\alpha(\lambda) = 2.303 \frac{A(\lambda)}{5 * 10^{3}} * 89.3\ cm^{-1} \quad (8\text{-}8)$$

Electrode preparation

The electrodes were prepared by deposition of the dispersed nickel oxide nanoparticles either by spin coating or by drop casting on QCM crystals (KVG 10 MHz QCM devices with gold electrodes from Quartz Crystal Technology GmbH). In a typical drop casting procedure, 4 µL of nickel oxide dispersion was cast on the Au layer of a QCM crystal. A mask was used to cover the non-active surface of the QCM chip exposing an area of 0.196 cm^2. The loaded QCM crystal was dried in air at ambient conditions for 5 min. For the spin coating method 8 µL of nickel oxide dispersion was deposited on a masked QCM crystal and spun at 1000 rpm for 10 s. The QCM electrodes prepared with both methods were subsequently heated to 240 °C in a laboratory oven with a heating ramp of 4 °C min^{-1} and a dwell time of 2 h.

Electrochemical measurements

Electrochemical measurements were performed in a three-electrode setup using an Autolab potentiostat/galvanostat PGSTAT302N with FRA32M module operating with Nova 1.9 software. All the measurements were performed in 0.5 M KOH electrolyte solution (Sigma-Aldrich, volumetric solution) at pH 13.43. Pt mesh (2 cm^2) was used as a counter electrode. Au/QCM crystals with NiO nanoparticles deposited on one side (preparation is described above) were used as working electrodes. To provide an electric connection to the QCM

electrode, a silver wire was connected to the respective tag of the QCM crystals using silver lacquer. The silver lacquer and the wire were sealed afterwards in inert two-component epoxy resin (Gatan, Inc). All potentials were measured vs. Ag/AgCl/KCl sat. reference electrode, whose potential is +0.989 V vs. the reversible hydrogen electrode (RHE) at pH 13.43 (+0.197 V vs. NHE). The electrochemical data were corrected for uncompensated resistance R_s. The R_s was determined as minimum total impedance in the frequency regime between 10 and 50 kHz at open circuit conditions and at a potential of 0.2 V vs. Ag/AgCl electrode, where no Faradaic processes take place. The resistance was taken as an average of 3 measurements, 90 % of this value was compensated. R_s was typically around 6 – 7 Ohm for the NiO-coated Au/QCM electrodes. The overpotential η was calculated using the equation $\eta = E - E_{OER} - iR_s$, where E is the potential recorded vs. Ag/AgCl reference electrode, E_{OER} is the reversible potential of the OER vs. Ag/AgCl reference electrode (0.240 V at pH 13.43), and i is the current. Current densities are calculated using the geometric surface area of the Au/QCM electrode (0.197 cm^2).

The pre-conditioning of the NiO electrodes was achieved using cyclic voltammetry (CVA). The electrodes were cycled between 0 V and 0.7 V vs. Ag/AgCl in 0.5 M KOH at a scan rate of 20 mV s^{-1} until the current has reached stable values and did not change anymore with repetitive cycling (typically 30 cycles). The CVA measurements on these pre-conditioned electrodes were made at scan rates from 2 mV s^{-1} to 20 mV s^{-1} without stirring the electrolyte. The aging was performed galvanostatically by applying a current density of 7.5 mA cm^{-2} for 2.5 h in a two-electrode mode in a stirred 0.5 M KOH solution. The electrolyte was replaced after the aging procedure by a fresh one for subsequent CVA measurements.

The turn-over frequency (TOF) at an overpotential of $\eta = 0.3$ V was calculated on the basis of surface Ni atoms according to:

$$TOF = \frac{j}{4 \cdot F \cdot n_{surf}} \tag{8-9}$$

where j is the current density (A cm^{-2}), F is the Faraday' constant, and n_{surf} is the surface concentration of Ni atoms (mol cm^{-2}). The surface concentration of Ni atoms was calculated from the mass loading of the films m (g cm^{-2}), the BET surface area of the nanoparticles of 2.1 10^6 cm^2 g^{-1} determined by Kr sorption and estimated surface density N_{NiO} of Ni atoms in NiO of $4.08 \cdot 10^{14}$ cm^{-2} according to:

$$n_{surf} = m * BET * N_{NiO}/N_A \tag{8-10}$$

where N_A is the Avogadro constant.

Alternatively, the number of electrochemically accessible Ni atoms was determined from the charge corresponding to the NiO redox reaction according to the equation:

$$NiO + OH^- - 1e^- \rightarrow NiOOH \tag{8-11}$$

assuming that only one electron is transferred per Ni atom. As the charge obtained from the anodic peak of the NiO redox process may contain some contribution from the OER process we have used the cathodic peak to determine the amount of the catalytically active Ni atoms.

8.5 References

(1) Finnerty, C. M.; Coe, N. J.; Cunningham, R. H.; Ormerod, R. M. *Catalysis Today* **1998**, *46*, 137.

(2) Shulga, J.; Kisand, V.; Kink, I.; Reedo, V.; Matisen, L.; Saar, A. In *Journal of Physics: Conference Series*; IOP Publishing: 2007; Vol. 93, p 012006.

(3) Nuli, Y.-N.; Zhao, S.-L.; Qin, Q.-Z. *Journal of power sources* **2003**, *114*, 113.

(4) Broussely, M.; Perton, F.; Biensan, P.; Bodet, J.; Labat, J.; Lecerf, A.; Delmas, C.; Rougier, A.; Peres, J. *Journal of power sources* **1995**, *54*, 109.

(5) Lv, W.; Sun, F.; Tang, D.-M.; Fang, H.-T.; Liu, C.; Yang, Q.-H.; Cheng, H.-M. *Journal of Materials Chemistry* **2011**, *21*, 9014.

(6) Srinivasan, V.; Weidner, J. W. *Journal of The Electrochemical Society* **1997**, *144*, L210.

(7) Avasthi, D.; Mehta, G. In *Swift Heavy Ions for Materials Engineering and Nanostructuring*; Springer: 2011, p 142.

(8) Ni, X.; Zhang, Y.; Tian, D.; Zheng, H.; Wang, X. *Journal of Crystal Growth* **2007**, *306*, 418.

(9) Ge, M.; Han, L.; Wiedwald, U.; Xu, X.; Wang, C.; Kuepper, K.; Ziemann, P.; Jiang, J. *Nanotechnology* **2010**, *21*, 425702.

(10) Titirici, M.-M.; Antonietti, M.; Thomas, A. *Chemistry of materials* **2006**, *18*, 3808.

(11) Liu, B.; Yang, H.; Zhao, H.; An, L.; Zhang, L.; Shi, R.; Wang, L.; Bao, L.; Chen, Y. *Sensors and Actuators B: Chemical* **2011**, *156*, 251.

(12) Pang, H.; Lu, Q.; Li, Y.; Gao, F. *Chemical Communications* **2009**, 7542.

(13) Yuan, Y.; Xia, X.; Wu, J.; Yang, J.; Chen, Y.; Guo, S. *Electrochemistry Communications* **2010**, *12*, 890.

(14) Salimi, A.; Sharifi, E.; Noorbakhsh, A.; Soltanian, S. *Biosensors and Bioelectronics* **2007**, *22*, 3146.

(15) Tench, D.; Warren, L. F. *Journal of The Electrochemical Society* **1983**, *130*, 869.

(16) Irwin, M. D.; Servaites, J. D.; Buchholz, D. B.; Leever, B. J.; Liu, J.; Emery, J. D.; Zhang, M.; Song, J.-H.; Durstock, M. F.; Freeman, A. J. *Chemistry of Materials* **2011**, *23*, 2218.

(17) Steirer, K. X.; Chesin, J. P.; Widjonarko, N. E.; Berry, J. J.; Miedaner, A.; Ginley, D. S.; Olson, D. C. *Organic Electronics* **2010**, *11*, 1414.

(18) Davar, F.; Fereshteh, Z.; Salavati-Niasari, M. *Journal of Alloys and Compounds* **2009**, *476*, 797.

(19) Garnweitner, G.; Niederberger, M. *Journal of the American Ceramic Society* **2006**, *89*, 1801.

(20) Djerdj, I.; Arčon, D.; Jagličić, Z.; Niederberger, M. *Journal of Solid State Chemistry* **2008**, *181*, 1571.

(21) Palanisamy, P.; Raichur, A. M. *Materials Science and Engineering: C* **2009**, *29*, 199.

(22) Deng, X.; Chen, Z. *Materials letters* **2004**, *58*, 276.

(23) Lai, T.-L.; Shu, Y.-Y.; Huang, G.-L.; Lee, C.-C.; Wang, C.-B. *Journal of Alloys and Compounds* **2008**, *450*, 318.

(24) Wuled Lenggoro, I.; Itoh, Y.; Iida, N.; Okuyama, K. *Materials research bulletin* **2003**, *38*, 1819.

(25) Qiao, H.; Wei, Z.; Yang, H.; Zhu, L.; Yan, X. *Journal of Nanomaterials* **2009**, *2009*, 2.

(26) Dharmaraj, N.; Prabu, P.; Nagarajan, S.; Kim, C.; Park, J.; Kim, H. *Materials Science and Engineering: B* **2006**, *128*, 111.

(27) Farhadi, S.; Roostaei-Zaniyani, Z. *Polyhedron* **2011**, *30*, 971.

(28) Wang, D. S.; Xie, T.; Peng, Q.; Zhang, S. Y.; Chen, J.; Li, Y. D. *Chemistry-A European Journal* **2008**, *14*, 2507.

(29) Wang, X.; Song, J.; Gao, L.; Jin, J.; Zheng, H.; Zhang, Z. *Nanotechnology* **2005**, *16*, 37.

(30) Thota, S.; Kumar, J. *Journal of Physics and Chemistry of Solids* **2007**, *68*, 1951.

(31) Sue, K.; Kawasaki, S.-i.; Suzuki, M.; Hakuta, Y.; Hayashi, H.; Arai, K.; Takebayashi, Y.; Yoda, S.; Furuya, T. *Chemical Engineering Journal* **2011**, *166*, 947.

(32) Beach, E. R.; Shqau, K.; Brown, S. E.; Rozeveld, S. J.; Morris, P. A. *Materials Chemistry and Physics* **2009**, *115*, 371.

(33) Feckl, J. M.; Fominykh, K.; Döblinger, M.; Fattakhova-Rohlfing, D.; Bein, T. *Angewandte Chemie International Edition* **2012**, *51*, 7459.

(34) Liu, Y.; Szeifert, J. M.; Feckl, J. M.; Mandlmeier, B.; Rathousky, J.; Hayden, O.; Fattakhova-Rohlfing, D.; Bein, T. *ACS nano* **2010**, *4*, 5373.

(35) Szeifert, J. M.; Feckl, J. M.; Fattakhova-Rohlfing, D.; Liu, Y.; Kalousek, V.; Rathousky, J.; Bein, T. *Journal of the American Chemical Society* **2010**, *132*, 12605.

(36) Desvaux, C.; Amiens, C.; Fejes, P.; Renaud, P.; Respaud, M.; Lecante, P.; Snoeck, E.; Chaudret, B. *Nat Mater* **2005**, *4*, 750.

(37) Mironova-Ulmane, N.; Kuzmin, A.; Steins, I.; Grabis, J.; Sildos, I.; Pärs, M. In *Journal of Physics: Conference Series*; IOP Publishing: 2007; Vol. 93, p 012039.

(38) Gorschlüter, A.; Merz, H. *Physical Review B* **1994**, *49*, 17293.

(39) Gonzalez-Elipe, A. R.; Holgado, J. P.; Alvarez, R.; Munuera, G. *The Journal of Physical Chemistry* **1992**, *96*, 3080.

(40) Adler, D.; Feinleib, J. *Physical Review B* **1970**, *2*, 3112.

(41) Li, X.; Zhang, X.; Li, Z.; Qian, Y. *Solid state communications* **2006**, *137*, 581.

(42) Biesinger, M. C.; Payne, B. P.; Lau, L. W. M.; Gerson, A.; Smart, R. S. C. *Surface and Interface Analysis* **2009**, *41*, 324.

(43) Lyons, M. E.; Brandon, M. P. *Int. J. Electrochem. Sci.* **2008**, *3*, 1386.

(44) Yeo, B. S.; Bell, A. T. *The Journal of Physical Chemistry C* **2012**, *116*, 8394.

(45) Trotochaud, L.; Ranney, J. K.; Williams, K. N.; Boettcher, S. W. *Journal of the American Chemical Society* **2012**, *134*, 17253.

9 Enhancement of the water splitting efficiency of mesoporous hematite films by surface enrichment of Sn-atoms

This chapter is based on the following publication:

Halina K. Dunn*, Johann M. Feckl*, Alexander Müller, Dina Fattakhova-Rohlfing, Laurence M. Peter, Christina Scheu, Thomas Bein, to be submitted.

*these authors contributed equally

9.1 Introduction

The photoelectrochemical splitting of water into hydrogen and oxygen under solar irradiation could provide a vital fuel for a future low-carbon energy economy. In order to utilize as much of the solar spectrum as possible, a tandem architecture is likely to prove the most efficient design for a water splitting system. This can either be achieved by using one wider bandgap semiconductor in contact with an aqueous solution connected in optical series to a low-cost solar cell absorbing in the near IR part of the solar spectrum,[1,2] or by a series connection of two semiconductor photoelectrodes - one n-type and one p-type - in contact with an aqueous electrolyte. Regardless of which design ultimately proves to be the most effective, research into semiconductor materials able to perform one of the half-reactions must overcome the many factors that currently limit performance.

Chemical stability, abundance, visible light absorption and suitable valence band energy make hematite a very promising material for the light-driven oxygen evolution reaction. However, its relatively weak absorbance (owing to its indirect bandgap) and poor carrier mobilities lead to an inherent trade-off between sufficient light absorption and carrier collection. Nano-

structuring provides an elegant solution to this issue by decoupling the hole collection depth from the light absorption depth.[3] Vapor-phase deposition techniques and spray pyrolysis have been used to produce high surface area materials.[4,5] However, these usually consist of comparably large structures with textural porosity, rather than homogeneously porous structures. Various solution-based synthetic routes have provided hematite films with a more uniform porosity, but the performance of these materials has not yet matched the efficiencies of films prepared by vapor phase methods when moderate calcination temperatures of around 600 °C are used.[6-9] Indeed, the first high-efficiency colloidal-based films required an 800 °C calcination step,[6] during which the crystallites grew, and it was suggested that the hematite film was doped by Sn-atoms from the fluorine-doped tin oxide (FTO) substrate. Bohn *et al.*[9] subsequently proved this hypothesis by preparing hematite films on substrates that did not contain Sn, which showed no photoactivity even after an 800 °C heat treatment. However, such high-temperature treatments lead to a degradation of the FTO substrate along with a decrease in surface area of the porous hematite layer and inhomogeneous and uncontrolled doping by tin and fluorine. Incorporation of tin into the hematite particles from a suitable precursor during low temperature synthesis is therefore an attractive alternative to high-temperature processing. Ling[7] and co-workers obtained Sn-doped hematite nano-corals by a hydrothermal procedure, yielding AM 1.5 photocurrents of 0.94 $mAcm^{-2}$ at 1.23 V vs. RHE with calcination temperatures as low as 650 °C. However, the addition of a Sn-precursor to the synthesis led to a substantial morphological change, making it difficult to distinguish between the electronic and morphological effects of the Sn dopant. Very recently,[8] Sn-doping has been achieved by spin-coating a solution containing tin and iron precursors onto FTO glass followed by a 650 °C sintering step. These films gave currents of up to 0.45 mA cm^{-2} at 1.43 V vs. RHE under AM 1.5 illumination.

Here, we report a synthetic strategy allowing Sn-inclusion up to 3.2 ± 1.5 % atomic ratio into mechanically stable mesoporous hematite films with limited morphological change. Our synthesis requires a calcination temperature of only 600 °C, the lowest reported calcination temperature for solution-processed hematite resulting in efficiencies comparable to vapor-deposited materials. Mesoporous layers up to 350 nm thick prepared by sequential spin coating and sintering steps give AM 1.5 photocurrent densities of 0.41 mA cm^{-2} at 1.23 V vs. RHE at pH 13 – over a third higher than previous work on a similar system.[8] The in-depth characterization of the prepared hematite layers was performed using analytical transmission electron microscopy (TEM), which probes the degree of Sn-incorporation in the bulk of the crystallites, and enables insights into the spatial distribution of Sn in the mesoporous hematite.

Similar to Sn,[6-9] many substituents, such as Si,[4,5,10] Ti,[11-14] Pt,[15,16] Cr,[17] Mo,[17] Zn[18] and I,[19] have been reported to significantly improve the performance of hematite photo-anodes. In practice, one of the most widely encountered effects of 'doping' is a modification of the nanostructure morphology, leading in many cases to a reduction in feature size, and thus an increase in surface area.[4,6,7,9-11,14,17,20,21] Although this effect may be partly responsible for the improved photoelectrochemical (PEC) characteristics, it complicates the task of uncovering the other possible roles played by the dopant atoms. Several studies have attributed the effect of 'doping' to changes in properties such as conductivity,[9] electron density[7,9,10,20] or crystallinity.[4] We have taken a different approach, in which the role of dopants is inferred from the PEC behavior itself. For example, comparison of the photocurrent for illumination from the electrolyte and substrate sides can help identify improvements in electron collection brought about by doping. Kahn and Zhou[19] found that I-doping in hematite prepared by spray pyrolysis increased the effective electron collection depth from 50 to 100 nm. Cesar *et al.*[20] did not encounter electron collection limitations in Si-doped hematite grown by CVD up to

600 nm, whereas undoped films suffered very high collection losses for 300 nm films. A thickness-dependence study on Ti-doped hematite grown by ALD revealed that doping reduced electron-hole recombination at the FTO-hematite interface, also known as the so-called "dead layer effect".[22] A reduction in recombination upon Pt-doping was also deduced from the dependence of photocurrent on light intensity, which changed from square root to linear upon Pt-doping.[15] Furthermore, frequency-resolved methods such as intensity-modulated photocurrent spectroscopy (IMPS)[23] and electrochemical impedance spectroscopy (EIS)[24-27] can help identify relevant time constants such as those associated with recombination and hole transfer kinetics.

The results of the present study show that the incorporation of tin into mesoporous hematite films not only improves the efficiency of hole transfer to the electrolyte but also suppresses electron-hole recombination at the FTO substrate as reported recently by Zandi *et al.*[22] for Ti-doped hematite.

The following experiments have been performed as a joint project: The Sn-containing hematite electrodes were synthesized and characterized by Johann M. Feckl. TEM measurements were conducted by Alexander Müller in the group of Prof. Christina Scheu. Testing of the performance in photoelectrochemical water splitting was done by Halina K. Dunn in the group of Prof. Thomas Bein.

9.2 Experimental

Synthetic route for incorporation of Sn in mesoporous hematite electrodes

Hematite precursor solutions were prepared according to the following procedure. 0.630 g (1.56 mmol) $Fe(NO_3)_3 \cdot 9\,H_2O$ was dissolved in a solution of the block copolymer Pluronic P123 (0.25 g) in 10 mL *tert*-butanol under sonication for 15 minutes. 2.5 mL water (Millipore) was then added, forming a dark red solution. The solution was stirred at room temperature overnight resulting in a light brown dispersion of iron oxide (Fe_2O_3). The synthesis is a development of the protocol described by Redel *et al.*.[28] However these authors did not use Pluronic P123, and the synthesis led to formation of a two-phase mixture of hematite and maghemite, in the ratio of 65:35.

For the preparation of the Sn-containing hematite, $Sn(OAc)_4$ was added to the solution described above. The desired amounts of $Sn(OAc)_4$ were first dispersed under vigorous stirring for 5 h and 15 min sonication in the above mixture of Pluronic P123 and *tert*-butanol, followed by the remaining steps as described above for pure hematite. Throughout the following text, the Sn:Fe-ratio refers to the atomic ratio of the two elements in the precursor solutions, unless otherwise stated.

After cleaning the FTO glass (Pilkington TEC 15 Glass™, 2.5 x 1.5 cm) by sequential sonication for 15 min each in detergent (1 mL Extran in 50 mL Millipore water), water (Millipore) and ethanol, the substrates were dried and masked with Scotch Tape on the conducting side to retain a non-covered area of 1.5 x 1.5 cm. The backs of the substrates were completely masked to avoid contamination during the spin-coating procedure.

Before spin-coating, the fresh solutions were filtered through a 220 nm syringe filter (Sartorius minisart cellulose acetate membrane) to remove agglomerates, ensuring the preparation of homogeneously smooth films. The masked substrates were covered with 100 µL of solution and spun at 1000 rpm for 30 seconds. To obtain thicker films, the films were dried for 5 minutes at 60 °C and the spin-coating step was repeated. To remove the template and crystallize the material, the samples were calcined in a laboratory oven (3 hour ramp to 600 °C, 30 min dwell time). This results in films of about 50 nm thickness, which can be scaled up linearly by repeating the complete procedure. Powders for X-Ray diffraction (XRD) and TEM analysis were obtained by scraping material off the thin films with a razor blade.

Thin film characterization

XRD measurements were performed on a STOE powder diffractometer in transmission geometry (Cu-Kα_1, λ = 1.5406 Å) equipped with a position-sensitive Mythen-1K detector or in reflection mode using a Bruker D8 Discover with Ni-filtered Cu-K_α-radiation and a position-sensitive detector (LynxEye). Scanning electron microscopy (SEM) was performed on a JEOL JSM-6500F scanning electron microscope equipped with a field emission gun. The UV-visible transmission and reflection of the mesoporous thin films on FTO was measured with a Perkin Elmer Lambda 1050 spectrophotometer equipped with an integrating sphere. For transmission measurements, the sample was placed directly outside the integrating sphere with the film facing in, and for reflection measurements, the sample was placed directly after the integrating sphere with the glass facing the incoming beam. The absorbance *A* was calculated from the transmission *T* and reflectance *R* according to the following formula:

$A = \log(T+R)^{-1}$. The absorbance of the FTO substrate, calculated in the same way, was then subtracted from the full sample, resulting in the absorbance of the hematite film alone.

Material was scraped from the thin films, and deposited on a copper grid with a carbon film for TEM analysis. The analysis was carried out on a FEI Titan 80-300 (S)TEM with a Fischione Instruments (Model 3000) high angle annular dark field (HAADF) detector and an EDAX Energy-dispersive X-Ray Spectroscopy (EDX) detector. All measurements were conducted at an acceleration voltage of 300 kV.

Photoelectrochemical characterization

Hematite photoelectrodes, such as those depicted in Figure 9-4, were masked with a Teflon-coated glass fiber adhesive tape leaving a circular area of 1 cm in diameter exposed to a 0.1 M NaOH aqueous electrolyte. All electrochemical measurements were carried out with glass or quartz cells using a µ-Autolab III potentiostat equipped with a FRA2 impedance analyzer connected to a saturated Ag/AgCl (or a Hg/HgO) reference electrode and a Pt mesh counter electrode. The light intensity was measured inside the cells using a 4 mm^2 photodiode, which had been calibrated against a certified Fraunhofer ISE silicon reference cell equipped with a KG5 filter.

The current-voltage characteristics of the films were obtained by scanning from negative to positive potentials in the dark or under illumination, with a 20 mV s^{-1} sweep rate. Illumination that was either provided by a power light emitting diode (LED, Thorlabs, 455 nm), or AM1.5G solar simulator (Solar Light Model 16S) at 100 mW cm^{-2}, was incident either through the substrate (SI) or the electrolyte (EI). For external quantum efficiency (EQE) measurements, chopped monochromatic light (chopping frequency 2 Hz) was provided by a 150 W xenon lamp in combination with a monochromator and order-sorting filters. The cell

was biased to 1.23 V vs. RHE under simulated solar irradiation to ensure realistic operating conditions. The current recorded by the Autolab potentiostat was output to a lock-in amplifier synchronized to the chopper frequency. Current transients were used to determine the transfer efficiency of holes to the solution phase.[23] The high power LED was switched on and off every 500 ms. The hematite electrodes were held at a given potential, and the transient current was sampled at 0.1 ms intervals. This fast sampling allowed the instantaneous current to be determined. In cases where the current transient had not reached a steady state value after 500 ms, additional photocurrent transients were recorded with 5 s on/off times, sampled at 1 ms intervals.

9.3 Results and discussion

Materials

Synthesis. In this work, hematite thin films were prepared via a solution-based method. An iron precursor ($Fe(NO_3)_3 \cdot 9\ H_2O$) was dissolved in a solution of Pluronic P123 in *tert*-butanol. For the preparation of the Sn-containing hematite, $Sn(OAc)_4$ was added to this solution in different Sn:Fe-ratios. Throughout the following text, the Sn:Fe-ratio is described as the atomic ratio of the two elements in the precursor solutions, unless otherwise stated. After the addition of water, the solution was aged overnight forming a brown precipitate. This mixture was then filtered through a syringe filter with 220 nm pores to remove agglomerates and the filtrate was utilized for spin-coating the hematite films. Pluronic P123 and solution ageing are necessary to provide the porous morphology of the films and the good crystallinity of the hematite, respectively, necessary for high performance in water splitting experiments. To remove the organic structure-directing agent and to fully crystallize the hematite films, the

films were calcined at 600 °C. By using this protocol it is possible to produce very thin films of around 50 nm. Films up to 350 nm in thickness were obtained by repeatedly coating multiple layers with an intermediate heat treatment at 600 °C.

Evidence of Sn-inclusion. The powder XRD spectra in Figure 9-1a exclusively show the α-Fe_2O_3 hematite phase, with a peak shift of approximately 0.1° to smaller angles upon Sn-inclusion, indicating a lattice distortion brought about by inclusion of impurity atoms.[29] This shift corresponds to an increase of the lattice parameter, *a*, from 5.036 to 5.043 Å. Additionally, the inversion of intensities of the two reflections in the range of 33 to 36° 2θ as described by Berry et. al can be observed.[29] The mean crystallite size, as calculated from the broadening of the (104) reflection according to the Scherrer equation, drops from 50 to 30 nm upon inclusion of Sn.

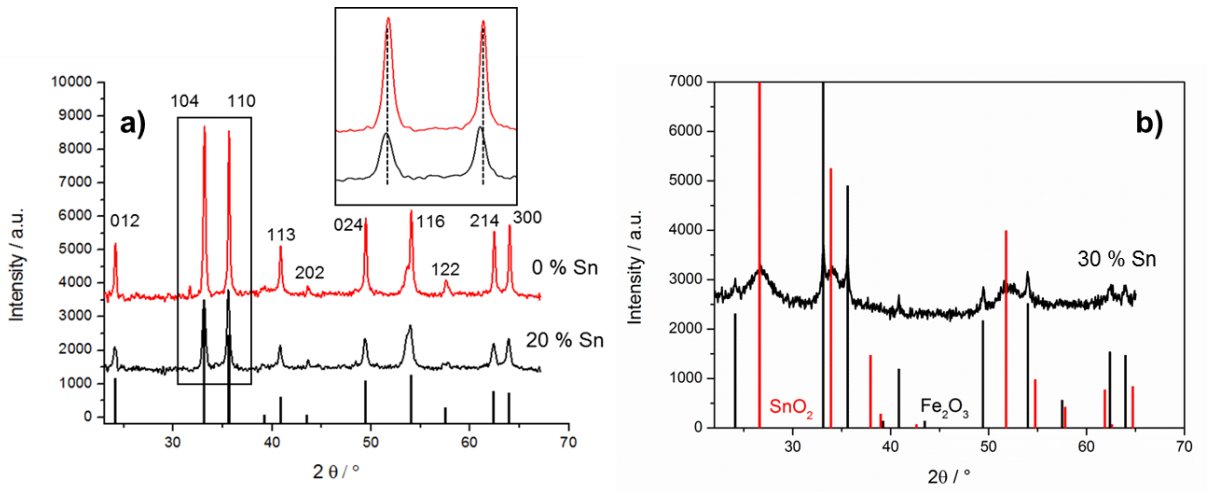

Figure 9-1: a) Powder XRD data of hematite and 20% Sn-containing hematite and below the ICDD card 01-085-0987 of hematite. The inset shows peak shifts due to lattice distortion upon inclusion of Sn atoms. b) XRD data of 30 % Sn-containing (as precursor) hematite with phase impurities of SnO_2 (ICDD 01-075-9493).

Effect of Sn-inclusion on morphology. The effect of Sn-incorporation into hematite was studied by SEM and TEM, see Figure 9-2. The SEM images show a disordered mesoporous "worm-like" structure for both the pure hematite sample (Figure 9-2a), and the sample prepared with 20 % Sn-precursor added to the synthesis (Figure 9-2b). The morphology is very similar to that seen for hematite films prepared by other solution-based synthetic routes.[6,7,9,30,31] Also in accordance with literature, the feature size appears to decrease slightly upon doping. The morphology of the films was further examined by TEM. In both pure hematite (Figure 9-2c) and that prepared with 20 % Sn-precursor (Figure 9-2d), nanoparticles with an elongated morphology were observed, along with smaller particles with an undefined morphology. The size histograms of both samples as shown in Figure 9-2 e and f were calculated for the particle lengths with bin widths of 5 nm. Both histograms show a broad size distribution peaking at around 40 nm, with a length to width ratio of around two in both cases. However, the distribution extends to longer particle lengths for the pure hematite sample as compared to the Sn-containing sample. Hence, our XRD, SEM and TEM investigations agree on a reduction in feature size upon Sn-incorporation. Although this observation fits the general trend, we note that this change in feature size is less extreme than in other reports, such as the reduction in hematite nanowire length from 600 to 100 nm upon Sn-doping reported by Ling *et al.*[7]

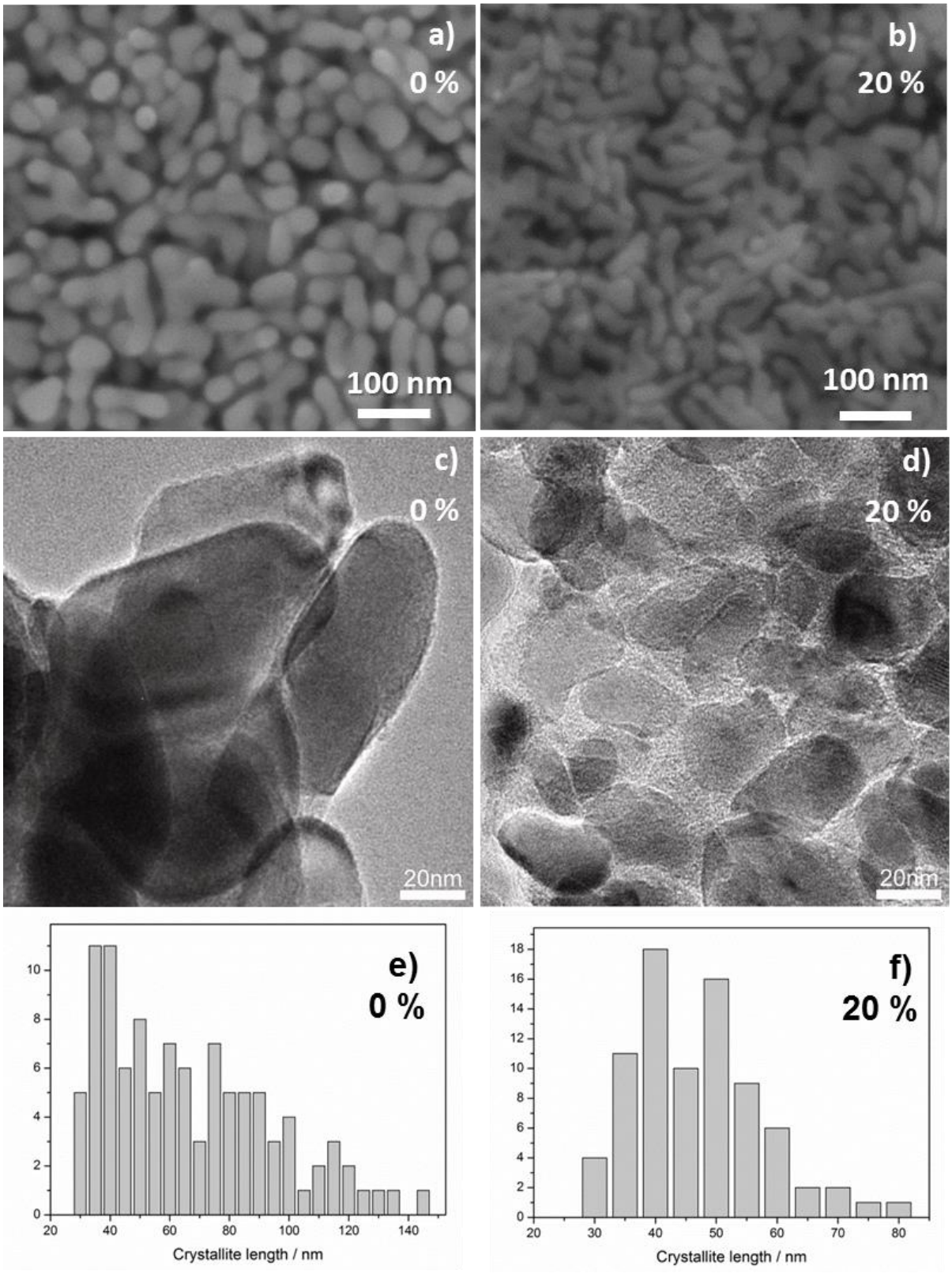

Figure 9-2: Effect of Sn-inclusion on morphology of the pure hematite sample (left side) and the sample prepared with 20 % Sn-precursor added to the synthesis (right side). Top-view SEM images, a) and b). Bright field TEM images, c) and d). Histograms of the length of the nanoparticles, e) and f). The width of each integral was chosen to be 5 nm. Each item is labeled with the percentage of Sn-precursor added to the hematite synthesis.

Quantification of Sn-inclusion. To quantify the Sn-inclusion in the 20 % Sn-precursor containing sample, EDX was employed and 25 spectra were acquired. For these measurements, both the position of the electron beam and its diameter were chosen at random, leading to EDX-measurements of large areas of multiple micrometers as well as of individual particles. As all measurements yielded similar Sn contents, homogeneity at this scale can be assumed and a mean Sn-concentration of 3.2 ± 1.5 % was calculated.

Since these measurements did not probe the distribution of Sn within the individual particles, scanning transmission electron microscopy (STEM) was employed in combination with EDX to probe the Sn-content with a spatial resolution of approximately 2 nm. Line scans across the width of a particle can reveal inhomogeneities between surface and bulk compositions, as illustrated in the inset of Figure 9-3b. A total of 6 particles were probed along lines approximately perpendicular to the surface, such as the one depicted in Figure 9-3a. Due to an insufficient signal-to-noise (S/N)-ratio, the spectra could not be quantified. However, the ratio of the intensity of the signal attributable to Sn and that obtained from both Sn and Fe revealed a Sn-enrichment at all measured surfaces. The Sn-content strongly decays towards the middle of the particle, where very little signal attributable to Sn was detected. Thus, the introduction of a Sn-precursor into the hematite synthesis leads to a core-shell structure with incorporated Sn-atoms preferentially located near the surface.

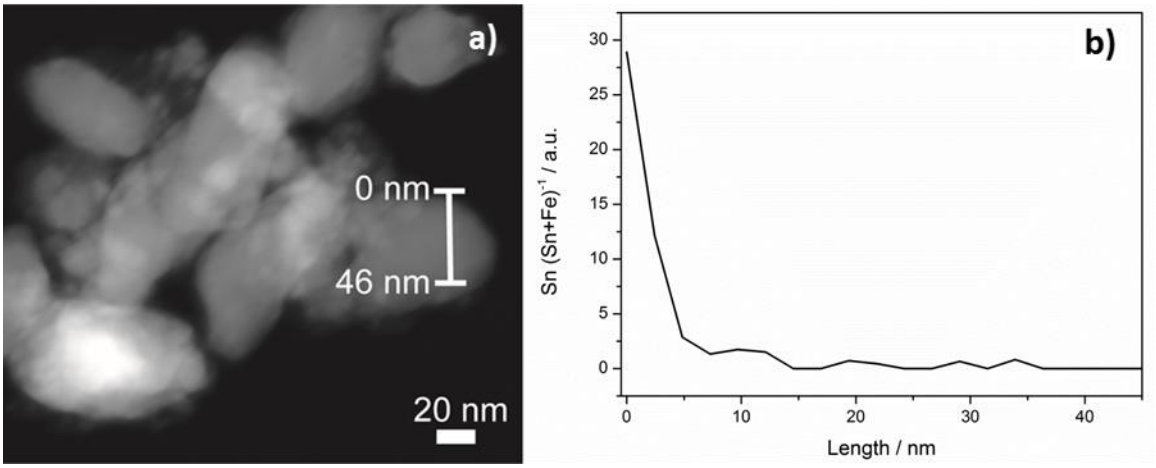

Figure 9-3: a) a HAADF-STEM image of the particles probed with EDX and b) relative atomic content of Sn detected in the line scan. The placement of the line scan displayed in b) is marked in a).

Multilayer films. In order to optimize the light harvesting potential and to allow studies of the electron collection efficiency across the porous network, multilayer-films with thicknesses ranging from 50 to 350 nm were prepared. The SEM cross-section images and photographs of films of 1 to 7 layers, which can be seen in Figure 9-4 a and b, suggest that the film thickness scales well with the number of layers. This is confirmed by the UV-visible absorption spectra of the films in Figure 9-5.

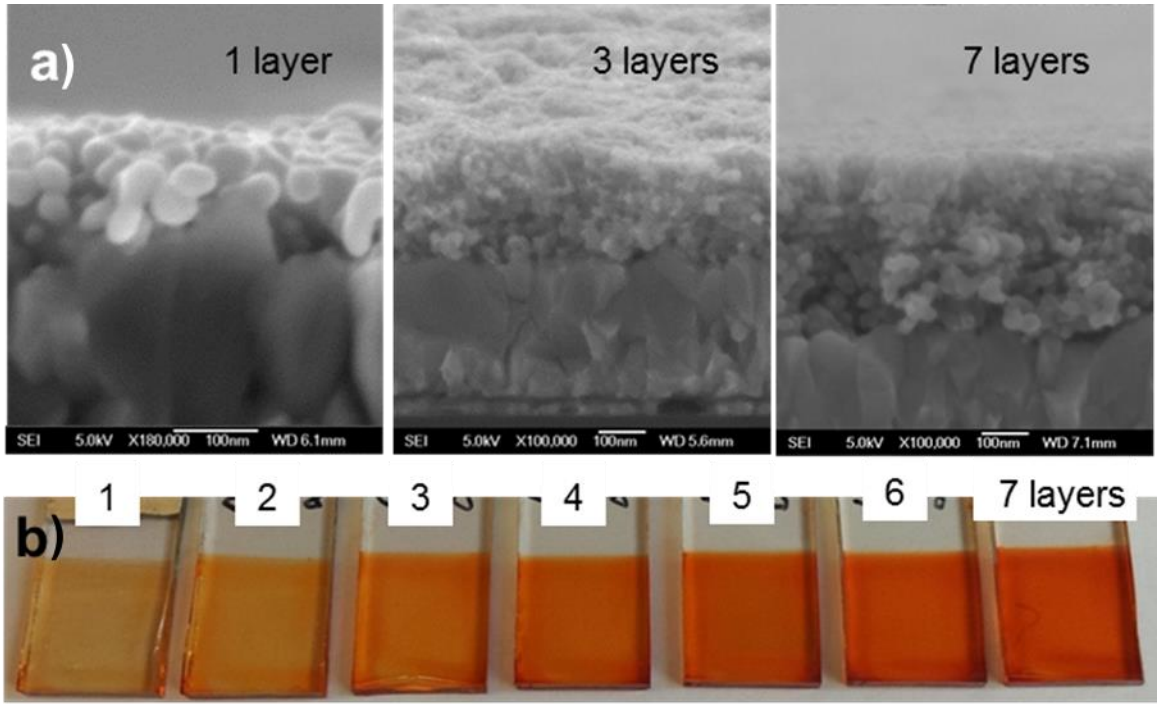

Figure 9-4: Thickness and morphology of multilayer films. a) SEM cross sections of 1, 3 and 7 layered films. b) Photograph of 1 to 7 layer films. All films were prepared with 20 % Sn-precursor added to the synthesis.

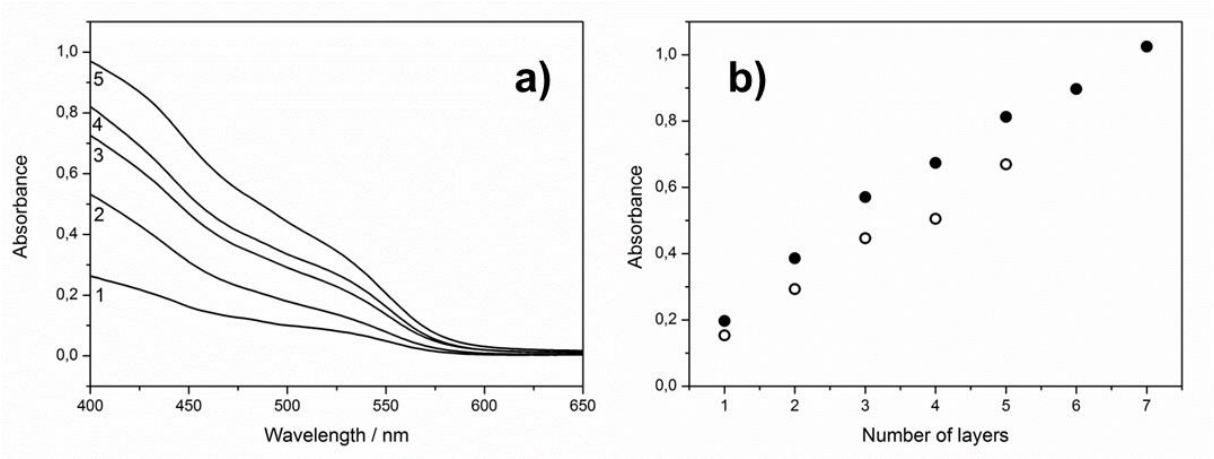

Figure 9-5: a) UV-visible absorption spectra of 1 to 5 layer films. b) Comparison of the absorbance at 454 nm as a function of the number of layers: 20 % Sn-precursor containing hematite films (filled markers) and films of pure hematite (empty markers).

Optimization of Sn content

Figure 9-6 compares the current-voltage characteristics of single-layer films prepared by adding 0 %, 5 %, 10 %, 20 % and 30 % of a Sn-precursor to the hematite synthesis. In the case of the pure hematite film, the photocurrent barely reaches tens of microamperes. For films prepared by using precursor solutions with a Sn-content above 5 %, the photocurrent increases substantially, reaching a maximum for the film prepared from the solution containing 20 % Sn. The drop in photocurrent at 30 % Sn-incorporation is accompanied by a significant change in morphology, and there is evidence for a phase separation and the appearance of a SnO_2 phase (Figure 9-1b).

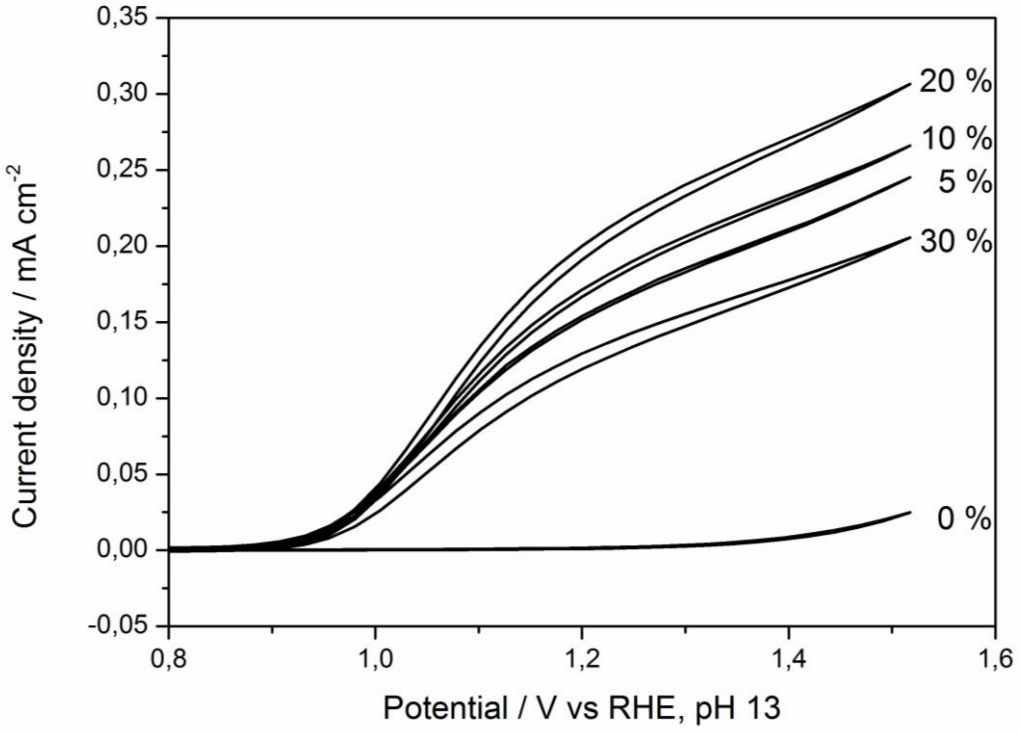

Figure 9-6: Current-voltage curves for single layers of mesoporous hematite (red) and hematite to which 5 %, 10 %, 20 % and 30 % Sn-precursor was added to the synthesis. Illumination through the substrate from a high power 455 nm LED, incident photon flux: 10^{17} $cm^{-2}s^{-1}$.

Role of Sn

To elucidate the role of Sn-incorporation in our system, photocurrent transients were recorded (Figure 9-7 a). The spike and overshoot of the current transients are typical of semiconductor electrolyte interfaces with a large degree of surface electron-hole recombination.[23] The instantaneous photocurrent can be thought of as a charging current of photo-generated holes to the surface. The steady-state photocurrent corresponds to the flux of holes transferred to the electrolyte without undergoing recombination with electrons at the surface. The ratio of steady state to instantaneous photocurrents is thus a measure of the efficiency of hole-transfer from the electrode to the electrolyte. It should be noted that this interpretation is valid for a bulk semiconductor with a well-defined depletion layer at the interface with the electrolyte. Although here this is not strictly speaking the case, the morphology of the films used to produce Figure 9-6 and Figure 9-7 (a monolayer of crystallites 50 – 100 nm in size) does approximate this situation, albeit one with a rather rough surface. Indeed, in a recent study, Zandi et al.[22] showed that for compact hematite films up to 70 nm in thickness, the depletion region did not extend across the whole film over the voltage range relevant here. Given that the size of our particles is of this order, we conclude that they should not be fully depleted, and the analysis of current transients should be valid, if only qualitatively for the comparison of films with similar morphologies. It is clear from the photocurrent transients in Figure 9-7a that almost all holes reaching the surface of the pure hematite sample recombine, leading to a negligible steady state photocurrent. The transfer efficiency, extrapolated from the current transients, increases steadily with increased doping (Figure 9-7b). Although the 30 % Sn-containing film appears to exhibit the highest hole transfer efficiency, this value should be taken with caution, as the morphology of that sample differs significantly from the rest of the series.

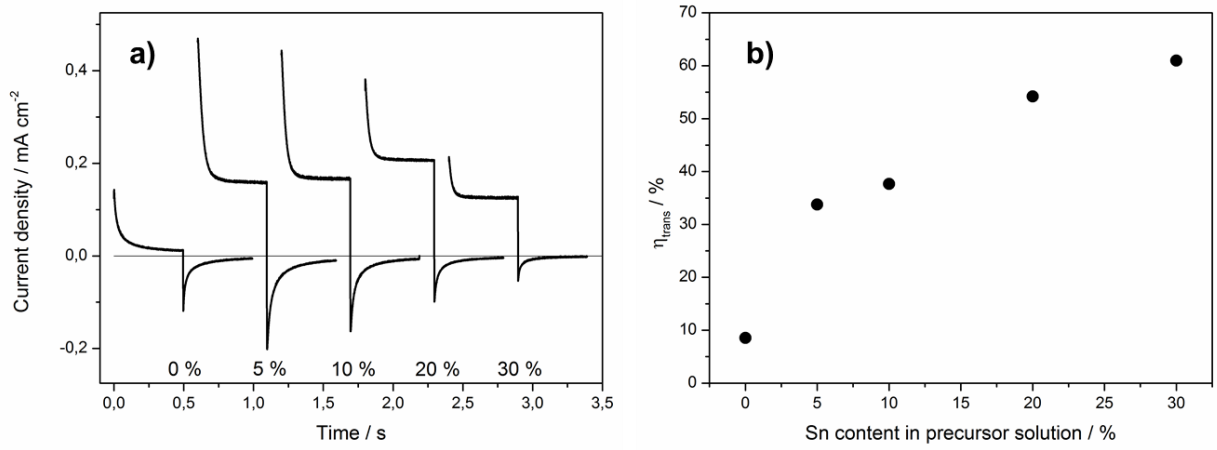

Figure 9-7: a) Photocurrent transients of hematite and Sn-doped hematite and b) transfer efficiency in relation to Sn content (0 %, 5 %, 10 %, 20 % and 30 % Sn precursor). Measured at 600 mV vs. sat. Ag/AgCl under 455 nm illumination, intensity 10^{17} $cm^{-2}s^{-1}$.

The observation that the beneficial effect of Sn-incorporation is related to an increase in transfer efficiency narrows down the possible physical explanations for this effect. On the one hand, the transfer efficiency can be affected by the rate of transfer of holes across the interface, the kinetics of which are known to be very slow in hematite.[32] On the other hand, given the slow transfer kinetics mentioned above, surface electron-hole recombination can be very detrimental to the transfer efficiency, and suppression of recombination significantly enhances performance.[23,33] Methods to differentiate between these two effects include the direct observation of the decay kinetics of surface holes by transient absorption spectroscopy (TAS),[32,33] and the extrapolation of the relevant time constants from frequency-resolved perturbation techniques, such as intensity modulated photocurrent spectroscopy (IMPS).[23] We expect an ongoing investigation in this area to further distinguish between these two possibilities. Furthermore, the spatial segregation of Sn to the surface of the nanoparticles, revealed by STEM in Figure 9-3, fits well to the observation that Sn-inclusion improves a surface property such as the transfer efficiency.

Ultrathin layers of hematite are known to perform particularly badly as photoanodes for water splitting, which has been explained by pronounced recombination between electrons and

holes at the FTO-hematite interface. Interfacial layers, such as SiO_x[34] or Nb_2O_5,[35] as well as Ti-doping[22] have been shown to reduce surface recombination. Similarly, attempts to produce ultra-small capacitors are limited by the so-called “dead layer effect”, possibly due to recombination at the semiconductor metal interface.[36] A parallel has been drawn between these two phenomena, and the poor performance of thin hematite is also commonly referred to as the “dead layer effect”.

The photocurrents of hematite films of different layer thicknesses based on 0 % and 20 % Sn-precursor are displayed in Figure 9-8. For very thin films of pure hematite, a negligible steady state photocurrent is detected, only beginning to increase above 3 layers. This is likely to be a manifestation of the dead layer effect. For films prepared with 20 % Sn-precursor content, in contrast, even the very thinnest films yield a significant photocurrent, indicating that the inclusion of Sn-atoms may be passivating electron-hole recombination centers at the interface between the FTO substrate and the hematite absorber layer. The steep rise in photocurrent between the 1- and 2-layer films indicates that the dead layer effect could still be affecting the Sn-containing films, only to a lesser degree. Recently, Zandi *et al.*[22] observed a similar effect upon Ti-doping of hematite layers formed by atomic layer deposition (ALD). For thin films, the photocurrent was significantly lower for the undoped material. Interestingly, above 40 nm the undoped material’s performance reached that of the doped material in their system.

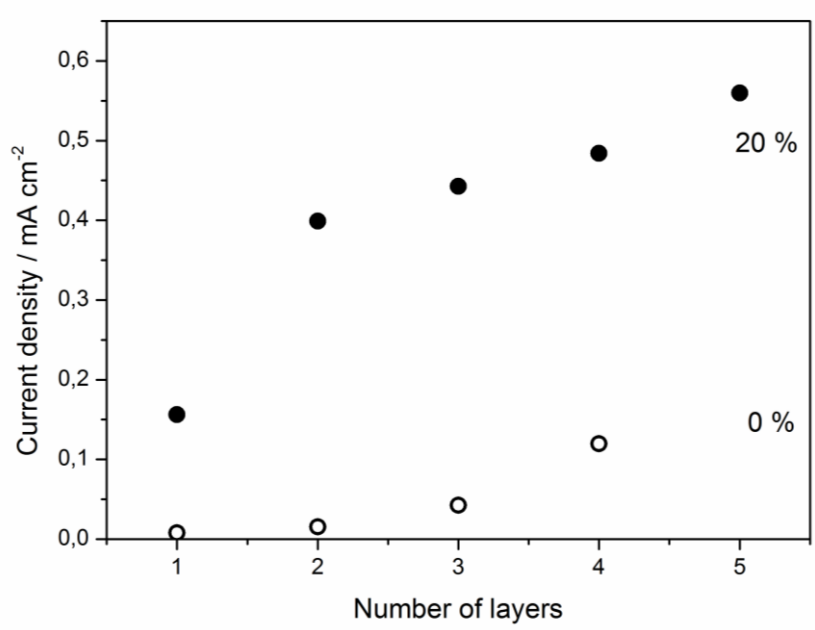

Figure 9-8: Thickness dependence of the photocurrent density obtained at 500 mV vs. sat. Ag/AgCl under 455 nm illumination with a photon flux of 10^{17} $cm^{-2}s^{-1}$ through the substrate (J_{SI}).

Evidence for recombination

In order to study how efficiently electrons are collected throughout the mesoporous layers, the current response to strongly absorbed illumination incident from the substrate (SI) and the electrolyte (EI) were compared. Firstly, the EI and SI photocurrents due to illumination by a high-power blue LED were recorded for films one to five layers thick. It is clear from Figure 9-9a that when light is incident through the electrolyte, electrons are less efficiently collected than when illuminated through the substrate, in particular as the film thickness increases. This is evidence that a significant proportion of electrons generated far from the collecting substrate are lost to recombination. The same effect is also observed in the IQE data recorded from EI and SI. The IQE, which is the quotient of the EQE and the light harvesting efficiency determined from absorbance measurements, corresponds to the product of charge separation efficiency (i.e. the formation of long-lived electrons and holes, in competition with electron hole recombination) and the hole transfer efficiency. When illumination is incident from the electrolyte, the IQE decreases linearly as the film thickness increases, indicating that electrons

are not efficiently collected. When illuminated through the substrate, in contrast, the IQE initially increases from 1 to 2 layers, and is then approximately constant for thicker films. Assuming the hole transfer efficiency to be independent of the position across the film, this would be evidence that this composition of matter still suffers from significant electron-hole recombination. Further synthetic work will thus address this issue by developing surface treatments or to chemically modify the photoactive materials to reduce this recombination.

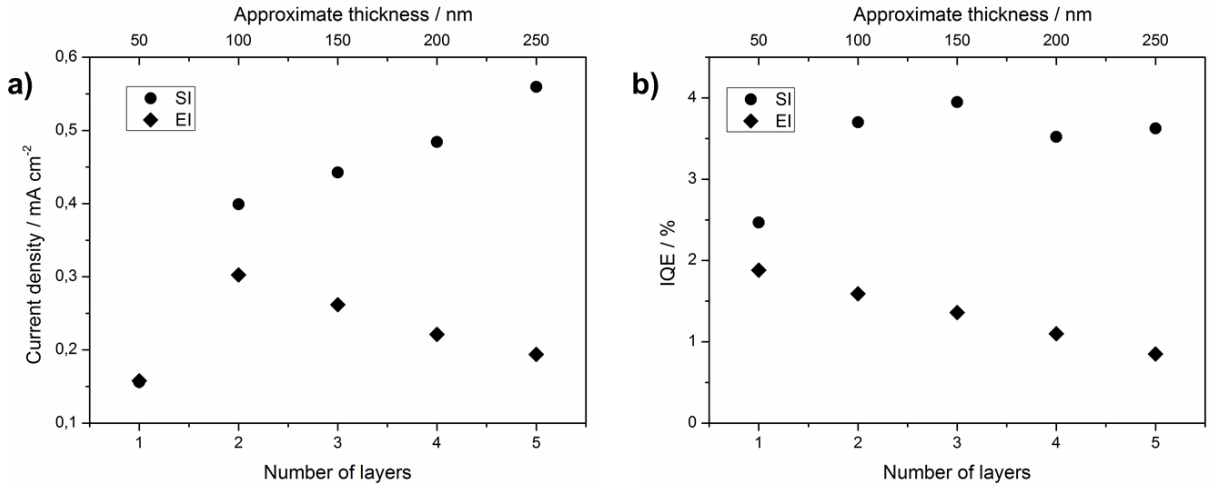

Figure 9-9: Response to illumination from the substrate (SI, circles) and the electrolyte (EI, diamonds) of 20 % Sn-precursor containing hematite layers of various thicknesses, recorded at 1.19 V vs. RHE. a) Photocurrent under 455 nm irradiation (10^{17} $cm^{-2}s^{-1}$) b) IQE measured at 455 nm under 1 Sun bias light.

Optimized photoanode

By inclusion of Sn atoms into our mesoporous hematite layers, we achieved a photocurrent of 0.41 $mAcm^{-2}$ under AM 1.5 illumination at 1.23 V vs. RHE for a 300 nm film after calcination at only 600 °C (Figure 9-10). These relatively thick films, obtained by sequential spin coating and sintering steps, allowed us to reach 0.62 $mAcm^{-2}$ at 1.43 V vs. RHE at pH 13 under one Sun illumination, which is more than a third higher than solution-processed films prepared by Frydrych *et al.*[8] As they remarked in their recent article, although this photocurrent does not rival those of vapor-phase deposited hematites, the simplicity of the

synthesis may make it a very attractive approach for industry. Furthermore, the solution-processed nature makes this route highly applicable to host-guest architectures that are comprised of an electron conducting porous host and a photoactive material as a guest in the pores.

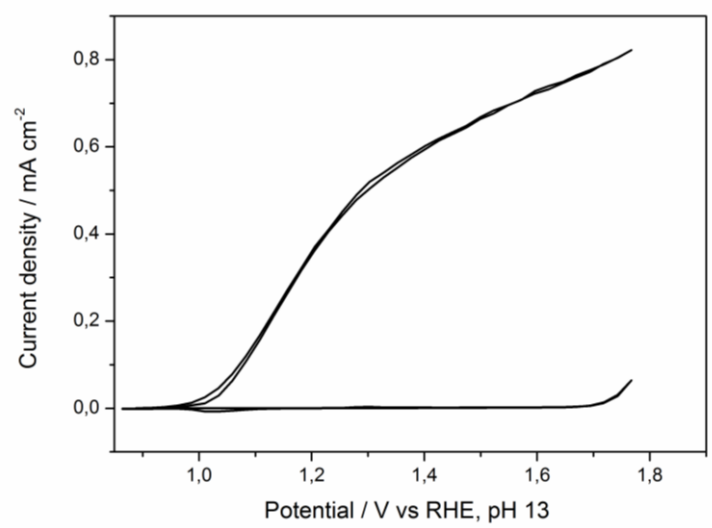

Figure 9-10: Current-potential curve of a 5-layer mesoporous hematite film prepared with 20 % Sn-precursor under AM 1.5 illumination.

9.4 Conclusion and outlook

We present an efficient synthetic strategy to produce mesoporous Sn-containing hematite films up to 350 nm thick that give photocurrents of 0.41 mA cm^{-2} under AM 1.5 illumination at 1.23 V vs. RHE. A detailed TEM/EDX study of both the bulk mesoporous thin-film material and a large number of individual particles concluded a 3.2 ± 1.5 % atomic ratio of Sn-inclusion for 20 % Sn-precursor samples. STEM EDX line scans revealed a Sn-enrichment at the surface of the nanoparticles. By studying photocurrent transients to chopped illumination, we can assign the role of Sn-doping to an increase in hole transfer efficiency to the electrolyte. Ongoing TAS and IMPS studies will determine whether this is due to an increase in catalytic activity or a reduction in electron hole recombination at the

semiconductor electrolyte interface. A thickness-dependence study also indicated that a passivation of the so-called “dead layer effect” contributes to the beneficial effect of Sn-inclusion, by reducing electron-hole recombination at the FTO hematite interface. The photocurrent response to illumination from the substrate and the electrolyte side reveals that efficient electron collection is only achieved for films up to approximately 200 nm thick. Synthetic strategies, such as surface treatments or the modification of the photoactive material, leading to a further reduction in recombination, will allow the use of thicker porous electrodes to harvest more light and will form a central part of our future work.

9.5 References

(1) Brillet, J.; Cornuz, M.; Le, F. F.; Yum, J.-H.; Gratzel, M.; Sivula, K. *J. Mater. Res.* **2010**, *25*, 17.

(2) Neumann, B.; Bogdanoff, P.; Tributsch, H. *J. Phys. Chem. C* **2009**, *113*, 20980.

(3) Sivula, K.; Le, F. F.; Gratzel, M. *ChemSusChem* **2011**, *4*, 432.

(4) Cesar, I.; Kay, A.; Martinez, J. A. G.; Gratzel, M. *Journal of the American Chemical Society* **2006**, *128*, 4582.

(5) Kay, A.; Cesar, I.; Graetzel, M. *Journal of the American Chemical Society* **2006**, *128*, 15714.

(6) Sivula, K.; Zboril, R.; Le Formal, F.; Robert, R.; Weidenkaff, A.; Tucek, J.; Frydrych, J.; Graetzel, M. *Journal of the American Chemical Society* **2010**, *132*, 7436.

(7) Ling, Y.; Wang, G.; Wheeler, D. A.; Zhang, J. Z.; Li, Y. *Nano Lett.* **2011**, *11*, 2119.

(8) Frydrych, J.; Machala, L.; Tucek, J.; Siskova, K.; Filip, J.; Pechousek, J.; Safarova, K.; Vondracek, M.; Seo, J. H.; Schneeweiss, O.; Graetzel, M.; Sivula, K.; Zboril, R. *Journal of Materials Chemistry* **2012**, *22*, 23232.

(9) Bohn, C. D.; Agrawal, A. K.; Walter, E. C.; Vaudin, M. D.; Herzing, A. A.; Haney, P. M.; Talin, A. A.; Szalai, V. A. *Journal of Physical Chemistry C* **2012**, *116*, 15290.

(10) Saremi-Yarahmadi, S.; Wijayantha, K. G. U.; Tahir, A. A.; Vaidhyanathan, B. *Journal of Physical Chemistry C* **2009**, *113*, 4768.

(11) Zhang, P.; Kleiman-Shwarsctein, A.; Hu, Y.-S.; Lefton, J.; Sharma, S.; Forman, A. J.; McFarland, E. *Energy & Environmental Science* **2011**, *4*, 1020.

(12) Wang, G.; Ling, Y.; Wheeler, D. A.; George, K. E. N.; Horsley, K.; Heske, C.; Zhang, J. Z.; Li, Y. *Nano Letters* **2011**, *11*, 3503.

(13) Lian, X.; Yang, X.; Liu, S.; Xu, Y.; Jiang, C.; Chen, J.; Wang, R. *Applied Surface Science* **2012**, *258*, 2307.

(14) Deng, J.; Zhong, J.; Pu, A.; Zhang, D.; Li, M.; Sun, X.; Lee, S.-T. *Journal of Applied Physics* **2012**, *112*.

(15) Hu, Y.-S.; Kleiman-Shwarsctein, A.; Forman, A. J.; Hazen, D.; Park, J.-N.; McFarland, E. W. *Chemistry of Materials* **2008**, *20*, 3803.

(16) Mao, A.; Park, N.-G.; Han, G. Y.; Park, J. H. *Nanotechnology* **2011**, *22*.

(17) Kleiman-Shwarsctein, A.; Hu, Y.-S.; Forman, A. J.; Stucky, G. D.; McFarland, E. W. *Journal of Physical Chemistry C* **2008**, *112*, 15900.

(18) Kumari, S.; Tripathi, C.; Singh, A. P.; Chauhan, D.; Shrivastav, R.; Dass, S.; Satsangi, V. R. *Current Science* **2006**, *91*, 1062.

(19) Khan, S. U. M.; Zhou, Z. Y. *Journal of Electroanalytical Chemistry* **1993**, *357*, 407.

(20) Cesar, I.; Sivula, K.; Kay, A.; Zboril, R.; Graetzel, M. *Journal of Physical Chemistry C* **2009**, *113*, 772.

(21) Tang, H.; Matin, M. A.; Wang, H.; Deutsch, T.; Al-Jassim, M.; Turner, J.; Yan, Y. *Journal of Applied Physics* **2011**, *110*.

(22) Zandi, O., Klahr, B.M., Hamann, T.W. *Energy & Environmental Science* **2013**, *6*.

(23) Peter, L. M.; Wijayantha, K. G. U.; Tahir, A. *Faraday Discussions* **2011**.

(24) Wijayantha, K. G. U.; Saremi-Yarahmadi, S.; Peter, L. M. *Phys. Chem. Chem. Phys.* **2011**, *13*, 5264.

(25) Klahr, B.; Gimenez, S.; Fabregat-Santiago, F.; Bisquert, J.; Hamann, T. W. *Journal of the American Chemical Society* **2012**, *134*, 16693.

(26) Klahr, B.; Gimenez, S.; Fabregat-Santiago, F.; Hamann, T.; Bisquert, J. *Journal of the American Chemical Society* **2012**, *134*, 4294.

(27) Gimenez, S.; Dunn, H. K.; Rodenas, P.; Fabregat-Santiago, F.; Miralles, S. G.; Barea, E. M.; Trevisan, R.; Guerrero, A.; Bisquert, J. *Journal of Electroanalytical Chemistry* **2012**, *668*, 119.

(28) Redel, E.; Mirtchev, P.; Huai, C.; Petrov, S.; Ozin, G. A. *Acs Nano* **2011**, *5*, 2861.

(29) Berry, F. J.; Greaves, C.; McManus, J. G.; Mortimer, M.; Oates, G. *Journal of Solid State Chemistry* **1997**, *130*, 272.

(30) Morrish, R.; Rahman, M.; MacElroy, J. M. D.; Wolden, C. A. *Chemsuschem* **2011**, *4*, 474.

(31) Hamd, W.; Cobo, S.; Fize, J.; Baldinozzi, G.; Schwartz, W.; Reymermier, M.; Pereira, A.; Fontecave, M.; Artero, V.; Laberty-Robert, C.; Sanchez, C. *Physical Chemistry Chemical Physics* **2012**, *14*, 13224.

(32) Barroso, M.; Mesa, C. A.; Pendlebury, S. R.; Cowan, A. J.; Hisatomi, T.; Sivula, K.; Graetzel, M.; Klug, D. R.; Durrant, J. R. *Proceedings of the National Academy of Sciences of the United States of America* **2012**, *109*, 15640.

(33) Barroso, M.; Cowan, A. J.; Pendlebury, S. R.; Graetzel, M.; Klug, D. R.; Durrant, J. R. *Journal of the American Chemical Society* **2011**, *133*, 14868.

(34) Le Formal, F.; Graetzel, M.; Sivula, K. *Advanced Functional Materials* **2010**, *20*, 1099.

(35) Hisatomi, T.; Dotan, H.; Stefik, M.; Sivula, K.; Rothschild, A.; Graetzel, M.; Mathews, N. *Advanced Materials* **2012**, *24*, 2699.

(36) Stengel, M.; Spaldin, N. A. *Nature* **2006**, *443*, 679.

10 Ultrasmall Co_3O_4 nanoparticles drastically improving solar water splitting on mesoporous hematite

10.1 Introduction

Efficient photoelectrochemical water splitting to hydrogen and oxygen may be one of the technologies to overcome our dependency on fossil fuels and help to establish a carbon-neutral hydrogen economy.[1,2] Although hydrogen is the desired end product, the very slow kinetics and high overpotential of the oxygen generation are the limiting factors for the efficiency of the total water splitting process. Therefore, searching for efficient materials for (photo-)electrochemical oxygen generation is of great importance for improving the efficiency of water splitting.

Cobalt compounds are known to be among the most efficient materials for the oxygen evolution reaction (OER). This was demonstrated for the electrolysis of water as well as for photoelectrochemical water splitting in combination with absorbing semiconductors. Artero *et al.* have shown the catalysis of both the hydrogen and oxygen evolving reactions with cobalt-based complexes.[3] Alternatively, a cobalt-oxo/hydroxo-phosphate layer is reported to mediate H_2 evolution and this layer can also be electrochemically converted into an amorphous cobalt oxide film ("Co-Pi") catalyzing the OER.[4]

Surface treatments with cobalt compounds were found especially important for enhancing the photoelectrochemical water splitting efficiency on hematite photoanodes. Hematite has attracted a lot of attention in the last years because of the combination of several attractive features for solar water splitting.[5-7] Hematite is a cheap, non-toxic and abundant semiconductor absorbing in the visible region with suitable energy levels for the water oxidation.[8] However, hematite also suffers from serious limitations such as a low hole

mobility, poor optical absorption and especially the sluggish kinetics of the oxygen evolution reaction, limiting the OER efficiency to only 1.17 %.[1,9] Furthermore, electron recombination at the surface is another serious factor drastically deteriorating the OER efficiency. This factor becomes dominating for nanostructured hematite with a high surface area, which is however considered one of the most promising morphologies for photoelectrochemical water splitting.[7,10-12] The surface treatments of these hematite films include the deposition of a several hundred nanometers thick electrodeposited cobalt-phosphate "Co-Pi" catalyst[13-16] or the atomic layer deposition of submonolayers of a $Co(OH)_2/Co_3O_4$ catalyst.[12] The role of these surface treatments is not yet fully understood.[17] Alternatively, a deposition of cobalt(II)-nitrate is reported to suppress the surface recombination but not to catalyze the hole transfer.[18]

In spite of the obvious benefits brought by surface treatments of hematite with cobalt compounds, there are still significant problems concerning the fabrication of suitable cobalt oxide morphologies in a controllable way on different substrates. The reported approaches rely either on in-situ formation or electrochemical deposition of cobalt compounds. Furthermore, the reported methods are not always applicable to the desired substrates or have dimensions too large (e.g. several 100 nm thick layers) to be compatible with porous or structured substrates. From this point of view, it is very desirable to have dispersible nanoparticles that can be deposited in a controllable process with a tunable thickness. Nanocrystalline Co_3O_4, which exhibits a spinel structure, was prepared in a TOPO ligand-stabilized procedure and can be dispersed in toluene.[19] Co_3O_4 is known to show the highest turnover frequency for dark water oxidation among the cobalt oxides, and the catalytic activity is enhanced with decreasing size of the crystalline domains.[19] However, the reported TOPO-based procedure only yields agglomerated particles with sizes that are above 10 nm, which makes them incompatible for the application on mesoporous structures and does not

exploit the full potential of decreased size. Defined Co_3O_4 nanoparticles that were grown *in situ* on hematite nanorods were reported to lead to an increased photocurrent by about 67 %.[20] However, the fabrication of single dispersible Co_3O_4 nanoparticles was not reported so far.

Here we report the solvothermal synthesis of ultrasmall, dispersible and crystalline Co_3O_4 nanoparticles that can be easily and homogeneously distributed on a mesoporous Sn-containing hematite electrode by a simple drop-casting process. Increases in photocurrent of up to 340 % were observed, and could be attributed to an improved effective electron collection depth, probably related to a decrease in electron recombination.

The following experiments have been performed as a joint project: The Co_3O_4 nanoparticles and the Sn-containing hematite electrodes were synthesized and characterized by Johann M. Feckl. TEM measurements were conducted by Alexander Müller in the group of Prof. Christina Scheu. Testing of the performance in photoelectrochemical water splitting was done by Halina K. Dunn in the group of Prof. Thomas Bein.

10.2 Results and discussion

Co_3O_4 nanoparticle synthesis

Co_3O_4 nanoparticles were prepared in a solvothermal sol-gel procedure in *tert*-butanol. This solvent was already shown to be suitable for the preparation of other highly dispersible, crystalline and ultra-small metal-oxide nanoparticles, such as TiO_2, Nb-doped TiO_2, $Li_4Ti_5O_{12}$ and NiO (Chapters 3 – 8).[21-23] In a typical procedure for the preparation of Co_3O_4 nanoparticles, $Co(OAc)_2$ was dispersed in a solution of Pluronic P123 in *tert*-butanol. After the addition of concentrated nitric acid to the reaction solution, the reaction mixture was autoclaved at 120 °C for 17 h. We found that only a combination of $Co(OAc)_2$, nitric acid and

Pluronic leads to the formation of small non-agglomerated particles. The use of $Co(NO_3)_2$ as precursor causes a fast uncontrollable growth of larger nanocrystals whose size cannot be decreased by reaction conditions or by addition of stabilizing ligands. On the other hand, the use of $Co(OAc)_2$ as precursor leads to formation of mainly amorphous material. We believe that the combination of $Co(OAc)_2$ precursor with nitric acid leads to an in-situ formation of reactive $Co(NO_3)_2$ which can form Co_3O_4, but is effectively capped by acetate ligands limiting the particle growth. Additionally, the presence of Pluronic P123 helps to stabilize and limit the particle growth.

After cooling to room temperature the nanoparticles can be collected by simply drying the processed solution. X-ray diffraction of the obtained solid proves the formation of about 7 nm small nanoparticles of Co_3O_4 (size calculated with Scherrer equation from the broadening of the 311 reflection) (Figure 10-1). The high background in the XRD pattern is attributed to the fluorescence of cobalt-containing material using Cu K_α radiation. The solid is easily re-dispersible in ethanol upon addition of a drop of concentrated acetic acid, as indicated by dynamic light scattering measurements (DLS) in Figure 10-1, which show a narrow peak at around 7 nm.

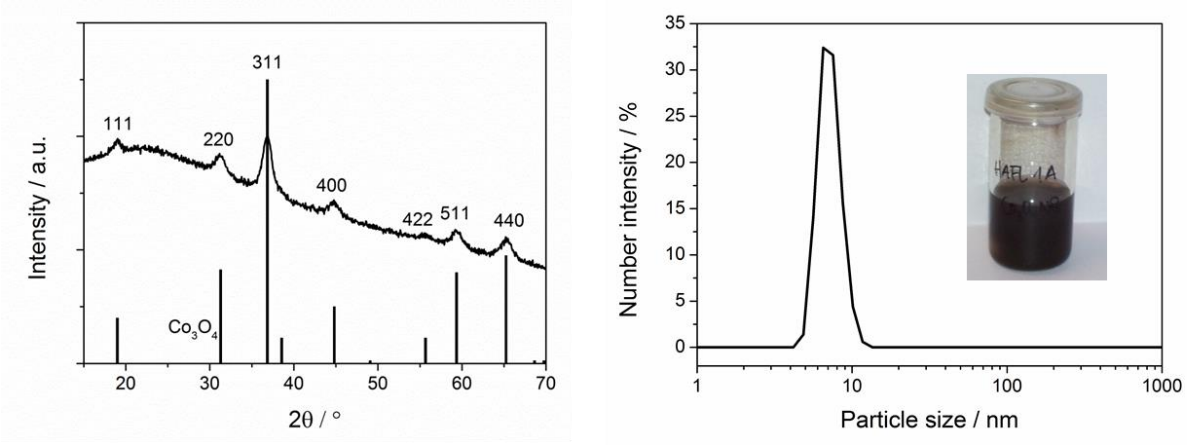

Figure 10-1: Left: XRD pattern of the Co_3O_4 nanoparticles with the corresponding ICDD card 00-043-1003. Right: DLS measurement of the Co_3O_4 nanoparticle dispersion, the inset shows a photograph of a dispersion with a concentration of 22.8 mg Co_3O_4 nanoparticles after drying, dispersed in 4 mL ethanol.

Data from thermogravimetric analysis measurements (TGA) confirm the presence of organic residues on the surface of the nanoparticles with a weight loss of about 70 % above 300 °C, which can be attributed to the evaporation and combustion of the surface ligands and the Pluronic P123 on the Co_3O_4 nanoparticles (Figure 10-2).

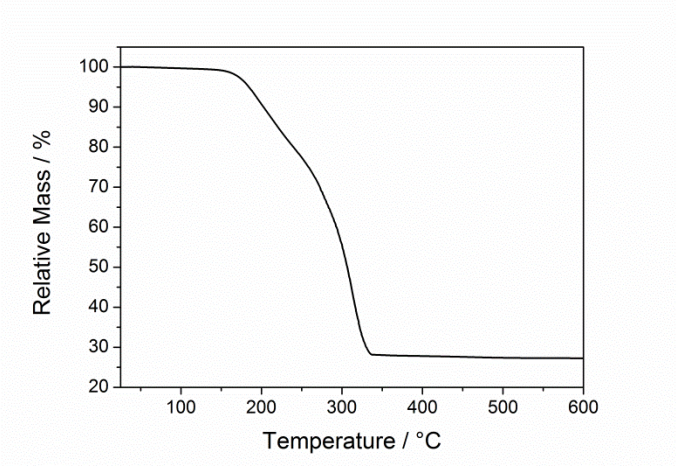

Figure 10-2: TGA curve of the dried Co_3O_4 nanoparticles.

In good agreement with the data obtained by XRD and DLS, high-resolution transmission electron microscope images (HRTEM) show nanoparticles in the range of 3 – 7 nm exhibiting lattice fringes with typical d-spacings for Co_3O_4 (Figure 10-3). The particles are non-

agglomerated and equally distributed on the surface of the TEM grid, indicating the high dispersibility in ethanol (Figure 10-3, left).

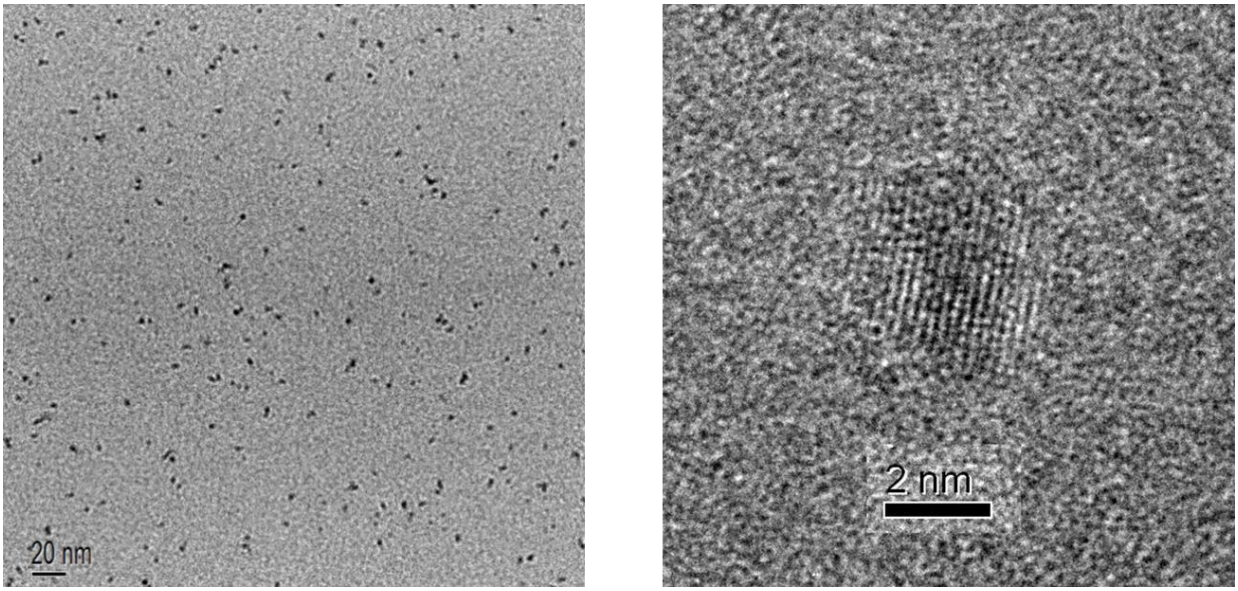

Figure 10-3: Left: TEM image of finely dispersed Co_3O_4 nanoparticles. Right: HRTEM image of a single Co_3O_4 nanoparticle.

The ultrasmall and dispersible Co_3O_4 nanoparticles were applied as a surface treatment on mesoporous Sn-containing hematite layers that were prepared as described in Chapter 9. The deposition was conducted via a simple drop-casting procedure from an ethanolic dispersion. After the deposition onto the electrodes, these were heated to 150 °C. This step was necessary to provide a good adhesion of the nanoparticles to the mesoporous layer. The resulting homogeneous distribution of the nanoparticles in the porous structure is depicted in Figure 10-4. The cross-sectional TEM image shows the dense FTO substrate on the bottom and the porous Sn-containing hematite layer on the top (Figure 10-4, left). HAADF-TEM imaging reveals the homogeneous distribution of the Co_3O_4 nanoparticles on the porous hematite (Figure 10-4, right). The mass loading of the Co_3O_4 nanoparticles (derived from the concentration in solution) onto an electrode area of 2.25 cm^2 corresponds to 57 µg.

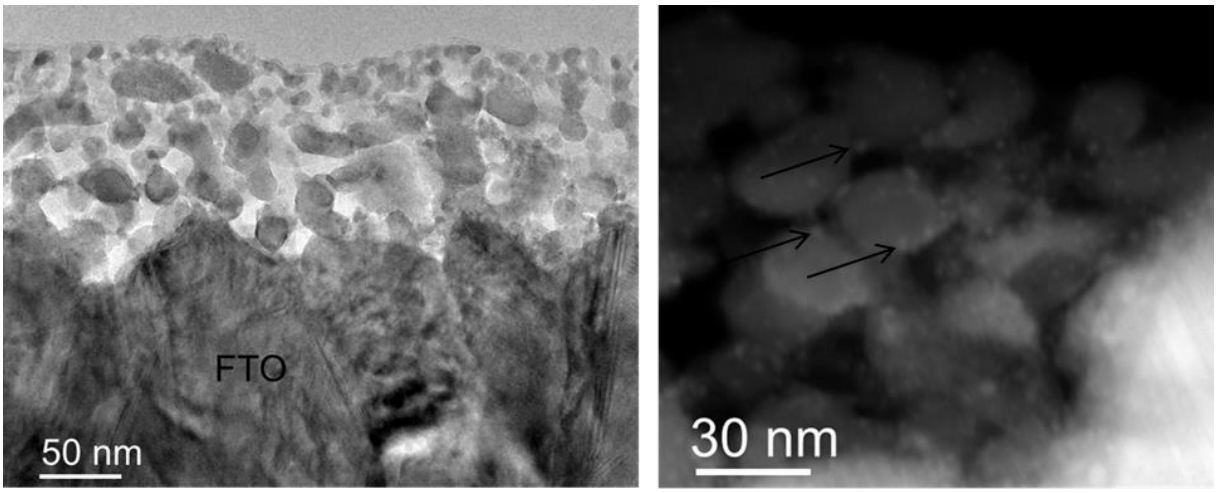

Figure 10-4: Left: Cross-section TEM image of a Sn-containing hematite film with finely dispersed cobalt-oxide nanoparticles on the surface of the mesoporous electrodes. Right: HAADF image in which the Co_3O_4 nanoparticles appear as bright spots and are indicated with arrows.

The hematite films treated in this way were tested in photoelectrochemical water splitting experiments as electrodes for the OER. The photocurrent-voltage curves obtained under AM1.5 illumination are displayed in Figure 10-5 for a 250 nm mesoporous hematite film with and without the Co_3O_4 nanoparticle surface treatment. The treatment leads to a substantial increase in photocurrent of about 90 %. No cathodic shift in onset potential was detected as would be expected if the Co_3O_4 nanoparticles were acting as catalysts. Therefore, we can assume that some other mechanism is the cause of the Co_3O_4 activity. To get some insights into the mechanism, we have investigated the photoelectrochemical characteristics of the electrodes illuminated from the substrate side (SI) and the electrolyte side (EI). For EI illumination, the electrons are generated far away from the surface and therefore have a long pathway to be collected at the FTO substrate, whereas for SI illumination the electrons are generated very close to the surface. This method enables us to distinguish whether the Co_3O_4 surface treatment reduces electron hole recombination on the porous electrodes. For the untreated hematite electrode, the measured photocurrent upon illumination through the electrolyte (EI) is approximately a quarter of that obtained upon illumination through the substrate (SI). Assuming a uniform porous layer, this indicates that a considerable proportion

of photogenerated electrons are not collected when generated far from the collecting FTO substrate. Upon application of Co_3O_4 nanoparticles to the 250 nm thick mesoporous hematite layer, the photocurrent when illuminating through the electrolyte (EI) increases drastically by 340 % which is even higher than the 90 % increase for substrate illumination (SI), (Figure 10-5a). This result indicates that the role of this surface treatment is a reduction of electron-hole recombination.

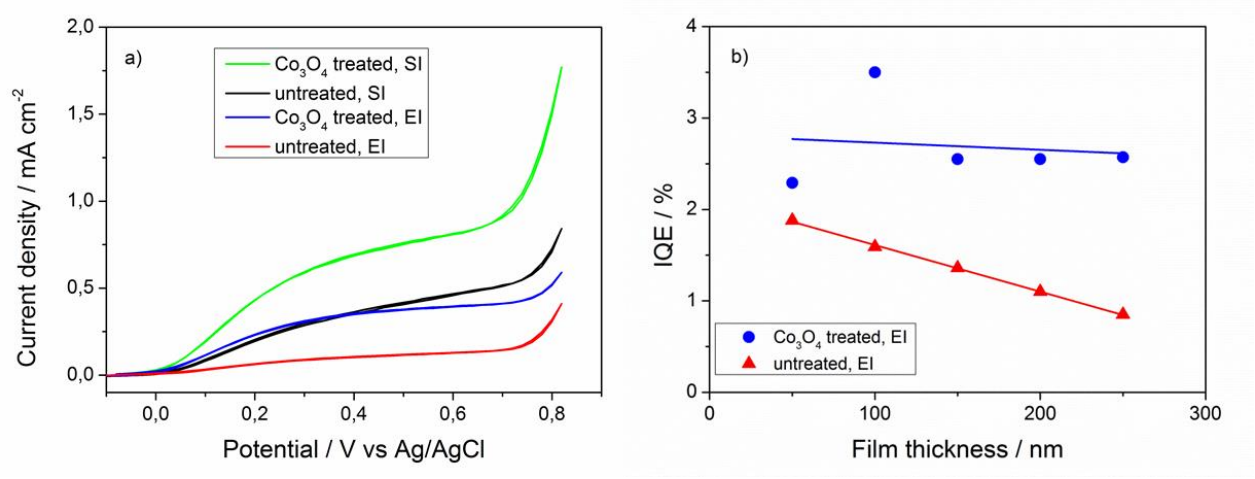

Figure 10-5: a) Current-potential curves of 250 nm thick mesoporous hematite films prepared with 20 % Sn-precursor with and without Co_3O_4 treatment under AM 1.5 illumination for different illumination directions. b) IQE of the untreated and Co_3O_4 treated films with different film thicknesses measured at 455 nm illumination under 1 Sun bias light.

In order to further investigate this point, the internal quantum efficiency (IQE) of mesoporous layers with thicknesses ranging from approximately 50 nm to 250 nm was determined for strongly absorbed illumination (λ = 455 nm), incident through the electrolyte (EI). The IQE of untreated photoanodes decreases continuously with the film thickness, while that of the Co_3O_4 treated photoanodes remains constant over the whole range of thicknesses studied here (Figure 10-5b). The efficiency of electron collection for Co_3O_4 treated photoanodes therefore does not depend on their thickness, which is strong evidence that electron recombination is significantly reduced by application of the Co_3O_4 nanoparticle surface treatment.

The observed reduction in electron recombination upon cobalt oxide treatment is in agreement with Peter *et al.*, whose intensity modulated photocurrent spectroscopy study showed that application of cobalt nitrate to compact hematite films reduced the rate of surface electron hole recombination by up to 2 orders of magnitude.[24] Barroso *et al.* also demonstrated an increase in photogenerated hole lifetime by three orders of magnitude by transient absorption spectroscopy.[15]

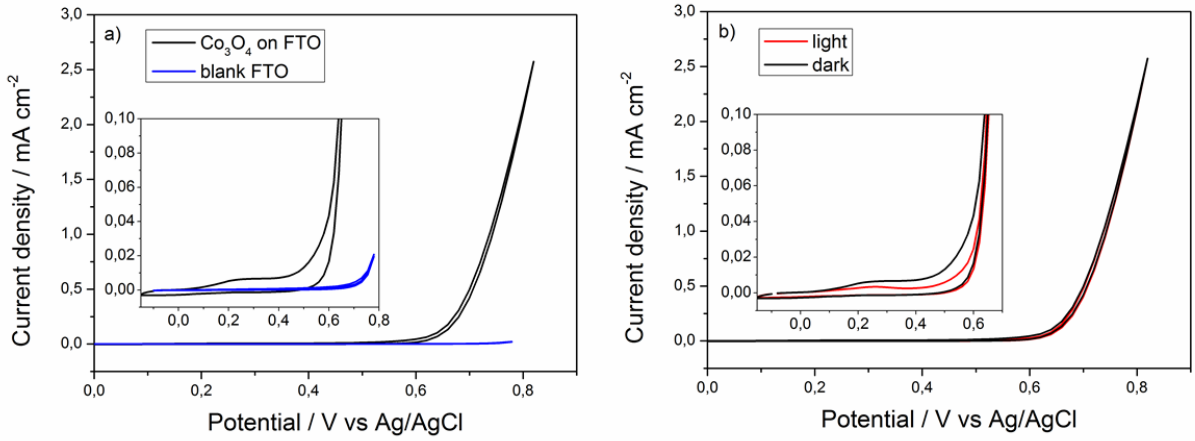

Figure 10-6: a) Dark cyclic voltammograms of a blank and a Co_3O_4 treated FTO electrode. b) Cyclic voltammograms of a Co_3O_4 treated FTO electrode in the dark und under illumination (AM 1.5).

To verify that the observed increase in photocurrent for the Co_3O_4 nanoparticle treated films is an effect of reduced surface recombination and not due to a photoelectrochemical activity of the Co_3O_4 nanoparticles, measurements of the nanoparticles alone on FTO glass substrates were conducted. The dark current of FTO glass substrates coated with Co_3O_4 nanoparticles was compared to blank FTO electrodes (Figure 10-6a). The anodic onset potential shifts almost 200 mV cathodically, indicating that Co_3O_4 nanoparticles are acting as catalysts for electrochemical water oxidation on FTO. This is in agreement with studies that proved Co_3O_4 to be a good alternative to expensive catalysts such as IrO_2 for electrochemical water oxidation.[19,20] However, comparing the photocurrent of a Co_3O_4 nanoparticle treated FTO

electrode under AM 1.5 illumination to the current from the dark measurement, no photoactivity of Co_3O_4 can be observed (Figure 10-6b). This is in good agreement with the results of the IQE and different illumination side studies, which indicated that the Co_3O_4 treatment causes a reduced surface recombination on the photoactive hematite layers.

10.3 Conclusions

Ultra small Co_3O_4 nanoparticles were synthesized via a *tert*-butanol synthesis. The high dispersibility and the very small size allows for an easy distribution of these crystalline nanoparticles on mesoporous surface Sn-enriched hematite layers by a simple drop-casting process. This treatment brings about significant improvements in photoelectrochemical water oxidation, increasing the obtained photocurrent by up to 340 %. This improved photocurrent is attributed to a significant reduction in electron hole recombination at the surface of the mesoporous network.

10.4 Experimental

Ultra-small Co_3O_4 nanoparticle synthesis

Co_3O_4 nanoparticles were synthesized in *tert*-butanol. All chemicals were purchased from Sigma-Aldrich and used as received. *tert*-Butanol was dried over a 4 Å molecular sieve at 28 °C and filtered prior to use. In a typical reaction 50 mg (0.2 mmol) of $Co(OAc)_2$ tetrahydrate was dispersed in a solution of 58 mg Pluronic P123 in 14 mL *tert*-butanol. To accelerate the synthesis, 48 mg of concentrated nitric acid was added to the reaction solution. The reaction mixture was transferred into a Teflon lined steel autoclave (20 mL volume) and kept at 120 °C for 17 h. The nanoparticles can be collected by simply drying the processed

solution. The content of Co_3O_4 of the resulting solid was determined to be 30 wt% by thermogravimetric analysis (Netzsch STA 440 C TG/DSC). The solid was then redispersed in ethanol with concentrated acetic acid (35 mg acetic acid per 22.8 mg solid in 4 mL ethanol). This dispersion was used as prepared for DLS measurements, the preparation of TEM samples and the photo-electrochemical water splitting experiments.

Photoelectrode preparation

The precursor solution for the 20 % Sn-precursor based hematite was prepared according to a procedure described in detail in Chapter 9. In brief, 0.111 g (0.313 mmol) $Sn(OAc)_4$ was first dispersed under vigorous stirring for 5 h and 15 min sonication in a mixture of Pluronic P123 (0.25 g) and 10 mL *tert*-butanol. Afterwards, 0.505 g (1.25 mmol) $Fe(NO_3)_3 \cdot 9H_2O$ was dissolved in the dispersion under sonication for 15 minutes and then 2.5 mL water (Millipore) was added forming a dark red solution. The solution was stirred at room temperature overnight resulting in a light brown dispersion of iron oxide. After cleaning the FTO glass (TEC 15 Pilkington TEC Glass™, 2.5x1.5 cm) by sequential sonication for 15 min each in detergent (1 mL Extran in 50 mL Millipore water), water (Millipore) and ethanol, the substrates were dried and masked with Scotch Tape on the conducting side to retain a non-covered area of 1.5x1.5 cm². The back of the substrates was completely masked to avoid contamination during the spin-coating procedure that would lead to a deterioration of the optical transparency of the substrates. Before spin coating, the fresh solutions were filtered through a 220 nm syringe filter (Sartorius minisart cellulose acetate membrane) to remove agglomerates, ensuring the preparation of homogeneously smooth films. The masked substrates were covered with 100 µL of solution and spun at 1000 rpm for 30 seconds. To increase the film thickness the films were dried for 5 minutes at 60 °C and spin-coated again.

To remove the template and crystallize the material, the samples were calcined in a laboratory oven (3 hour ramp to 600 °C, 30 min dwell time). This results in films of about 50 nm thickness, which can be increased linearly by repeating the complete procedure.

A Co_3O_4 nanoparticle surface treatment was applied to the Sn-containing mesoporous hematite thin films by drop casting. After depositing 10 µL of the Co_3O_4 nanoparticle dispersion in ethanol as described above onto a projected electrode area of 2.25 cm^2, the films were heated to 150 °C for 30 min. This step was necessary to provide a good adhesion of the nanoparticles to the mesoporous layer.

Materials characterization

X-ray diffraction analysis of the powders on microscopy slides was carried out in reflection mode (Bragg-Brentano) using a Bruker D8 Discover with Ni-filtered CuK_α-radiation and a position-sensitive detector (LynxEye). Raman spectra were recorded on a Jobin Yvon Horiba HR800 UV Raman microscope using a HeNe laser emitting at 632.8 nm. Scanning electron microscopy (SEM) was performed on a JEOL JSM-6500F scanning electron microscope equipped with a field emission gun. The analysis of the cross-section samples in TEM was carried out on a FEI Titan 80-300 (S)TEM with a Fischione Instruments (Model 3000) high angle annular dark field (HAADF) detector and an EDAX Energy-dispersive X-Ray Spectroscopy (EDX) detector. All measurements were conducted at an acceleration voltage of 300 kV. Dynamic light scattering (DLS) of the cobalt oxide nanoparticles was performed using a Malvern Zetasizer-Nano equipped with a 4 mW He-Ne laser (633 nm) and an avalanche photodiode detector. The scattering data were weighted based on particle number.

Photoelectrochemical characterization

Hematite photoelectrodes were masked with a Teflon-coated glass fiber adhesive tape leaving a circular area of 1 cm in diameter exposed to a 0.1 M NaOH aqueous electrolyte. All electrochemical measurements were carried out with glass or quartz cells using a μ-Autolab III potentiostat equipped with a FRA2 impedance analyzer connected to a saturated Ag/AgCl (or a Hg/HgO) reference electrode and a Pt mesh counter electrode. The light intensity was measured inside the cells using a 4 mm^2 photodiode, which had been calibrated against a certified Fraunhofer ISE silicon reference cell equipped with a KG5 filter.

The current-voltage characteristics of the films were obtained by scanning from negative to positive potentials in the dark or under illumination, with a 20 $mV\ s^{-1}$ sweep rate. Illumination, which was either provided by a high power light emitting diode (LED, Thorlabs, 455 nm), or an AM1.5G solar simulator (Solar Light Model 16S) at 100 $mW\ cm^{-2}$, was incident either through the substrate (SI) or the electrolyte (EI). For external quantum efficiency (EQE) measurements, chopped monochromatic light (chopping frequency 2 Hz) was provided by a 150 W xenon lamp in combination with a monochromator and order-sorting filters. The cell was biased to 1.23 V vs. RHE under simulated solar irradiation to ensure realistic operating conditions. The current recorded by the Autolab potentiostat was output to a lock-in amplifier synchronized to the chopper frequency. The UV-visible absorbance spectra necessary for the calculation of the internal quantum efficiency (IQE) of the mesoporous thin films on FTO were calculated from the transmission and reflectance according to the following formula: $A = \log(T+R)^{-1}$. The absorbance of the FTO substrate, calculated in the same way, was then subtracted from the full sample, resulting in the absorbance of the hematite film only.

10.5 References:

(1) Bolton, J. R.; Strickler, S. J.; Connolly, J. S. **1985**, *316*, 495.

(2) Walter, M. G.; Warren, E. L.; McKone, J. R.; Boettcher, S. W.; Mi, Q.; Santori, E. A.; Lewis, N. S. **2010**, *110*, 6446.

(3) Artero, V.; Chavarot-Kerlidou, M.; Fontecave, M. **2011**, *50*, 7238.

(4) Cobo, S.; Heidkamp, J.; Jacques, P.-A.; Fize, J.; Fourmond, V.; Guetaz, L.; Jousselme, B.; Ivanova, V.; Dau, H.; Palacin, S. **2012**, *11*, 802.

(5) Hamann, T. W. **2012**, *41*, 7830.

(6) Lin, Y.; Yuan, G.; Sheehan, S.; Zhou, S.; Wang, D. **2011**, *4*, 4862.

(7) Sivula, K.; Le Formal, F.; Grätzel, M. **2011**, *4*, 432.

(8) Katz, M. J.; Riha, S. C.; Jeong, N. C.; Martinson, A. B. F.; Farha, O. K.; Hupp, J. T. **2012**, *256*, 2521.

(9) Brillet, J.; Yum, J.-H.; Cornuz, M.; Hisatomi, T.; Solarska, R.; Augustynski, J.; Graetzel, M.; Sivula, K. **2012**, *6*, 824.

(10) Cesar, I.; Kay, A.; Martinez, J. A. G.; Gratzel, M. **2006**, *128*, 4582.

(11) Kay, A.; Cesar, I.; Graetzel, M. *J. Amer. Chem. Soc.* **2006**, *128*, 15714.

(12) Riha, S. C.; Klahr, B. M.; Tyo, E. C.; Seifert, S.; Vajda, S.; Pellin, M. J.; Hamann, T. W.; Martinson, A. B. F. **2013**.

(13) Klahr, B.; Gimenez, S.; Fabregat-Santiago, F.; Bisquert, J.; Hamann, T. W. **2012**, *134*, 16693.

(14) Zhong, D. K.; Sun, J.; Inumaru, H.; Gamelin, D. R. **2009**, *131*, 6086.

(15) Barroso, M.; Cowan, A. J.; Pendlebury, S. R.; Grätzel, M.; Klug, D. R.; Durrant, J. R. **2011**, *133*, 14868.

(16) Zhong, D. K.; Gamelin, D. R. **2010**, *132*, 4202.

(17) Gamelin, D. R. **2012**, *4*, 965.

(18) Cummings, C. Y.; Marken, F.; Peter, L. M.; Tahir, A. A.; Wijayantha, K. G. U. **2012**, *48*, 2027.

(19) Chou, N. H.; Ross, P. N.; Bell, A. T.; Tilley, T. D. **2011**, *4*, 1566.

(20) Xi, L.; Tran, P. D.; Chiam, S. Y.; Bassi, P. S.; Mak, W. F.; Mulmudi, H. K.; Batabyal, S. K.; Barber, J.; Loo, J. S. C.; Wong, L. H. **2012**, *116*, 13884.

(21) Liu, Y.; Szeifert, J. M.; Feckl, J. M.; Mandlmeier, B.; Rathousky, J.; Hayden, O.; Fattakhova-Rohlfing, D.; Bein, T. **2010**, *4*, 5373.

(22) Feckl, J. M.; Fominykh, K.; Döblinger, M.; Fattakhova-Rohlfing, D.; Bein, T. **2012**, *51*, 7459.

(23) Szeifert, J. M.; Feckl, J. M.; Fattakhova-Rohlfing, D.; Liu, Y.; Kalousek, V.; Rathousky, J.; Bein, T. **2010**, *132*, 12605.

(24) Wijayantha, K. G. U.; Saremi-Yarahmadi, S.; Peter, L. M. *Physical Chemistry Chemical Physics* **2011**, *13*, 5264.

11 Conclusion and Outlook

The focus of this thesis was the development of a general chemical synthesis method for ultra-small, crystalline metal-oxide nanoparticles in *tert*-butanol. The high dispersibility and the extremely small sizes down to about 3 nm enabled the fabrication of mesoporous materials in low-temperature bottom-up surfactant templated syntheses. Additionally, the unique properties of the solvent and reactant *tert*-butanol allow for the formation of materials with aromatics-free surfaces that are easily accessible in electronic applications. Hence, the obtained materials were applied successfully in energy storage and conversion applications, such as lithium ion batteries, dye-sensitized solar cells and photoelectrochemical water splitting.

The synthesis of ultrasmall and dispersible titania nanoparticles and their assembly into nanostructured mesoporous thin films was shown in Chapters 3 – 5. These were applied as electrodes for electrochemical lithium ion storage, as photoanodes in dye-sensitized solar cells and as high-refractive index porous layers in Bragg stacks for chemical vapor sensing. The increased performance of the films in these applications was made possible by the unique properties of the nanoparticulate building blocks and the high crystallinity of the mesoporous materials. The high crystallinity compared to sol-gel processed samples is attributed to a seeding effect of the nanoparticles in the pore walls. Furthermore, the high surface area enables high dye loadings which lead to an improved performance in DSCs, while thin pore walls lead to shorter diffusion pathways, thereby improving the performance in electrochemical lithium insertion. The electronic properties of the titania nanoparticles and the corresponding mesoporous films can be modified by doping the nanoparticles with niobium in an adapted *tert*-butanol nanoparticle synthesis (Chapter 6). The resulting Nb-doped titania is a

transparent conducting oxide which can be a suitable candidate for applications in optoelectronic devices.

Nanostructuring of lithium titanate in a similar approach as for the mesostructuring of titanium dioxide was achieved in a non-aqueous solvothermal synthesis in *tert*-butanol (Chapter 7). The fully interconnected crystalline mesoporous framework with pore walls of a few nanometers thickness drastically decreases the ion diffusion pathways in electrochemical lithium ion insertion. This enables the fabrication of electrodes with extremely fast charging kinetics which can be charged in only 4.5 s to 73 % of their maximum capacity.

The last part of this thesis discusses the application of ultrasmall nanoparticles for (photo-)electrochemical water splitting. In order to achieve this, the *tert*-butanol route was extended to non-titania systems and dispersible nickel oxide and cobalt oxide nanoparticles were synthesized (Chapters 8 and 10). The nickel oxide nanoparticles were assembled into thin film electrodes for electrochemical water splitting, reducing the onset potential for the oxygen evolution reaction by 180 mV. The high surface-to-volume ratio leads to very high turnover frequencies demonstrating the efficient catalytic properties of the material.

Cobalt oxide nanoparticles were applied as a surface treatment on mesoporous electrodes of Sn-containing hematite, which were prepared in a sol-gel surfactant directed synthesis in *tert*-butanol (Chapter 9). The combination of these two materials showed substantially increased photocurrents in photoelectrochemical water splitting experiments. This effect is attributed to reduced surface recombination, caused by both the Sn-inclusion at the surface of the mesoporous photoactive hematite electrodes and the homogeneous distribution of the ultrasmall cobalt oxide nanoparticles on the surface.

In conclusion, we have developed a novel synthesis strategy for the production of ultra-small, highly dispersible, crystalline nanoparticles of various metal-oxides in *tert*-butanol. These were successfully used as building blocks for the formation of mesoporous materials or homogeneously distributed as catalysts in porous hosts. The structural benefits and unique surface properties of the materials substantially enhanced device performance in the fields of (photo-)electrochemistry, photovoltaics and electrochemical energy storage.

Possible further developments aim at the expansion of the *tert*-butanol nanoparticle synthesis pathway to other (ternary) metal oxides and doped modifications thereof, for further applications in energy conversion and storage, or even beyond these fields, such as in biomedical or imaging applications. Furthermore, a model reaction system should be established to elucidate the reaction mechanism in the *tert*-butanol nanoparticle synthesis. Moreover, detailed surface characterization techniques could help to shed light on the surface chemistry of these nanoparticles and relate it to their unique properties.

12 Publications and Presentations

12.1 Publications

1. Ultrasmall Titania Nanocrystals and Their Direct Assembly into Mesoporous Structures Showing fast Lithium Insertion

   Szeifert, J. M., Feckl, J. M., Fattakhova-Rohlfing, D., Liu, Y., Kalousek, V., Rathousky, J. & Bein, T. *J. Am. Chem. Soc.* **2010**, *132*, 12605 – 12611.

2. Niobium-Doped Titania Nanoparticles: Synthesis and Assembly into Mesoporous Films and Electrical Conductivity

   Liu, Y., Szeifert, J. M., Feckl, J. M., Mandlmeier, B., Rathousky, J., Hayden, O., Fattakhova-Rohlfing, D. & Bein T. *ACS Nano.* **2010**, *4*, 5373 – 5381.

3. One-dimensional Metal-Organic Framework Photonic Crystals Used as Platforms for Vapor Sensing

   Hinterholzinger, F. M., Ranft, A., Feckl, J. M., Bein, T. & Lotsch, B. V., *J. Mater. Chem.*, **2012**, *22*, 10356 – 10362.

4. Nanoscale porous framework of lithium titanate for ultrafast lithium insertion

   Feckl, J. M., Fominykh, K., Döblinger, M., Fattakhova-Rohlfing, D. & Bein, T., *Angew. Chem. Int. Ed.* **2012**, *51*, 7459 – 7463.

5. Highly soluble energy relay dyes for dye-sensitized solar cells

   Margulis, G., Lim, B.G., Hardin, B., Unger, E.L., Yum, J., Feckl, J.M., Fattakhova-Rohlfing, D., Bein, T., Grätzel, M., Sellinger, A., McGehee, M., *Phys. Chem. Chem. Phys.* **2013**, *15*, 11306-11312.

6. Ultrasmall dispersible crystalline nickel oxide nanoparticles as high performance catalysts for electrochemical water splitting

   Fominykh, K.*, Feckl, J. M.*, Döblinger, M., Bein, T. & Fattakhova-Rohlfing, D, manuscript in preparation

7. Enhancement of the water splitting efficiency of mesoporous hematite films by surface enrichment of Sn-atoms

   Dunn*, H. K, Feckl, J. M.*, Müller, A., Fattakhova-Rohlfing, D., Peter, L. M., Scheu, C., Bein, T., manuscript in preparation.

8. Ultrasmall Co_3O_4 nanoparticles drastically improving solar water splitting on mesoporous hematite

   Feckl, J. M.*, Dunn, H. K.*, Zehetmaier, P., Müller, A., Peter, L. M., Scheu, C., Bein, T. & Fattakhova-Rohlfing, D., manuscript in preparation.

   *these authors contributed equally

12.2 Oral presentations

1. Mesoporous titania electrodes assembled from ultrasmall nanocrystals showing fast lithium insertion

   Johann Feckl, Johann Szeifert, Dina Fattakhova-Rohlfing, Yujing Liu, Vit Kalousek, Jiři Rathouský, Thomas Bein

   E-MRS Spring Meeting & E-MRS / MRS Bilateral Conference on Energy, **2011**, Nice, France.

2. Mesoporous metal oxide framework for ultrafast lithium insertion

   Johann Feckl, Ksenia Fominykh, Markus Döblinger, Dina Fattakhova-Rohlfing, Thomas Bein

   24. Deutsche Zeolith-Tagung, **2012**, Magdeburg, Germany.

3. Mesoporous photo-active hematite for solar water splitting

   Johann Feckl, Halina Dunn, Dina Fattakhova-Rohlfing, Thomas Bein

   25. Deutsche Zeolith-Tagung, **2013**, Hamburg, Germany.

4. Ultra-fast lithium insertion in a nanoscale porous framework of lithium titanate

   Johann Feckl, Ksenia Fominykh, Markus Döblinger, Dina Fattakhova-Rohlfing, Thomas Bein

   2nd International Conference on Materials for Energy, **2013**, Karlsruhe, Germany.

5. Mesoporous photo-active hematite for solar water splitting

   Johann Feckl, Halina Dunn, Dina Fattakhova-Rohlfing, Thomas Bein

   E-MRS Spring Meeting, **2013**, Strasbourg, France.

12.3 Poster presentations

1. Crystalline mesoporous titania films through surfactant-assisted assembly of ultrasmall and dispersible anatase nanocrystals.

   Johann Szeifert, Johann Feckl, Dina Fattakhova-Rohlfing, Yujing Liu, Thomas Bein

   16th International Zeolite Conference, **2010**, Sorrento, Italy

2. Crystalline mesoporous titania films through surfactant-assisted assembly of ultrasmall and dispersible anatase nanocrystals.

   Johann Szeifert, Johann Feckl, Dina Fattakhova-Rohlfing, Yujing Liu, Thomas Bein

   22. Deutsche Zeolith-Tagung, **2010**, Munich, Germany.

3. Crystalline mesoporous titania films through surfactant-assisted assembly of ultrasmall and dispersible anatase nanocrystals

   Johann Szeifert, Johann Feckl, Dina Fattakhova-Rohlfing, Yujing Liu, Thomas Bein

   CeNS Workshop "Nanosciences – Merging Disciplines", **2010**, Venice, Italy.

4. Synthesis of mesoporous titania films From ultrasmall anatase nanocrystals for applications in dye-sensitized solar cells

   Johann Feckl, Johann Szeifert, Dina Fattakhova-Rohlfing, Thomas Bein

   3rd international Conference on Hybrid and Organic Photovoltaics, **2011**, Valencia, Spain.

5. Nanoscale porous metal oxide framework for ultrafast lithium insertion

   Johann Feckl, Ksenia Fominykh, Markus Döblinger, Dina Fattakhova-Rohlfing, Thomas Bein

   MRS Spring Meeting, **2012**, San Francisco, USA.

6. Non-aqueous synthesis route for ultra-small metal-oxide nanoparticles

   Johann Feckl, Dina Fattakhova-Rohlfing, Ksenia Fominykh, Thomas Bein

   CeNS Workshop "Nanosciences: Soft, Solid, Alive and Kicking", **2012**, Venice, Italy.

7. Non-aqueous synthesis route for ultra-small metal-oxide nanoparticles

   Johann Feckl, Dina Fattakhova-Rohlfing, Ksenia Fominykh, Thomas Bein

   Soltech Inauguration Workshop, **2012**, Munich, Germany.

8. Non-aqueous synthesis route for ultra-small metal-oxide nanoparticles

   Johann Feckl, Dina Fattakhova-Rohlfing, Ksenia Fominykh, Thomas Bein

   1st Herrenhausen Conference (Volkswagen Foundation) “Downscaling Science”, **2012**, Hannover, Germany.

9. Light-driven water splitting on nanostructured hematite

   Halina Dunn, Johann Feckl, Alexander Müller, Ilina Kondofersky, Dina Fattakhova-Rohlfing, Christina Scheu, Thomas Bein

   Soltech Workshop, 2013, Kloster Banz, Germany.

10. Solvothermal synthesis of ultra-small semiconducting metal oxide nanoparticles

    Ksenia Fominykh, Johann Feckl, Thomas Bein, Dina Fattakhova-Rohlfing

    Soltech Workshop, 2013, Kloster Banz, Germany.